TIMING OBSERVATIONS OF THE VELA PULSAR, PSR0833-45

by

Reid
Andrew R. Klekociuk BSc. Hons.
Department of Physics.

Submitted in fulfilment of the requirements for the degree of
Doctor of Philosophy
University of Tasmania, December, 1989.

DECLARATION

This thesis contains no material which has been accepted for the award of any other higher degree or graduate diploma in any tertiary institution. To the best of the candidate's knowledge and belief, this thesis contains no material previously published or written by another person, except where due reference is made in the text of the thesis.

Andrew R. Klekociuk

ABSTRACT

The analysis is presented of pulse arrival time measurements of the Vela pulsar, PSR0833-45, obtained principally from near-daily observations conducted at the Llanherne Radiophysics Observatory (LRO) between October, 1981, and September, 1986. During this interval, the secular decrease in the rotation rate of the pulsar was interrupted by *glitch* events which occurred in October, 1981, August, 1982, and July, 1985. Each glitch was accompanied by an abrupt change in rotation frequency of fractional magnitude $\Delta\nu/\nu \approx -2\times10^{-6}$ of which less than 10% decayed within a subsequent interval of one year. The characteristics of these events were similar to those reported for the four previous glitches of the Vela pulsar. However, because of the regularity of the LRO observations, sufficient post-jump data were obtained to allow the reappraisal of the existing glitch models.

The timing obtained immediately prior to each glitch were found to be completely devoid of any distinctive precursor signatures above the level of measurement noise, even to within one hour of the July, 1985, glitch. In addition, there were no significant changes in the characteristics of the radio emission about the time of each glitch.

The timing signature of each glitch was investigated in terms of the existing viable models. The two-component model was rejected on the grounds of its inability to account for the long term relaxation behaviour. In addition, there was no evidence of the decoupling time predicted by the vortex creep model.

The phase noise on timescales less than 6 hours was found to exhibit excess power in comparison with the expectation from measurement uncertainties. There was no evidence for any significant systematic behaviour of the autocorrelation function of the phase fluctuations with respect to time lag. Evidence was found that the excess noise has a power-law dependence on observing frequency, which may be a result of magnetospheric processes.

Dual frequency measurements made between March and September, 1986, have for the first time enabled the character of short timescale variations in the dispersion delay along the path to the pulsar to be determined. The measurements are consistent with the motion of the line-of-sight through a region of inhomogeneous plasma located within the Gum Nebula.

ACKNOWLEDGEMENTS

It is with pleasure that I acknowledge the contribution made by my supervisors Dr. P.M. McCulloch and Prof. P.A. Hamilton in the preparation of this thesis. I thank Dr. McCulloch for providing expert advice on matters associated with the construction and operation of the radio-frequency instrumentation at the Llanherne observatory, and for his support during the project. My owe a debt of gratitude to Prof. Hamilton for providing encouragement and support, and advice on computational matters. I am indebted to both of my supervisors for relating their expert knowledge in the field of pulsar astronomy.

My heart-felt appreciation is extended to my mother for her care, support, and encouragement.

I am indebted to the expert technical support freely provided by the workshop staff of the Physics Department and in particular Mssrs. P. Button, G. Gowland, D. Harding, and B. Wilson.

My thanks are extended to Prof. G.R.A. Ellis for his encouragement during the project. The energy and enthusiasm displayed by Prof. Ellis has been a source of inspiration. I commend the efforts of Mr. G. Royle for his role in the development of the pulsar timing system used at the Llanherne observatory, and the collection of the data set prior to November, 1984. I thank Ms. C. Flanagan for providing a set of raw timing observations of the Vela pulsar for inter-comparison with the Llanherne data. Thanks also go to Mr. R. Yates of Telecom Austalia, and Dr. J. Luck of the Commonwealth Bureau of Mineral Resources for providing time transference data that was essential for the accurate alignment and tracking of the observatory time standard.

I express my appreciation of the support extended by the staff and graduate students of the Department of Physics. In particular, I wish to thank Dr. M.E. Costa, Dr. M.L. Duldig, Dr. K.B. Fenton, Dr. P.J. Hall, and Mr. T.D. van Ommen. I am indebted to Dr. G. Burns of the Upper Atmosphere Physics Section, Antarctic Division, Commonwealth Department of Arts, Sport, the Environment, Tourism and Territories, who has been my full-time employment supervisor since May, 1987. Dr. Burns provided invaluable support and encouragement which enabled the completion of this thesis. While writing this thesis I spent 16 months conducting an auroral research programme on Macquarie Island. I gratefully acknowledge support from a Commonwealth Postgraduate Research Award during the first four years of this project.

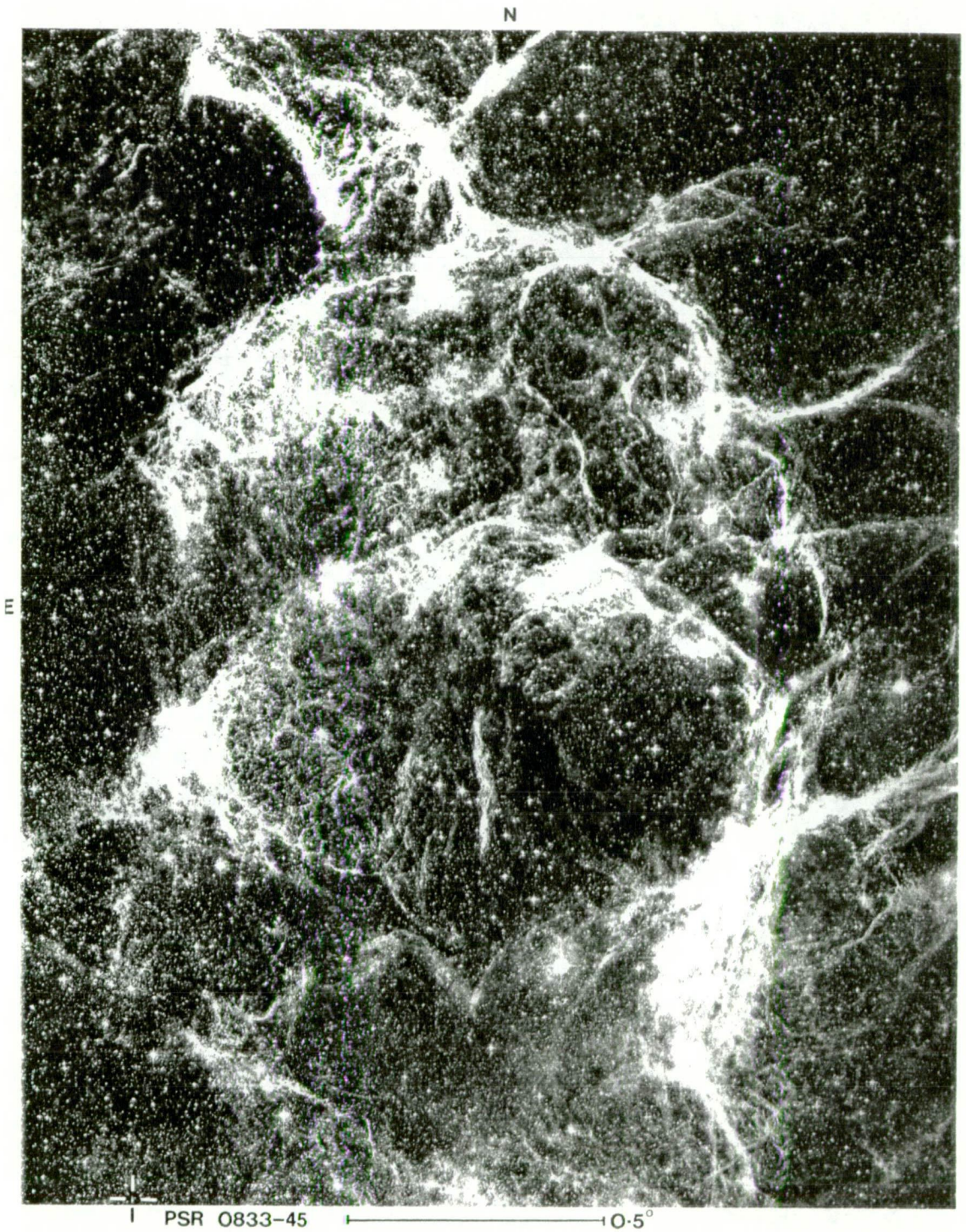

Frontispiece The north-west section of the Vela supernova remnant as recorded in H-α light. This region is part of the nebulosity known as Stromlo 16, and contains a highly inhomogeneous plasma which has been disturbed by the supernova explosion responsible for the creation of the Vela pulsar, PSR0833-45. The diffuse emission, most prominent in the lower portion of the photograph, is contributed by the Gum Nebula. The region contains several coeval stellar associations with early-type UV emitting members, as well as dark HI clouds. Unsharp mask photograph courtesy of the Royal Observatory Edinburgh.

CONTENTS

COMMONLY USED SYMBOLS

Boldface symbols denote vector quantities

α	Right Ascension
α_s	scattering spectral index
$\mathbf{B}$,B	magnetic field strength, vector
c	speed of light
C_n^2	scattering structure coefficient
D	dispersion coefficient
δ	declination
Δ_n	superfluid neutron energy gap
$\mathbf{E}$	electric field
E_P	pinning energy
ϕ	pulse phase
f	wave frequency
$\mathbf{F}_M$	Magnus force
I	total moment of inertia
$I_{c,p}$	normal matter, pinned superfluid moment of inertia
κ	quantum of vorticity
λ_p	London penetration depth
m_e	mass of electron
ν	pulse frequency
n_B	braking index
n_e	electron number density
N_m	torque
n_v	superfluid vortex number density
$\ddot{\nu}$	second time derivative of pulse frequency
$\dot{\nu}$	first time derivative of pulse frequency
P	pulse period
Q	fraction of glitch frequency jump recovered
q	wavenumber
q_e	charge of electron
ρ	mass density
ρ_0	nuclear matter density
r_e	classical electron radius
t	time
τ_{age}	characteristic age
t_s	spindown timescale
Ω	angular frequency
ω_{cr}	maximum differential angular rotation rate
$\ddot{\Omega}$	second time derivative of angular frequency
$\dot{\Omega}$	first time derivative of angular frequency
$\xi_{n,p}$	neutron, proton superfluid coherence length

COMMONLY USED ABBREVIATIONS

B1950.0	Besselian date of 0 UT on 0 January, 1950.
dec	declination
DM	dispersion measure
EOS	equation of state
JD	Julian date
MJD	modified Julian date = JD - 2440000.5
$M_\odot$	solar mass
MHD	magnetohydrodynamic
pc	parsec
RA	Right Ascension
RM	rotation measure
SN	signal-to-noise
SNR	supernova remnant
TI	tensor interaction (equation of state)
TJD	truncated Julian date = JD - 2440000.0
TOA	time-of-arrival
UTC	Coordinated Universal Time

CHAPTER 1 - NEUTRON STARS AND THE VELA PULSAR

1.1 INTRODUCTION

The Vela pulsar, PSR0833-45, is a particularly well-studied astrophysical object. It emits highly regular pulses of electromagnetic radiation throughout the radio, optical, and gamma-ray regions of the spectrum. Vela's characteristic pulse period of ~ 89 ms is evidently controlled by the rotational dynamics of an underlying magnetized neutron star, an entity remarkable by terrestrial standards, that is characterized by a radius of ~ 10 km, a mass of ~ 1.4 $M_{\odot}$, a central density exceeding that of nuclear matter (2.4×10^{14} g cm^{-3}), and a surface magnetic field strength of ~ 10^{12} G.

Neutron stars have been under scrutiny for the past five decades, and are today familiar objects. Shortly after the discovery of the neutron, Baade and Zwicky (1934) postulated their existence in order to account for the enormous energy release of supernova explosions. Oppenheimer and Volkoff (1939) showed that neutron stars were theoretically viable by considering the fully general-relativistic equation of hydrostatic balance within a Fermi gas of non-interacting neutrons. After this development, work proceeded slowly, concentrating on the refinement of the equation of state, which expresses pressure as a function of mass-density for matter under extreme physical conditions, in order to more precisely model the structure of neutron stars. Notably, it was shown that neutron stars of reasonable age and distance should be highly inconspicuous sources of thermal radiation (Tsuruta and Cameron, 1966) and as a result, it was widely regarded that they would remain theoretical curiosities.

This view changed dramatically with the serendipitous discoveries of radio pulsars and several classes of discrete and highly luminous galactic X-ray and gamma-ray sources (X-ray pulsars, bursters, quasi-periodic oscillators, galactic bulge sources, and gamma-ray bursters). The interpretation of the bewildering cache of observational data that has been accumulated for these objects has provided unequivocal evidence that magnetized neutron stars are intimately linked with their behaviour[a].

---

[a] For background information, the reader is referred to reviews of the characteristics of radio pulsars by Manchester and Taylor (1977) and Taylor and Stinebring (1986), and of high energy manifestations of neutron stars by White, Swank, and Holt (1983), Lewin and Joss (1981), van der Klis (1987), Joss and Rappaport (1984) and Bignami and Hermsen (1983).

The supernova origin of neutron stars is now well accepted (Woolsey and Weaver, 1986), largely due to the existence of the Crab pulsar (PSR0531+32) within the remnant of an historically recorded supernova. In addition, the processes of accretion-induced collapse and stellar coalescence within close binary systems are recognized as important birth mechanisms (van den Heuvel, 1987) based on the study of X-ray pulsars, and radio pulsars with millisecond periods.

Arguably, the most valuable information on neutron stars has been obtained from studies of pulse timing measurements of the radio and X-ray pulsars. The pulsed radiation of these objects evidently represents the cross-section of directional emission beams which sweep around the sky in rotational phase with the crust and magnetic field of an underlying neutron star. This interpretation is the corner-stone for the study of neutron-star rotational dynamics, a field that has significantly advanced the basic understanding of the evolution and structure of these objects.

Pulse timing measurements involve determination of the time of arrival of a fiducial phase of a pulse period in some frame of reference. In order to study phenomena intrinsic to the rotating neutron star and its immediate environment, the reference frame is chosen as that of the barycentre (centre of mass) of the solar system. In this way, the influence of the acceleration of the observer with respect to the neutron star due the orbital and rotational motion of Earth is accounted for. Usually, individual pulses are too weak to be detected above the intrinsic noise of the measurement system. This problem is overcome by the integration of the signals synchronous with an accurate estimate of the apparent pulse frequency. The important feature of the signals of radio pulsars is that the shape or *profile* of the waveform obtained after integrating over a few hundred or thousand periods is remarkably stable with time; the integration process averages out pulse-to-pulse temporal fluctuations imposed by phenomena related to the generation of the emission, and scattering processes in the line-of-sight plasma. Additionally, the pulse profile of radio pulsars is often simple and of narrow duty cycle. These features assist in the accurate determination of arrival times.

Normally, the fiducial phase of a profile is assigned a value ϕ representing the total number of phase cycles that have occurred since a reference epoch t_0. If the evolution of the pulse period is known with sufficient accuracy, pulse numbering is unambiguous. The value of ϕ is paired with the arrival time t which becomes the dependent variable. The relationship between ϕ and the pulse frequency ν is

$$\phi(t) = \int_{t_0}^{t} \nu(t')\, dt' \qquad 1.1$$

By fitting a model to individual measurements of $\phi(t)$, the value of ν at a particular epoch may be estimated.

A distinguishing feature between radio and X-ray pulsars is the manner in which their pulse frequencies evolve. With the exception of PSR2127+11[b], all radio pulsars for which there are sufficient measurements show a dominant *decrease* in pulse frequency with time. This behaviour is attributed to the loss of angular momentum from the crust of the underlying neutron star due to the action of *braking torques* that arise from the radiation of electromagnetic energy and the ejection of particles. Over intervals of years, $\nu(t)$ in equation 1.1 is adequately modelled by a Taylor series expansion with terms involving third and higher order derivatives of ν neglected, although Barcons, Portilla, and Sanz (1988) have suggested that this simple expression is unlikely to be suitable for abitrarily long timescales. The advantage in adopting the truncated Taylor series representation for ν is that providing the pulses are phase locked to the rotation of the crust, then the measured value of $\dot{\nu}(t)$ (the first time derivative of the pulse frequency) is physically related to the torque acting on the neutron star. This is of particular relevance for the investigation of pulsar radiation process as well as internal dynamics.

Both radio and X-ray pulsars display stochastic fluctuations in their intrinsic pulse frequencies termed *timing noise*. This behaviour is thought to reflect variations in the torques applied to the crust of the associated neutron stars, and possibly from changes in the beaming of the radiation. The study of timing noise has provided information on the environment of these objects, as well as insights on the nature of the coupling of the interior of neutron stars to their crust.

A small group of radio pulsars are evidently members of binary systems in which the companion object is a white dwarf or neutron star (Taylor and Stinebring, 1986). This association is revealed by the doppler oscillation of their pulse frequency about the general spindown trend. Similarly, the X-ray pulsars also show evidence for an underlying binary stellar association. However, unlike the radio pulsars, the observed radiation from these objects is a result of the transfer of matter onto the magnetic poles of the neutron star from a more normal stellar companion. Importantly, X-ray pulsars generally exhibit an erratic *increase* in pulse frequency which suggests that the crustal torque imposed by matter accretion dominates over the radiation braking torque.

---

[b] This pulsar lies within the globular cluster M15. It has a positive first time derivative of pulse frequency. This is interpreted by Wolszczan *et al.* (1989) as resulting from the gravitational acceleration of the pulsar towards the Earth by the inferred massive core of the cluster. This effect masks the spindown due to radiation torques (Appendix G).

The most important information directly relating to the internal structure of neutron stars has been obtained from the study of the phenomenon known as *glitches*. Glitches are a characteristic of radio pulsars that have been displayed by seven objects to date, including the Vela and Crab pulsars. A glitch is an infrequent and seemingly abrupt increase in rotation frequency that is large in comparison to the variations due to spindown and timing noise. Each glitch is followed by a characteristic relaxation effect which removes a fraction of the excess rotation frequency. During the relaxation, the first derivative of frequency, which also increases at the time of the glitch, recovers towards its usual spindown value over timescales of days to years, depending on the pulsar involved. However, in several cases, the steady state value of the derivative that is eventually attained has been greater than that prior to the glitch. Although a number of theories have been put forward to account for glitches, the general consensus is that these events are intimately linked with the dynamical consequences of neutron-star spindown on states of interior superfluid matter (Pines and Alpar, 1985).

It is difficult to observe the behaviour at the onset of a glitch owing to the evidently short timescales of the phenomena involved and the infrequency at which glitches occur. To date, the development of models has been based solely on the characteristics of the relaxation process. Unfortunately, it is not yet possible to predict the occurrence of glitches, mainly because only sparse statistics have been accumulated thus far. However, the glitches exhibited by the Vela and Crab pulsars occur at quasi-regular intervals. As a result, these objects have received considerable attention. In the case of Vela, the glitch epochs are separated by 2-3 years (Cordes, Downs, and Krause-Polstorff, 1988; hereafter CDK-P), while this interval is several years for the Crab pulsar (Lyne and Pritchard, 1987, and references therein). It is therefore only a matter of patience in order to observe a glitch of one of these objects in its entirety. Because both pulsars are relatively conspicuous at radio frequencies, several groups have found it feasible to dedicate instrumentation to the regular monitoring of their timing behaviour, principally with the aim of capturing a glitch; the first successful observations of this type were recently made for the Vela pulsar by Hamilton *et al.* (1989). The wealth of data accumulated in these long-term projects has been particularly valuable in studying the rich variety of timing phenomena which these pulsars exhibit.

The scrutiny of the Vela pulsar over the past two decades has revealed the occurrence of eight glitches with a typical magnitude expressed by the fractional changes $\Delta\nu/\nu \approx 1\text{-}2\times10^{-6}$ and $\Delta\dot{\nu}/\dot{\nu} \approx 10^{-2}$ (CDK-P; Flanagan and Hamilton, 1988). These quantities are large in comparison with those for the majority of glitches of other

pulsars. In addition, two much smaller though characteristically similar jumps have also occurred (CDK-P; Hamilton, *personal communication*, 1989). Aside from these obvious discontinuities, the pulsar's timing noise comprises fluctuations on a range of timescales with a bimodal amplitude distribution characterized by $|\Delta\nu/\nu| \leq 10^{-9}$ and $|\Delta\dot{\nu}/\dot{\nu}| \leq 10^{-4}$ (CDK-P).

The only existing published analyses of Vela's long-term timing behaviour have been presented by Downs (1981), Manchester *et al.* (1983) and CDK-P. These works utilized radio timing data collected by the facilities of the Jet Propulsion Laboratory (JPL) at approximately weekly intervals over a period of 14.5 years which ended in March, 1983. Unfortunately, the resolution of the measurements precluded the quantification of the pulsar's timing behaviour on timescales between ~2 hours and several days. This lack of information, particularly with regard to the immediate post-glitch behaviour, motivated a programme of intensive contiguous timing measurements of the Vela pulsar at the Llanherne Radio Observatory in Tasmania. Between October, 1981, and September, 1986, near-daily observations of up to 5.4 hours duration were conducted. An analysis of the data collected is presented in this thesis.

The Llanherne data has provided detailed information for three glitches as well as the pulsar's timing noise. The first 18 months of Llanherne observations overlapped with JPL measurements. The Llanherne data set has been augmented with observations made at the Haretbeesthoek Radio Astronomy Observatory (HRAO) in South Africa in order to support the identification of intrinsic fluctuations in the pulsar's timing parameters over the subsequent period. The Llanherne and HRAO data have also been jointly employed to indirectly study the variability of the delay introduced by the interstellar plasma on arrival of Vela's pulses. In addition, this aspect has been directly measured with unprecedented resolution using a series of dual frequency timing measurements made during 1986.

The plan of this thesis is as follows. In the remainder of this chapter, the physics of neutron stars and the characteristics of pulsars, with particular regard to the Vela pulsar, are reviewed. In chapters 2 and 3, the phenomenology and theoretical interpretation of pulsar glitches from the literature are presented. The observation and reduction techniques used for the Llanherne timing data are presented in Chapter 4. The short timescale noise and the significance of pulse shape variations are examined in Chapter 5. A detailed analysis of three large glitches appears in Chapter 6. Measurements of the frequency dispersion of pulse arrival times are presented and interpreted in Chapter 7. Conclusions are drawn in Chapter 8. The survey of the supporting literature used in this thesis was concluded in May, 1989.

1.2 NEUTRON STAR PHYSICS

1.2.1 Neutron Star Structure[b]

The macroscopic parameters of neutron stars are largely governed by the still uncertain equation-of-state (EOS) in the regime where the mass-density ρ exceeds that of nuclear matter ($\rho_0 = 2.8 \times 10^{14}$ g cm^{-3}) (Pandharipande, Pines, and Smith, 1976; hereafter PPS). For lower densities, the EOS is now fairly well understood. In the sections that follow, an overview is presented of the *standard* interpretation of neutron star structure (figure 1.1). It must be pointed out that only certain aspects of this picture have been tested through observation.

1.2.2 The Outer Crust

The cooling of neutron star matter is expected to be extremely rapid after formation via neutrino (and possibly pion) emission (Tsuruta, 1986). The temperatures throughout the bulk of the interior (10^8 - 10^{10} K for objects of reasonable age) are negligible compared with Fermi energies and so phenomena such as quantum degeneracy and superfluidity are likely to occur.

The largest thermal gradient occurs in the outer crust where the structure of matter is most strongly influenced by magnetic and thermal effects. The direct inference of surface temperatures has been possible for several objects through X-ray observations. These results are generally consistent with the predictions of current interior cooling models (Nomoto and Tsuruta, 1986). At densities below ~ 4.3×10^{11} g cm^{-3}, matter is organized into a nuclear lattice immersed in an electron plasma. The most favourable nucleus for $\rho < 8 \times 10^6$ g cm^{-3} is ^{56}Fe, the stable end-point of thermonuclear processing. A trace of ^{4}He may initially coexist. These nuclei are formed from the photo-disintegration of iron-peak nuclei during the violent stellar birth (Rosen and Cameron, 1972) and are expected to be rapidly depleted by the action of the surface electric field (Michel, 1975).

The surface structure of neutron stars is of particular interest for models of pulsar glitches and radiation processes. Within a few hours of formation, the surface temperature is expected to drop significantly, enabling the crustal lattice to solidify. If the initial rotation rate is sufficiently high, it is likely that a non-spherical equilibrium shape will be set up before the end of the rapid cooling era. Unless relieved by plastic

---

[b] This topic has been reviewed by Baym and Pethick (1975,1979) and Irvine (1978).

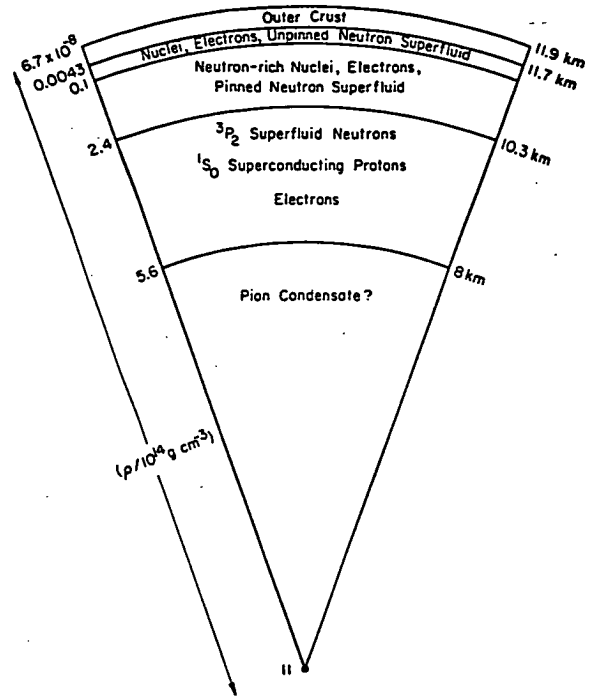

Fig. 1.1 Schematic cross section of a *standard* 1.4 solar mass neutron star. (After Pines and Alpar, 1985).

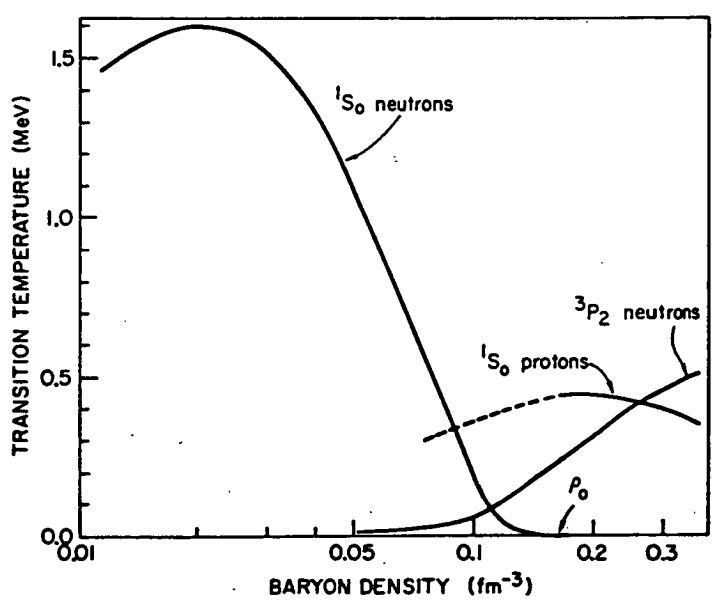

Fig. 1.2. Superfluid transition temperature T_c a function of density for superfluid components of neutron stars. The ambient temperatures are well below T_c for all but very young neutron stars. The superfluid energy gap, Δ, is given by $\Delta \approx 1.76\ T_c$ for $^1S_0$ pairing, and $\Delta \approx 2.4\ T_c$ for $^3P_2$ pairing. Note the low energy gap where the two neutron superfluids overlap. (After Baym and Pethick, 1975).

flow, increasing stresses will then build in the crust due to the influence of spindown from radiation torques. The possibility that the crust may fracture in this situation has been addressed in connection with pulsar glitches by Ruderman (1969) (section 2.3).

If ions can be freely ejected from the surface, they will be outwardly accelerated by the magnetic field, and may contribute to the observed radiation. However, the binding energy of surface ions is still uncertain, although irrespective of the initial surface structure, a short-lived thermally ejected atmosphere with a scale height of only a few centimeters is likely to form during the rapid cooling era.

Ruderman (1974) suggested that the magnetic field at the surface of pulsars is sufficiently intense for the electron clouds of the outer crustal atoms to be distorted into a cylindrical wavefunctions, each with an axis of symmetry that is parallel to the field and which passes through the associated nucleus. For such a situation it is energetically favourable for cylindrical atoms to bind to others along a field line by the quantum-mechanical sharing of electrons in the outer Landau orbitals (Flowers *et al.*, 1977) thereby creating polymetric chains of nuclei bathed in an anisotropic electron plasma. This configuration will have a significant effect on the surface conductivity, as the electrons are more mobile parallel to the magnetic field. The electrons are unable to completely shield the Coulomb fields of adjacent nuclei and as a result the chains will be relatively displaced so that the nuclei adopt a triangular lattice structure. Ruderman (1981) considered that despite the strength of this lattice, significant photo-ejection of ions continually occurs in the magnetic polar regions of the highly energetic rapidly rotating pulsars, such as Vela. In a more recent study, Neuhauser and Koomin (1987) have found that for $B \approx B_{12} \equiv 10^{12}$ G, isolated atoms are more energetically favoured than chains, raising the possibility that matter at the surface of a neutron star is only weakly bound.

The magnetic field is generally regarded as the result of flux conservation during birth. However, Blandford, Applegate, and Hernquist (1983) have suggested that as the crust cools, the magnetic field it possesses may be amplified by thermoelectric effects. The structure of the field is uncertain. Pulsar emission models generally infer a global dipolar structure, however the possibility of significant higher order moments at the surface is still largely unknown (Barnard and Arons, 1982). Because of the high conductivity of electrons (Baym, Pethick, and Pines, 1969a,b) the magnetic field is rigidly tied to the crust.

As depth and density increase, the electron Fermi energy rises, and exceeds the cyclotron energy of the inner orbital for $\rho > 2 \times 10^4$ g cm^{-3} (assuming $B \approx B_{12}$)

(Baym and Pethick, 1975). Below this level, the lattice structure take on a cubic crystalline form. The electron plasma is degenerate for $\rho > 10^5$ g cm^{-3}, and the degeneracy is fully relativistic for $\rho > 10^7$ g cm^{-3}. As the density increases, favourable regimes exist for the creation of heavier stable nuclei due to electron capture from the highest Fermi states by the protons within nuclei (Baym and Pethick, 1975). The neutrons so formed are stable against inverse beta-decay because the electron Fermi levels are critically occupied.

1.2.3 The Inner Crust

At a densities above ~ 4.3×10^{11} g cm^{-3}, the so-called *neutron-drip* point, neutrons created within nuclei become unbound and enter a gaseous phase which becomes degenerate at $\rho \approx 5 \times 10^{11}$ g cm^{-3} (Baym and Pethick, 1979). The neutron gas is prevented from decaying by a small population (~ 5% of the total baryon number density) of electrons which maintain charge neutrality with the bound protons (Alpar, Langer, and Sauls, 1984). At the onset of degeneracy, surplus neutrons which reside below the neutron gas Fermi level within nuclei are prevented from escaping.

Throughout the inner crust, the inter-neutron spacing is typically larger than the effective range of the strong force. The action of a long range attractive force between pairs of neutrons (both within the gas and the nuclei) eventually overwhelms their thermal motions and they form an isotropic $^1S_0$ Cooper superfluid. The transition temperature at which this behaviour first occurs is in the range 0.1-1.0 MeV (Yang and Clark, 1971) and is sensitive to the EOS chosen. The formation of the Cooper pairs produces a gap in the energy spectrum of the single particle state with magnitude $\Delta_n \approx 1.8\ T_c$, where T_c is the critical temperature for superfluidity (figure 1.2). The intra-nuclear superfluid density ρ_0 exceeds that of the surrounding superfluid ρ_G while ratio ρ_0/ρ_G decreases with increasing mass-density and becomes effectively unity at the base of the inner crust (Negele and Vautherin, 1973).

Superfluidity in neutron stars was first suggested by Migdal (1959) shortly after the development of the BCS theory of superconductivity. The support for this hypothesis has come principally from the modelling of relaxation processes in pulsar glitches and torque fluctuations in the accreting X-ray pulsars (Lamb, Pines, and Shaham, 1978a,b).

The state of the neutron superfluid corresponds to the macroscopic occupation by pairs of particles of a single quantum-mechanical wavefunction, and as a result, any hydrodynamical flow is irrotational. If the neutron superfluid is to mimic solid body rotation, it must contain an array of cylindrical vortices paraxially aligned with

the rotation axis (Ruderman and Sutherland, 1974). Macroscopically, each vortex column orbits the rotation axis at the *solid-body* rate. On the microscopic scale, the azimuthal velocity at a distance r from a vortex axis is

$$v_r = \frac{h}{4 \pi m_n r}$$

For $r \leq \xi_n/2$, where ξ_n is termed the coherence length, the neutron matter is normal and not superfluid;

$$\xi_n = \frac{2 E_F}{\pi k_F \Delta_n} \qquad 1.2$$

where E_F and k_F are the neutron Fermi energy and neutron Fermi-surface wavelength, respectively. Typically $\xi_n \approx 5$ fm for $\rho \approx 10^{13}$ g cm^{-3} (Epstein and Baym, 1988). It is useful to note than within the Vela pulsar, the expected value of ξ_n is such that only 10^{-18} of the available superfluid neutrons are normalized in the vortex cores. The vortex density n_v per unit area is quantized according to

$$n_v = \frac{2 \Omega_1}{\kappa} \qquad 1.3$$

where $\kappa = h/2m_n \approx 2 \times 10^{-3}$ cm^2 s^{-1} is the quantum of vorticity, and $\Omega_1 = 2\pi\nu_1$ with ν_1 being the solid-body rotation frequency. For Vela , $n_v \approx 7 \times 10^4$ cm^{-2}. A static tensional force is effective along vortex axes due to bulk rotation. This force resists deformation of the vortex line (Ruderman and Sutherland, 1974).

Within a neutron star undergoing spindown, the superfluid is not fully decoupled from the crust. The charged particles (which rotate with the lower rate of the crust and magnetic field) couple with and scatter off the vortex cores thereby inducing an azimuthal drag force which attempts to reduce the superfluid angular velocity. A radial force F_M (the *Magnus* force) acts to adjust the vortex density consistent with the deceleration. If the original and new rotation rates are Ω_1 and Ω_2 respectively, then

$$\mathbf{F_M} = n_v \kappa \times [(\Omega_2 - \Omega_1) \times \mathbf{r}] \qquad 1.4$$

where bold quantities are vectors (x denotes the operation of the vector cross-product) and $\mathbf{r}$ is the radius vector in the plane of rotation. However, the radial movement of vortices will be impeded at sites where they preferentially anchor or *pin*. Attractive (repulsive) pinning occurs where the energy gap of the superfluid is greater (less) than that of the neutrons within nuclei. In a decelerating superfluid, pinning causes the vortex density to be higher than the equilibrium value. The free energy associated with the excess vorticity is invoked as the source of pulsar glitches. Pinning may be broken by the build-up in the Magnus and drag forces, and by thermal fluctuations. Vortex pinning is further discussed in section 2.8 with regard to the initiation of glitches and their subsequent relaxation.

1.2.4 The Core

Because of the uncertainty of the EOS at trans-nuclear densities, it is unclear whether matter can exist in anything other than a liquid phase within the core. Migdal, Chernoustsan, and Mishustin (1978) have suggested that pi-meson condensation may occur where $\rho > 2\rho_0$. Quark matter is unlikely (Baym and Pethick, 1979).

At a density of ρ_0 the nuclei dissolve. This marks the transition to the core region. At this point, the matter exists in degenerate gases of neutrons, protons, and electrons, and by coincidence, the dominant neutron pairing shifts to the anisotropic $^3P_2$ state. The protons pair in a $^1S_0$ superconducting state, while any pions are also expected to be superconducting. The electrons are normal throughout the interior, as their transition temperature for superfluid behaviour is essentially zero (Alpar, 1977). The conducting and superfluid components within the core have a significant bearing on the behaviour of glitches, as described in section 2.7, through the evidently strong coupling which exists between the core matter and the crust.

1.3 THE VELA PULSAR

The discussion returns to the structural properties of neutron stars in chapters 2 and 3. In the remainder of this chapter, background information is provided on the Vela pulsar as well as aspects of the generation and propagation of pulsar emission, and pulsar rotational evolution. Reviews of Vela's timing activity are presented in the following two chapters. A summary of the general parameters of the pulsar is provided in table 1.1.

1.3.1 Location

The Vela pulsar is widely regarded as the product of a supernova event. The principle evidence comes from the similarity of the positions of the pulsar and the Vela supernova remnant (SNR) and the approximate equivalence of the inferred ages of the pulsar and remnant (Stothers, 1980; Bignami and Caraveo, 1988, and references therein). Bignami and Careveo placed an upper limit on the magnitude of the proper motion as 60 mas yr^{-1}, and on this basis concluded that the pulsar could not have travelled from the proposed centre of the remnant during its lifetime. Although the verification of the pulsar's distance is hampered by the lack of significant 21 cm HI absorption along the line-of-sight (Manchester, Murray, and Radhakrishnan, 1969) the estimation of the pulsar's transverse velocity through the analysis of scintillation

TABLE 1.1

PARAMETERS FOR PSR0833-45[a]

Timing[b]	
ν (Hz)	11.201539545±2
$\dot{\nu}$ (10^{-12} Hz s^{-1})	-15.680±1
$\ddot{\nu}$ (10^{-22} Hz s^{-2})	-6±3
epoch (TJD)	6363.4246210
epoch range of fit (TJD)	6309-6417
rms residual (μs)	65
$\dddot{\nu}$ (10^{-34} Hz s^{-3})[c]	-4.6
Position (B1950.0)	
RA[d]	$08^h\ 33^m\ 39.^s22\pm3$
dec[d]	-45°00'10".1±3
proper motion (mas yr^{-1})[e]	~ 260
galactic longitude	263°.6
galactic latitude	-2°.8
General	
DM (pc cm^{-3})[f]	69.08±0.01
RM (rad m^{-2})[f]	33.6±0.1
decorrelation bandwidth (kHz)[g,h]	0.28
mean structure coefficient $\langle C_n^2 \rangle$ ($m^{-20/3}$)[h,i]	1.5
scattering spectral index α [h]	3.9
transverse velocity (km s^{-1})[j]	53±5
equivalent pulse width (ms)[k,l]	2.6
mean linear polarization (%)[k]	82
mean flux density (mJy)[g,k]	4100
spectral index[f]	-1
magnetic field strength (10^{12} G)	3.4
distance (kpc)[f]	0.5
distance below galactic plane (pc)[f]	24
characteristic age (10^4 yr)	1.1

a errors are 95% confidence limits, and are quoted for the last significant digit except for DM and RM

b from Llanherne observations

c assuming a braking index of 3

d Manchester *et al.* (1978a)

e proper motion in RA and dec. from Ögelman, Koch-Miramond, and Auriére (1989, *preprint*)

f Taylor and Manchester (1975)

g at 635 MHz

h Cordes, Weisberg, and Boriakoff (1985)

i scattering coefficient averaged over the line-of-sight

j Cordes (1986)

k McCulloch *et al.* (1978)

l pulse energy divided by peak intensity

observations combined with VLBI and optical proper motion measurements is a means of obtaining an accurate independent check which has yet to be published.

The Vela SNR (frontispiece) is a shell of anomalous hot turbulent gas which represents the interaction of a supernova blast wave with a pre-existing inhomogeneous interstellar medium (Jenkins, Wallerstein, and Silk, 1984). It produces enhanced emission throughout the electromagnetic spectrum, and is a significant partially non-thermal continuum radio source (figure 1.3). Evidently, it has a diameter of ~ 40 pc (Green, 1984) and its centre is 500 pc distant.

The remnant lies wholly within the Gum Nebula. This is an ionized region estimated to have a diameter of 250 kpc, and a near edge 375 pc distant (Reynolds, 1976), although Brandt *et al.* (1971) have suggested much larger dimensions. Bruhweiler, Kafatos, and Brandt (1983; hereafter BKB) have summarized its characteristics. It contains highly inhomogeneous multi-phase components that form a hierarchy of structures regarded as representative for the interstellar medium (ISM) (McKee and Ostriker, 1977). Plausible models for the region have been reviewed by BKB. The lack of definite expansion suggests the region is an extensive HII cloud that has been modified by slow shocks induced by the stellar winds of embedded evolving stars, and perhaps more recently by the photopulse that accompanied the supernova explosion responsible for the Vela SNR.

The pulsar is surrounded by a localized synchrotron nebula (Harnden *et al.*, 1985). This probably originates from the interaction of the pulsar's high energy radiation with the local ISM.

1.3.2 Radio Emission

PSR0833-45 is one of the most conspicuous radio pulsars. The study of its characteristic pulsed emissions has significantly assisted in the quest for a general pulsar radiation model. Its spectrum is presented in figure 1.4. The pulsar is most readily detected at radio frequencies. The radio emission, when integrated synchronous with the apparent pulse period for several hundred periods, has a characteristic profile which is highly stable in shape with time (figure 1.5). Above ~ 1.6 GHz, the profile shows distinct bifurcation; the energy difference between the primary and secondary components shows evidence of variability (Manchester, Hamilton, and McCulloch, 1980).

Pulsar radiowaves are scattered by density turbulence within the ISM (e.g., Cordes, Pidwebetsky and Lovelace, 1986; hereafter CPL). Importantly, scattering

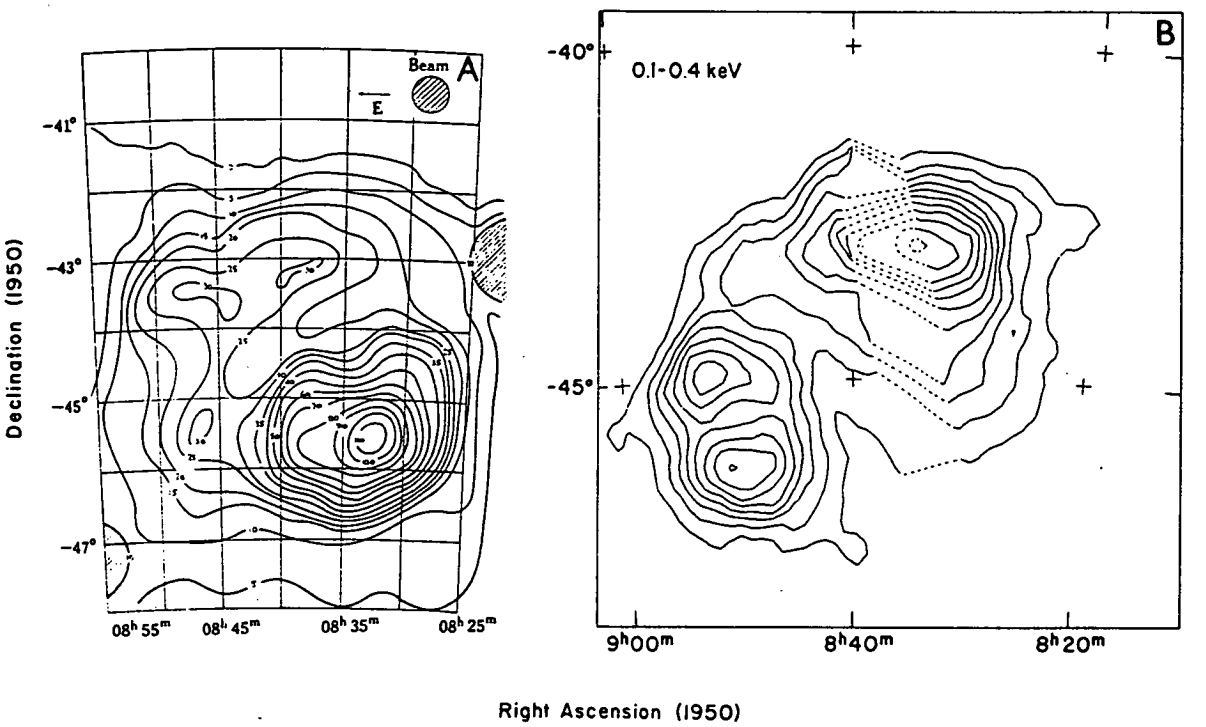

Fig. 1.3. The Vela SNR; (a) isotherms of brightness temperature at 635 MHz (Milne, 1967), (b) isophots in the X-ray band 0.1-0.4 keV (Hearn, Larsen, and Richardson, 1980).

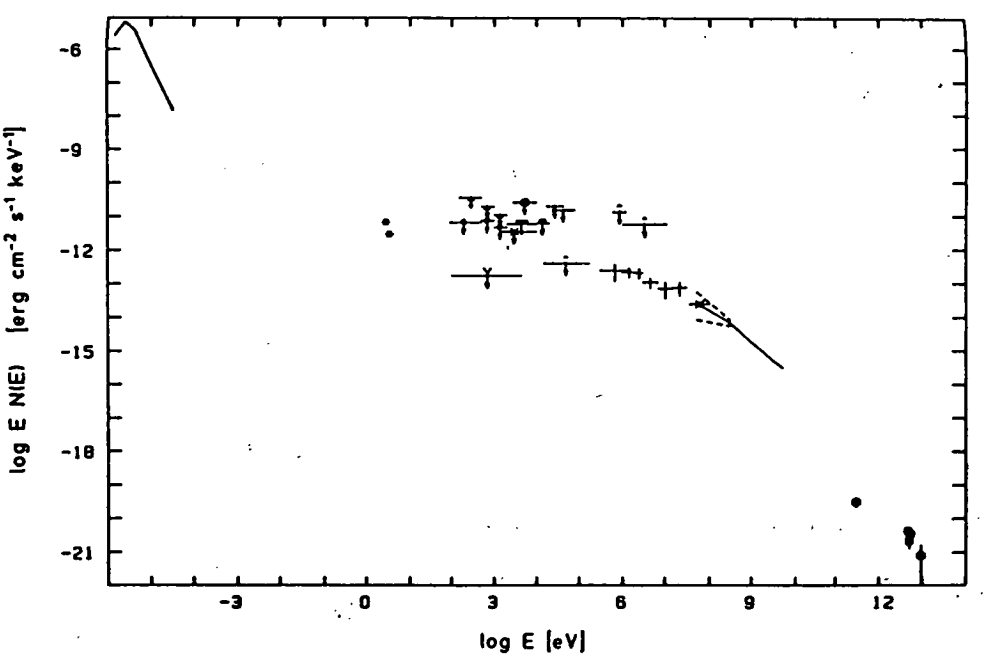

Fig. 1.4. Total energy spectrum of the Vela pulsar from the radio to gamma-ray regions of the spectrum compiled by Grenier, Hermsen, and Clear (1988). In the X-ray range, 3σ upper limits are shown assuming a pulsed duty cycle of 0.2. The broken lines indicate the extremities of variability of the gamma-ray emission.

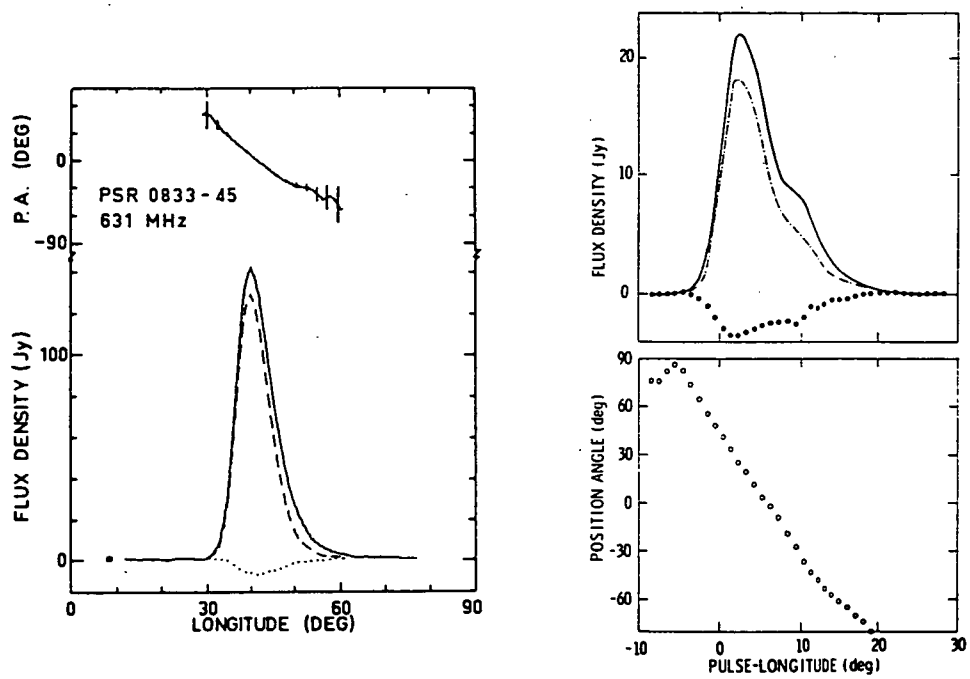

Fig. 1.5. Pulse profiles for PSR0833-45 at (a) 631 MHz (McCulloch *et al.*, 1978) and (b) 2.3 GHz (Krishnamohan and Downs, 1983). *Solid lines* - total intensity, *dashed line* - linear polarization, dotted line - circular polarization. The position angle (PA) of the linearly polarized vector is is also shown.

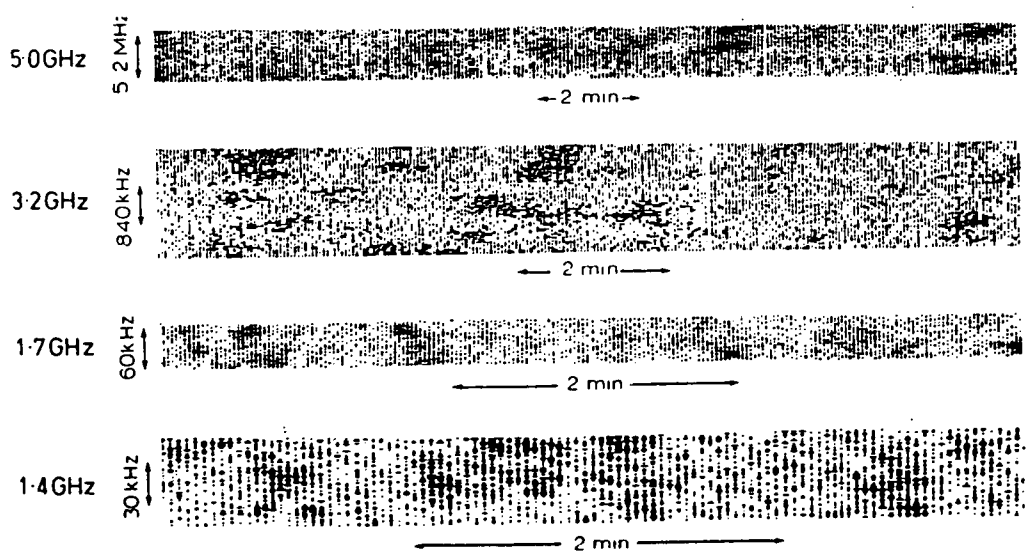

Fig. 1.6. Dynamic spectra of PSR0833-45 illustrating the finite frequency and time scales of correlated intensity scintillations due to scattering within the ISM. Note the decrease of these scales with observing frequency. Top to bottom; (receiver bandwidth, number of periods averaged per pixel) = (100 kHz, 50), (33 kHz, 30), (1 kHz, 20), and (1 kHz, 30). (After Roberts and Ables, 1982).

modifies the intrinsic profile shape; the effects become more pronounced as the observing frequency is decreased (figure 1.6). Below ~ 150 MHz for Vela, the timescale of the temporal transfer function for the line-of-sight plasma exceeds the pulse period thus hampering pulse energy measurements (Komesaroff, Hamilton, and Ables, 1972). In addition, scattering introduces intensity *scintillations* which are coherent only over finite frequency and time ranges (the *decorrelation bandwidth* and *decorrelation time*, respectively) as shown in figure 1.7.

A significant aspect of Vela's radiation is that it is highly linearly polarized throughout the radio spectrum, particularly on the leading edge of pulses (Radhakrishnan *et al.*, 1969; Manchester, Hamilton, and McCulloch, 1980). The position angle of the plane of polarization exhibits a smooth rotation across the pulse profile (figure 1.5). This behaviour is the corner-stone of the rotating-vector model of pulsar emission (section 1.3.6). In additional, the radiation exhibits a small percentage of circular polarization which increases with frequency and reaches ~ 14% at ~ 1.6 GHz. Below 400 MHz, the signals are increasingly depolarized by scattering within the ISM (Komesaroff, Hamilton, and Ables, 1972).

From single-pulse polarization measurements at 2.3 GHz, Krishnamohan and Downs (1983; hereafter KD) have found that the pulse profile has contributions from four distinct emission regions. Unfortunately the quantitative modelling of the multi-component nature of Vela's radio pulses suffers from the lack of a systematic study across the spectrum. Such a study may shed light on the magnetic field structure which although regarded as dominantly dipolar, may have significant higher order multipole components at low altitudes which subtly influence the emission geometry.

1.3.3 Dispersion

By far the most important modifications to the phase and amplitude of propagating pulsar radio waves occurs within the ISM. Of particular importance for pulsar timing studies are the isolation of dispersive arrival time delays and their fluctuations which may mask the intrinsic variations.

It has been demonstrated (e.g. Tanebaum, Zeissig, and Drake, 1968; Goldstein and James, 1969) that the constant term of dispersion delay for pulsar signals is described to within ~ 1 part in 10^4 by the first-order approximation to the familiar theory of propagation in a weakly-magnetized cold electron plasma. Waves of frequency f_1 and f_2 which have propagated a distance d are delayed by

$$t_2 - t_1 = \frac{2\pi q_e^2}{m_e c} (f_2^{-2} - f_1^{-2}) \, DM \qquad 1.5$$

Here $DM = \int_0^d n_e(l)dl$, the *dispersion measure*, expresses the total electron column density along the propagation path. The directly measurable part of equation 1.5 is the *dispersion coefficient* D;

$$D = \frac{(t_2 - t_1)}{(f_2^{-2} - f_1^{-2})} \qquad 1.6$$

with

$$DM\ (pc\ cm^{-3}) \approx 2.410086 \times 10^{-4}\ D\ (Hz) \qquad 1.7$$

From the model of the distribution of the galactic electron plasma (Manchester and Taylor, 1977, pp. 123-146), it is evident that approximately half of DM for the the Vela pulsar is contributed by the Gum Nebula (Manchester, Murray, and Radhakrishnan, 1969); the mean electron density to Vela is 0.14 cm^{-3} compared with the value of 0.025 cm^{-3} held typical for the ISM.

Hamilton *et al.* (1977) and Hamilton, Hall, and Costa (1985) have shown that DM for PSR0833-45 slowly and systematically varies with time by at least 4%. In addition, the amount of ISM Faraday rotation undergone by the plane of polarization of the signals is also variable. Hamilton *et al.* have interpreted these changes as due to the motion of a magnetized plasma filament out of the sight-line. The characteristic timescales and amplitudes of the plasma variations are poorly known owing to the infrequency of the reported measurements. In Chapter 7, new observations of Vela DM changes on short timescales (less than 200 days) are presented.

1.3.4 Scattering

The frequency scalings of scintillation parameters and the impulse response timescale for the line-of-sight to pulsars provides the primary evidence that the ISM contains three-dimensional electron density turbulence with a fluctuation power spectrum in wavenumber q given by

$$P_{\delta n_e} = C_n^2\, q^{-\alpha_s} \qquad 1.8$$

where C_n^2 is termed the structure constant, and α_s is the spectral index. Typically, $C_n^2 \approx 10^{-5} - 10^{-2}\ m^{-20/3}$ and $\alpha_s \approx 3.7$ (Armstrong, 1984). The turbulence is regarded as inertial (i.e. energy cascades through turbulent eddies of diminishing scale) at least for spatial scales $r = 2\pi/q$ near 10^8 m (Armstrong and Rickett, 1981; Rickett, 1977).

Diffractive scattering effects are caused by turbulence with scale sizes on the order of the Fresnel zone scale $r_F = \sqrt{\lambda L}$ where L is the distance of the phase screen from the observer and λ is the observing wavelength. The resulting fluctuations in the frequency-time plane that are usually narrow-band and rapid in comparison with the instantaneous bandwidth and period of pulsar signals, respectively. The temporal

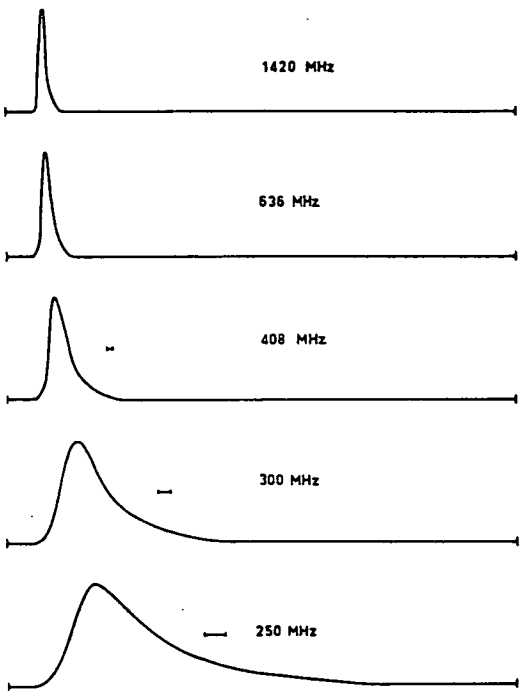

Fig. 1.7. Average pulse shape at five frequencies. The baseline covers one period. The peak intensities have been normalized and the leading edges have been arbitrarily aligned. The horizontal bars indicate the magnitude of instrumental dispersion smearing. (After Ables, Komesaroff, and Hamilton, 1970)

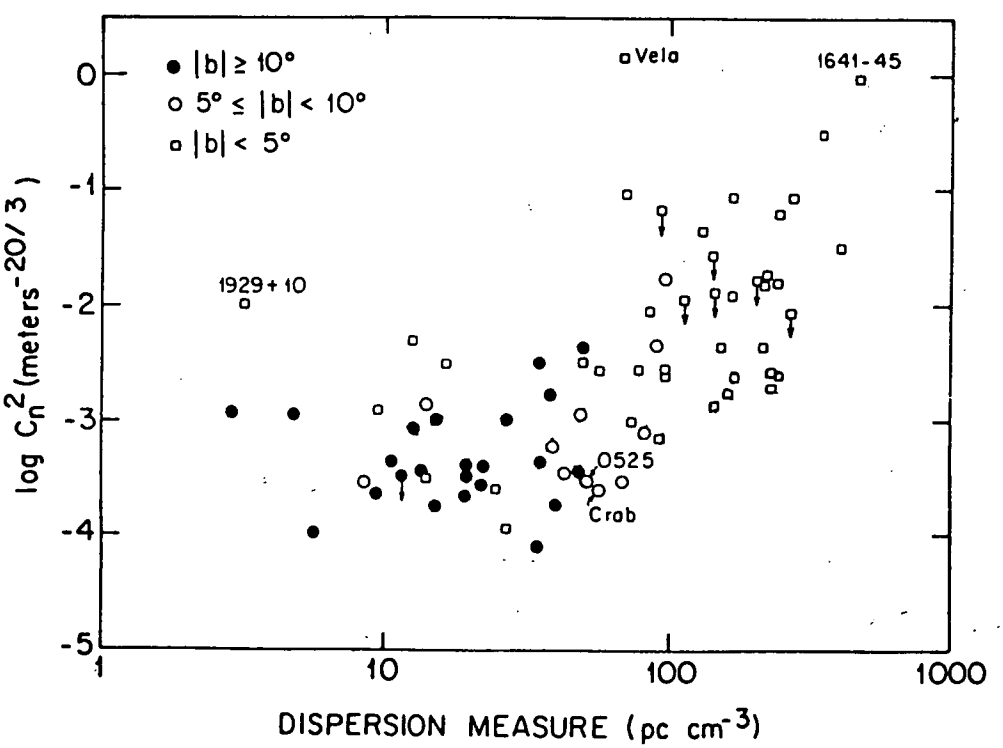

Fig. 1.8. Estimates of the mean line-of-sight scattering structure constant $\langle C_n^2 \rangle$ plotted against dispersion measure for three ranges of galactic latitude. (After Cordes, Weisberg, and Boriakoff, 1985)

smearing of pulsar profiles noted in section 1.3.2 is a manifestation of *diffractive* scattering. The ISM temporal transfer function has geometrical and dispersive contributions. The geometrical effect is essentially due to the variation of the path length traversed by the scattered rays. The dispersive term arises from the variation of the group delay as the scattered rays encounter plasma turbules with a range of densities. An additional result of the geometrical scattering is the apparent wandering of the angular position of the source.

The Vela pulsar's diffractive temporal delays are well modelled by assuming the existence of a thin *screen* of homogeneously distributed turbulence within the propagation path (Ables, Komesaroff, and Hamilton, 1970; Lee and Jokipii, 1976). Cordes, Weisberg, and Boriakoff (1985) have determined α_s and C_n^2 for the path to Vela on this basis; these values are listed in table 1.1. The structure constant for PSR0833-45 is evidently anomalous (figure 1.8). In addition, the fluctuation spectrum is marginally steeper than that expected for a Kolmogorov distribution of density turbulence for which $\alpha_s = 11/3$; this spectral index is consistent with the scintillation data for a portion of the pulsar population (CPL).

Turbulence with spatial scales larger than the Fresnel scale produces *refractive* scattering effects which are difficult to measure as a result of their slow evolution. The relative significance of refractive and diffractive effects is dependent on α_s and the inertial range of the turbulence scales. Vela's systematic radio flux variations (McAdam, 1981) have been attributed to refractive scintillations (Coles *et al.*, 1987), although intrinsic changes within the emission zone may also be responsible (Grenier, Hermsen, and Clear, 1988). If density turbulence is inertial at refractive scattering scales then dispersive arrival time delays will increase with the length of observing time. This is simply due to the increase in the probability that larger density structures will become interposed in the line-of-sight. The predictions of refractive scattering theory for dispersive delay fluctuations are compared with measurements for the Vela pulsar in Chapter 7. Inertial density turbulence will contribute a term to pulsar timing noise spectra with a characteristic (odd integer) spectral index. The significance of this term will depend on the observing frequency, the span of the observations, and the level of intrinsic timing noise. Ideally, the contamination of timing noise spectra is avoided by the removal of the dispersive arrival time fluctuations through the use of simultaneous observations made at two or more frequencies.

The estimation of refractive arrival time delays as a function of frequency and observing timespan is hampered by the uncertainty in the extrapolation of the diffractive-scale turbulence spectrum to small wavenumbers. Several authors have addressed observations of pulsar and continuum source refractive scattering to resolve

this problem. In general, an enhancement above the extrapolated diffractive-scale spectrum is indicated (Rickett, Coles, and Bourgois, 1985), however the interpretation of the results are hampered by the lack of a fully general theory. For example, the enhancement has been attributed to the presence of a low-wavenumber cutoff by Coles *et al.* (1987), while Blandford and Narayan (1985) have suggested that the diffractive-scale spectral index increases.

The true turbulence spectrum over a large wavenumber range is likely to be a piecewise ensemble of narrow-band forms. This is because the various phases of the ISM support different inertial wavenumber ranges (Cesarsky, 1980), and the galactic magnetic field anisotropizes the turbulence spectrum with smaller structures being supported orthogonal to the field than parallel with it (Higdon, 1984,1986). Southern hemisphere VLBI has the potential to clarify the refractive turbulence spectrum for PSR0833-45. However, interim statements are made in Chapter 7 based on the observed DM variations.

1.3.5 Emissions at Shorter Wavelengths

Of the 450 or so known rotation-powered pulsars, only the four youngest objects, including the Vela and Crab pulsars, have been observed outside the radio range (Manchester, 1987).

At optical wavelengths, Vela exhibits a bifarious pulse profile (figure 1.9). A significant steady component of emission exists which is too bright to be purely the result of blackbody radiation from the surface of the neutron star (Peterson *et al.*, 1978). The emission may arise from an extended pulse producing region in the magnetosphere, or from the reprocessing of energy in the vicinity of the surface (Peterson *et al.*, 1978). Manchester *et al.* (1980) have found evidence for a small variation in the unpulsed emission.

The pulsar does not produce a significant observable flux of pulsed or continuous X-rays (Harden *et al.*, 1985, Ögelman and Zimmerman, 1989, *preprint*). An estimate of 10^6 K has been placed on the temperature of the pulsar's surface (Harnden *et al.*, 1985); this is in reasonable agreement with the predictions of the vortex creep theory of internal dynamics (Alpar *et al.*, 1984a,b; section 2.9). The temperature estimate is based on the inferred contamination of the spectrum of the X-ray synchrotron nebula by blackbody radiation. Smith and Pounds (1977) have detected transient X-ray brightenings in a field containing the Vela pulsar, however no subsequent activity has been reported.

A significant pulsed component of gamma-rays is produced at energies above at least 0.3 MeV (Tümer *et al.*, 1984; Thompson *et al.*, 1977; Bennett *et al.*, 1977) (figure 1.9). Evidence reported by Caraveo *et al.* (1988) suggests that the gamma-photons are linearly polarized. Grenier, Hermsen, and Clear (1988) have demonstrated that the pulsed flux is variable, and may arise from five distinct emission regions indicating that the pulsar's outer magnetosphere is complex.

Bhat *et al.* (1987) have claimed the marginal detection of a pulsed signal at ultra-high energies (5-10 TeV) using ground-based Cerenkov detectors. Similar observations by Grindlay *et al.* (1975) were inconclusive.

1.3.6 Emission Models

Pulsar emission models are still largely schematic; in the main, no single model adequately describes the gross characteristics of all pulsars. It is not the intention to review the plethora of models in any depth here. For background information the reader is directed to the summaries of Michel (1987, 1982), Arons (1979), and Manchester and Taylor (1977, pp. 169-235) in particular.

In general, the *polar cap* models (Radhakrishnan and Cooke, 1969, hereafter RC; Arons and Scharlemann, 1979; Cheng and Ruderman, 1977a, 1977b, 1980) have been more consistent in accounting for the phenomenological aspects of pulsar emission than have the *light-cylinder* models (Ferguson, 1981). The interpretation of Vela's radio emission mechanism is simplified by the complete absence of (1) drifting sub-pulses (Biggs *et al.*, 1988), (2) orthogonal polarization modes (KD), and (3) an interpulse. The first two phenomena (which are exhibited by a portion of the pulsar population) together with observations of circular polarization and pulse micro-structure have proven difficult to model.

In this connection, the rotating-vector polar cap model of RC is no exception. However it does provide a convenient way of explaining pulsar polarization characteristics; indeed the Vela pulsar was used as the prototype for the theory. The model proposes that the radio emission arises from two main mechanisms which operate inside the light-cylinder within the open field line region above the magnetic polar caps. These are curvature radiation from bunches of charged particles moving along curved field lines, and from particles accelerated along the field lines. For both mechanisms the emission is linearly polarized, and has an overall radiation pattern with an annular cross-section centred on the magnetic axis. The observed position angle swing is the result of the changing projection of the magnetic field as the obliquely inclined magnetic axis sweeps around the sky. The pulse width is

determined by the inclination of the magnetic and rotation axes to the line of sight, and the angular divergence of the field lines at the emission region (figure 1.10). However, the two widely separated and relatively broad components of Vela's radiation at optical and higher frequencies clearly suggests that these emissions are produced with a distinctly different geometry.

A major unresolved issue of all emission models centre on the origin of the radiating particles; possible sources include pair cascades (Sturrock, 1971), photo-ejection from the stellar surface (Ruderman, 1981), the ablation of interstellar grains (Cheng, 1985), and ejection from a circumstellar disk (Michel and Dessler, 1981). In addition, the organization of global current flow and the magnetic field within the magnetosphere is not known with confidence. The high brightness temperature of the radio emission implies that it is generated coherently. A variety of mechanisms have been proposed which generally invoke some type of plasma instability process, however it is unclear whether these can operate effectively within the emission zone (Taylor and Stinebring, 1986, and references therein).

The primary particle acceleration sites for the polar cap models are generally regarded as the charge-depleted regions along field lines within the magnetosphere termed *gaps* (e.g. Ruderman and Sutherland, 1975; Arons, 1981, and references therein). According to Metsel (1971), the magnetospheric charge density for aligned and oblique rotators vanishes where $\Omega \cdot \mathbf{B} = 0$. The locii of the neutral points separate regions with charge density of opposite sign. A charged particle moving outward along an open field line outside the neutral sheet leads to an electric field $\mathbf{E}$ which forces charge of the opposite sign on either side of the sheet to accelerate inwards towards the stellar surface. This leads to a gap depleted of plasma with $\mathbf{E} \cdot \mathbf{B} \neq 0$ inside it, and $\mathbf{E} \cdot \mathbf{B} = 0$ on its surface (Cheng, Ruderman, and Sutherland, 1976). The accelerating particles below the gap may be sufficiently energetic to produce curvature radiation which extends into the gamma-ray region of the spectrum. This is likely the case for the fast and highly magnetized pulsars such as Vela and Crab for which Cheng, Ho, and Ruderman (1986a,b) predict the gaps to lie near the light-cylinder radius. Because of the field strength within the gap, it is favourable for transiting gamma-ray photons to pair-produce. Each member of a pair will generate synchrotron photons which may lead to further pairs and a consequent cascade which will terminate when the pair production energy threshold is reached. The surviving photons then constitute the high energy radiation. The low energy particles may contribute to the generation of the coherent radio and possibly optical emission. In the case of the radio emissions, the generation site is evidently well within the light cylinder if the polar cap models are valid (Cordes, 1978; Matese and Whitmire, 1980).

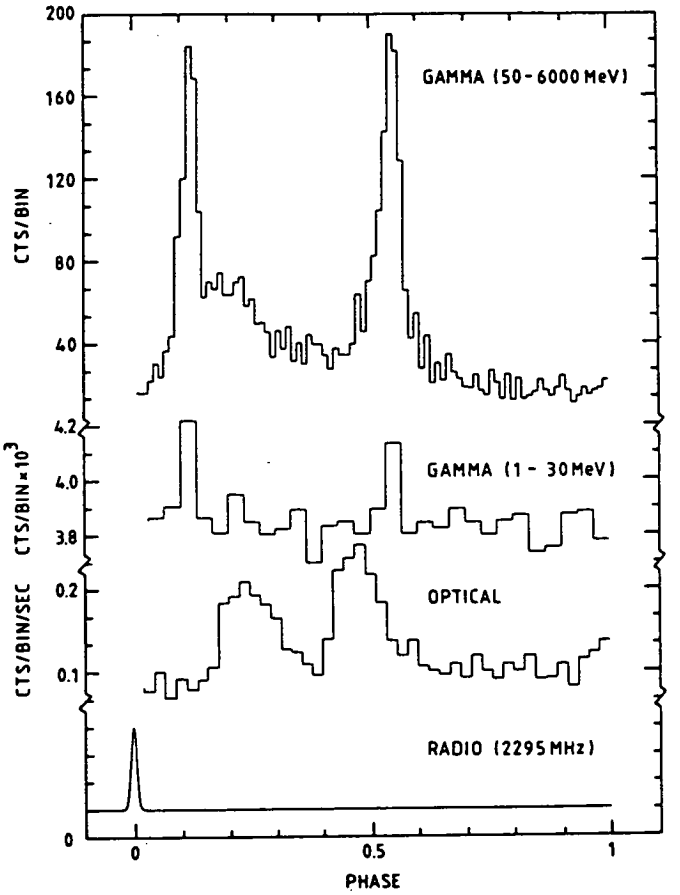

Fig. 1.9. Comparison of the pulse profiles for PSR0833-45 compiled by Grenier, Hermsen, and Clear (1988).

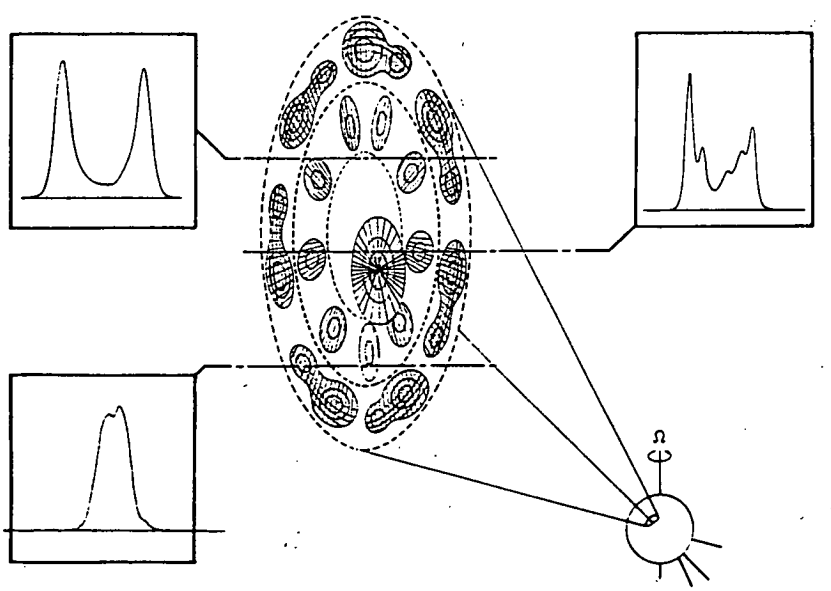

Fig. 1.10. Rankin (1983), in a morphological study of pulse shapes, has provided evidence for two different beaming geometries above pulsar polar caps; a filled and offset core beam, and a partially illuminated annular conal beam. Three different cross sections are shown suggesting how different pulse shapes arise.

1.3.7 Pulsar Spindown

Pulsar spindown is attributed to the loss of rotational energy and angular momentum via particle ejection and electromagnetic radiation. These processes are influenced by the evolution of the magnetic moment through the growth and decay of the field and the alignment or counter-alignment of the magnetic and rotation axes (Blandford and Romani, 1988; hereafter BR, and references therein). Additional processes may contribute to rotational energy loss; Peng, Huang, and Huang (1982) have suggested that neutrino emission by neutrons undergoing cyclotron movement may provide an important contribution to spindown in old pulsars.

If N_m is the applied spindown torque, then from Euler's equations of motion for a spherical rigid body,

$$\dot{\Omega} = -\frac{N_m}{I} \qquad 1.9$$

where $\Omega = 2\pi\nu$, and I is the total moment of inertia. Equation 1.9 with an appropriate expression for the torque acting on an inclined rotator gives the the evolution of ν as

$$\dot{\nu}(t) = -K(t)\,\nu^{n_B}(t) \qquad 1.10$$

where K is a slowly varying coefficient which quantifies the evolution of the magnetic and inertial moments, and n_B is termed the braking index. If K is assumed constant then the braking index is given by

$$n_B = \nu\,\ddot{\nu} / \dot{\nu}^2 \qquad 1.11$$

Cheng (1989) has provided general theoretical expressions for the braking index based on the standard pulsar radiation models, including terms which account for free nutation, axial alignment, and field decay. For the light-cylinder models, the dominant spindown torque is produced by the liberation of magnetic dipole radiation generated at the pulsar rotation frequency, and results in $n_B \geq 3$. For the *standard*[d] polar cap models, the dominant torque is due current flow from pair creation outside the light cylinder ; here $n_B \geq 1$.

BR have summarized accurate measurements of the braking index that have been made for the three fastest non-binary pulsars (which includes the Crab pulsar). It has been possible to accurately determine the secular second frequency derivative for only these objects; timing noise masks the true spindown behaviour for the remainder of the pulsar population. BR have suggested that the magnetic moment of each of these pulsars has increased since birth. In the case of the Crab pulsar, a non-zero third frequency derivative has been claimed (Lyne, Pritchard, and Smith, 1988), although

---

[d] The standard models are those which invoke polar cap current flow according to the model of Goldreich and Julian (1969).

this may be largely a manifestation of timing noise. Using information on the evolution of $\dot{\nu}$ and ν, it is possible to investigate the form of K(t) in equation 1.10.

For the Vela pulsar, the short term spindown trend is dominated by glitches which make it difficult to accurately measure the torque-related value of $\ddot{\nu}$ and hence the braking index. An upper limit to the age of the Vela pulsar (the so-called characteristic age) is inferred from the timing measurements using

$$\tau_{age} = -\frac{\nu}{\dot{\nu}\,(n-1)} = \frac{t_s}{2} \approx 10^4 \text{ yr} \qquad 1.12$$

assuming that the pulsar spindown is entirely due to magnetic dipole radiation (i.e., n=3) and K is constant; here t_s is termed the *spindown timescale.*

1.4 CONCLUSIONS

The Vela pulsar is a very important object from the viewpoint of probing the internal structure of neutron stars. It was the first pulsar to exhibit a discontinuity in rotation rate, and the recognition and investigation of this phenomenon has precipitated considerable development of neutron star models and theories of ultra-dense matter. However, much scope remains for the further progress in these areas. The continued development and verification of neutron star models hinges on the acquisition of pulsar timing data with improved resolution and contiguity. In addition, uncertainties remain as to the general applicability of internal models based on the characteristics of observed glitches to the entire neutron star population and so the continuation of pulsar timing surveys, particularly of southern hemisphere objects, is of importance in order to improve the statistical base for theoretical modelling.

It is particularly evident that the Vela's broad spectrum presents a challenge to current understanding of the emission mechanisms for young pulsars. The apparent multiplicity of emission regions and their variability at high energies suggests that the pulsar has a complex magnetosphere. A single-pulse multi-frequency polarization survey of Vela's radio emission should be considered as a means of clarifying the present uncertainty.

Little published data exists on the refractive scattering of Vela's radiowaves. It is apparent that the ISM along the path to the pulsar is particularly turbulent. This is held responsible for the small though significant changes in line of sight dispersion measure that have been observed. This effect complicates the interpretation of pulsar timing noise, and so its characterisation is of importance.

CHAPTER 2 - PULSAR GLITCHES

2.1 INTRODUCTION

In this chapter, an overview is presented of the current interpretation of pulsar glitches. A schematic representation of the typical behaviour of ν and $\dot{\nu}$ accompanying a glitch are shown in figure 2.1.

Although recurrent glitches are a feature of the young Vela and Crab pulsars, the slower and older objects PSR1641-45 (Manchester *et al.*, 1978; Flanagan, 1986, *personal communication*) and PSR0355+54 (Lyne, 1987) have each exhibited two glitches. In addition, three other pulsars have shown one distinct glitch; PSR0525+21 (Downs, 1982), PSR1325-43 (Newton, Manchester, and Cooke, 1981), and PSR2224+65 (Backus, Taylor, and Damashek, 1982).

The basic parameters that are used to characterize a glitch are the immediate fractional changes in rotation frequency and its first time derivative ($\Delta\nu/\nu$ and $\Delta\dot{\nu}/\dot{\nu}$, respectively), the timescale(s) of the relaxation effect(s), and the fraction of the original frequency jump that is eventually recovered (Q). These parameters vary from pulsar to pulsar as reflected in table 2.1. For only the first four pulsars in table 2.1 have detailed glitch analyses been presented, although in several cases the precise determination of the jump parameters is hampered by a lack of sufficiently frequent observations. By far the most detailed results have been obtained from observations of the four most recent Vela glitches and the 1986 Crab glitch. Importantly, it been possible to unambiguously determine the epoch of each of these events..

Vela's glitches appear to be divided into two classes based on their amplitudes. Two *milli-glitches* (Downs, 1981a,b; Hamilton, *personal communication*, 1989) have been identified. These events are approximately three orders of magnitude smaller than a typical large jump, while their relaxation behaviour is similar to that of the large glitches. McCulloch *et al.* (1983) found that the relaxation following the fifth large glitch was well modelled by two superimposed exponential decays with short (~ 5 day) and long (~ 150-300 day) time-constants. This behaviour has been observed following the three subsequent glitches (McCulloch *et al.*, 1987; Hamilton, *personal communication*, 1989). An important feature noted by Downs (1981b) and Cordes, Downs, and Krause-Polstorff (1988) is that immediately prior to each large glitch, the spindown has displayed a distinct value of $\dot{\nu}$ which is correlated with the value of the long time constant of the relaxation in ν for the previous glitch.

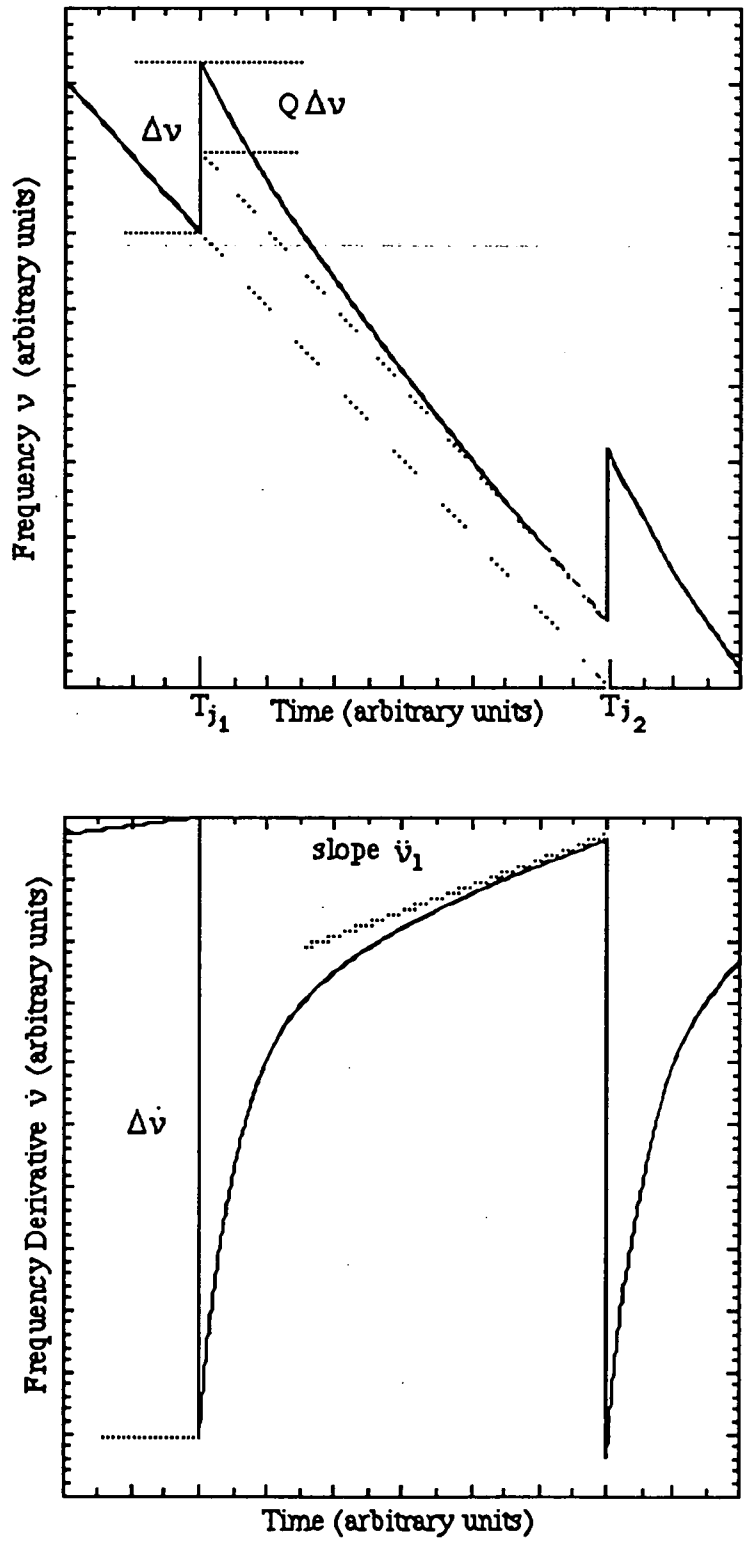

Fig. 2.1. Schematic of the behaviour in frequency and its time derivative for a glitching pulsar. The magnitude of the glitch is expressed in terms of the fractional changes $\Delta\nu/\nu$ and $\Delta\dot{\nu}/\dot{\nu}$ where ν and $\dot{\nu}$ are referenced to the glitch epoch T_j. The post-glitch relaxation is well characterized by one or more exponential decays with associated time-constants τ. The parameter Q measures how much of the initial jump in frequency is subsequently recovered. The relaxation in frequency derivative asymptotically approaches a trend with gradient $\ddot{\nu}_1 = \ddot{\nu}_0 + \ddot{\nu}_j$, where $\ddot{\nu}_0$ is a contribution from spindown, and $\ddot{\nu}_j$ is unique to a particular inter-glitch timespan.

TABLE 2.1

SUMMARY OF THE CHARACTERISTICS OF PULSAR GLITCHES[a]

Pulsar	Glitch	observables: Epoch TJD	-ΔP (x10^{-9} s)	Δν/ν (x10^{-9})	Δν̇/ν̇ (x10^{-3})	$\delta\nu_p$ (Hz)	t_0	t_0'	model parameters: τ_1 days	τ_2 days	Q
0833-45[b]	1	0276.8 - 0283.7	208	2345	10.1	2.6x10^{-3}	...	19 d	10.0±1.0	120±6	0.034
P=0.08927 s	2	1185.3 - 1199.2	174	2045	14.9	1.5x10^{-3}	...	17 d	4.0±1.0	94±5	0.035
	2a	1308.9 - 1315.9	1.3	1.2	1.9	7.1x10^{-5}	...	0.1 d	10.0±0.5	...	0.55
	3	2680.5 - 2685.7	179	1985	10.6	2.0x10^{-3}	...	17 d	4.0±0.4	35±2	0.088
	4	3681.4 - 3704.3	272	3060	18.4	1.9x10^{-3}	...	25 d	6.0±0.6	75±3	0.024
	5	4888.5707±2	102	1145	8.5	1.5x10^{-3}	1500 d	9 d	1.6±0.2	233±1	0.177
	6	5192.1395±9	182	2058	16.6	1.4x10^{-3}	1400 d	17 d	3.2±0.5	60±9	0.035
	7	6257.7309±8	143	1599	12.8	1.4x10^{-3}	...	11 d	6.5±0.5	332±10	0.155
	8	7250.3037±2	163	1806	7.9	2.5x10^{-3}	...	...	...	...	...
0531+32	1[c]	0494±1	0.17-0.43	5-13	...	...	...	...	...	5	0.9-1.0
P=0.03333 s	2[d]	2445-2451	0.3	10	21.6±1.6	1.0x10^{-6}	...	...	...	10.2±1.2	0.6-0.8
	3[e]	6664.42±5	0.31	9.2±0.1	2.5±0.2	1.2x10^{-7}	...	0.8 s	2.5±0.5	5.5±0.5	...
0355+54[f]	1	6079±7	0.9	5.56±3	0.0018±2	2x10^{-5}	...	2 d	...	...	...
P=0.15638 s	2	6433-6504	685	4385-4367	0.062–0.088	4(-2)x10^{-4}	832 yr	4.9 yr	...	44±2	...
0525+21[g]	1	2050-2064	4.9	1.30±0.22	4.6±0.9	1.1x10^{-6}	...	20 d	143±34	...	
P=3.74550 s	1a	3780-3834	1.1	0.3±0.8	-0.085±0.150	...	...		...	...	...

TABLE 2.1 (continued)
SUMMARY OF THE CHARACTERISTICS OF PULSAR GLITCHES[a]

Pulsar	Glitch	observables: Epoch TJD	-ΔP (10^{-9} s)	Δν/ν (x10^{-9})	Δν̇/ν̇ (x10^{-3})	$\delta\nu_p$ (Hz)	t_0	t_0'	model parameters: τ_1 days	τ_2 days	Q
1325+43[h] P=0.53270	...	3590±24	62	116	...	...	...	...	...	...	...
1641-45[i] P=0.45505 s	1	3390±62	86.8	1.907±14	1.6±1.2	2.6x10^{-6}	...	80±60yr	...	...	...
1906+00[j] P=1.01695 s	...	2161.1±6.2	0.7	0.7	...	...	...	...	...	37±7	...
2224+65[k] P=0.68253 s	...	3034-3109	1170	1710±20	<6	<1.5x10^{-8}	...	>17 yr	...	...	...

[a] $\delta\nu_p = \dot{\nu}\Delta\nu/\Delta\dot{\nu}$, $t_0' = \Delta\nu/|\dot{\nu}_\infty|$, $t_0 = \Delta\nu_s/|\dot{\nu}_\infty|$, where $\dot{\nu}_\infty$ is the long-term value of $\dot{\nu}$, and $\Delta\nu_s$ is the change in superfluid angular rotation frequency. Parameter errors are quoted as $\pm1\sigma$. The numbered glitches with an 'a' postfix have a much smaller amplitude than 'normal', and are classed as 'milli-glitches'. The event listed for PSR1906+00 may represent a large timing noise fluctuation. The appearence of '...' indicates that there is insufficient published data to provide that parameter.

[b] Data sources: glitches 1-4 inclusive, Cordes, Downs, and Krause-Polstorff (1988); glitches 5-7 inclusive, McCulloch *et al.* (1987); glitch 8, Hamilton *et al.* (1989).

[c] Groth (1975a)

[d] Demiański and Prószyński (1983)

[e] Lyne and Pritchard (1987)

[f] Lyne (1987)

[g] Downs (1982)

[h] Newton, Manchester and Cooke (1983)

[i] Manchester *et al.* (1983). Parameters for a second glitch of this pulsar (Flanagan, *personal communication*, 1986) have yet to be published.

[j] Gullahorn et al. (1976)

[k] Backus, Taylor, and Damashek (1982)

Lyne and Pritchard (1987) have found that the behaviour of the Crab pulsar following its third glitch shows evidence of a second rapid decay timescale in addition to the 6 day relaxation timescale noted following the previous two events. The second Crab glitch is notable in that not all of the jump in $\dot{\nu}$ diminished during the relaxation process (Demiański and Proszyński, 1983). It is evident that the Crab's spindown behaviour between glitches is complex, exhibiting a large level of timing noise, and possibly quasi-sinusoidal oscillations.

The second glitch of PSR0355+54 is the largest yet observed, being about twice the magnitude of a typical Vela event. Despite the uncertainty in the jump epoch, it is clear that the fractional change in the frequency derivative was large (table 2.1). While the majority of the change $\Delta\dot{\nu}$ appeared to decay exponentially with a relaxation time of ~ 50 days, a small positive shift in $\dot{\nu}$ with respect to the preglitch spindown value has persisted in the subsequent observations (Lyne, 1987).

Similarly, the glitch of PSR0525+21 was followed by an exponential decay with a long time-constant (~ 150 days), although measurement uncertainties and timing noise contributions are perhaps 20% of the residuals after the removal of the spindown trend (Downs, 1982). There was a small persistent enhancement of $\dot{\nu}$ following this glitch.

Several other pulsars including PSR1906+00, PSR1907+10 (Gullahorn *et al.*, 1976) and PSR1508+55 (Manchester and Taylor, 1974) have also exhibited small positive jumps in ν. However, these events (with the possible exception of that for PSR 1906+00) did not behave in the same manner as the recognized glitches, although in general the data coverage is sparse. They probably represent large timing noise fluctuations. This is also evidently the case for two jumps reported for the Crab pulsar (Groth, 1975c; Cordes and Helfand, 1980) and one for PSR0525+21 (Downs, 1982).

2.2 MODELS

Pulsar glitches have been attributed to a wide variety of causes involving processes both internal and external to neutron stars. Pines, Shaham, and Ruderman (1974) have reviewed the early theories. They found the models involving the influence of planetary orbits, matter accretion, and magnetospheric instabilities on the pulsar crust to be generally inconsistent with the perceived pulsar environment and the accumulated observational data on glitches. The most viable theories propose that glitches are initiated when a metastable threshold of the internal energy distribution is

reached by the action of the spindown torque. A sudden channelling of part of the rotational energy reservoir to the neutron star crust then occurs.

Alpar and Ho (1983) have examined the expectancy of glitches in pulsars older than the Vela using a sample of 267 objects in the light of the starquake and vortex creep models which are discussed below. They found that with either model, the statistics of the accumulated timing observations are consistent with the hypothesis that glitches occur in all pulsars, with increasingly long inter-glitch intervals as the pulsar ages.

In the remainder of this chapter, the development of glitch models is reviewed. The models have been used to infer details of the structure of neutron stars through the description of the post-glitch relaxation effects. The development of the models and the refinement of the equation-of-state (EOS) have generally proceeded along a common path. However, the adequate verification of inferences has generally been hampered by a lack of published well-sampled observations. As a result, uncertainties still remain.

2.3 THE CRUSTQUAKE HYPOTHESIS

The simple and readily visualized 'crustquake' glitch model was proposed by Ruderman (1969) shortly after the first Vela glitch, and was developed from his investigations of the surface structure of neutron stars (Ruderman, 1968). He assumed that a rapidly spinning neutron star solidifies with an oblate and highly rigid crust. Stresses steadily build within the crust due to the decrease of centrifugal forces relative to gravitational forces, as the spin of the neutron star slows under the influence of radiation torques. When the stresses reach a yield point, they are relieved by the breaking of the crust. The moment of inertia decreases as the crustal shape adjusts to a new equilibrium configuration. Conservation of angular momentum results in the sudden increase of the rotation rate;

$$\Delta\Omega/\Omega = -\Delta I/I$$

The timescale of the glitch is the time required for a shear wave to propagate across the stellar radius, which is expected to be << 1 sec. This model sought only to offer a mechanism for the glitches, and not the subsequent relaxation behaviour.

Ruderman (1969) gave a general expression for the fractional change in stellar radius as a function of latitude when the maximum crustal strain ϕ_m is reached and released. The fractional change in the moment of inertia due to the quake may be approximated using the expression for the fractional change in equatorial radius;

$$-\Delta I/I \approx \delta R/R \approx \frac{95\mu_C \delta\phi R}{7GM\rho} \qquad 2.1$$

where μ_C is the shear modulus of the crust, and R, M, and ρ are the radius, mass, and mean density of the star. Here it is assumed that $(R/R_i)^7 << 1$ where R_i is the radius of the inner crust.

In general, the crustal strain ϕ at a particular epoch is a function of latitude. At the equator,

$$\phi = \frac{7\ R^3}{8GM}(\Omega_0^2 - \Omega^2) \qquad 2.2$$

where Ω_0 is the rotation rate at which the crust is *unstressed*, and Ω is the current rotation rate. The maximum stress that can be relieved in a quake is $\delta\phi = \phi = \phi_m$. The shear modulus for the crustal Coulomb lattice is approximated by

$$\mu_C \approx (Zq_e)^2\ b^{-4}$$

where and Zq is the nuclear charge and b is distance between nuclei. Ruderman has argued that the magnitude of the strain needed to break the crust should be similar to that required to fracture terrestrial solids of the same composition; that is $\phi_m \approx 10^{-2}$.

The most critical test for this model came with the observation of the second glitches for both the Vela and Crab pulsars. This enabled the calculation of the relieved stress from equation 2.1, and also the stress accumulated since the previous glitch from equation 2.2 (assuming a reasonable stellar model). For the Crab pulsar, $\delta\phi \approx \phi_m \approx 10^{-6}$. For Vela $\delta\phi \approx 10^{-3}$-$10^{-4} >> \phi_m \approx 10^{-7}$ which was clearly not acceptable.

Before this revelation, Baym and Pines (1971) took up the crustquake idea, and proposed that only part of the excess strain was relieved in a quake. They presented a more rigourous solution which approached the problem by considering the time-dependence of the parameter characterizing the crustal distortion - the oblatness ε. This enabled them to calculate the inter-glitch timespan based on the parameters of the previous glitch.

For an axially symmetric neutron star at a particular epoch t, ε is defined according to $I_C = I_{C0}(1 - \varepsilon)$ where I_C is the crustal moment of inertia, and $I_{C0} = I_C(\Omega=0)$. The time-dependent mechanical energy is given by

$$E(t) = -\frac{I\Omega^2}{2}\varepsilon + A\varepsilon^2 + B(\varepsilon_0 - \varepsilon)^2$$

where ε_0 is a reference oblateness at a time t_0 when the stress in the crust had been relieved by a previous glitch, and I is the total moment of inertia. The rightmost two terms quantify the gravitational and elastic energy, respectively, stored in the crust as a result of rotation; here $A = 3GM^2/25R$ (M and R are the stellar mass and radius,

respectively) and $B = V_C\mu_C/2$ (V_C is the volume of the crust). The mean stress on the crust is

$$\sigma_C = \mu_C \frac{\partial I}{\partial \varepsilon} \frac{\Omega_0^2 - \Omega^2}{4(A + B)} = \mu_C (\varepsilon_0 - \varepsilon)$$

where $\Omega_0 = \Omega(t=t_0)$. A quake takes place when σ_C exceeds the critical yield stress; both ε and ε_0 then decrease according to

$$\Delta\varepsilon = \frac{B}{(A + B)} \Delta\varepsilon_0$$

where $\Delta\varepsilon = \Delta I_C / I_{C0} = -(1 - Q)\Delta\Omega / \Omega$. Here $\Delta I_C / I_{C0}$ is the fractional change in the crustal moment of inertia due to the glitch, and $\Delta\Omega / \Omega$ is the observed fractional change in the rotation speed. The stress builds after the glitch, until it is once again relieved; the inter-glitch timespan is given by

$$t_g \approx \frac{2A^2}{\Omega\,\Omega\,B\,(\partial I/\partial\varepsilon)} |\,\Delta\varepsilon\,| \qquad 2.3$$

assuming Ω is constant.

Uncertainty remained in the EOS, which was required to calculate the parameters A and B, until the work of Pandharipande, Pines, and Smith (1976; hereafter PPS). These authors suggested that if the Crab pulsar is characterized by a relatively *stiff* EOS (with a comparatively thick crust and a mass ~ 1.3 $M_\odot$) based on the tensor-interaction (TI) model (developed by Pandharipande and Smith (1975) in which the attraction of nucleons is due entirely to the contributions of pion-exchange tensor interactions), then the inter-glitch timespan should be on the order of several years. This hypothesis was supported by the parameters of the Crab's post-glitch relaxation in terms of the two-component model (section 2.5) assuming vortex pinning (section 2.6), and the subsequently reported observation of the second significant Crab glitch. In contrast, the comparatively short interval between the first two glitches of Vela required this pulsar to have to have an unreasonably low mass.

Baym and Pines (1971) examined plastic flow of the crust due to the thermally activated motion of dislocations; this process would be expected to relax strain energy slowly. Their analysis suggested that the inter-glitch timespan would be marginally increased by this process. Pines and Shaham (1972) expanded the crustquake treatment of Baym and Pines (1971) to consider the influence of a misalignment between the rotation and elastic reference axes of the neutron star. They found that the action of a radiation torque may increase the misalignment and hence also the crustal stress. As a result, the time between glitches would be reduced, although not significantly enough to improve the viability of the crustquake model for Vela.

2.4 THE COREQUAKE HYPOTHESIS

Pines, Shaham, and Ruderman (1972; hereafter PSR) proposed an alternative explanation for the Vela glitches in terms of their *corequake* theory. The development of an EOS by Canuto and Chitre (1973) suggested the possibility of solid neutron matter at the centre of neutron stars more massive than 0.6 $M_{\odot}$. Such a core is expected to be rigidly coupled (via its electrons and protons) to the magnetic field (and hence the crust) and will therefore be acted upon by the braking torque. The shear modulus of an oblate solid core will be considerably larger than that of the crust, and as a result, the core will posses a substantial reservoir of gravitational and elastic energy. PSR conceived a mechanism whereby the *working* of the core material by preceding quakes (which release the oblateness strain in a manner similar to the crustquake hypothesis) weakens the low-latitude outer core, which then becomes more susceptible to cracking under lower strain loading.

This model seems capable of accommodating both the magnitude and intervals for the Vela glitches. However, the existence of solid cores in pulsars is now doubted (Baym and Pethick, 1979). If frequent corequakes do occur within Vela, then the consequent crustal heating should make it a substantially brighter X-ray source than it actually is. An observational consequence of solid interior matter is the free precession of the star with a period which will depend on the oblateness of the core (Ruderman, 1970; Baym, Lamb, and Lamb, 1976; PPS); for Vela, the period should be of the order of minutes (PPS). However, it is evident that mechanisms related to interior superfluidity will act to dampen such an effect (Shaham, 1977). The topic of precession is explored further in section 3.4.3.

2.5 THE TWO-COMPONENT MODEL

The preceding models make no predictions of the post-glitch relaxation effect. Following on from Ruderman's (1969) crustquake hypothesis, Baym *et al.* (1969) developed the so-called *two-component* neutron star model in order to explain the behaviour following the first Vela glitch. They based their theory on the conclusions drawn by Baym, Pethick, and Pines (1969a,b). These workers argued from the estimation of the Alfvèn velocities within a neutron star and its magnetosphere that the crust and sub-crustal charged particles are rigidly coupled via the magnetic field. In addition, the response of the neutron superfluid to a crustal speed-up should be communicated more slowly through the scattering of the charged particles on the vortex cores. Baym *et al.* (1969) then set about describing the interaction of the *rigid* and superfluid components.

The equations of motion governing the two regimes are based on the consideration of Euler's equation for spindown (equation 1.8) ;

$$\dot{\Omega}_c = -N + (I_c/\tau_r)(\Omega_n - \Omega) \qquad 2.4$$

$$\dot{\Omega}_n = -(I_c/\tau_r)(\Omega_n - \Omega) \qquad 2.5$$

where I_c and I_n are the moments of inertia of the charged and neutron superfluid components, N is the external braking torque (assumed constant in Ω), τ_r is the relaxation time between the two components, and Ω_n is the bulk rotation rate of the neutron superfluid (assumed isotropic). Here the total moment of inertia is given by $I = I_n + I_c$. In the equilibrium situation $\dot{\Omega} = \dot{\Omega}_n = -N/I$ and so

$$\Omega_n - \Omega = \frac{I_n}{I_c}\frac{\tau_r}{T}\Omega \qquad 2.6$$

where $T = -\Omega/\dot{\Omega}$. Thus the interior superfluid rotates more rapidly than the crust with an excess lead velocity related to the ratio of the inertial moment of the superfluid to that of the rigid component.

A glitch is viewed as the sudden adjustment of ΔI_c and ΔI_n which forces $\Omega_n - \Omega$ below its equilibrium value. As a result, the braking torque on the rigid component increases providing an excess in $\dot{\Omega}$ until the equilibrium is attained. The fractional change in $\dot{\Omega}$ is given to first order by

$$\frac{\Delta\dot{\Omega}}{\dot{\Omega}} = \frac{\Delta\Omega}{\Omega}\frac{T}{\tau_r}\left\{1 - \frac{\Delta I_n/I_n}{\Delta I_c/I_c}\right\}$$

In the case of Vela, $\Delta\dot{\Omega}/\dot{\Omega} \approx 10^{-2}$ and $\Delta\Omega/\Omega \approx 10^{-6}$, which implies that $\Delta I_n/I_n < \Delta I_c/I_c$; this is consistent with the crustquake theory where changes in the crustal oblateness are not expected to significantly influence the shape of the superfluid core. From equations 2.4 and 2.5, and neglecting the spindown behaviour (equation 1.9), the rotation rate at time $t \geq T_j$ is

$$\Omega(t) = \Omega_0(t) + \Delta\Omega\{1 - Q(1 - \exp[-(t-T_j)/\tau])\} \qquad 2.7$$

where T_j is the glitch epoch, Ω_0 is the pre-glitch extrapolated value of the rotation frequency, and $\tau = \tau_r I_n/I$ is the relaxation time constant of the excess glitch frequency (figure 2.1). The parameter Q ($0 \leq Q \leq 1$) measures the fraction of the speedup $\Delta\Omega$ which decays away, where

$$Q = \frac{\Delta\Omega^2}{\Delta\dot{\Omega}\,\Delta\Omega} = \frac{I_n}{I}\left\{1 - \frac{\Delta I_n/I_n}{\Delta I_c/I_c}\right\}$$

In the case of the Crab pulsar, detailed analyses have been presented for the first two glitches in terms of the two-component model (Boynton *et al.*, 1972; Demiański and Prószyński, 1983), yielding $\tau \approx 10$ days and $Q \approx 0.85 \pm 0.15$. The uncertainty in the Q value stems from the precision to which the glitch epochs are known, and the small amplitudes of the glitches relative to the inherent timing noise. The observed Q suggested that the neutron superfluid constitutes the bulk of the star.

This fact, amongst others, lead Pines and Shaham (1972) to propose that the Crab is a light ($M < 0.5\ M_\odot$) neutron star. The TI model for neutron stars of mass $M \approx 1.3\ M_\odot$ provides $Q \approx 0.5$ for the two-component theory. However, if pinning processes occur between the superfluid vortices and the crustal lattice (section 2.6), then $Q \approx 0.8$ is predicted which is in modest agreement with the interpretation of the timing measurements.

However, quite a different situation exists for Vela. The data published by Reichley and Downs (1969) for the first Vela glitch gave $Q \approx 0.15$. This value was not too difficult to accept in terms of the corequake model with the EOS of Canuto and Chitre (1973), providing the stellar mass is ~ $0.7\ M_\odot$ (PSR). However, Downs (1981b) found from the analysis of subsequent glitches and the re-evaluation of the original data that $Q \approx 0.045$. For this value, the TI model predicted a similar mass however this did not admit the possibility of a solid core. The discrepancy was worse for the model of Canuto and Chitre on which the original corequake hypothesis was based. Softer equations of state, contemporary to the TI model gave a similar result (PPS). So the situation arose where although the two-component model fitted the post-glitch relaxation behaviour well, the parameters it suggested for the internal structure of Vela were incompatible with the quake hypotheses of glitches.

An important step was made by McCulloch *et al.* (1983) who were able to fit to timing data within one day of the 5th Vela glitch. They found that after removing the pre-glitch spindown trend, the post-glitch ($t \geq T_j$) data over a span of ~ 50 days was adequately modelled by augmenting equation 2.7 with a second exponential term representing a short-timescale (~ 2-5 day) relaxation effect;

$$\Omega(t) = \Omega_0(t) + \Delta\Omega_C + \Delta\Omega_0 \exp[-(t-T_j)/\tau_0] + \Delta\Omega_1 \exp[-(t-T_j)/\tau_1] \quad 2.8$$

where $\Delta\Omega_C$ is the permanent part of the jump in Ω, and the parameters subscribed with 0 (except Ω_0) and 1 refer to the long and short relaxation processes, respectively (figure 2.1 and table 2.1). The applicability of this model is discussed in section 6.6. In the same spirit as the two-component model, McCulloch *et al.* proposed that the new term was due to a previously unforeseen region of the superfluid that is closely coupled with the crust. As it was not possible to determine what fraction of the initial decay contributed to the permanent part of the frequency jump, the Q parameter of the new strongly coupled region was set to one. In this case, for the weakly coupled region (using the definition of equation 2.7 with equation 2.8)

$$Q = \frac{\Delta\Omega_0}{\Delta\Omega_C + \Delta\Omega_0} \quad 2.9$$

which gave a value consistent with the previous glitches.

The recognition of the second decay term immediately meant that the relaxation process was more complicated than previously believed. Although it was possible to arbitrarily *add-on* another superfluid region to the two-component model (McCulloch *et al.*, 1983; Lodenquai, 1984), the new behaviour demanded a closer investigation of the microphysics involved. In addition, the predictions of the two-component model were in conflict with the observed persistent shift in the *steady-state* frequency derivative following the 1975 Crab glitch (Demiański and Proszyński, 1983) and the large jump for PSR0525+21 (Downs, 1982), and also the timing noise spectrum for the Crab pulsar (Boynton, 1981). These facts lead to the increased scrutiny of the dynamics of the interior superfluid, and the subsequent development of the *vortex creep* theory for glitches (section 2.10).

2.6 THE HEAT-PULSE MODEL

Greenstein (1975, 1976) and Harding, Guyer, and Greenstein (1978) proposed that the angular velocity of the superfluid decreases with radius (in contrast to the isotropic rotation proposed by Baym *et al.* (1969)), and modified the two-component model of pulsar spindown on this basis. Significantly, their model totally neglected the effects of vortex pinning, which is now regarded as of fundamental importance for neutron star dynamics (section 2.9). Greenstein (1975) proposed that the force acting to slow the rotation of the neutron superfluid is given by

$$\mathbf{F} = \frac{\rho_n \rho_c}{\rho \tau} (\mathbf{v_c} - \mathbf{v_n})$$

where ρ_n and ρ_c are the mass densities of the neutron and charged components, $\rho = \rho_n + \rho_c$, and τ is the relaxation time scale for the interaction of the charged particles and the neutrons (discussed in section 2.7). In the steady-state, $v_c < v_n$. At the time of a glitch **F** decreases, and will become negative if $v_c > v_n$; it this latter situation arises, the superfluid will accelerate. The total torque on the charged particles is

$$N = N_{ext} + \int(\mathbf{r} \times \mathbf{F})d\mathbf{r}$$

where the latter term is the reaction torque from the superfluid; a glitch increases N which results in the enhancement of the deceleration of the crust. Eventually, N relaxes back to its steady-state behaviour.

The most serious drawback with the model was that it failed to accommodate the observed post-glitch relaxation timescales for the Crab pulsar (Greenstein, 1976) unless the temperature of the pulsar was reduced to an unacceptably low level. In addition, it was implied that the frequency and magnitude of glitches increases as a pulsar ages, which appears to conflict with the available, though sparse, statistics. Harding, Guyer, and Greenstein (1978) considered the relaxation timescales produced

by neutron beta decay, and neutron scattering against phonons and lattice defects within the crust. They found that the latter process would result in the rotation rate decaying substantially faster than that suggested by the observations.

Greenstein (1979,1981) proposed a model for the Vela glitches based on the response of the neutron star to a perturbation in temperature. The glitch magnitude of $\Delta\nu/\nu \approx 10^{-6}$ could be accounted for by a 50% change in internal temperature. The temperature perturbation would lead to the decrease of **F**. Although the general form of the relaxation of the crustal rotation rate is similar to the data for the 5th Vela glitch as briefly discussed by McCulloch *et al.* (1983), the predicted jump in the frequency derivative was over two orders of magnitude larger than that observed. In addition, the comparatively slow evolution predicted for the initial increase in rotation rate is in conflict with the data for the 8th Vela glitch (Hamilton, *personal communication*, 1989). The source of the thermal perturbation must not only be periodic, but also produce glitches with a specific range of characteristic parameters; Greenstein suggested the action of corequakes and (less convincingly) magnetospheric instabilities.

2.7 COUPLING MECHANISMS

Of fundamental importance for the modelling of pulsar spindown and glitches has been the development of an understanding of the interaction between the neutral and charged matter within neutron stars. In developing the two-component model, Baym *et al.* (1969) assumed that the neutron superfluid vortices within the inner crust do not significantly interact with the crustal lattice other than through the scattering of electrons on the normal cores. They regarded the forces that pin vortices to lattice nuclei as weak in comparison to the forces imposed radially by the Magnus relation (equation 1.3) and azimuthally by drag. Ruderman and Sutherland (1974) showed that if electron scattering from vortex cores was the predominant means of decelerating the interior superfluid, then the development of bulk turbulence through a Rayleigh instability, as suggested by Greenstein and Cameron (1969) and Greenstein (1970), was unlikely. Because of the large magnetic field strength and high conductivity of the degenerate crustal electrons, the field and the crust are locked in rigid corotation. Easson (1979b) determined the minimum requirements for the strength and organization of the interior field for the corotation of both normal and condensate phases of the plasma with the field. Easson (1979a) showed that the crust and the normal charged particles within the core are coupled on a characteristic timescale which depends on the internal temperature. For cool pulsars (those with an age of $\sim 10^6$ yr) neutron spin-up is affected via viscous coupling with the plasma, with a

timescale $\tau_S \propto T\,\Omega^{-1/2}\,R\,\rho^{-7/12}$ (where T is the internal temperature, R is the stellar radius, and ρ is the density of the coupling layer), the so-called Ekman time. For young pulsars, such as Vela, the coupling via the magnetic field is the dominant mechanism, with $\tau_S \propto B^{-2/3}\,\Omega^{-1/3}\,R^{2/3}\,\rho^{1/3}$. Typically, τ_S is of the order of 1-10 seconds.

The first detailed work to determine the timescale over which a change in the rotation rate of the crust and the plasma is communicated to the superfluid neutrons was presented by Feibelman (1971) who considered the effects of scattering of electrons on the magnetic moments of thermally excited normal neutrons within vortex cores of the $^1S_0$ neutron superfluid of the inner crust. The characteristic relaxation time $\tau(^1S_0)$ is critically dependent on Δ_n and the electron temperature T_e. Within the weak pinning regions of the Vela pulsar, $\tau(^1S_0)$ is of the order of days to months. Bildsten and Epstein (1988, *preprint*) have subsequently found that a longer timescale (months to years) relaxation exists due to Coulomb scattering from the long-range charge distribution around vortex cores set up by the action of the Bernoulli force F_B.

The problem of the coupling of the electrons to the $^3P_2$ superfluid neutrons was left open by Feibelman. The important difference between the $^1S_0$ and $^3P_2$ paired neutrons is that the latter poses a small spontaneous magnetization which modifies the scattering process. It was not until the work of Sauls, Stein, and Serene (1982; hereafter SSS) that this situation was considered in detail. These authors considered two coupling processes. The first was due to the neutron-excitation scattering mechanism considered by Feibelman for the s-phase superfluid. SSS found that the scattering relaxation time $\tau(^3P_2)$ is sensitive to T_e, but weakly dependent on Δ_n. For $\rho \approx \rho_0$, $\tau(^3P_2) \approx 1$ year for the Vela pulsar. The second coupling is due to the spontaneous magnetization of neutron vortices, which has a characteristic relaxation time of $\tau_g \approx 50$ days for Vela.

The above efforts all suggested that the bulk of the interior matter is not rigidly coupled with the crust, and therefore takes part in the relaxation process. Recently, the work of Alpar, Langer, and Sauls (1984) has changed this view. These authors have built on the efforts of SSS to consider more closely the magnetic structure of neutron vortices. However, before discussing this work, a digression is made to the original picture of the interior proton gas provided by Baym, Pethick, and Pines (1969a; hereafter BPP). These workers showed that the high electrical conductivity of the degenerate electrons causes the magnetic field to pervade the interior of a newly formed neutron star. When sufficient cooling has taken place for the protons to make the transition to a superfluid state, they organize into vortex structures because of the

presence of the field. BPP showed that the proton superfluid will behave like type II superconductor and confine one quantum of magnetic flux

$$\Phi_m = \frac{hc}{2q_e} \approx 2x10^{-7} \text{ G cm}^2$$

within a radius of λ_p of each vortex axis. Here λ_p (~ 10^{-11} cm) is termed the London penetration depth, which satisfies $\lambda_p > \xi_p \sqrt{2}$ where ξ_p (~ 10^{-13} cm) is the coherence length of the proton superfluid. The vortex density is quantized according to the local mean field strength. The upper critical mean H field strength beyond which the type II superconductive behaviour is disrupted is ~ 10^{16} G (BPP); this is not likely to be exceeded within neutron stars. Shakhabasyan (1986) has shown that a state of anisotropic superconductivity due to spin paramagnetism of the protons is unlikely on the basis of the expected internal field strength. The electrons and protons are coupled with a relaxation time of order 10^{-14} s (Sedrakyan, Shakhabasyan, and Moveseyan, 1985); any significant differential rotation would lead to energetically unfavourable current flows. BPP proposed that because only a very small fraction of the superfluid protons are normal, the coupling between the proton and neutron superfluids is extremely weak, and is dominated by the electron-neutron scattering discussed subsequently by Feibelman.

However, Alpar, Langer, and Sauls (1984) have shown that the proton-neutron coupling is likely to be strong. They investigated the effects of the drag induced on the superfluid protons by the rotation of the superfluid neutrons. The drag gives rise to a proton charge current around each neutron vortex (for both the $^1S_0$ and $^3P_2$ states) which induces a magnetic field of magnitude ~ 10^{15} G. Within a penetration length of ~ 30 fm, a magnetic flux of $\Phi_* = \Phi_m(\delta m_p^*/m_n)$ is confined, where δm_p^* is the difference between the proton effective mass and its bare mass. The coupling of the magnetic field to the core neutron superfluid is thus very effective. The relaxation timescale is insensitive to the temperature and energy gap of the superfluids; a representative value throughout the core is

$$\tau_d \approx 100(m_p/\delta m_p^*)^2/\nu$$

(Alpar and Sauls, 1988). Typically τ_d is expected to be of the order of seconds to a few minutes.

A similar investigation has yet to be reported for the case where a pion condensate is present within the core, although qualitatively similar results are expected. Because the penetration length of condensate is less than that for more normal matter (Harvey, Ruderman, and Shaham, 1986), the coupling timescale is expected to be shorter.

Workers have yet to detail the configuration of the internal magnetic field and how it behaves when proton superconduction is established. The action of the

neutron-proton drag suggests that the core magnetic flux is threaded along the neutron vortex lines and hence parallel to the rotation axis. Within the crust, the original field is effectively frozen by the electron distribution. It is evident that the axis of the surface field is not necessarily aligned with that of rotation. This poses the question as to the topography of the field lines at the lower boundary of the inner-crust, and in particular their dynamical behaviour in response to a glitch. Sedrakyan (1986) has considered the dissipation of magnetic energy at the lower boundary of the inner crust where radially moving magnetic $^3P_2$ neutron vortices undergo the phase change to the $^1S_0$ state. He provides an expression for the rate of energy release, which gives for the Vela pulsar ~ 10^{27} erg s^{-1}; this value is very much less than the thermal energy dissipated by vortex creep (section 2.9).

2.8 VORTEX PINNING

In addition to the influence of the various coupling mechanisms between the normal and superfluid components, vortex pinning has been shown to be of importance in the dynamics of neutron stars. Packard (1972) briefly suggested that vortex unpinning may be linked with glitches. The first quantitative account of vortex pinning was presented by Anderson and Itoh (1975). They investigated the phenomenon by considering the similarities between the parameters of matter-currents in neutron-star superfluids and supercurrents in laboratory type II superconductors. They estimated the pinning force per unit length between a vortex core and a nucleus and suggested that this force may be sufficiently strong so that the movement of vortices via the Magnus force will fracture the crustal lattice. They proposed that small-scale unpinning and the subsequent dissipation of the angular momentum of expelled vortices on the inner crust leads to the rotational fluctuations of timing noise.

Ruderman (1976) extended this work by investigating pinning-induced lattice fracturing as a mechanism for glitches. He assumed that the nature of the pinning force is invariant throughout the crust. Because of the uncertainty of the overlap between the energy gap of the $^1S_0$ and $^3P_2$ superfluids (figure 1.2), Ruderman considered two configurations of the interior superfluid. In the first situation, the $^1S_0$ superfluid in the inner crust is pinned to the crustal lattice and is separated from the $^3P_2$ superfluid by a region of normal matter. In this case, which would be expected for young neutron stars, only the outer superfluid will share some of its angular momentum with the rest of the star if the lattice is to break causing the expulsion of vortices. Ruderman showed that for Vela, the magnitude and interval between glitches can be explained by this situation. However, the presence of a layer of normal matter between the two different superfluid neutron phases is doubted. In the second configuration, vortices

exist throughout the star and the majority of the superfluid is pinned to the crust. As a result, the change in the moment of inertia and rotation rate brought about by lattice breaking is much larger. The interval between Vela glitches is reduced to not unreasonable values, however the predicted increase in rotation rate is an order of magnitude larger than that observed. The calculations for the Crab pulsar are in larger disagreement with observation for both situations. Subsequently, Anderson *et al.* (1981) showed that vortex crust-breaking is not dynamically plausible because the global pinning forces are more strongly constrained by the gravitational force and not by elasticity.

Alpar (1977) provided a substantially more detailed account of vortex pinning. Following on from the work of Negele and Vautherin (1973), he examined the pinning force as a function of density. A vortex line will pass through a nucleus if the energy cost per particle ($3\Delta^2/8E_F$) to normalize the matter within the vortex core is thereby reduced. Alpar (1977) found that lattice pinning is favourable in the density range $\sim 3\times10^{13}$ to $\sim 2\times10^{14}$ g cm^{-3}. By treating the superfluid neutrons within the nuclei as equilibriated Fermi systems, the pinning energy per nucleus is

$$E_P = \frac{3V}{8}\left[\left\{\frac{k_F(\rho_G)}{3\pi^2}\frac{\Delta_n^2(\rho_G)}{E_F(\rho_G)}\right\} - \left\{\frac{k_F(\rho_0)}{3\pi^2}\frac{\Delta_n^2(\rho_0)}{E_F(\rho_0)}\right\}\right] \qquad 2.10$$

where V is the overlap volume (taken as V_n/x where V_n is the volume of a lattice site and x is the greater of ξ_n, the coherence length of the inter-nuclear superfluid, and the radius of the nucleus R_N) (Alpar, 1977; Anderson *et al.*, 1981).

The pinning force per unit length of vortex line is $F_p = E_P(\Delta,\rho)/\xi_n b$ where b is the spacing between successive pinning centres.Where $\xi_n \approx R_n$, the pinning is maximal and F_p is sufficiently strong to displace nuclei from their equilibrium locations. Deeper within the crust, $\xi_n > b_z/2$ (where b_z is the lattice constant), and the pinning becomes progressively weaker because vortex cylinders can overlap more than one lattice column. The pinning is eventually sufficiently weak so that thermally activated unpinning can occur. As a result, vortex motion in such regions is akin to plastic flow.

The vortices *thread* the space between lattice sites instead of pinning when

$$\xi_n < \frac{b_z}{4}$$

For this situation, which occurs within the outermost region of the inner crust, the vortices are repelled by the lattice sites with a force per unit length of $F_T = -\gamma F_P\sqrt{3}/2a$, where $\gamma(\Delta,\rho) < 1$ is a correction factor to E_p (given by Alpar, 1977) to account for the fact that threading vortices do not pass through nuclei.

Throughout the pinning and threading regions, a long-range repulsive Bernoulli force, F_B, acts to repel nuclei from vortex cores thereby enhancing the threading force and producing a pinning energy barrier. The Bernoulli force redistributes the vortices to minimize the kinetic energy of the superfluid due to the fact that the higher density superfluid within nuclei is unable to take part in the vortex motion. Alpar (1977) has estimated the height of the barrier as $\leq$ 1 MeV. In order for vortices to repin, E_p must exceed the barrier energy. The effectiveness of the pinning force is also dependent on the strength of the local Magnus force. The maximum differential angular rotation rate that the pinning force can tolerate over a radial distance r is given by

$$\omega_{cr} \equiv (\Omega - \Omega_c)_{max} = \frac{F_p}{\rho_G \kappa r} \qquad 2.11$$

where Ω and Ω_c are the rotation rates of the local superfluid and the crust respectively (Alpar *et al.*, 1984a). As is discussed below, large-scale unpinning by this process has been invoked as a glitch mechanism.

The work of Alpar (1977) provided the foundation for the understanding of vortex movement during pulsar spindown. Pines *et al.* (1980) subsequently developed a model for the dynamical behaviour of a superfluid container with regions of weakly or strongly pinned vortices. Importantly, these workers provided the first description of the effects of radial movement of vortices through the pinning regions. Firstly, Pines *et al.* considered the steady state behaviour for a superfluid containing a strong pinning layer in a radial range $R_1 \leq r \leq R_2$. Within a non-pinning region ($0 \leq r < R_1$; region I) and a threading zone ($R_2 < r \leq R$; region II), the vortices move radially outwards as the container undergoes spindown. Whether vortices entering the pinning zone accumulate either in a thin layer or throughout the region depends on the rate at which vortex capture occurs by potential pinning locations. Within region II, the vortex density near $r = R_2$ decreases with time because of the influence of the strong pinning zone. Eventually the Magnus force exceeds the pinning force and a catastrophic release of pinned vorticity occurs leading to a glitch.

A second situation was investigated where vortices entering the strong pinning zone are not rapidly trapped. Alternating zones of excess and low vortex density become established within the pinning region; these zones undergo episodic radial movement and cause a quasi-oscillatory behaviour of the crustal spindown rate. This behaviour would produce a characteristic signature in the timing noise and would not lead to glitches.

Pines *et al.* also considered the case of weak pinning. In this case, spindown will proceed macroscopically smoothly as pinning energy barriers are easily overcome

by thermal effects. If the pinned superfluid is *shaken* or locally heated, bulk unpinning may occur to produce a glitch.

Based on these investigations, Pines *et al.* concluded that the glitches for Vela are produced by the sudden unpinning of a fraction of the vortices within a strong pinning region by the Magnus force. On the other hand, the Crab pulsar was regarded as containing a zone of only weakly pinned superfluid. A glitch is produced by a small quake which initiates vortex unpinning; it is the motion of the vortices that produces the majority of the change in the moment of inertia. Pines *et al.* regarded the post-glitch relaxation for both pulsars as reflecting the time taken for the recoupling of the superfluid within the glitch region.

2.9 VORTEX CREEP THEORY

2.9.1 Pulsar Spindown and Glitches

The work of Alpar (1977), Pines *et al.* (1980), Alpar *et al.* (1981) and Anderson *et al.* (1981) was extended by Alpar *et al.* (1984a,b) in the development of the vortex creep theory of pulsar spindown. The basis of this theory is that the dominant internal torque acting on the surface arises from the pinning of vortex lines within the inner crust. The equation of motion of the normal stellar component (the crust plus the corotating charged particles and core superfluid) is written as

$$I_c\dot{\Omega}_c(t) = N_{ext} + N_{int} = N_{ext} - \int dI_p\, \dot{\Omega}(r,t)$$

where N_{ext} and N_{int} are the external and internal torques respectively, and I_c and $I_p = \int dI_p$ are the moments of inertia of the normal and pinned components respectively. It is regarded that vortex pinning takes place over a limited density range of the inner crust.

Within regions where the relative superfluid angular velocity ($\omega \equiv \Omega - \Omega_c$) is below and sufficiently close to ω_{cr} (equation 2.11) within the pinning region, Alpar *et al.* (1984a) have shown that is is favourable for vortices to thermally tunnel between adjacent pinning sites in a radially outward direction. The superfluid spindown is thus affected by vortex creep.

The glitch temporarily decouples all of the pinned superfluid from the spindown of the neutron star. The post-glitch relaxation is then contributed by the recoupling of the vortex creep process in two physically distinct regions. At the time of the glitch, creep is terminated in the inner region, and a bulk unpinning of vortices takes place in an inner region G, the glitch site. The cause of the unpinning is a chain-reaction brought about when a fluctuation in vortex density brings the local value of ω

up to ω_{cr}. The free vortices move radially outwards through a region B and eventually repin in a second region, G', where the creep process becomes re-established. The re-establishment of creep within regions G and G' is shown to produce a fundamentally non-linear torque on the crust which is manifest as exponential decays in the pulsar's rotation frequency. A third torque, which is shown to be linear in the angular velocity lag between the crust and superfluid, is produced by the recoupling of creep in the boundary region B through which vortex transport takes place.

Cheng *et al.* (1988) have examined the distribution of vortices in a region where ω_{cr} has large spatial variations due to structural inhomogeneities, and have found that vortices may be either accumulated or depleted in these regions. Specifically, where $\partial\omega_{cr}/\partial r > 2\Omega_c/r$, a free vortex line entering an accumulation region may initiate the bulk unpinning of a layer of vortices. Cheng *et al.* (1988) have suggested that this situation may give rise to small frequent unpinning events which contribute to timing noise.

Figure 2.2 illustrates the behaviour at the boundary between regions G and G'. If it assumed that N_v vortices travel from region G to G', then the average change in the superfluid velocity in region B is

$$\delta\Omega_B = \frac{N_v \kappa}{2\pi r_B^2}$$

where r_B is the location of the transition region (whose width is small in comparison with r_B). Clearly, in regions G and G', $\delta\Omega$ changes from 0 to $\delta\Omega_B$ and $\delta\Omega_B$ to 0 respectively. The changes are bound not to be smooth, but contain local fluctuations about these trends. Alpar *et al.* (1984a) disregard the fluctuations, and modelled the change in $\delta\Omega$ in regions G and G' by a linear averaging procedure.

The angular momentum transferred from the superfluid to the crust due to the sudden vortex motion is

$$(\tfrac{1}{2}I_A + I_B)\delta\Omega_B = I_C \Delta\Omega_C \qquad 2.12$$

where $I_A \equiv I_G + I_{G'}$ is the total moment of inertia of the pinned superfluid in regions G and G', and I_B is the moment of inertia of the pinned superfluid in region B. The vortex creep theory predicts that the re-establishment of creep in the three regions will contribute internal torques of the form

$$N_i(t) = |N| \frac{I_i}{I} \frac{1}{1 + [\exp(t_i/\tau_i)-1]\exp(-t/\tau_i)} \qquad 2.13$$

where $t_i = \dfrac{\delta\Omega_i}{|\Omega_\infty|}$ (with $\delta\Omega_i$ the change in superfluid velocity in the ith region, and $|\Omega_\infty| = |N_{ext}| / \{I_C + \sum_i I_i\}$). In the regions G and G', $\delta\Omega_i = \Delta\Omega_C$, crust velocity at the time

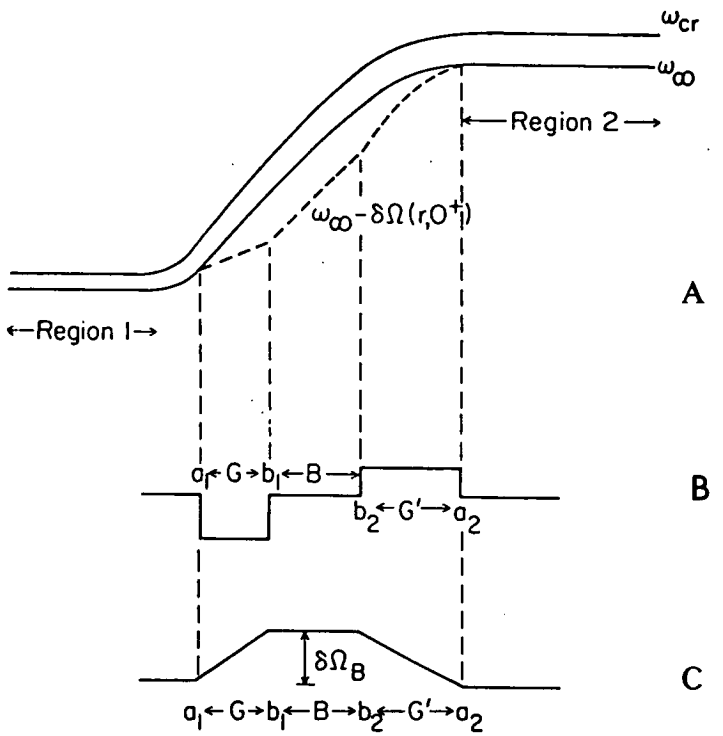

Fig. 2.2. Schematic description of the boundary region for the Vela pulsar. The distance from the rotation axis increases to the right, and density to the left; (a) variation of ω_{cr} and ω_∞, (b) vortex density, (c) the change in the superfluid rotation rate. (After Alpar *et al.*, 1984b).

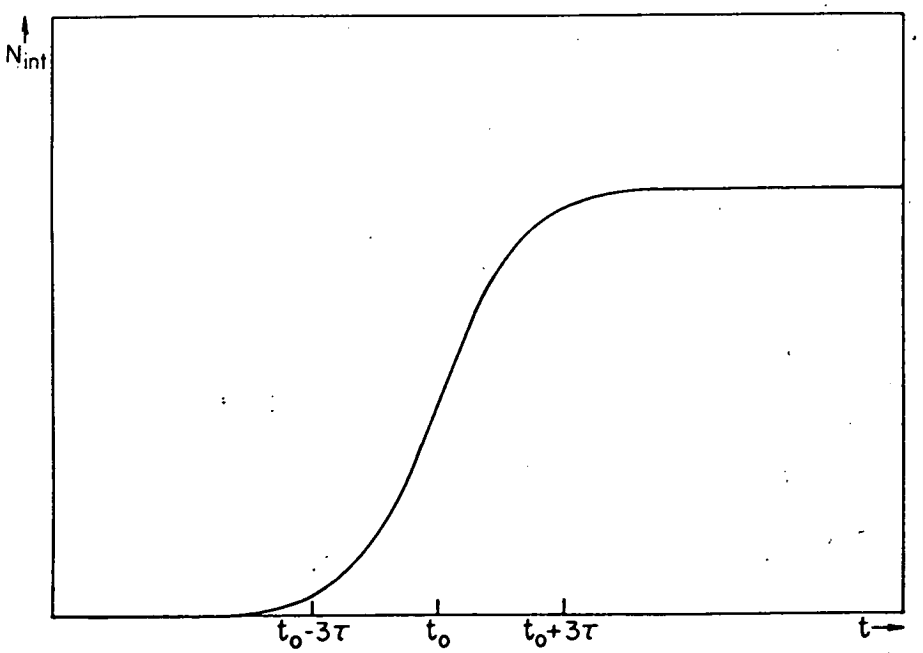

Fig. 2.3. The behaviour of the torque contributed by region i for the case $t_i >> \tau_i$. (After Alpar *et al.*, 1984a).

of the glitch, and in region B, $\delta\Omega_i = \delta\Omega_B$. The form of equation 2.13 is illustrated in figure 2.3.

The term τ_i describes the average creep relaxation rate and is given by

$$\tau_i = \alpha_i \frac{T}{|\dot{\Omega}_\infty|} \qquad 2.14$$

where T is the internal temperature of the neutron star. Thus for times $t < \text{minimum}(t_i)_i$, the change in the rotation rate of the pulsar will simply reflect the external magnetospheric torque.

2.9.2 Post-Glitch Relaxation

Alpar *et al.* (1984b) provide a general expression for the post-glitch relaxation for $t < t_B = \frac{\delta\Omega_B}{|\dot{\Omega}|_\infty}$ as

$$\Omega_c(t+\Delta) - \dot{\Omega}_c(\Delta) = \sum_{i=1}^{2} \left\{ \frac{|N|\, I_i}{I_c\, I} \cdot E_1 \cdot E_2 \right\} + \frac{|N|\, I_A\, t}{I_c\, I\, t_B} \qquad 2.15$$

where

$$E_1 = \frac{\exp(-\Delta/\tau_i)\,[\exp(t_0/\tau_i)-1]}{1+ \exp(-\Delta/\tau_i)\,[\exp(t_0/\tau_i)-1]}$$

$$E_2 = \frac{\exp(-\tau/\tau_i)}{1 + \exp[-(t+\Delta/\tau_i)]\,[\exp(t_0/\tau_i)-1]}$$

Here τ_i is the relaxation time for the i-th pinning region, and Δ is the uncertainty in the epoch of the glitch ($0 \le \Delta \le \Delta_m$, where Δ_m is the interval between the last pre-glitch observation and the first post-glitch observation). In addition

$$t_0 = \frac{\Delta\Omega_c}{|\dot{\Omega}|_\infty} \approx \frac{\Delta\Omega_c\, t_s}{\Omega_c}$$

where t_s is the spindown timescale (equation 1.9). The separate terms of equation 2.15 are illustrated in figure 2.4. Possibilities for the the long term behaviour, which depend on t_B in comparison to the inter-glitch timespan, are illustrated in figure 2.5.

Alpar *et al.* (1984b) have shown that this model provides a reasonable description of the post-glitch behaviour in $\dot{\Omega}_c$ for Vela through the analysis of the JPL data on 4 large glitches and one milli-glitch presented by Downs (1981b). The parameters obtained from the fits to the first four glitches vary (table 2.1), although the analysis is hampered by the lack of data immediately following each glitch. The time constants obtained are on the order of $(\tau_1,\tau_2) \approx$ (3 days, 60 days). They note that a limited range of relaxation time constants should be associated with each of the

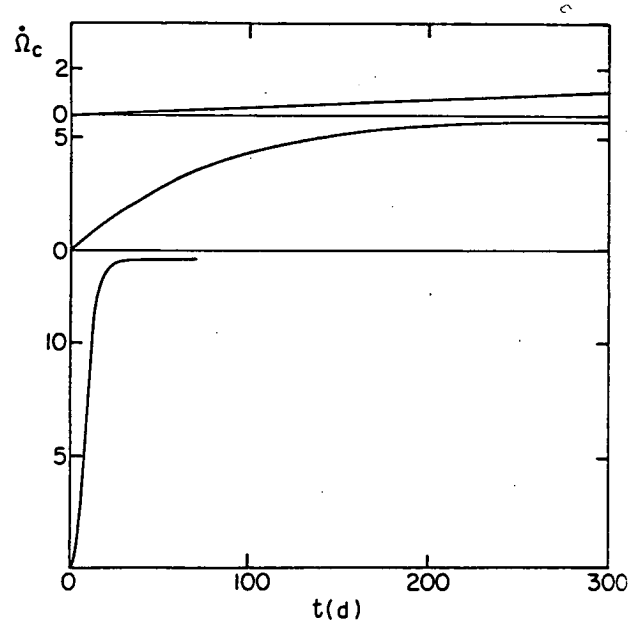

Fig. 2.4. The separate effects of the three torques N_1, N_2, and N_A on $\Omega_c(t)$ (lower, middle, and upper curves respectively). Plotted is $\dot{\Omega}_c(t+\Delta) - \dot{\Omega}_c(t)$ in units of 10^{-13} rad s^{-2} as a function of $t > t_0$. (After Alpar *et al.*, 1984b).

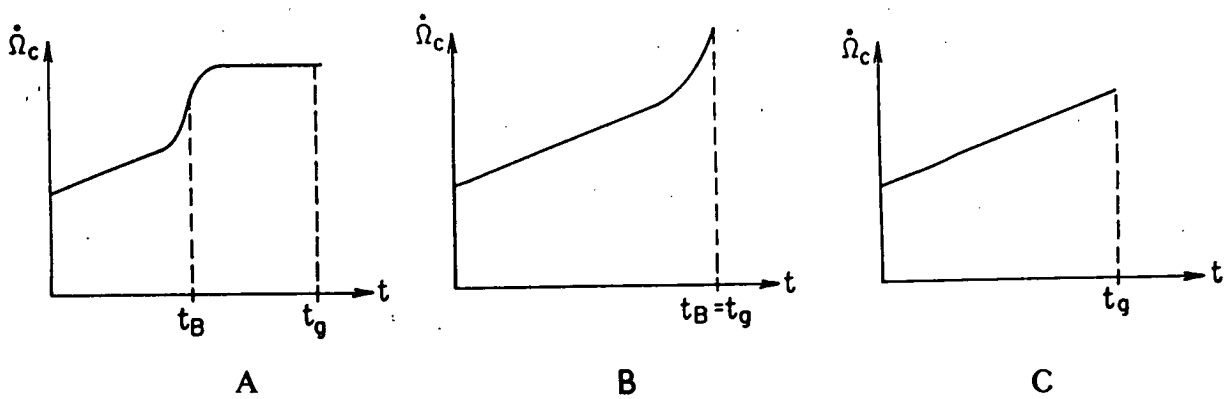

Fig. 2.5. The effect that reestablishment of vortex creep in boundary region B would have on the observed $\dot{\Omega}_c(t)$. (a) if $t_B < t_g$, the time to the next glitch, creep would be reestablished in region B, and $\dot{\Omega}_c(t)$ would then take on a non-linear behaviour with time. (b) the recoupling of region B is interrupted by a glitch. (c) no recoupling takes place before the next glitch. Alpar *et al.* (1984a) have suggested that the reestablishment of coupling in region B may in fact initiate a glitch. (After Alpar *et al.*, 1984b).

pinning regions 1 and 2, rather than a unique value. In addition, they predict $t_0 \approx 25$ days, and $t_B \approx 1500$ days.

Based on the observed relaxation timescales and glitch magnitudes, it is apparent that the EOS for the Vela pulsar is stiff, lying between the predictions of the mean field (MF) model (which attributes the inter-nucleon attraction to the exchange of an effective scalar meson; Panharipande, Pines, and Smith, 1976) and the tensor interaction (TI) model (Cheng, 1987a).

Alpar *et al.* (1984b) have been able to calculate the internal temperature of the Vela pulsar based on the creep rate deduced from the relaxation times. They suggest that if the regions 1 and 2 of figure 2.2 contain superweak and weak pinning respectively, then $T \approx 10^7$ K, in agreement with the predictions of cooling calculations, and the upper limit of the surface temperature set by X-ray observations.

Cordes, Downs, and Krause-Polstorff (1988; hereafter CDK-P) have provided a more detailed analysis of the JPL Vela timing data, extending the fits to the fifth and sixth glitches. They have suggested that the variation of the relaxation time constants is due to the change of the radial location of the pinning/unpinning regions between glitches. On the basis of the strong anticorrelation between τ_2 and $\Omega_{c3} = \Omega_c I_A/I_c t_B$ (where Ω_c is the second time derivative of the spindown due to the external torque), CDK-P have tentatively suggested that τ_2 is associated with a region of strongly pinned superfluid; this is in conflict with the conclusions of Alpar *et al.* (1984b).

Although the vortex creep theory adequately predicts the form of the relaxation, the strongest test is to examine the rotational behaviour for post-glitch times $< t_0$ where the internal torques should be decoupled. In Chapter 6, it is shown from the Llanherne measurements that Ω_c exhibits a distinct relaxation for times to within 1.2 days after each glitch epoch.

Alpar, Nandkumar, and Pines (1985; hereafter ANP1) have successfully applied the vortex creep model to the Crab pulsar and PSR0525+21. They explained the persistent shift in Ω_c for these pulsars as due to the pile-up of vortices in a trapping zone within the weak pinning region. The trapped vortices add to the internal torque following a glitch. The theoretically derived internal temperatures for the two pulsars are in reasonable agreement with observational limits. ANP1 suggested that creep is a significant source of heat in old pulsars, modifying the cooling trend from that based solely on photon emission from the surface.

The vortex creep model has recently been applied by Alpar *et al.* (1988) to the large glitch of PSR0355+54 (Lyne, 1987). For this pulsar, $t_0 \approx 5$ years, which is significantly greater than the interval between the glitch and the first post-glitch observation. Importantly, the pulsar exhibits relaxation for all post-glitch observations. On this basis, Alpar *et al.* (1988) have modified the vortex creep theory to account for these observations.

2.10 GLITCH-INDUCED TIMING FLUCTUATIONS

The possibility of the rotational oscillation of the crust of a neutron star following a glitch has been addressed by several workers. High resolution timing observations offer a means of testing these ideas. Baym, Pethick, and Pines (1969a) suggested that internal magneto-hydrodynamic (Tkachenko) waves are initiated by a glitch (see also Pines *et al.*, 1980). The waves propagate throughout the superfluid, causing the axial oscillation of vortex cores. This situation is akin to acoustic lattice vibrations in solids. Ruderman (1970) idealized the situation for neutron stars by considering the dynamics of Tkachenko oscillations in a rotating cylindrical container of superfluid in the absence of vortex pinning. He suggested that the surface of the cylinder oscillates with a characteristic frequency Ω_T about its mean rotation rate Ω due to the variation in the vortex density immediately adjacent to the inner surface of the container. He expressed the fundamental oscillation frequency as

$$\Omega_T \approx \frac{1.1\times10^{-5}\sqrt{\Omega}}{R} \qquad \text{Hz}$$

where R is the cylinder (or stellar) radius (m). For the Crab pulsar, Ruderman calculated $2\pi/\Omega_T \approx 4$ months, which was in agreement with the period of the quasi-sinusoidal oscillations about the spindown behaviour that were reported by Richards *et al.* (1970). For Vela, $2\pi/\Omega_T \approx 200$ days.

However, in a more realistic model, the oscillation period and amplitude will depend on the processes of vortex pinning and the coupling between the superfluid and charged particle and magnetic field. Jones (1988) has suggested that the drag between the neutron and proton superfluids restricts undamped Tkachenko modes to the inner crust where superconducting protons are absent. Sonin (1987) has suggested that pinning will increase the oscillation frequency, with a maximum value given by

$$\Omega_L = \left\{ \frac{\kappa}{4\pi R^2} \ln\frac{r_v}{r_c} \right\}^{1/4} (2\Omega)^{3/4}$$

where r_v/r_c is the ratio of the inter-vortex spacing to the vortex core radius. For Vela, $2\pi/\Omega_L \approx 16$ minutes. A detailed treatment of this problem is clearly lacking.

According to Ellison and Kazanas (1983), rapid crustal heating from glitch-induced Tkachenko waves may play a significant part in the emission mechanism of gamma-ray bursters. In addition, magnetospheric shocking and disruption may also occur. For pulsars, this aspect could be experimentally investigated through the careful measurement of dispersion and pulse parameters. The existence of discrete glitch-related changes of the dispersion measure for the Crab pulsar are questionable (Rankin *et al.*, 1988), although such an event may be associated with the most recent Vela glitch (Hamilton, *personal communication*, 1989).

2.11 CONCLUSIONS

Glitch models have undergone extensive development during the two decades since the phenomenon was first identified, largely as the result of the accumulation of observational data for the Vela and Crab pulsars. Currently, all models are in conflict with the observations at some level.

The standing of the models for the Vela pulsar can be broadly summarized as follows. The crustquake model has not been able to account for the frequency and magnitude of the glitches. The corequake model has also been rejected on the basis of surface temperature estimates and the refinement of equations-of-state which suggest that solid cores are unlikely. The two-component model has failed to predict the rapid post-glitch relaxation effect. In addition, it is not compatible with the corequake model as it suggests an internal structure which is in conflict with the viable equations-of-state. The heat-pulse model has failed to provide a reasonable prediction for the post-glitch frequency derivative and the immediate post-glitch behaviour. The vortex creep theory in its original form predicts an interval during which the crust and superfluid are decoupled that is not supported by the observations. However, the model does achieve a fundamentally non-linear post-glitch relaxation effect based on interior micro-physics that is in reasonable agreement with observation. In addition, it predicts a surface temperature that is compatible with the best available upper limit.

The application of the vortex creep model to the glitches of the Crab pulsar, PSR0525+21, and PSR0355+54 has experienced some general success. Although this model has achieved the most comfortable acceptance of any proposal to date, a confident general theory is considerably lacking. A major aim of future modelling must be the reconciliation of the seemingly inherent variability of the magnitude of the basic glitch observables that not only occurs for each event of the Vela pulsar, but also between those of different pulsars. This feature may owe its very nature to the operation of a fundamentally unstable glitch initiation process that indecisively sets its

own threshold level oblivious to the wishes of the external observer hoping to catch an event in its entirety during his or her research lifetime.

Aspects demanding additional theoretical study are the viability and significance of glitch-induced magneto-hydrodynamic oscillations in the modification of the rotational behaviour and external environment of pulsars, and the description of the interior magnetic field topology. In addition, it is evident that the exploration of interior coupling mechanisms is yet to be exhausted.

CHAPTER 3 - PULSAR TIMING NOISE

3.1 INTRODUCTION

It is common practice to fit pulsar arrival time measurements (referenced to an inertial frame) with a spindown model which may include terms to absorb any glitch events. This work is required, for example, as part of the procedure to obtain a prediction of the apparent pulse frequency for a future epoch at which synchronous pulse integrations are performed. However, when account is made of the contributions of spindown, glitches, relative motion, propagation delays, and measurement uncertainties, the residual phase values of most pulsars exhibit the signature of inherent timing noise.

The characterization and interpretation of timing noise is of considerable interest for the understanding of neutron star dynamics. Aside from this aspect, timing noise ultimately limits the usefulness of most pulsars as precision time reference standards and tools for the detection of low-frequency gravitational radiation (Mashhoon, 1982; Hellings and Downs, 1983; Romani and Taylor, 1983). The millisecond-class pulsars exhibit very little measurable timing noise, and as a result have received considerable attention in connection with the aforementioned areas (e.g. Blandford, Narayan, and Romani, 1984; hereafter BNR).

Several workers have undertaken detailed analyses of pulsar timing noise and through their efforts it has been possible to restrict models for the underlying phenomena. It is evident that the timing noise of an individual pulsar is largely due to genuine changes in the rotation rate of the crust of the associated neutron star, rather than because of processes that influence the emission and propagation of the pulses. Given an understanding of the internal structure and external environment of pulsars, several physical processes that may conspire to produce the timing activity of an individual object are currently considered viable. Each of these processes involves the application of a time-varying component of torque on the neutron star crust which then responds over a characteristic timescale. In the next section, the methods that have been employed in characterizing timing noise are summarized. In section 3.3, the observational data for the Vela pulsar are examined, while the viable physical processes for pulsar timing noise are reviewed in section 3.4.

3.2 THE CHARACTERIZATION OF TIMING NOISE

Timing noise of radio and X-ray pulsars is studied through the characterization of the statistical and temporal behaviour of pulse phase ϕ and its higher order time derivatives, specifically the frequency parameters ν and $\dot{\nu}$. In the case of radio pulsars, the analysis is hindered by secular spindown (and additionally in some cases, by glitches) which contaminates the phase values, and by the uneven way in which the phases are usually sampled in practice.

The first published description of timing noise was made by Boynton *et al.* (1972) who examined the first three years of timing data for the Crab pulsar. From their work, it was apparent that statistics with *stationary* (that is, time-independent) behaviour could be applied to fluctuations in $\dot{\nu}$, but not to the lower order parameters of ν and ϕ. The evidence for this result came from the ability to characterize the evolution of ν and ϕ in terms of *random-walk* processes driven by *white noise* in $\dot{\nu}$. This suggested that a stochastic component of torque acts on the crust of the underlying neutron star.

Random-walk analysis (Appendix A.2) has been applied to other radio pulsars by Cordes and Helfand (1980) and Cordes and Downs (1985; hereafter CD). These surveys have found that stochastic torque fluctuations are not solely responsible for all manifestations of timing noise. Indeed, pure random-walk behaviour is not exhibited by many pulsars, some of which show discrete jumps in their timing parameters. Loshen (1972, 1975, 1981) identified significant seemingly abrupt jumps in the timing parameters of the Crab pulsar which Cordes and Helfand (1980) regarded as having a signature distinctly different to that of glitches. A number of other studies, including those of Manchester and Taylor (1974), Gullahorn *et al.* (1976) and Gullahorn and Rankin (1978, 1982) have revealed additional examples of discrete timing events. Importantly, Cordes, Downs, and Krause-Polstorff (1988) have shown that discrete activity is apparent in the spindown of the Vela pulsar.

Cordes and Helfand (1980) have shown from an analysis of the timing data for 50 pulsars that idealized random walks in ϕ, ν, and $\dot{\nu}$ are most consistent with the behaviour of two, four (and possibly as many as seven), and two different objects, respectively. These authors briefly discussed a means of obtaining limits on the rate R for steps in an idealized random walk; typically, the inferred step rate lies in the range many per day to one every few hundred days for pulsars exhibiting a pure walk in ν. In addition, they proposed that apparent steps in ν and distinct values of $\dot{\nu}$ (aside from that of the Crab pulsar) were possibly the result of fluctuations in a random walk process.

CD have examined the data for a sample of 24 pulsars in considerable detail. They concluded that the timing activity of most objects can not be modelled in terms of idealized, large rate random walks. Instead, they suggested that timing activity contains discrete, identifiable events in one or more of the parameters ϕ, ν, and $\dot{\nu}$, which may be superimposed on an idealized random walk process, or a mixture of idealized walks, or another type of process. However, a small number of objects did show timing activity consistent with a preferred form of idealized random walk, a result supporting the work of Cordes and Helfand (1980).

The temporal structure of discrete timing activity has been investigated by CD utilizing *structure function* analysis (Appendix A.3); this method has found application in the study of the stability of laboratory frequency standards (Rutman, 1978), and radiowave scattering phenomena (Simonetti, Cordes, and Heeschen, 1985). The primary aspect addressed by this work is whether the discrete activity can be reconciled as the result of fluctuations in a random walk process, or by other phenomena of internal or external origin.

The description of timing noise in terms of the power spectrum of fluctuations in ϕ and its derivatives (Appendix A.4) has been investigated by Deeter and Boynton (1982) and Deeter (1984); this approach has found particular utility in testing theoretical models. The spectral techniques developed and assessed by these authors are most suited where noise spectra are anticipated as having excess power at low frequencies (in which case the noise is termed to be *red*), and additionally, where the noise observable is non-uniformly sampled. It has been shown that the choice of power density estimators based on polynomials provides an accurate and computationally simple method of extracting spectra in the face of red noise, albeit with low resolution. However, the application of this method and alternatives considered by the aforementioned authors have only been examined on the basis that purely white noise exists in the r-th derivative of ϕ, in which case the lower order k-th derivatives of ϕ exhibit noise spectra with a spectral index given by $s = 2(r - k)$. As BNR have pointed out, interstellar scattering and background gravitational radiation will be associated with characteristic odd integral values of s. Work by Boynton and Deeter (1986, *preprint*) has shown that some pulsars (e.g. the Crab) have a white power spectrum in $\dot{\nu}$, while others have a composite spectrum with red and white noise components. In some of the latter cases, power in the high cyclic frequency domain has the attributes of *blue* noise.

3.3 TIMING NOISE OF THE VELA PULSAR

Three major works have quantified the non-glitch timing activity of the Vela pulsar.

Cordes, Downs, and Krause-Polstorff (1988) have examined 14.5 years of JPL Vela timing data up to March, 1983. They fitted an appropriate model with spindown and glitch terms (as described in Chapter 6) to phase values within each inter-glitch timespan of the data. Phases over shorter intervals (10-60 days, depending on the adequacy of sampling) were then fitted with a cubic model, and estimates of ν and $\dot{\nu}$ for the central epoch t were obtained. These were subtracted from the appropriate parameters from the fit to the entire data set to yield differences $\delta\nu(t)$ and $\delta\dot{\nu}(t)$. The differences were detrended by removing a running linear fit in order to highlight fluctuations. The results for observation intervals common to the Llanherne data set are shown in figure 3.1. Importantly, this work revealed several apparently discrete changes in $\dot{\nu}$ with $| \delta\dot{\nu} / \dot{\nu} | < 10^{-4}$. A detailed statistical description of this activity in the same vein as conducted by CD for 23 pulsars is yet to be published.

Alpar, Nandkumar, and Pines (1986; hereafter ANP2) have presented low resolution power spectra in Ω for the Vela pulsar calculated using cubic and quartic polynomial estimators from work by Boynton and Deeter (1986, *preprint*) using JPL data. As shown in figure 3.2, the spectra exhibit power in excess of that contributed by measurement noise at cyclic temporal frequencies corresponding to observation spans greater than ~ 20 days. This suggests that the timing behaviour cannot be simply ascribed to white torque noise.

Downs and Krause-Polstorff (1986; hereafter DK-P) have examined the short timescale fluctuations in pulse phases for the sample of 24 pulsars, including Vela, in the JPL timing programme. Earlier, CD provided evidence (figure 3.3) showing that, for most pulsars, the fast (relative to the pulse period) fluctuations in the observed phase values are in excess of the estimated contribution due to measurement noise alone (Appendix A.2). The origin of this effect has remained unresolved. By examining data from at least two separate observation systems, DK-P demonstrated that the excess residuals were independent of system sensitivity. A cross-correlation analysis was performed between the residuals and associated values of the moments quantifying the stability of the integrated profile shapes and measures of the profile perimeter. No significant correlations were found to exist, suggesting that pulse shape changes do not contribute to the excess residuals.

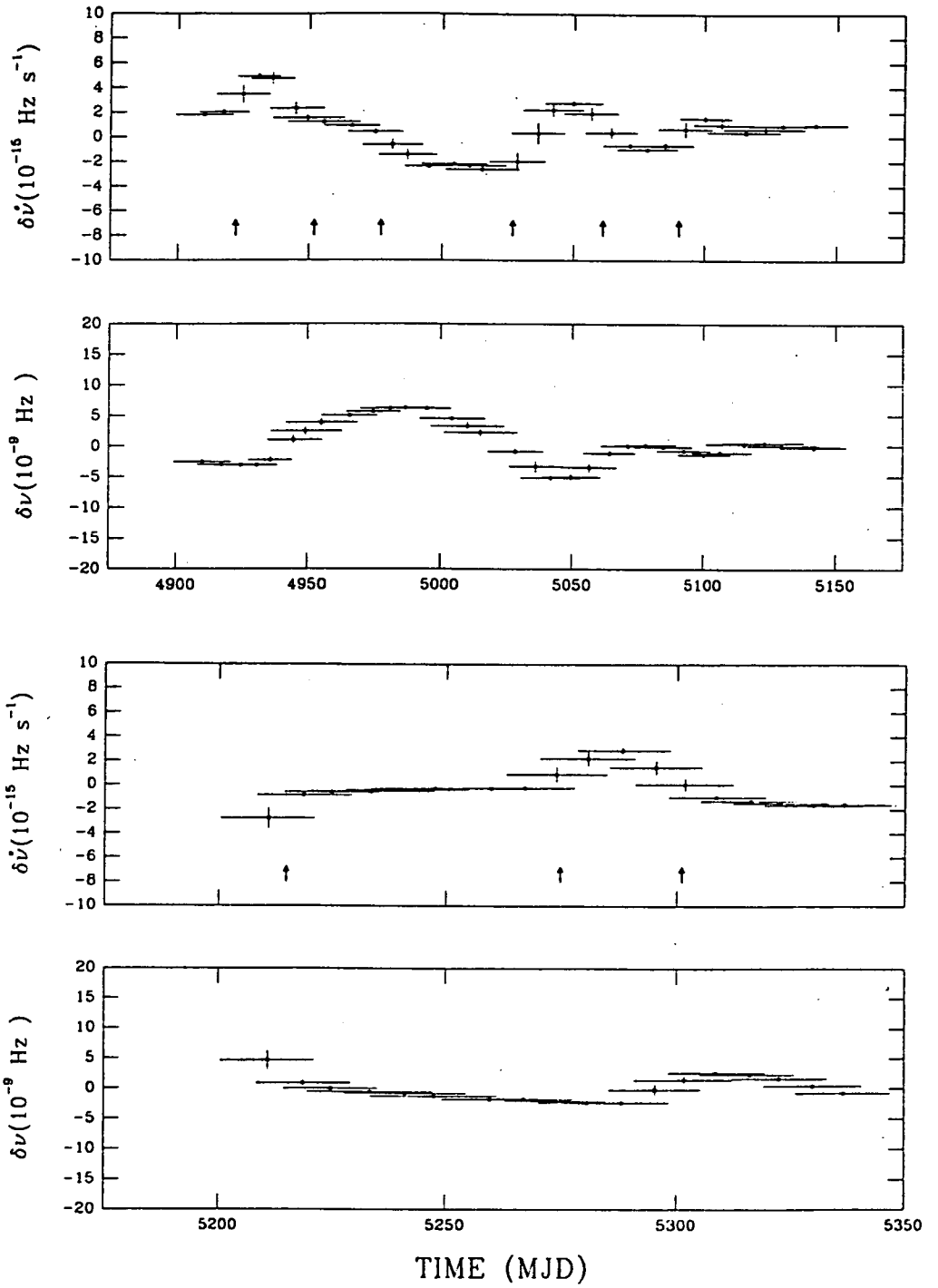

Fig. 3.1. Data presented by Cordes, Downs, and Krause-Polstórff (1986; hereafter CDK-P) from JPL observations of PSR0833-45 illustrating fluctuations in ν and $\dot{\nu}$ during the interval spanned by both the JPL and LRO timing programmes. The plots show $\delta\nu(t)$ and $\delta\dot{\nu}(t)$ from short polynomial fits after detrending as discussed in the text. Vertical bars are $\pm 1\ \sigma$ formal errors. Horizontal bars indicate the time interval for the polynomial fit. Vertical arrows identify the epochs of candidate micro-jumps selected using a threshold test described by CDK-P.

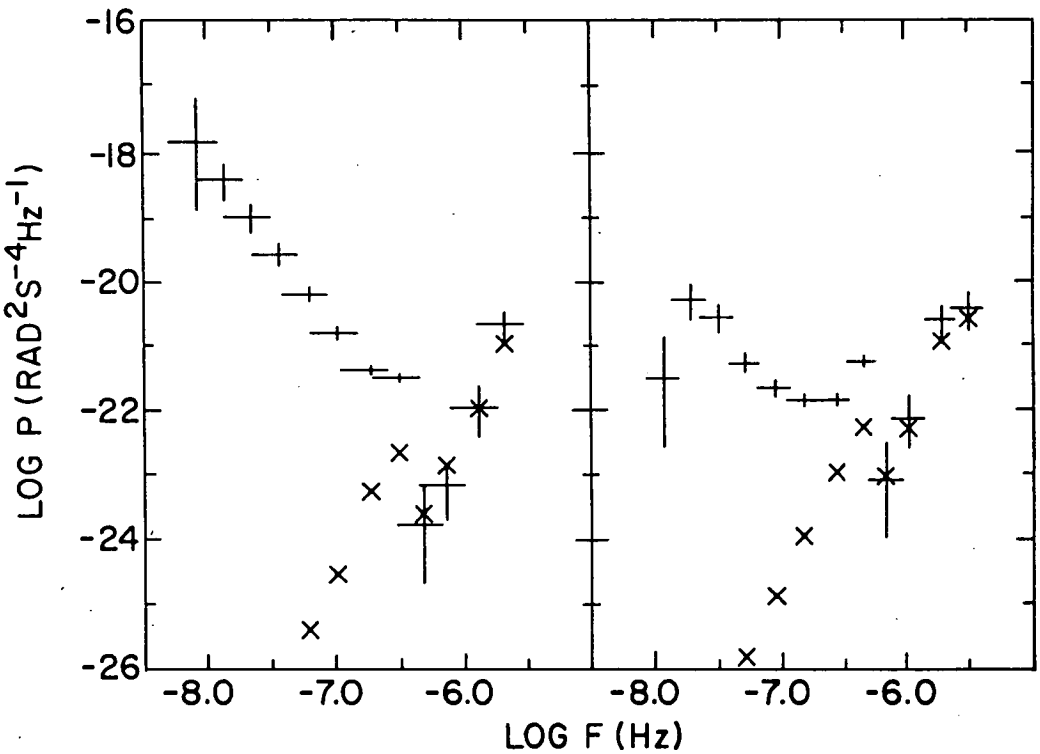

Fig. 3.2. Logarithm of power density in $\dot{\nu}$ as a function of cyclic frequency for PSR0833-45. The noise power obtained using cubic and quartic estimators is shown in (a) and (b) respectively. The vertical bars give the uncertainty in each power estimate, while the horizontal bars approximate the frequency bandpass of the estimator. The estimated contribution to each power density from measurement white noise is indicated by a diagonal cross. (After Alpar, Nandkumar, and Pines, 1986; Boynton and Deeter, 1986 *preprint*).

DK-P evaluated the autocorrelation function R_a of the timeseries representing residuals averaged in non-overlapping spans of 30 minutes. As shown in figure 3.4, R_a exhibits significant non-stationary behaviour with time lag τ, particularly for $\tau < 2$ hours, the maximum contiguous span of arrival time estimates for the JPL observations. A similar behaviour is claimed to be exhibited by other pulsars of the observing programme. Additionally, for the Vela pulsar in particular, R_a at a fixed lag shows evidence of non-stationarity with the central epoch of the data set utilized. DK-P have represented $R_a(\tau)$ as the combination of an unresolved rapidly decaying component, and a second term characterized by a Gaussian function with a half width of ~ 1 hour. The former component remains unresolved with bin widths down to 3 minutes. DK-P briefly discussed possible sources of the observed behaviour of R_a and found no viable explanation in terms of magnetospheric, interstellar, and observing effects. They called for the confirmation of the observed behaviour; this is addressed in Chapter 5 utilizing the Llanherne data for which the maximum contiguous sampling span is 5.4 hours.

3.4 MODELS

In this section, the conclusions of several studies that have addressed the origins of timing noise are summarized.

3.4.1 Internal Torque Fluctuations

Cordes and Greenstein (1981) and Greenstein (1981) have examined the ability of the heat pulse model (section 2.6) to account for timing noise. They found that torque fluctuations caused by the change in coupling between the stellar interior and crust due to a local perturbation of temperature are capable of yielding strength parameters consistent with those observationally obtained by Cordes and Helfand (1980).

Padmaraj and Nair (1985) have examined the possibility that fluctuations in the interior temperature of neutron stars leads to a sympathetic change in the stellar radius. These authors do not provide a specific mechanism for generating the temperature variations, but suggest that in the case of the Crab pulsar, changes in the stellar moment of inertia due to temperature jumps of magnitude ~ 10^3 K occurring at a rate of approximately one per day is consistent with the timing noise data.

Boynton (1981), following on from the work of Lamb, Pines, and Shaham (1978a,b) showed that the form of the noise spectrum for the Crab pulsar was

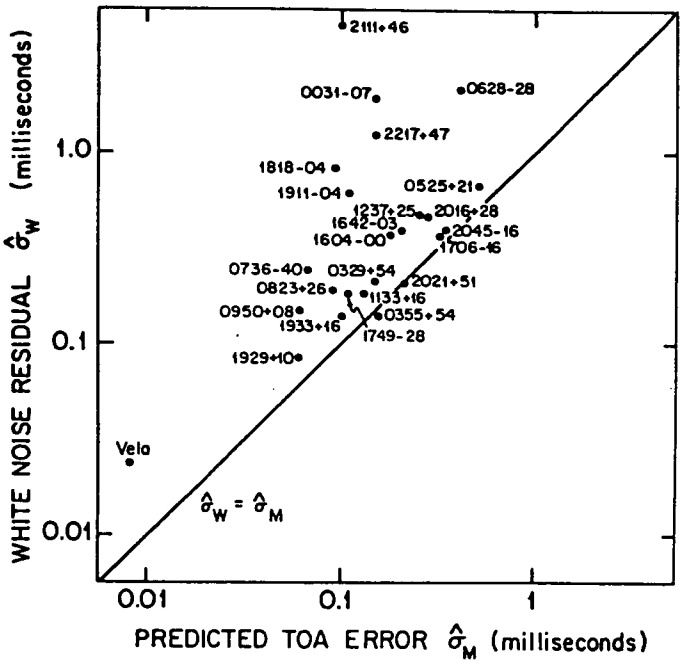

Fig. 3.3. Root mean square white-noise residual against rms time-of-arrival (TOA) error due to additive noise for 24 pulsars in the JPL timing programme. Note the excess in the white noise residual for the majority of pulsars. (After Cordes and Downs, 1985).

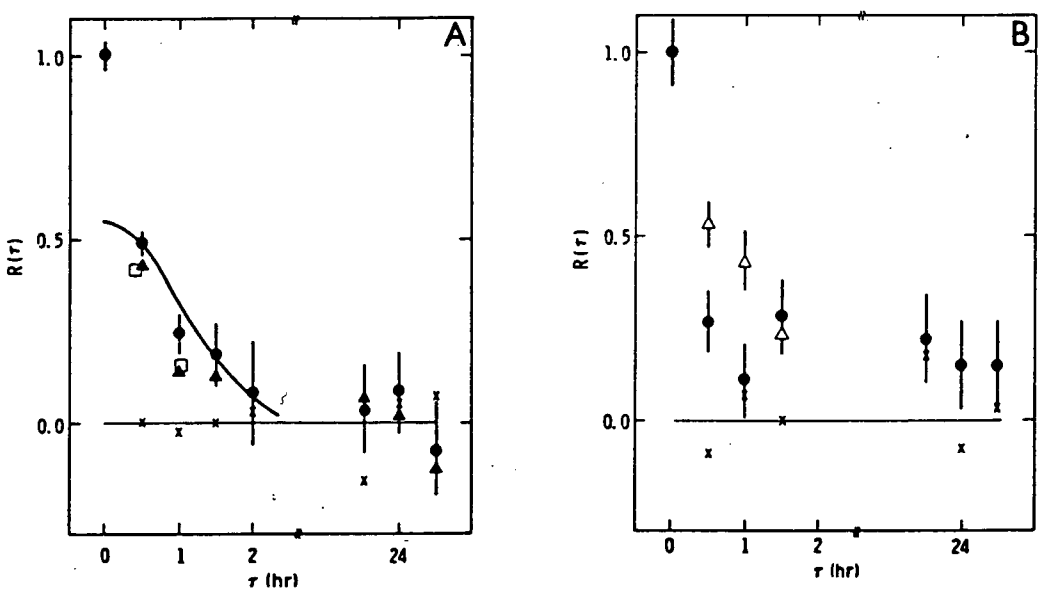

Fig. 3.4. Autocorrelation function of the timing residuals of PSR0833-45. Bin width: 30 minutes. (a) *Filled circles:* mean autocorrelation for all JPL data except TJD 4557-4582. *Filled triangles:* data for TJD 183-2671. *Open squares:* data from TJD 2685-4491. *Crosses:* random sequence in place of the observed residuals. *Solid line:* Non-rigorously fitted Gaussian function. (b) *Filled circles:* data from TJD 4557-4852, *Open triangles:* data from TJD 4029-5380. *Crosses:* random sequence in place of the observed residuals. (After Downs and Krause-Polstorff, 1986).

inconsistent with that expected for white torque noise acting on a two-component neutron star with interior parameters derived from the observed post-glitch relaxation behaviour.

ANP2 have predicted the form of the timing noise spectrum for a pulsar with rotational dynamics described by vortex-creep theory of Alpar *et al.* (1984a,b) for each of three processes producing torque noise; (1) pure episodic vortex unpinning, (2) a process which is accompanied by unpinning of some vortices, for example, the breaking of the crustal lattice by the Magnus force (Ruderman, 1976; Cordes and Greenstein, 1981; Cheng, 1987b), and (3) a process which is not associated with any vortex unpinning.

ANP2 characterized the spindown rate of the crust by

$$\Delta\dot{\Omega}_c(t) = Q^{-1}\,\Delta\Omega_c\,\delta(t) + \Delta\dot{\Omega}_{ci}(t) \qquad 3.1$$

where the frequency jump $\Delta\Omega$ results in a change $\Delta\dot{\Omega}_{ci}(t)$ of the internal torques; the delta function $\delta(t)$ defines the epoch of the jump. In a similar vein to its usage in the two-component model, the parameter Q is defined as the fraction of the initial jump in Ω_c that relaxes;

$$Q \equiv \frac{\int_{0^+}^{\infty} \Delta\dot{\Omega}_{ci}(t)\,dt}{\Delta\Omega_c} \qquad 3.2$$

where the lower integration limit identifies the time immediately after the jump epoch. It is presumed that the core superfluid and the crust are rapidly coupled (on the timescale of minutes) so that the only component which may contribute an evolving internal torque in response to a jump in Ω is the pinned crustal superfluid. The vortex lines in this component are presumed to move radially, overcoming pinning energy barriers via thermally activated creep. Equation 2.13 describes the evolution of the internal torque on the crust contributed by an individual pinning layer following a jump. Although ANP2 provide a general mathematical analysis, they restrict the comparison of theory and observation for the situation $t_0 << \tau$, where t_0 is the delay time (equation 2.17) and τ is the dominant creep-related relaxation time associated with the glitch region. This situation is anticipated where the jumps in Ω are very much smaller than those of identifiable glitches. It is expected that the creep relaxation timescale is similar to that of the weak or superweak pinning regions (100-200 days for the Vela pulsar).

The jumps in Ω are regarded as a stochastic process. On this basis, ANP predict the noise spectrum in Ω to be

$$P_\Omega(\omega) = R\,\Delta\Omega_c^2\,\frac{(1 - Q)^2 + \omega^2\tau^2}{(1 + \omega^2\tau^2)} \qquad t_0 << \tau \qquad 3.3$$

where ω is the cyclic temporal frequency, R is the rate of jumps per unit time, and $\Delta\Omega_c$ is the jump in the crustal rotation frequency.

For the pure unpinning process, each jump is presumed to be a scaled down version of a glitch in terms of physical origin and timing signature. In this case, Q = 1, and so the spectrum of equation 3.4 has a turnover point at $\omega = 1/\tau$ as shown in figure 3.5a.

For mixed events, the domains of interest are $Q >> 1$ and $Q << 1$. The spectra for these cases are given in figures 3.5b and 3.5c respectively. When Q = 2, the power spectrum shows purely white noise.

In the case of a process that does not produce vortex unpinning, but whose response is governed by the internal torque contributed by vortex creep, $Q = I_p/I_c$ where I_p and I_c are the moments of inertia of the superfluid and normal stellar components, respectively. From the observation of the large glitches of the Vela pulsar, $Q \approx 10^{-2}$ and so the spectrum has the same form as the case $Q << 1$ for mixed events (figure 3.5c). This situation differs from that investigated in the light of the two-component model by Boynton (1981) for which the core superfluid, with its large moment of inertia giving $Q \approx 0.9$, was regarded as the lagging component

ANP2 examined the experimental timing noise spectra obtained from the work of Boynton and Deeter (1986, *preprint*) with the aim of identifying structure in ω which would indicate the type of process responsible for the noise. Importantly, they were able to place limits on the range of possible τ and Q values under the assumption $t_0 << \tau$. For the Vela pulsar, all Q values and τ in the range 1 - 10^4 days were rejected with more than 98% confidence. This result indicates that pure unpinning events are not responsible for Vela's timing noise, nor is there a continuous range of magnitudes of unpinning events which extends from glitches down to the unresolved events that lead to the noise. For the Crab pulsar, values of $\tau < 1$ day and $Q \approx 2$ or 0 are not significantly rejected, which is consistent with the view that noise events are initiated external to the pinning region. The results were inconclusive for other pulsars, some of which exhibited complicated timing noise power spectra. However, it appears that the noise of most pulsars is not consistent with the predictions of the pure and mixed unpinning models, at least for the range of t_0 and τ values that could be examined with the available data.

3.4.2 External Torque Fluctuations

The response of neutron stars in binary systems to fluctuations in accretion

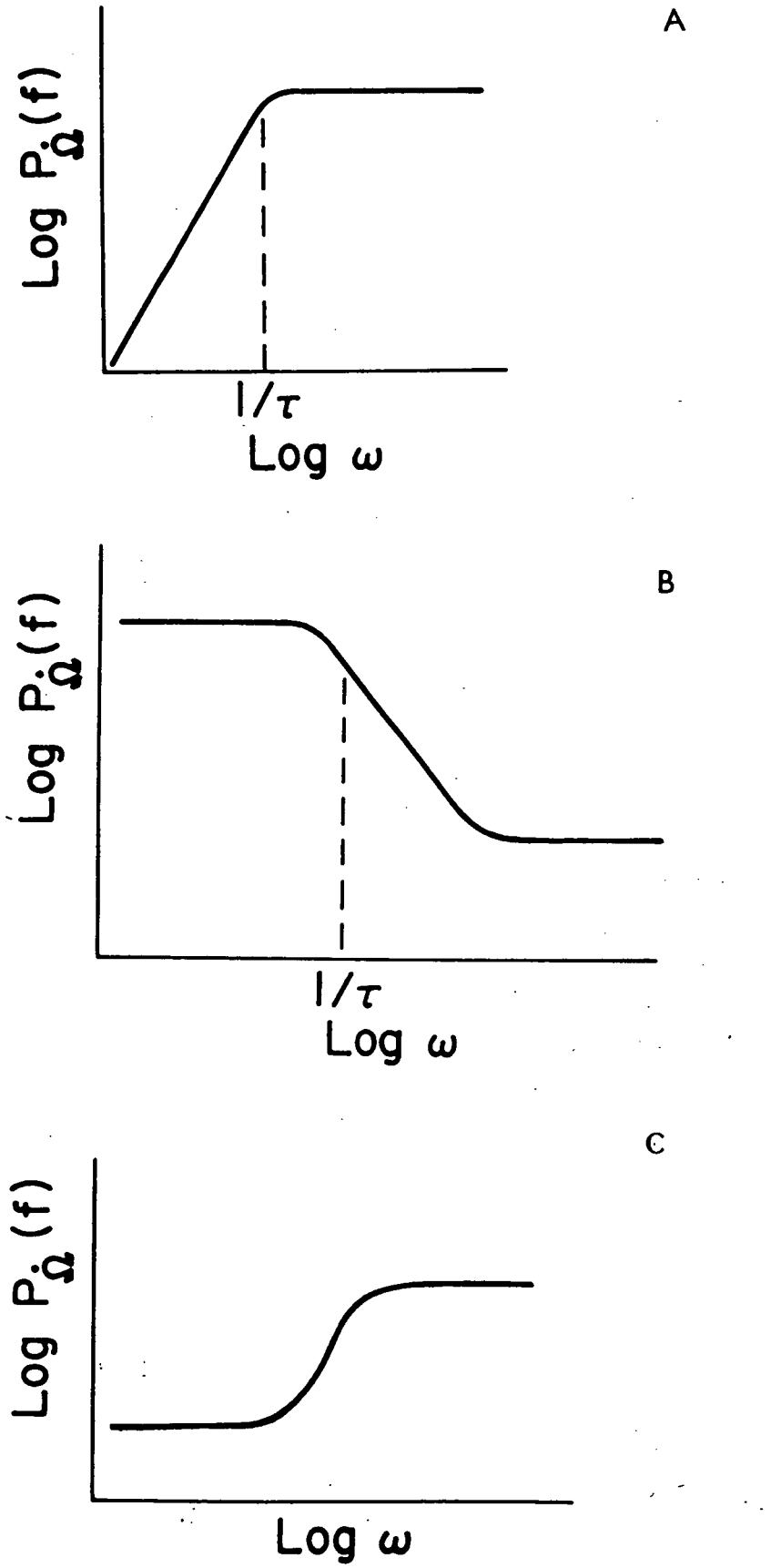

Fig. 3.5. Theoretical timing noise spectra under the hypothesis that vortex creep provides the dominant internal torque. Plotted is the logarithm of power density in $\dot{\nu}$ as a function of cyclic frequency for $t_0 << \tau$. (a) pure vortex unpinning noise. (b) mixed events when $(1 - Q)^2 > 1$. (c) mixed events when $(1 - Q)^2 < 1$. (After Alpar, Nandkumar, and Pines, 1986).

torque has been studied in connection with timing noise by Baym, Lamb, and Lamb (1976), Lamb, Pines, and Shaham (1978a,b), Boynton and Deeter (1979), and Boynton *et al.* (1988). However, accretion torques are not considered of importance in the case of solitary pulsars because the entrainment of plasma from the interstellar medium is likely to be insignificant due to the action of the inferred pulsar wind (Cordes and Greenstein, 1981).

Cordes and Greenstein (1981) have investigated eight different mechanisms for timing noise. In particular, they considered torque fluctuations arising from perturbations in plasma flow and current braking assuming a polar cap emission model. Although these workers did not discuss the origin of such fluctuations, they concluded that the rate of occurrence of step-like torque variations of magnetospheric origin were not precluded by the observed strength parameters of pulsar frequency noise under the random walk model.

Cheng (1987a) has investigated timing noise in the context of the outer gap model of pulsar emission (Cheng, Ho, and Ruderman, 1986a,b). In the application of this model to the Crab pulsar, it is proposed that primary e^+/e^- pairs created in the gap lose the majority of their energy via curvature radiation to γ-rays, which in turn produce secondary pairs through collision with X-ray photons. The X-rays represent the synchrotron radiation from pairs moving beyond the gap boundary. The radiation beams of the X-ray photons are narrow and do not uniformly illuminate the outer gap. Because the secondary X-rays are largely responsible for the radiation cascade process, variations in their flux can significantly change the brightness of optical and higher energy emissions (which are observed to vary in the case of the Crab pulsar), and the current braking torque N_{JxB} acting on the crust of the neutron star.

Cheng (1987a) considered a simple model in which a neutron star is idealized as a rigid body (that is, the relaxation effects due to coupling processes were neglected) and provided estimates for the random walk strength parameters. For example,

$$S_{2(ext)} \approx \frac{R\Omega^2}{16\pi^2} \left\{ \frac{N_{JxB}}{N_T} \right\}^2 \left\{ \frac{\delta N_{JxB}}{N_{JxB}} \right\}^2 \frac{1}{\tau_{age}^2} \qquad Hz^2\ s^{-3} \qquad 3.4$$

(Cheng, 1987b) where R is the rate of noise events, δN_{JxB} and N_{JxB} are the torque perturbation and its steady value, respectively. In addition $N_T = I_T \Omega$ is the total torque acting on the star, where I_T is the total moment of inertia. The noise power spectrum in the frequency derivative has an inverse square dependence in cyclic frequency;

$$P_{\dot{\Omega}}(\omega) = S_{2(ext)}\, \omega^{-2}\, (4\pi^2)^{-1} \qquad 3.5.$$

Cheng (1987a) estimated the frequency strength parameter $S_{1(ext)}$ for the Crab pulsar (as this object shows white noise in Ω) by selecting $(\delta N_{JxB}/N_T)^2 \approx 0.1$ and assuming that the ratio of the I_T/I_C is similar to that for the Vela pulsar (which is assumed to be characterized by a comparatively stiff equation of state). The value obtained is approximately an order of magnitude less than that determined observationally. Cheng has argued that $(\delta N_{JxB}/N_T)^2$ may be of order unity for older pulsars with sufficiently small $\Omega^2 B$ (for which the outer gap model is inappropriate). By estimating internal temperatures based on the vortex creep theory, and the perturbation and spin-up timescales, $S_{2(ext)}$ has been evaluated for the pulsars in the survey of CD which exhibit timing noise consistent with a random walk in ν, based on the torque perturbation model for both soft and stiff equations of state. Cheng has suggested that cases for which the modelled and observed strength parameters are comparable may support the existence of a superfluid (as distinct to a Fermi liquid) core within the associated neutron stars.

In the case of the Vela pulsar, Cheng (1987b) has proposed that the outer gap is inherently stable. However he has suggested that a micro-glitch in rotation frequency leads to a perturbation of the magnetospheric current flow which alters the current braking torque. The variation of the torque persists until the next jump. In this model, the timing noise spectrum has contributions due to both external and internal physics. Cheng has evaluated the noise spectrum assuming that the external torque fluctuations have a stochastic occurrence rate equal to that of torque variations generated internally by the pure and mixed unpinning processes considered by ANP2.

Cheng considered the case where $Q \approx 1$ as being of most physical relevance. The overall noise spectrum was evaluated as

$$P_{\dot{\Omega}}(\omega)_{tot} = P_{\dot{\Omega}}(\omega)_{int} + P_{\dot{\Omega}}(\omega)_{ext}$$

where the terms on the RHS are internal (equation 3.3) and external contributions, respectively. By combining equations 3.3 and 3.5,

$$\begin{aligned} P_{\dot{\Omega}}(\omega)_{tot} &\approx S_{2(ext)}\, \omega^{-2}\, (4\pi^2)^{-1} && \text{for } \omega \text{ small} \\ &\approx 4\pi^2\, S_{1(int)} && \text{for } \omega \text{ large and } \omega\tau >> 1 \\ &\approx S_{0(int)}\, \omega && \text{for } \omega \text{ large and } \omega\tau << 1 \end{aligned} \qquad 3.6$$

where $S_{1(int)} = R\, \Delta\Omega_c^2$ and $S_{0(int)} = 4\pi^2 R\, \Delta\Omega_c^2\, \tau^2$ are the frequency and phase noise strength parameters due to pure and mixed unpinning, respectively. Thus the noise spectrum is predicted to be blue at high frequencies, and (depending on the type of internal noise process) red or white at low frequencies.

Cheng (1987b) compared data from Boynton and Deeter (1986, *preprint*) and Cordes and Helfand (1980) with the predictions of his model, and found the observed timing noise spectra of several pulsars to have qualitative similarities. Importantly, the

predicted random walk noise strengths were more consistent with vortex creep as providing the dominant heating mechanism in older pulsars.

3.4.3 Precession

Trümper *et al.* (1986) have identified a 35 day modulation in the arrival times of pulses from the X-ray pulsar Her X-1 that is phase-coherent with the well-known light curve of the system. The authors have proposed that precession of the underlying neutron star, excited by external torques, is responsible. A similar explanation has been offered by Jones (1988) to account for the quasi-periodic (~ 620 day) oscillations in the timing residuals of the Crab pulsar.

Shaham (1977) has shown that if the superfluid vortex lines are rigidly pinned to the crust, then the precession frequency ω_p is of the order $\omega_p \approx \Omega I_p/I$ where I_p/I is the fraction of the moment of inertia of the pinned component. For a typical neutron star, $\omega_p \approx 10^{-2}\,\Omega$. Shaham (1986) has noted that in the case of Her X-1, because of the observed amplitude of the precession, the lag between the crustal and superfluid rotation rates exceeds the critical value below which absolute pinning occurs.

Alpar and Ögelman (1987; hereafter AÖ) have closely examined the conditions imposed on neutron star precession due to internal torques imposed by vortex motion with particular application to Her X-1. Importantly, they have provided theoretical evidence to suggest that a steady state situation can arise in which the superfluid component precesses with the crust. The pinned superfluid in the inner crust takes part in precession through vortex creep which is linear in the lag between the rotation rates of the pinned superfluid and the crust. Additionally, the required magnitude of the external excitation torque is consistent with the torques available in the accreting binary system, although AÖ do not discuss how the precession is forced. AÖ have also suggested how steady-state precession can arise for a particular initial condition and propose that Her X-1 is in this situation

For single radio pulsars, precession is likely to be damped by internal torques on timescales less than 1000 years, because the external torques are not considered sufficient or appropriate for the development of a steady-state situation (AÖ). However, only limited theoretical discussion of possible internal or external excitation mechanisms have been published to date. Additionally, the timing residuals of the Crab pulsar have yet to be adequately examined in the light of the current understanding of precession and neutron star structure.

3.5 CONCLUSIONS

The study of pulsar timing noise provides an important means of investigating the internal structure and external environment of neutron stars.

A number of techniques have been developed to quantify timing noise. In several cases it has been shown that the observed noise is consistent with an idealized random walk in ϕ, ν, or $\dot{\nu}$ which suggests that a stochastic process influences the rotation rate of the underlying neutron star. Several objects exhibit apparent discontinuities in rotation rate that are not consistent with fluctuations of a random walk process. The adequate characterization of these events has been considerably hampered by a lack of well sampled timing observations.

The origin of timing noise is still a subject of debate. It is evident that certain mechanisms may be specific to only a limited number of objects. It is possible that the events leading to timing noise are related to the large glitches observed in only a small proportion of the pulsar population. In this connection, crust-quakes, vortex unpinning, and temperature fluctuations have been investigated and are considered viable.

By assuming a large-rate random origin for rotation fluctuations, it has been demonstrated that the timing noise spectra of the Vela and Crab pulsars does not exhibit structure on timescales characteristic of the internal torque relaxation processes for the two-component and vortex creep models of internal dynamics. On this basis, there is evidently a threshold for the occurrence of glitches. The level of timing noise exhibited by a broader group of pulsars is generally consistent with vortex creep providing the dominant heat source.

Braking torque fluctuations due to instability in outer magnetospheric-gaps has been suggested as a contributor of noise in rotation of energetic pulsars. In addition, the possibility that internally generated discrete jumps in rotation rate leads to changes in the magnetospheric current braking torque has also been proposed. For both of these models, a blue noise component in the spectrum of $\dot{\nu}$ is predicted.

Evidence of neutron star precession has been used to modify the vortex creep theory of internal dynamics. Little work has been conducted to examine the possibility of small-amplitude precession as a contributor to timing noise. It is likely that such a process will have a narrow-band signature in timing noise spectra. However, the established method of spectral estimation is of inherently low resolution, which may be inadequate to reveal such a feature.

CHAPTER 4 - LLANHERNE TIMING OBSERVATIONS

4.1 INTRODUCTION

In this chapter, the observing and data reduction procedures that were adopted for the pulsar timing programme at the Llanherne Radiophysics Observatory (LRO) during the interval October, 1981, to September, 1986, are described.

The author was responsible for all aspects of the Llanherne pulsar observations described herein subsequent to November, 1984. Prior to this time, the measurements were largely under the direction of Mr. G. Royle. In addition to the Vela timing programme, regular observations were also conducted of PSR1749-28 and PSR1641-45.

The Llanherne timing programme initially built on experience gained by Dr. P.M. McCulloch and Dr. P.A. Hamilton through collaborative work with Dr. R.N. Manchester and Dr. J.H. Taylor. These latter workers provided the initial ideas for the basic arrival time modelling algorithm. Dr. Hamilton and Dr. McCulloch made significant contributions to the initial software and hardware developments, respectively. Mr. G. Royle was involved with the development of the receiver and the analysis of the initial observations. The contribution of the author was the design and construction of the dual frequency receiver and related observing software, the collection and processing of the daily data, and the analysis and interpretation presented in this thesis. During the course of this project, the data collected by Mr. Royle have been reworked.

Some additional data for the Vela pulsar that have been used in the analysis presented in chapters 7 and 8 have kindly been provided by Ms. C. Flanagan from observations at the Hartebeesthoek Radio Astronomy Observatory (HRAO), South Africa, and by Dr. R.N. Manchester from observations at Tidbinbilla, Australia; due indication is made where these data have been employed.

4.2 THE RECEIVING EQUIPMENT

The parameters for the Llanherne and Hartebeesthoek observation systems are summarized in table 4.1. At Llanherne, observations were made with an equatorially mounted 14m parabaloid. Due to restrictions imposed by the mounting, the maximum daily tracking time available for PSR0833-45 was 5.4 hours; PSR1749-28 and

TABLE 4.1

RECEIVER AND SAMPLING PARAMETERS FOR PSR0833-45

Site Name	Llanherne	Hartebeesthoek
Geocentric Coordinates		
longitude λ	147°.510711	-27°.685441
latitude β	-42°.653972	-25°.739300
radius R (km)	6386.406	6375.525
Telescope		
aperture (m)	14	26
mounting	equatorial	equatorial
Receiver		
feed type	disc	horn
polarization	linear	linear/circular[a]
centre frequencies (MHz)	635.0/954.0	2320.0/2325.6[b]
system temperature (K)	100/45	40
3dB predet. bandwidth (MHz)	0.25/0.80	10.0
radiometer bandwidth (MHz)	0.32/1.0	12.6
dispersion smearing (period)	0.006/0.006	0.006
rotation smearing (degrees)	0.4/0.4	0.3
post-det. time constant (μs)	470/470	150
Sampling System		
sampling rate (period^{-1})	256	512
integration duration (period)	1008	500
integrations per session	200	4
Timing Parameters		
typical pulse SN ratio	20	20
measurement uncertainty (μs)	80	40
frequency standard	Rubidium	Rubidium

a Circular polarization used after TJD 6286

b 2320.8 MHz used prior to TJD 6208; 2325.6 MHz used after this date.

PSR1641-45 were observed for similar durations. The remainder of this chapter, aside from section 4.13, deals with the Llanherne observations of the Vela pulsar.

A schematic diagram of the Llanherne system is presented in figure 4.1. A disc feed (Howell, 1975) was used at the prime focus of the telescope. It provided two orthogonal linearly polarized channels centred at 635 MHz. Calibration signals of equal amplitude and phase were injected into each channel from a probe on the feed. From March, 1986, a novel dual frequency stacked disc feed was used, which provided orthogonal linearly polarized channels centred at 635 MHz and 954 MHz. Calibration signals for this feed were radiated from a circularly polarized antenna at the vertex of the dish.

Each receiver channel was of the same basic configuration. Broadband GaAs FET preamplifiers were operated at ambient temperature. Five-pole Butterworth interdigital filters provided a 25 MHz bandpass at radio-frequency (RF) which was then mixed to an intermediate-frequency (IF) band centred at 30 MHz. The local oscillator signals used in the mixing process were phase-locked to the observatory Rubidium frequency standard. Further band-limiting was provided by 3-pole Butterworth helical resonator bandpass filters which were followed by square-law detectors. The pairs of channels were phase and amplitude matched throughout.

4.3 THE SAMPLING SYSTEM

Each detector output was sampled using voltage-to-frequency converters (VFCs) at intervals of P_a/N_s, where P_a is the apparent pulsar period, and N_s is an integer. In this way N_s phase bins were provided per period. The limitation of the speed of the observatory computer necessitated that $N_s = 256$. This provided approximately 10-15 on-pulse bins for PSR0833-45.

Each VFC output a waveform with an instantaneous frequency directly proportional to the instantaneous input voltage. A 16-bit counter accumulated the number of waveform cycles. At the end of a sample interval, each counter was read by the computer and then reset. The maximum delay between reading adjacent channels was 2 μs. The data were then used to modify the running mean for the relevant phase bin and channel using a stable averaging algorithm. This integration process continued for a preset number of pulse periods.

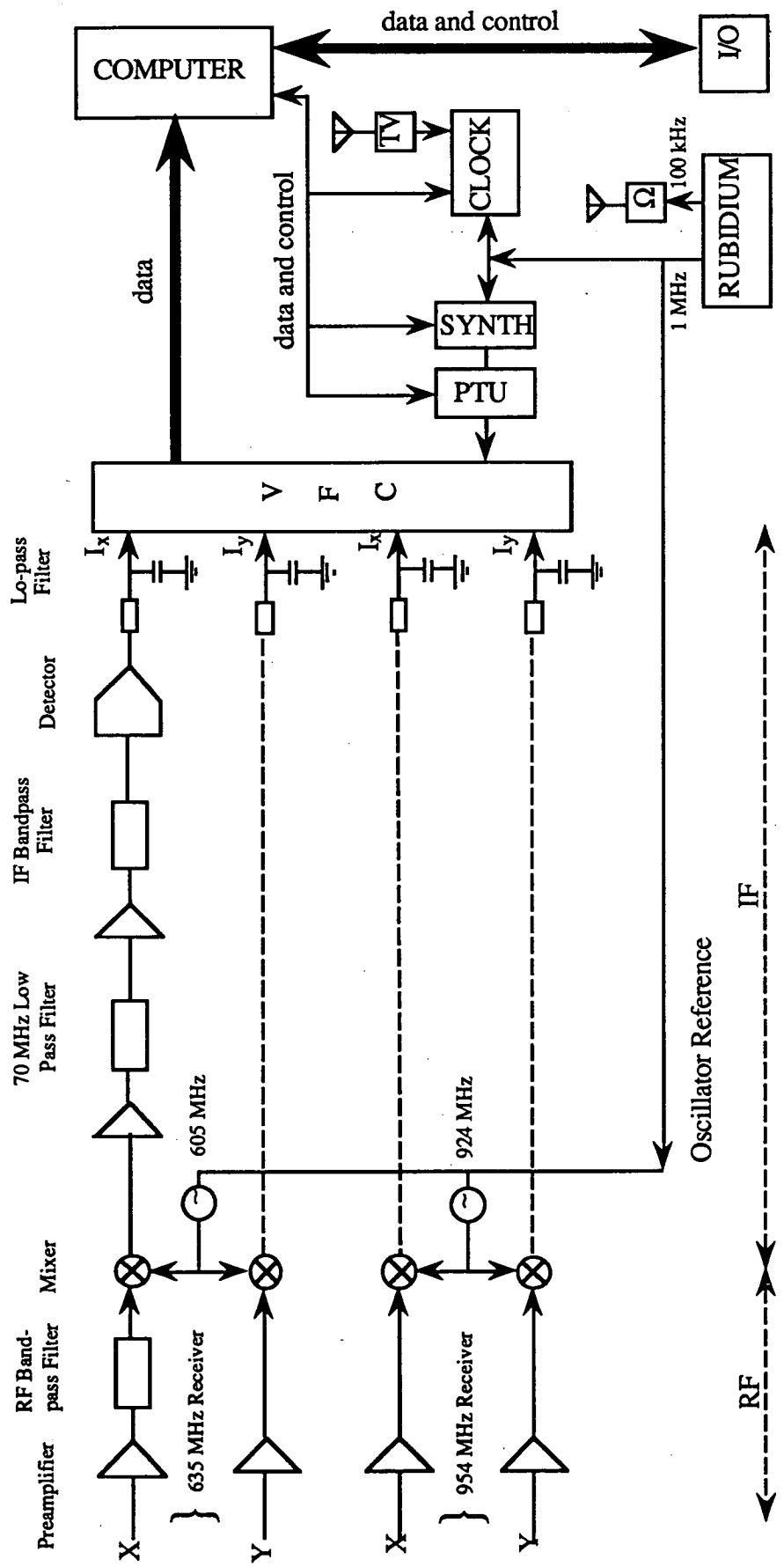

Fig. 4.1. Schematic diagram of the Llanherne observing system.

A barycentric timing model, derived from a recent arrival-time analysis and adjusted for the motion of the observatory, was used to calculate P_a for the epoch of the mid-sample of each integration.

The sampling frequency was governed by the Pulsar Timing Unit (PTU) which suitably divided the frequency of $2^{16}/P_a$ produced by a programmable synthesiser. The synthesiser was phase-locked to the Rubidium standard and could be set with the significance of mHz. The PTU also produced a *frame* pulse with frequency of $1/P_a$.

The time as read from the Observatory clock (with the significance of microseconds) was buffered in hardware simultaneous with the first sample pulse. Upon completion of the integration, the buffered time was transferred to a computer disk file together with the integrated profiles of each channel (designated I_x and I_y for each frequency) and the value of P_a used. A new value of P_a was then calculated, and the appropriate settings for the PTU and synthesiser were automatically made. After the completion of these and some additional house-keeping tasks, the next integration proceeded on receipt of the following frame pulse.

4.4 CALIBRATION

During the operation of the single-frequency receiver, the relative gains of the channels were determined by the synchronous integration of the calibration noise source which was pulsed with a 2 second period and 50% duty cycle. This procedure was conducted on-source prior to the first integration of each session, and the information was retained for use in the off-line processing.

During the dual-frequency observations, the calibration signal was pulsed out of phase with the pulsar signal with period P_a and 25% duty cycle. This occurred during two consecutive integrations per hour.

The noise source was not calibrated against continuum sources of known flux with sufficient regularity to enable the accurate determination of pulse flux values.

Receiver frequency calibrations were made at approximately six-month intervals by radiating a signal from an accurate frequency synthesiser in place of the noise source. The centre frequency of each channel was measured as the radiated frequency required to produce a signal centred between the -3dB points of the IF filter

output. No changes greater than the 10 kHz measurement resolution was noted between October 1984 and August, 1986.

4.5 RECEIVER AND SAMPLING PARAMETERS

The selection of Δf_p, the predetection equivalent (or radiometer) bandwidth, τ, the time constant of the post-detection RC filter, and N, the number of periods integrated, were aimed at minimizing both the temporal smearing of the pulsar's waveform and the smallest detectable change in signal noise temperature.

In order to satisfy the Nyquist sampling theorem, the condition $\tau > P_a/1028$ was required; for observations of PSR 0833-45, $\tau = 470$ μs was chosen.

The temporal smearing of each pulse due to dispersion across the bandpass of each receiver may be expressed as

$$\Delta t_D = 2\ D\ \Delta f_p\ f^{-1}$$

where D is the dispersion coefficient, and f is the receiver centre frequency. For 3-pole Butterworth filters, $\Delta f_p = 1.26\ \Delta f_{3dB}$ where Δf_{3dB} is the -3 dB bandwidth (Kraus, 1986, p. 7.8). Using $D \approx 2.84 \times 10^5$ sMHz^2 for the Vela pulsar, the values of Δf_{3dB} (table 4.1) were chosen to give $\Delta t_D \approx \tau \approx 0.006 P_a \approx 0.5$ ms.

In order to provide integrated profiles with signal-to-noise (SN) ratio (pulse amplitude divided by off-pulse standard deviation) of ~ 15 for PSR0833-45 , N = 1008 was chosen. In practice, the SN ratio for the profiles of the 954 MHz channels were higher than those for the 635 MHz channels due to a sensitivity advantage resulting from the frequency scaling of the pulsar and background fluxes and the the antenna beam solid angle.

The e-folding geometric time delay τ_g (interpolated from the observations of Komesaroff, Hamilton, and Ables, 1972) due to interstellar scintillations was ~ 5 ms ($>> \tau$) at 635 MHz and ~ 0.1 ms ($< \tau$) at 954 MHz. Thus, the pulses received at 954 MHZ were more strongly modified by the temporal response of the receiver than the pulses at 635 MHz.

From interpolation of the observations of Backer (1974), the decorrelation bandwidth Δf_c was estimated as 0.3 kHz at 635 MHz and 1.5 kHz at 954 MHz. In addition, the decorrelation time Δt_c at these frequencies is < 10 s. As the bandwidth of the receiver and the time-scale of each integration exceeded Δf_c and Δt_c respectively, by some two orders of magnitude, the effect of intensity scintillation on the pulse SN

ratio is regarded as minimal. Indeed, in figure 4.2, which shows data from a typical observing session, the amplitude of the profiles at each frequency appear stable with time.

In order to illustrate the similarity of the pulse profile shape at the two observation frequencies, the individual I integrations of a particular session were shifted to a common phase lag and averaged. The results are presented in figure 4.3. In figure 4.4, the corresponding averaged I_x and I_y profiles are illustrated, together with the limits of one standard deviation either side of the mean at each phase bin within the pooled integrations. Note the absence of power in the orthogonal channels of each frequency. This was the result of a fortuitous choice of observation frequencies and feed orientation, combined with the prevailing value of the rotation measure. Using RM = 38 radians m^{-2} as an estimate of the rotation measure at the epoch of the data presented in figure 4.3 (Costa, 1989, *private communication*), the differential Faraday rotation between the two frequencies ($\Delta\Psi = RM\ c^2\ [f_1^{-2} - f_2^{-2}]$) was approximately equal to the position angle difference of 1.5π radians between the two like-named probes on the feed (as measured in the sense of rotation of the plane of polarization).

4.6 PULSE PHASE ESTIMATION

The phase, ϕ, of each total intensity (I) pulse was estimated as the lag (measured as a fraction of P_a from the phase origin of the integration) at which the cross-correlation between the pulse and a template profile was a global maximum. The maximization procedure involved the interpolation of the 2nd degree polynomial that was fitted to the set of five correlation values about the maximum via a least-squares method.

Template profiles for each frequency were constructed from appropriate total intensity profiles obtained by McCulloch *et al.* (1978) with the Parkes 64m telescope; these represented the integration of approximately 2×10^4 periods of the Vela pulsar with a sampling interval of 0.1 ms and a receiver smearing time-constant of ~ 0.4 ms. Each Parkes profile was adjusted to match the lower Llanherne sampling rate through interpolation.

For each phase estimate, a root-mean-square (rms) uncertainty $\hat{\sigma}_M$ was calculated using the formula given by Downs and Reichley (1983) ;

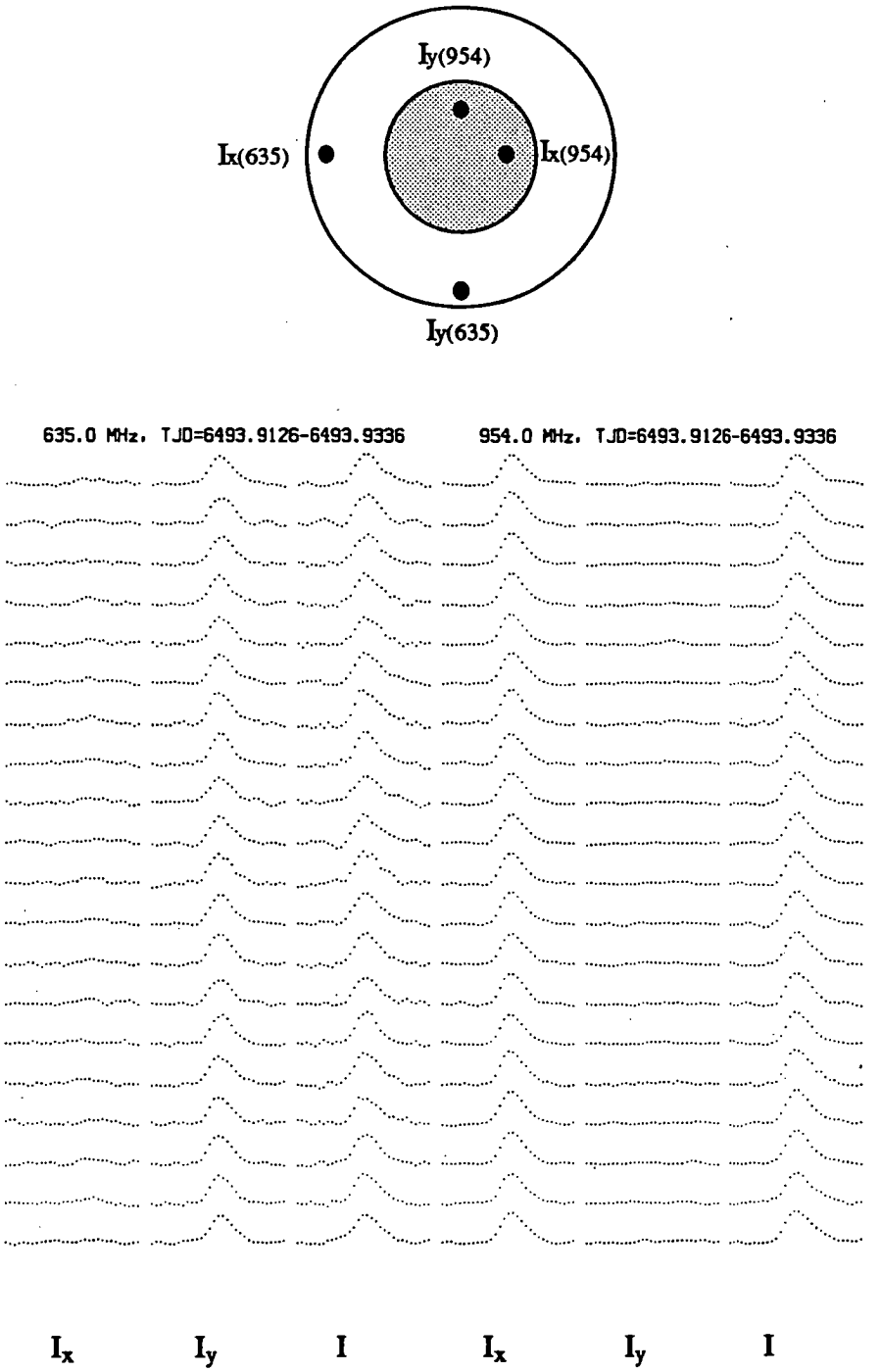

Fig. 4.2. Stacked integrations of PSR0833-45 simultaneously recorded at 635 MHz (left three plots) and 954 MHz. For each frequency, the I_x, I_y, and I profiles are presented. For each frequency, the I_x and I_y profiles were scaled according to the calibration data, and then summed to provide a total intensity I profile. The I profiles have been used to determine local pulse arrival times as described in section 4.6. The mean off-pulse level has been subtracted from each channel. The profiles have resulted from the synchronous integration of 1008 periods, and have been windowed to show a total of 30 bins (10.5 ms) about the peak of each I pulse (thereby removing the relative phase offset between the profiles of the two frequencies due to dispersion delay). The vertical scale is arbitrary but has been adjusted so that the off-pulse standard deviation of the I profiles of both frequencies (averaged over the observing session) are equal. Increasing time runs from to to bottom. The orientation of the probes on the feed for a clockwise rotating polarization vector is shown.

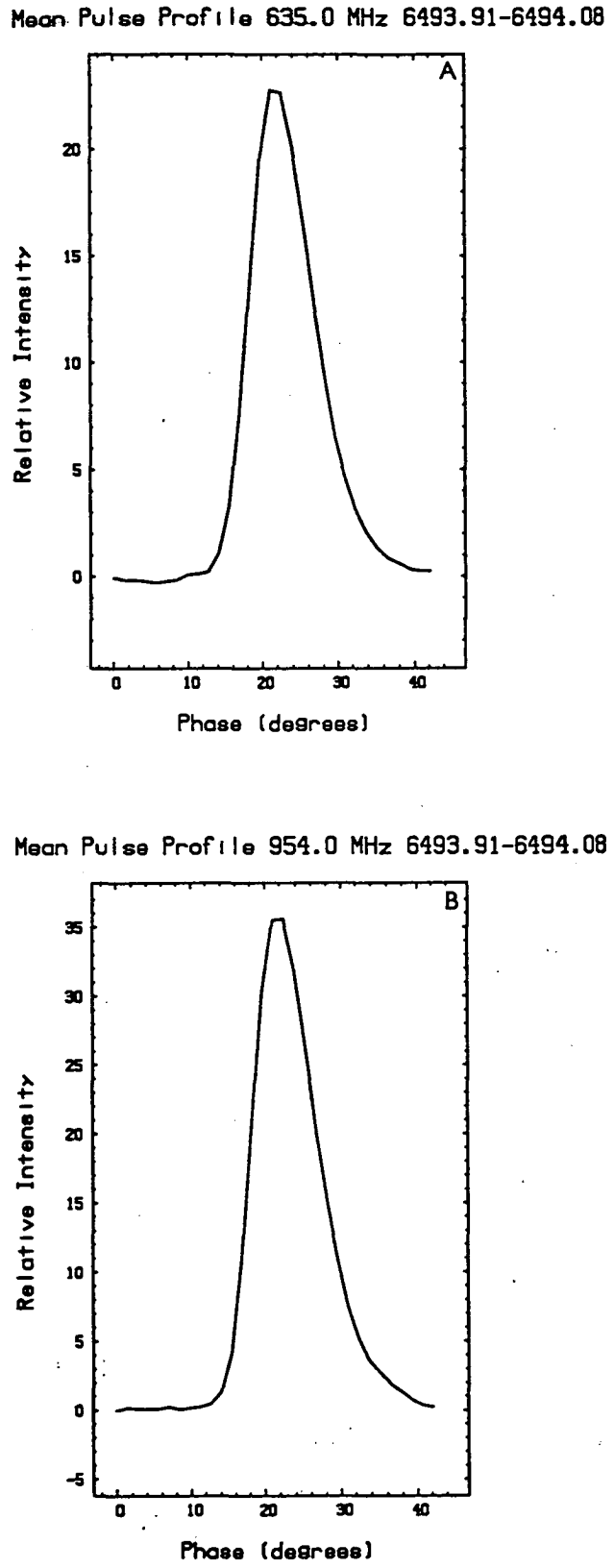

Fig. 4.3. Mean pulse profiles for (a) 635 MHz, and (b) 954 MHz obtained by averaging the integrations for a particular day. The vertical scale is arbitrary, but has been adjusted so that the standard deviation of the off-pulse noise for both profiles is equal to one unit. The bin width is 1.4° of phase.

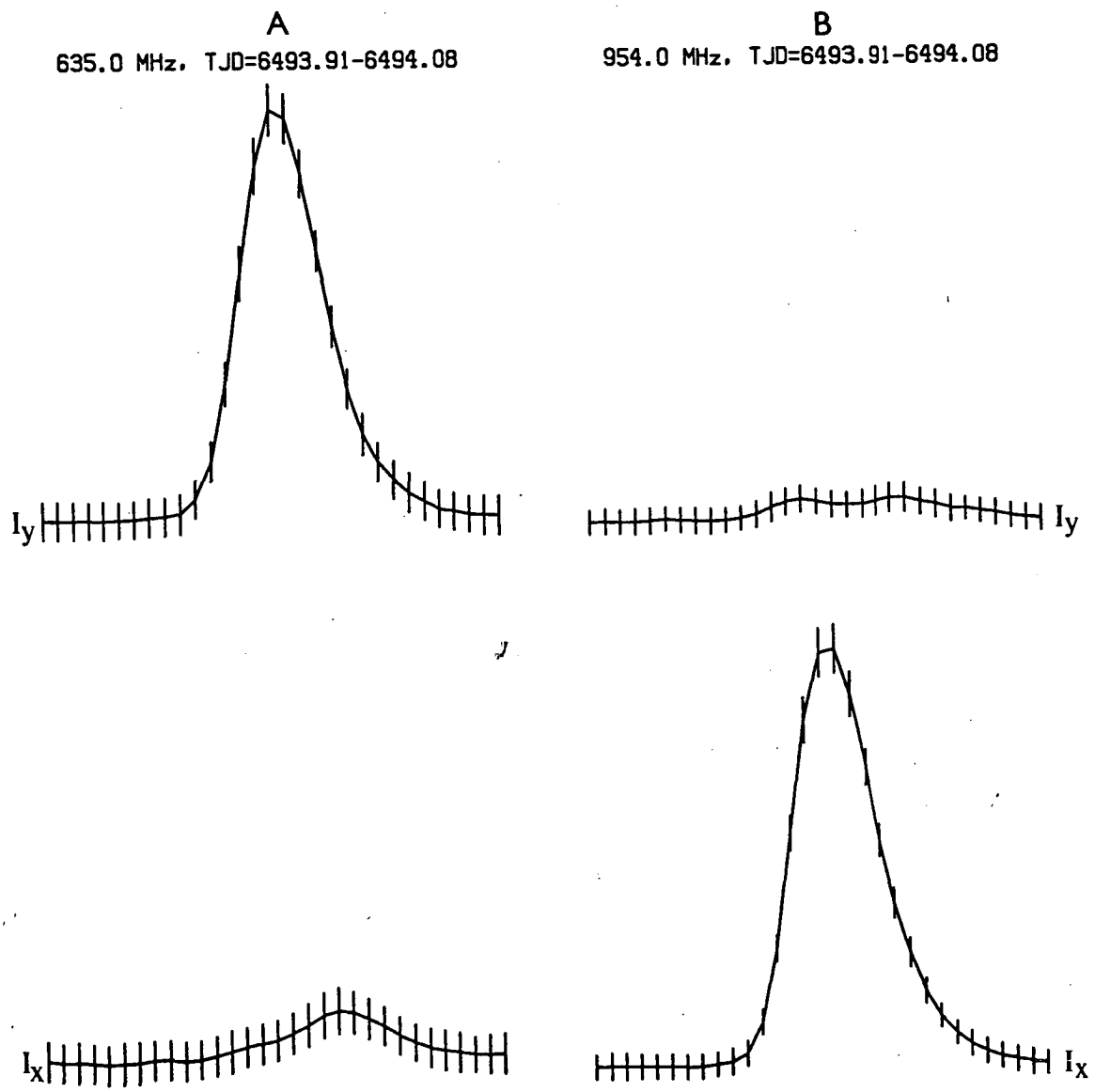

Fig. 4.4. Mean I_x and I_y profiles for (a) 635 MHz, and (b) 954 MHz for a particular day. Each vertical bar represents two standard deviations of the pooled values at the corresponding phase bin. Note the similarity of the on-pulse and off-pulse bars indicating the stability of the pulse intensity during the session. The phase range of each plot is 42°.

$$\hat{\delta}_M = \frac{(P_a \tau_b)^{1/2}}{R_s \left\{ \int_0^1 (dU/d\phi)^2 d\phi \right\}^{1/2}} \qquad 4.1$$

where τ_b is the sampling interval, R_s is the profile SN ratio, and U is the normalized (unit height) template. Equation 4.1 seeks to estimate the arrival time uncertainty in the presence of finite gaussian noise on the pulse profile (see also Hertz and Azaria, 1985). Typically, $\hat{\delta}_M \approx 40$ - 60 μs for individual Llanherne integrations.

In order to test the pulse phase estimation procedure, values of $\hat{\delta}_M$ were chosen in 5 μs steps from the interval [5 μs, 300 μs], and corresponding values of R_s were calculated using equation 4.1. Gaussian noise with variance $(I_0/R_s)^2$ (where $I_0 = 1$ is the height of the template) was then added to each template to produce simulated pulse profiles. A total of 200 simulated profiles were created for each $\hat{\delta}_M$ and template. The pulses and their corresponding template were then cross-correlated to generate sets of phase lags. In determining each lag, both 3-point and 5-point parabolic fits were used in the maximization procedure. The standard deviation σ_M of the lags for each $\hat{\delta}_M$ in the interval [5 μs, 200 μs] are displayed in figure 4.5.

The range of the independent ordinates in figure 4.5 corresponds to a change in R_s of ~ 127 to ~ 3. It is evident that the expected and observed rms phase errors are in close agreement over this range which atests to the accuracy of the phase estimation procedure. For values of $\hat{\delta}_M > 250$ μs ($R_s < 2.5$), the cross-correlation method was found to fail as evidenced by the divergence of the relationship between $\hat{\delta}_M$ and σ_M from the expected linear trend. Of additional note is the similarity in the results provided by the lag estimation procedure based on 3-point and 5-point fits.

4.7 DATA COMPRESSION

The raw phase measurements for which the SN ratio exceeded 2.5 were compressed into two additional data sets. Firstly, the phases in non-overlapping spans representing ~ 20 integrations were fitted with a first-degree polynomial using a least-squares procedure, with each point weighted by the inverse of the measurement variance, $\{\hat{\delta}_M\}^{-2}$. Fits were not made across obvious phase discontinuities which occurred whenever observations were temporarily suspended during a power failure. If the largest residual from the trend removal exceeded 3.3 standard deviations from the unweighted mean[a], the phase estimate was removed, and the model fit was

[a] The probability of a residual of this magnitude occurring is 0.001 assuming that the residual distribution is normal.

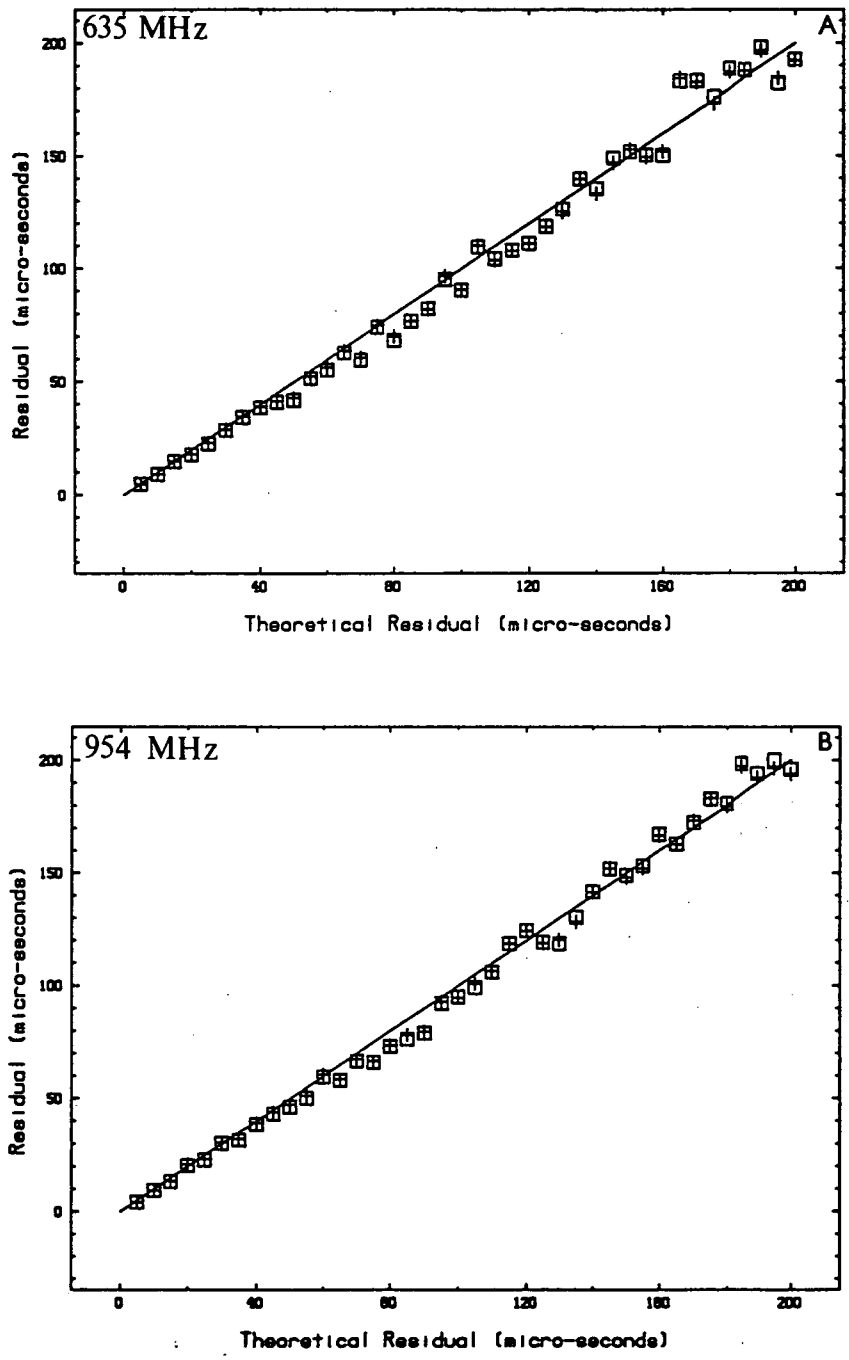

Fig. 4.5. Test of the cross-correlation procedure used to determine the local pulse arrival phase in the presence of Gaussian noise. Plotted is the rms phase error (obtained from a sample of 200 simulated pulses constructed using template profiles as described in the text) against the expected rms phase error (*crosses* - 3-point maximization method, *squares* - 5-point maximization method, *solid line* - expected trend). Plots (a) and (b), have been evaluated using the 635 MHz and 954 MHz Vela template profiles, respectively.

repeated. This procedure was terminated when no further rejections occurred or too few phase values remained for a meaningful fit. The polynomial phase was then evaluated for the epoch of the centre of the span. This method gave typically 8-10 points per day and a rejection rate of ~ 4%; the data produced formed the medium time resolution set. The uncertainty of each phase estimate was taken as the rms phase residual of the fit; this was typically 20 μs.

A similar procedure was used with all of the data of each session to provide one point per day; in this case a second degree polynomial was used. The compressed data were used in the initial evaluation of the raw data (as described in section 5.2) and in some aspects of the timing noise investigation (in order to reduce computing time). These data constituted the low time resolution observations.

4.8 TOPOCENTRIC ARRIVAL TIMES

The topocentric pulse arrival time for the i-th integration was defined as

$$T_i = \phi_i P_{a_i} + 0.5 P_{a_i} N + t_s + C(t_s) + U(t_s) \qquad 4.2$$

where t_s is the epoch of the start of the integration as read from the clock, C is a polynomial describing the offset of the clock time from *Coordinated Universal Time* (UTC), and $U(t_s)$ is a step function describing the lag between UTC and atomic time (due to leap seconds). In this way, each value of T_i represents the arrival time of the zero-reference phase at the observatory.

The difference $\Delta T_i = T_i - T_i'$, where T_i' is the true topocentric arrival time, was minimized to first order by referencing each phase centroid to the commencement epoch of the mid-period of each integration. The contribution of higher order corrections to equation 4.2, due primarily to the non-zero true barycentric first period derivative, were calculated as < 2 μs using the rigourous drift correction formula of Downs and Reichley (1983) and have been neglected.

The rate of phase drift between successive integrations of a session was typically < 3 milliperiods per hour. This reflected the drift rate of the Rubidium frequency standard and the precision at which the sampling frequency could be set. However, a drift rate of up to -33 milliperiods per hour occurred immediately after a glitch and before an improved timing ephemeris could be incorporated into the software of the observation system.

The stability of the profile shape is investigated in connection with short timescale phase residuals in Chapter 5.

4.9 THE OBSERVATORY CLOCK

The observatory clock was compared on a near-daily basis with the Telecom Australia national time standard via a television time transference method. The television signals originated from the Australian Broadcasting Corporation transmitter in Sydney. The times of arrival of identical synchronization pulses were measured at Llanherne and by Telecom in Melbourne. A travelling clock was used to determine the propagation delay to within 0.5 μs between the transmitter and the measurement sites. The Telecom version of UTC was compared with that maintained by the US Naval Observatory, UTC(USNO), on a regular basis through the use of the satellites of the Global Positioning System. The measurements enabled the quantity

$$\Delta T_t = UTC(USNO)_t - UTC(Llanherne)_t$$

to be determined for a set of discrete times t; ΔT_t was then modelled over intervals of weeks to months by a low degree polynomial approximation C(t).

A new expression was required for C(t) after a jump in the phase or rate of the local Rubidium standard. A check on the behaviour of the standard was made by comparing its phase with the received phase of the signals from the Omega Australia transmitter located 300 km north of the observatory using a phase tracking receiver. For each polynomial approximation used, the rms time residual

$$\sigma_c = < (C(t) - \Delta T_t)^2 >^{1/2}$$

was typically 5 μs.

4.10 BARYCENTRIC ARRIVAL TIMES

The standard expression (e.g. Downs and Reichley, 1983) for the barycentric arrival time of the i-th pulse is

$$T_{b_i} = T_i + t_r + \frac{\mathbf{n}\cdot\mathbf{r}_i}{c} + t_d \qquad 4.3$$

where $\mathbf{n}$ and $\mathbf{r}_i$ are vectors directed from the barycentre to the assumed position of the pulsar, and from the observatory to the barycentre, respectively (Appendix B); t_r and t_d are corrections for the difference between coordinate and terrestrial times (Appendix C), and the dispersion delay to a pseudo-infinite wave frequency, respectively. The magnitudes of the right-most three terms of equation 4.3 are summarized in table 4.2.

Equation 4.3 is a first order approximation to the more rigourous expression given by Backer and Hellings (1986) which includes terms for the parallax, radial, and proper motions of the pulsar, and spacetime curvature. These terms are negligible for Vela (table 1.1).

TABLE 4.2

CONTRIBUTIONS TO THE BARYCENTRIC CORRECTION FOR PSR0833-45

Source	Annual Amplitude
Geometric delay :	499 s
Time dilation :	1.66145 ms
Dispersion delay[a] :	
contribution from doppler shift	140 μs @ 635 MHz 60 μs @ 954 MHz
constant term	0.7049 s @ 635 MHz 0.3123 s @ 954 MHz

[a] for DM = 69.08 pc cm^{-3}

4.10.1 The Geometric Correction

The third term of equation 4.3, the geometric correction, represents the light-time difference between the positions of the observatory and the barycentre with respect to the pulsar.

The vector $\mathbf{r}_i$ is evaluated using a barycentric ephemeris (Appendix B). For the Llanherne and Hartebeesthoek data, the MIT PEP 311 ephemeris (Ash, Shapiro, and Smith, 1967) was used. This reference frame for this ephemeris is nominally that of the FK4 stellar reference system at the epoch B1950.0; the unit of time is the atomic second. Since the development of the MIT ephemeris, estimates of the planetary masses have been refined. The amplitude of likely errors in the calculated arrival times are summarized in table 4.3 following the method of Mulholland (1970) outlined in Appendix D. Fomalont *et al.* (1984) have compared the alignment of coordinate frame of the VLA (known to agree with the FK4 system to ≤ 0.05 arc-sec from the work of Perley, 1982) with those of the of the MIT ephemeris and more recent JPL DE96 ephemeris. (The DE96 ephemeris has been used by Cordes, Downs, and Krause-Polstorff (1988) in the analysis of Vela timing data from 1968 to 1983). Due to systematic alignment differences (most likely due to errors in the assumed values of the planetary masses), the timing data reduced using both ephemerides are likely to have small (~10 μs) residual errors which will leak power into evaluations of the timing noise spectrum.

TABLE 4.3

ESTIMATES OF THE CONTRIBUTION BY ERRORS IN ESTIMATES OF PLANETARY MASSES ON THE DEDUCED VALUES OF ROTATION PARAMETERS
PSR 0833-45

Planet	Mass Ratio (M/m) MIT	Mass Ratio (M/m) IAU_{1976}	Period [yr]	Orbital Radius (r) [$x10^6$ km]	$\Delta(M/m)_m$	Δt [s]	Δr [km]	$\Delta P/P$ [$x10^{-13}$]	$\Delta \dot{P}/\dot{P}$ [s^{-1}] [$x10^{-20}$]	$\Delta \ddot{P}/\ddot{P}$ [s^{-2}] [$x10^{-27}$]
Mercury	6021000	6026000	0.24	57.9	$4.42x10^{-2}$	$1.88x10^{-8}$	0.80	1.56	1.29	10.7
Venus	408250	408523.5	0.62	108.2	$1.60x10^{-3}$	$4.18x10^{-7}$	0.18	1.34	4.30	13.8
Earth+Moon	328900	328900	1.0	149.6	$9.33x10^{-4}$					
Mars	3111200	3098710	1.9	227.9	$5.77x10^{-3}$	$6.96x10^{-7}$	0.30	0.73	0.76	0.80
Jupiter	1047.355	1047.355	11.9	778.3	$5.71x10^{-7}$					
Saturn	3501.6	3498.5	29.5	1427.0	$1.04x10^{-6}$	$8.51x10^{-4}$	361	57.4	3.87	0.26
Uranus	22869	22869	84	2869.6	$3.38x10^{-6}$					
Neptune	19314	19314	165	4496.6	$1.82x10^{-6}$					
Pluto+Charon	360000	$1.47x10^8$	247	5900	$1.06x10^{-2}$	$3.85x10^{-2}$	16000	311.0	2.50	0.02

Notes :

M is the mass of the Sun, while m is the mass of the planet. The quantity $\Delta(M/m)_m$ represents the fractional change in the International Astronomical Union (IAU_{1976}) reciprocal mass of the planet which will produce at maximum a 1 microsecond error in the barycentric arrival time. The IAU_{1976} planetary masses have been taken to represent the true values. For each planet, the difference between the IAU_{1976} value and that used in the calculation of the MIT PEP 311 ephemeris (where it occurs) has been taken to represent the reciprocal mass error $\Delta(M/m)$ (see Appendix D). Δt and Δr are the likely maximum arrival time and barycentric position errors respectively for the MIT ephemeris contributed by each planet over one orbital period. Similarly, the three right-most columns contain the likely maximum timing parameter errors contributed by the inaccuracies in the MIT ephemeris. The reciprocal mass value for Pluto+Charon in the third column is by Tholen (1985).

In the evaluation of vector **n** (Appendix B) for PSR0833-45, the optical position (with the E-terms of annual abberation removed) given by Manchester *et al.* (1978b) was used. Timing positions were used for the reduction of PSR1749-28 (Downs and Reichley, 1983) and PSR1641-45 (Manchester *et al.*, 1978a) data.

4.10.2 The Dispersion Correction

From equation 1.5, the time delay between the arrival of pulses at the doppler corrected observation frequency f_d (Appendix B) and a pseudo-infinite frequency is approximated as

$$\Delta t_d = - \frac{DM}{2.410086 \times 10^{-4} f_d^2} \qquad 4.4.$$

Initially, the values of DM given for the pulsars by Taylor and Manchester (1975) were used to remove the dispersion delay from the arrival times.

An error ΔDM in the assumed dispersion measure will produce errors in the arrival times with a constant term proportional to $\Delta DM\ f^{-2}$ and an annual term with peak-to-peak amplitude proportional to $2\Delta DM\ v_e\ c^{-1}\ f^{-2}$, where f is the uncorrected observation frequency, and v_e is the velocity of the observer in the direction of the pulsar. As shown in Chapter 7, the dispersion measure of PSR0833-45 has been observed to vary by up to $\Delta DM \approx 0.02$ pc cm^{-3} over a time-span of 200 days. At 635 MHz, a change of this magnitude contributes an arrival time offset of ~ 200 μs. Of less consequence is the contribution of the annual term which has an amplitude of less than 1 μs.

4.11 CONTRIBUTIONS TO THE BARYCENTRIC PHASE

From equation 1.1, the accumulated pulse phase between epochs t_i and t_0 is expressed as

$$\phi_b(t_i) - \phi_b(t_0) = \int_{t_0}^{t_i} \nu(t')\, dt' \qquad 4.5$$

where the subscript b (which is dropped in all subsequent discussion) identifies barycentric estimates, and ν is the pulse frequency.

Following the notation of Cordes and Downs (1985), the barycentric phase may be written as

$$\phi = (\phi_{TN} + \phi_G)_{slow} + (\phi_S + \phi_J + \phi_M)_{fast} + \phi_d$$

where the *slow* (relative to one pulse period terms) are due to timing noise and glitches, respectively. The *fast* terms are contributed by the spindown behaviour,

phase jitter (conceivably related to fluctuations of size and orientation of the emission beam within the pulsar's magnetosphere), and measurement noise. The final term is due to refractive group delay fluctuations not accounted for by equation 4.4.

Cordes and Downs (1985; hereafter CD) have estimated the rms contribution of ϕ_J (in units of time) over the time-span of an integrated profile as

$$\hat{\sigma}_J = P \langle \phi_J^2 \rangle^{1/2} = \frac{\Delta t_w}{2} \cdot \sqrt{\frac{F}{2N \cdot \ln(2)(1+F)}} \qquad 4.6$$

where Δt_w is the width (FWHM) of the integrated profile. F is a dimensionless quantity obtained from the relation

$$\Delta\tau = \Delta t_I \sqrt{1 + F^2},$$

or equivalently,

$$F = \Delta\tau / \tau$$

where $\Delta\tau$ is the rms fluctuation of the width (FWHM) τ of an individual pulse.

CD estimate $F \approx 1$. Romani, Narayan, and Blandford (1986; hereafter BNR) have provided expressions for the τ and $\Delta\tau$ assuming a power-law spectum for interstellar density turbulence. The scalings of $\Delta\tau$ and τ are critically dependent on the spectral index α_s of the density turbulence, which for Vela is approximately 4.1 (table 1.1). Using expressions given by BNR, $F \sim 0.3$ for $\alpha_s = 11/3$ (diffractive Kolmogorov turbulence spectrum) and $F \sim 0.6$ for a steeper (refractive) turbulence spectrum with $\alpha_s = 4.3$. Using $F = 1$ as an upper limit, $\hat{\sigma}_J \approx 20$ μs for the LRO Vela observations. As CD note, phase fluctuations that are correlated from pulse to pulse will cause F to be underestimated. Due to sensitivity limitations, no single pulse observations were possible, and so F could not be experimentally evaluated.

CD have considered that the white noise contributions due to fluctuations in pulse shape and dispersion delay are dominated by pulse jitter. Both effects are considered in Chapter 5. The latter effect is due to density turbulence in the line-of-sight plasma which alters the effective observing centre frequency. For Vela observations, the rms component of the dispersive delay was calculated as $\hat{\sigma}_d << 1$ μs on the timescale of an observing session using expressions given by Cordes, Pidwerbetsky, and Lovelace (1986) in conjunction with the spectral index of the density turbulence (α_s; table 1.1) and the assumed distance of the pulsar. Ionospheric and interplanetary dispersive effects can be ignored as the total delay through these regions amounts to at most 0.1 μs for the LRO observations of Vela at 635 MHz (Muhleman and Anderson, 1981; Davies and Hartmann, 1976; Ebel, Schmidt, and Taurianen, 1976).

4.12 ARRIVAL TIME MODELS

As noted in section 1.1, a convenient expression for ν which adequately describes the spindown behaviour over epochs where the effects from any previous glitches have 'healed' is the truncated Taylor series[b]

$$\nu(t) = \nu_0 + \dot{\nu}_0(t - t_0) + \frac{\ddot{\nu}_0}{2}(t - t_0)^2 \qquad 4.7$$

where $\nu_0 = \nu(t_0)$ (Manchester and Taylor, 1977).

Combining equations 4.5 and 4.7 gives the cubic phase model

$$\hat{\phi}(t) = \phi_0 + \nu_0(t - t_0) + \frac{\dot{\nu}_0}{2}(t - t_0)^2 + \frac{\ddot{\nu}_0}{6}(t - t_0)^3 \qquad 4.8$$

where $\hat{\phi}_0 = \hat{\phi}(t_0)$. In modelling the phase measurements, initial estimates of the frequency parameters were made, and then equation 4.8 was applied to the data over a span of length T in order to yield a set of phase *residuals*. Providing that the estimates of ν_0, $\dot{\nu}_0$ and $\ddot{\nu}_0$ are sufficiently precise, the accumulated phase will remain close to the integral number of actual phase cycles that have elapsed since $t = t_0$. For convenience, it is assumed that $\hat{\phi}_0 = 0$. The residual R_i at $t = t_i$ may be expressed as

$$R_i = (\phi_i - \hat{\phi}_i)$$

Here ϕ_i is the observed phase of the i-th pulse and R_i is in units of cycles. An iterative least-squares procedure is used to fit the model

$$\hat{R}_i = (t_i - t_0)\,[\Delta\nu_0 + \frac{1}{2}\Delta\dot{\nu}(t_i - t_0) + \frac{1}{6}\Delta\ddot{\nu}(t_i - t_0)^2] + R_p \qquad 4.9$$

to the R_i where the terms prefixed by Δ are correction coefficients, and R_p is an optional term which accounts for proper motion and errors in the assumed position of the pulsar (Appendix F). The final value of each frequency parameter is obtained from the addition of the initial estimate and the correction. These quantities were substituted into equation 4.8 to form the new phase model. The rms value of the residuals obtained from the difference of the new model and the observations is given by

$$\sigma_R = \left[N^{-1} \sum_i R_i^2(m,T) \right]^{1/2} \qquad 4.10$$

where N is the total number of phase measurements, and m is used to denote the order of the Taylor series polynomial used for the frequency model (in the case of equation 4.7, m=3). It is noted that the frequency parameters have small contributions due to the velocity vector of the pulsar with respect to the barycentre; these are evaluated in Appendix G where it is shown that this effect is of no concern for the Vela observations.

---

[b] The models presented here are defined in terms of parameters relating to pulse frequency and its derivatives. These quantities find more utility is describing pulsar dynamics than do parameters based on pulse period and its derivatives. Affine transforms relating the two types of quantity are presented in Appendix E.

On substituting the typical values of $\dot{\nu}$ and $\ddot{\nu}$ for PSR 0833-45 (table 1.1) into equation 4.8, it is evident that an increase in the residual of one milliperiod will occur in ~ 0.5 day if both the $\dot{\nu}$ and $\ddot{\nu}$ terms are disregarded. If $\ddot{\nu}$ alone is neglected and $\dot{\nu}$ is set equal to its true value, then the same phase difference will be attained in ~ 50 days. The values of $\dot{\nu}$ and $\ddot{\nu}$ are sufficiently small and well known that pulse numbering is normally unambiguous. However, immediately after a glitch of magnitude $\Delta\nu/\nu \approx 10^{-6}$, the the phase residual reaches a whole period after ~ 1 day. This fact alone suggests the necessity for the daily monitoring of the pulsar so that the pulse numbering sequence is not lost. The discussion of the fitting of glitch models for ϕ is presented in Chapter 6.

4.13 OBSERVATIONS OF PSR1749-28 AND PSR1641-45

Observations of PSR1749-28 were made to assist in the interpretation of the dispersion delay measurements of the Vela pulsar (Chapter 7). PSR1641-45 was observed in the hope of detecting a glitch. The receiver and sampling parameters used for both pulsars are presented in table 4.4. Long integrations were required on both pulsars to obtain an adequate pulse SN ratio. Because of this, a larger percentage of the integrations in comparison with those for PSR0833-45 were subjected to the effects of local impulsive noise. Arrival-time estimates not conforming to the general spindown behaviour were rejected using the method described in Appendix H.

4.13.1 PSR1749-28

Templates for each frequency were constructed by superposed epoch integration of all of the available profiles that had a signal-to-noise ratio in excess of 5. The shape of each template was in good agreement with the profiles obtained by McCulloch *et al.* (1977). The cross-correlation procedure used to obtain pulse phase estimates yielded typical r_c values of 0.85. Although PSR1749-28 is a relatively bright object, it lies close to the line-of-sight to the galactic centre. The high background noise level resulted in the relatively low value of the correlation coefficient. Data from a typical observation session are presented in figure 4.6 and show evidence of slow intensity scintillations.

4.13.2 PSR1641-45

The integrated profiles exhibited the effects of strong scattering. Individual profiles were cross-correlated with a template (from McCulloch *et al.*, 1978) and then shifted so that their phase centroids coincided with that of the central integration. A

TABLE 4.4
PARAMETERS FOR PSR1749-28 AND PSR1641-45[a]

Pulsar	PSR 1749-28	PSR 1641-45
Timing[b]		
ν (Hz)	1.77759548831±5	2.1975160257±7
$\dot{\nu}$ (10^{-14} Hz s^{-1})	-2.578±4	-9.63±5
epoch (TJD)	6552.9984179	6288.9508212
epoch range of fit (TJD)	6507 - 6593	6227 - 6345
rms residual (ms)	1.0	11.1
Position (B1950.0)[c]		
RA	$17^h\ 49^m\ 49.^s271±6$	$16^h\ 41^m\ 10.^s313±4$
dec	-28°6'0".7±5	-45°53'38".7±1
μ_α (mas yr^{-1})	19.1±13.7	
μ_δ (mas yr^{-1})	< 40	
galactic latitude	1°.5	339°.2
galactic longitude	-1°.0	-0°.2
epoch (TJD)	352	
Llanherne Observations[d]		
periods integrated[e]	2130	2200
sampling interval (ms)	2.2	1.8
time constant (μs)	470	470
dispersion smear (period)	2.3×10^{-4}	2.6×10^{-2}
SN ratio	10	5
50% pulse width (ms)[b]	25	95
integrations per session	15	15
$\Delta f_c/\Delta f_p$ [f]	0.25/0.45	2.5×10^4
General		
DM (pc cm^{-3})[g]	50.88±0.14	450±10
RM (rad m^{-2})[h]	95±2	
mean linear polarization (%)[i]	10	3
mean flux density (mJy)[b,i]	580	1300
spectral index[j]	-3.1	-1.0
distance (kpc)[k]	1.7	8.2
characteristic age (10^6 yr)	1.1	0.36

a Errors are 95% confidence limits, and are quoted for the last significant digit, except for proper motion and DM
b Near 635 MHz
c Downs and Reichley (1983)
d For observations of PSR1749-28 at 635 MHz/954 MHz, and PSR1641-45 at 635 MHz.
e Timing ephemeris from Newton, Manchester, and Cooke (1981) for PSR1749-28, and Manchester *et al.* (1978a) for PSR1641-45.
f Ratio of decorrelation to radiometer bandwidths from Cordes, Weisberg, and Boriakoff (1985).
g Lyne and Rickett (1968)
h Manchester (1974)
i McCulloch *et al.* (1978)
j Taylor and Manchester (1975)
k Assuming a braking index of 3.

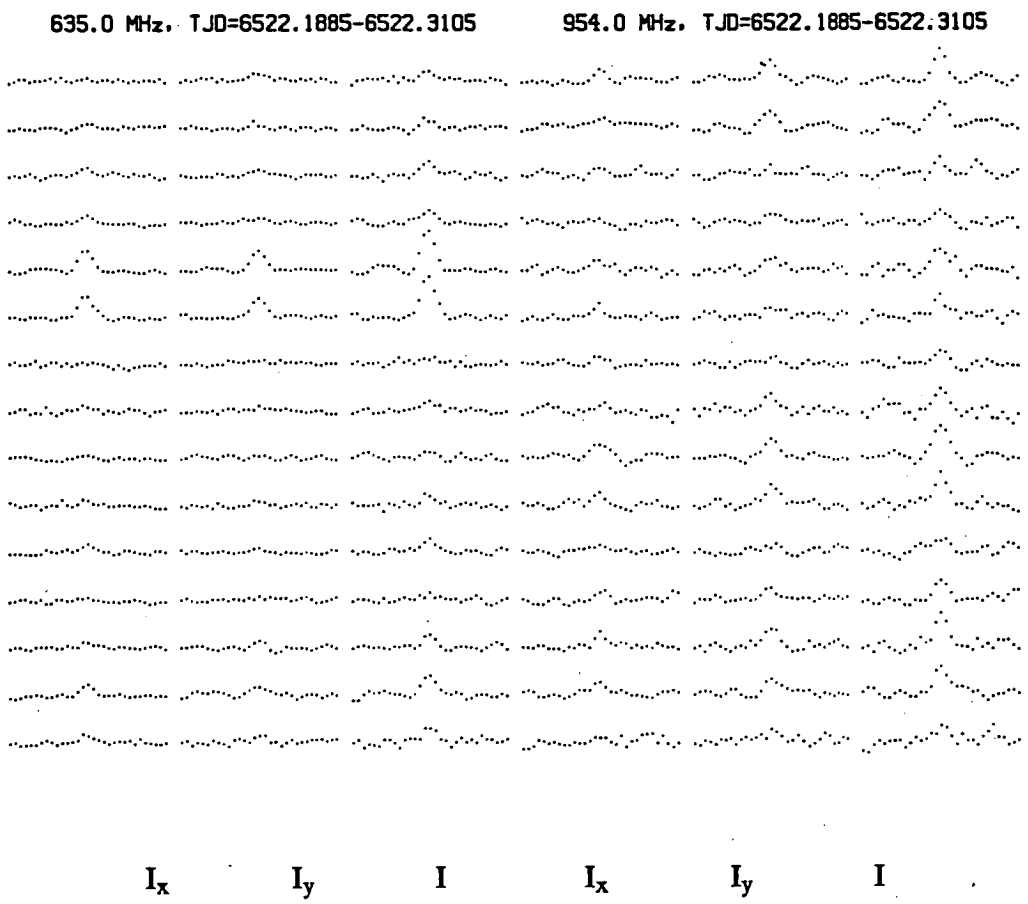

Fig. 4.6. Stacked integrations of PSR1749-28 simultaneously recorded at 635 MHz (left three plots) and 954 MHz. For each frequency, the I_x, I_y, and I profiles are presented. The I_x and I_y profiles represent the synchronous integration of 2130 periods, and have been windowed to show a total of 30 bins (0.066 s) about the peak of the pulse (thereby removing the relative phase offset between the I profiles of the two frequencies due to dispersion delay). The vertical scale is arbitrary but has been adjusted so that the grand-average off-peak standard deviation of the I profiles of both frequencies are equal. Increasing time runs from top to bottom.

mean profile was then produced and its phase lag was determined.

4.13.3 Timing Parameters

The spindown model of equation 4.7 was fitted to the barycentric data. Proper motion corrections were ignored. The dispersion measures of table 4.4 were assumed when calculating the dispersion correction. The results from the fits are presented in table 4.4 and Appendix H.

The observed frequency derivative for PSR1749-28 of $(2.578\pm0.004)\times10^{-14}$ Hz s^{-1} is in good agreement with the value of $(2.563\pm0.019)\times10^{-14}$ Hz s^{-1} obtained by Newton, Manchester, and Cooke (1981).

The rotation frequency of PSR1641-45 is compared with previous measurements in figure 4.7; there is no evidence of any large glitch events between 1978 and 1985. The observed frequency derivative of $(-9.63\pm0.05)\times10^{-14}$ Hz s^{-1} is in reasonable agreement with the value of $(-9.709\pm0.017)\times10^{-14}$ Hz s^{-1} quoted by Manchester *et al.* (1983) following the 1977 glitch.

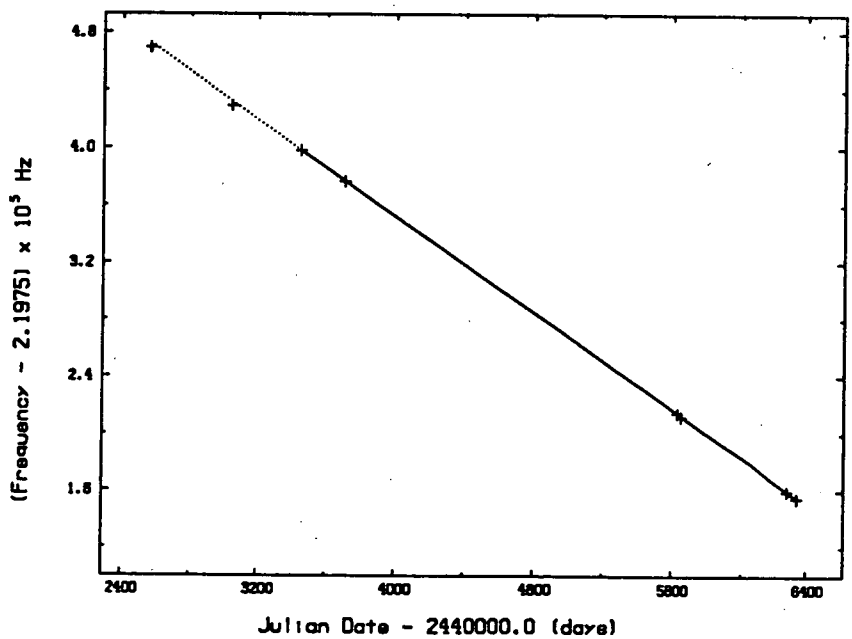

Fig 4.7. Timing behaviour of PSR1641-45 from 1972 to 1985. The points from TJD ~ 5600 onward are the result of LRO observations. They represent extrapolations of spindown fits to data collected during 1983 and 1985 to the endpoints of the respective data spans. The other data in the plot have been obtained from Manchester *et al.* (1978,1983). A linear fit to the data after TJD = 3390, the epoch of the glitch inferred by Manchester *et al.* (1978), is also shown.

4.14 CONCLUSIONS

The methods that were adopted for the collection and reduction of pulsar timing data from the Llanherne Radio Observatory, with particular reference to PSR0833-45, have been described. Of importance has been the quantification of the uncertainty in the barycentric arrival times which constitute the basis for the detailed study of the pulsar, its immediate environment, and the line-of-sight interstellar medium; these topics are addressed in the following chapters.

The cross-correlation method employed to obtain the pulse phase within individual integrations was robust in the presence of random noise for SN ratios in excess of approximately 2.5. Through suitable choice of the parameters of the observation system, the typical pulse SN ratio was ~ 15, for which the rms phase uncertainty was calculated as ~ 60 μs on the basis of the estimator provided by Downs and Reichley (1983). This estimator is valid if the intrinsic pulse shape is stable on the timescale of each integration. This aspect is addressed in the following chapter. Additional sources of short timescale phase fluctuations, principally due to pulse jitter, were estimated to have an rms amplitude of ~20 μs.

An aspect of the timing programme that received considerable attention was the determination of the time offset between the observatory clock and the atomic timescale. The method of time transference was sufficiently reliable to confidently predict the uncertainty in the absolute time of commencement of the majority of integrations as < 5 μs. However, between December, 1984, and March, 1985, and from March, 1986, limited data were available on the local arrival times of the television synchronization pulses. Time corrections were applied through extrapolation of correction polynomials and examination of the output of the phase tracking receiver. Due indication has made in the chapters that follow where data associated with intervals lacking high quality timing corrections have been employed.

The accuracy of the MIT ephemeris at the microsecond level is unknown but it is anticipated as having only a marginal influence on the timing data particularly over intervals less than a few years.

The modification of the intrinsic pulse shape due to the choice of receiver bandwidth and post-detection time constant has been quantified. In addition, it was noted that the stochastic effects of interstellar scintillation on the integrated profiles are expected to be minimal as a result of the choice of integration time and receiver bandwidth.

Data has also been collected for PSR1749-28 and PSR1641-45. There is no evidence for any significant glitch events for the latter object between 1983 and 1985.

CHAPTER 5 - SHORT TIMESCALE PHASE NOISE AND PULSE PROFILE SHAPE

5.1 INTRODUCTION

As summarized in section 3.3, Downs and Krause-Polstorff (1986; hereafter DK-P) found JPL timing measurements of the Vela pulsar to exhibit phase noise in excess of that ascribable to measurement effects. These authors were unable to definitively identify the origin of this phenomenon. This revelation motivated the analysis of the LRO data set in order to examine the long term stability of Vela's pulse profile, and the influence of pulse shape changes on the determination of arrival times. An additional aim was to quantify arrival time fluctuations on short (< 1 day) timescales in order to validate the work of DK-P. The results of these investigations are presented in this chapter.

5.2 DATA SELECTION

The medium resolution compressed data were subdivided into non-overlapping intervals of approximately 100 days duration, with the provision that no interval was to contain pre- and post-glitch observations[a]. A cubic phase model (based on equation 4.7) was fitted to each span to yield the coefficient values provided in table I.1. The success of the model fits can be gauged in plots of figure I.1a-I.16a. Obvious structure is present on a variety of timescales. Broadly speaking, this behaviour is the manifestation of processes intrinsic to the pulsar (post-glitch relaxation and timing noise) and the interstellar medium (dispersion measure fluctuations); these topics are the subjects of the following chapters. The level at which discrete observing-system related structure may be present is considered in section 8.2.

Each model of table I.1 was applied to high resolution data over an equivalent epoch span in order to yield sets of residuals. For each session, the unweighted mean residual and its 95% confidence limits were obtained. These values were used to determine the validity of any outlying residuals in a manner similar to the rejection procedure described in section 4.7. If the ratio of largest deviation from the mean to the population standard deviation exceeded 3.3, the residual and its arrival time estimate were discarded, and the mean and standard deviation were recomputed. This

---

[a] The identification of glitches is discussed in section 6.2.

procedure was repeated until no further rejections occurred. The observations removed amounted to 4% of those available.

5.3 PHASE NOISE

A cubic model was fitted to each 'cleaned' set of data. As expected, the resulting coefficient values (table I.1) were in very close agreement with those obtained from the fits to the compressed data. The temporal behaviour of each resulting residual set is shown in figure I.1b-I.16b. The dual frequency arrival time data are treated separately in Chapter 7.

The normalized probability distribution was evaluated for the residuals of each session after the removal of the session mean. The bin width chosen was 20 μs. The daily distributions were then pooled to obtain the mean and associated 95% confidence limit at each bin. The distributions obtained are presented in figures I.1c-I.16c, together with theoretical gaussian distributions. A simulation consisting of 100 sets of 160 gaussian numbers with a standard deviation of 100 μs was also binned, and this is presented in figure 5.1.

The aim of the binning procedure was to verify that the daily residuals were approximately normally distributed. This behaviour is apparent in figures I.1c-I.16c, although the width of each distribution shows evidence of time dependence (table I.1). If the residuals exhibit a significant systematic trend, then the daily distributions will be skewed relative to their first moment. This effect will result in the overall broadening of the mean distribution. In addition, any variation of pulse energy, receiver sensitivity, and intrinsic phase noise will also influence the width of the daily distributions.

As noted in Chapter 4, measurement noise was expected to provide the largest contribution to the short timescale residuals. It was anticipated as having a white spectrum on the basis of the lack of intensity scintillations achieved through the choice of receiver and integration parameters. Cordes and Downs (1985; hereafter CD) and DK-P found the level of short-timescale fluctuations in residuals from model fits to be in excess of that expected from the contribution of the measurement uncertainty. CD used the following structure function to quantify phase noise;

$$\sigma_S^2 = (2N)^{-1} (R_{j+1} - R_j)^2 \qquad 5.1$$

where $R_j = R(m,T,t_j)$ is the j-th phase residual (defined in equation 4.9) from a polynomial fit of order m to data within a span of length T, and N is the number of

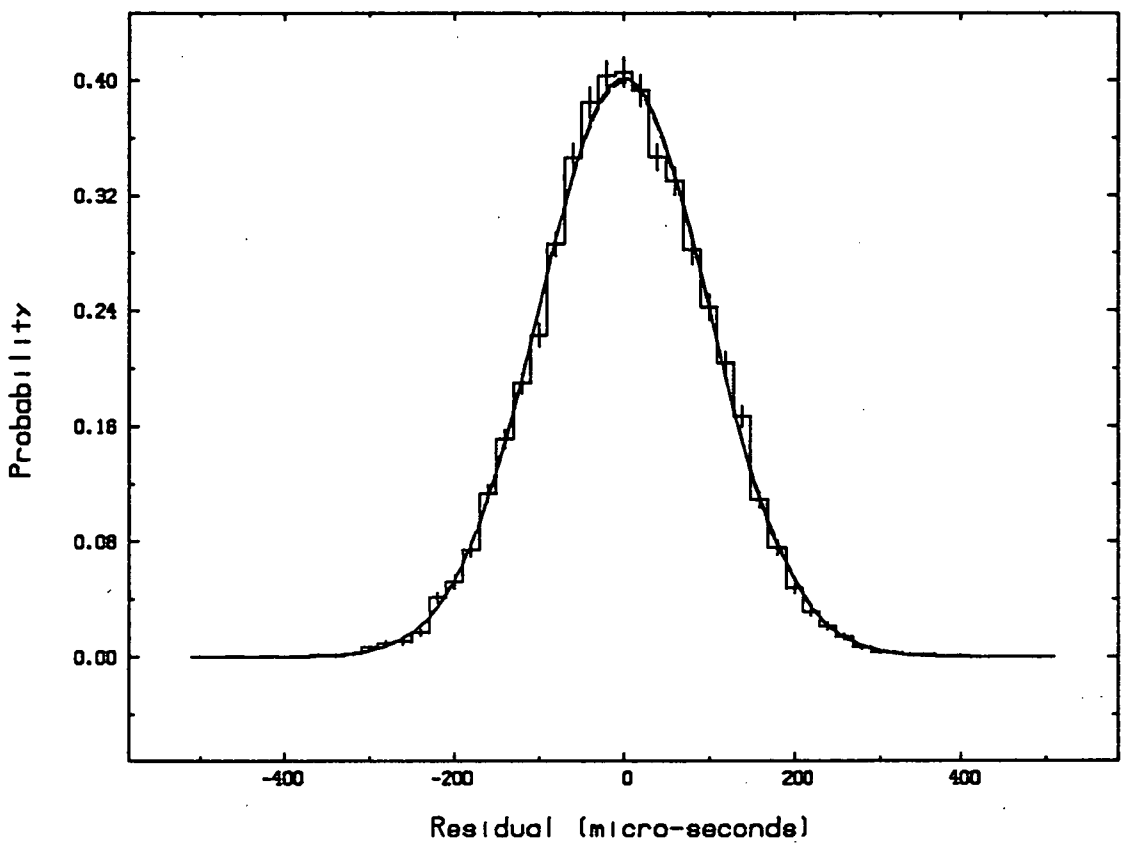

Fig. 5.1. Distribution obtained from the average of the distributions for 100 sets of residuals consisting of 160 members. The raw values were generated with a standard deviation of 100μs. The bin width is 20μs. The error bar at each bin represents the standard error of the mean value. Superimposed is a solid curve representing a gaussian with the same area and variance as the observed distribution, while the almost imperceptible dashed curve represents a gaussian with standard deviation of 100μs.

paired quantities. The residual pairs are only included in the summation if $t_{j+1} - t_j < \Delta t_{max}$. For normally distributed R and large N, σ_S^2 is equal to the variance of the population.

For each set of residuals from the cubic model fits to the compressed data, values of σ_S were calculated for Δt_{max} selected from an *octave*[b] set based on half the maximum span length. Values of σ_S for each Δt_{max} are presented in figure 5.2. It is apparent that σ_S becomes an unbiased estimator of white noise for $\Delta t_{max} \leq 2$ days. A similar procedure was adopted for the residuals from the cubic fits to the high resolution data. Plots of σ_S for $\Delta t_{max} < 10$ days are provided in figure 5.3, which explore timescales down to approximately 5 minutes. In general, no structure is evident for $\Delta t_{max} < 1$ day. The interval fitted by model 4 contained relatively few sessions of which most produced typically only 20 minutes of contiguous data with generally low SN profiles. As a result, the mean value and variability of σ_S for this data span appear enhanced relative to other spans over short timescales.

The value of σ_S for $\Delta t_{max} = 1$ day was assigned as a measure of the rms white noise strength σ_W. This quantity was evaluated for each observing session using the high resolution residual sets. In addition, data from adjacent pairs of sessions were fitted with a linear spindown model, assuming fixed $\dot{\nu}$ and $\ddot{\nu}$, to obtain a second set of σ_W estimates. Each σ_W was divided by the rms (quadratic average) of the theoretical measurement error over the associated data span to obtain the quantity r_σ; this parameter was tagged with the central epoch of the timespan covered by the observations.

The behaviour of each set of noise ratios is shown in figure 5.4. As shown in table 5.1, both ratios exhibit significant mutual correlation and have very similar mean magnitudes. This latter result indicates that any distribution skewing introduced into the daily residuals of the 100 day model fits does not have a significant bearing on the estimation of σ_W. This is also borne out by the absence of glitch signatures in figure 5.4(b).

The results of figure 5.4 confirm the existence of phase noise in excess of the level attributable to the measurement process found by CD and DK-P. CD observed $r_\sigma \sim 3$, while the LRO data provide $r_\sigma \sim 1.5$ (table 5.1).

---

[b] The span lengths in the 'octave' set are expressed as $\Delta t_{max_i} = T_m\, 2^{i-1}$ where i = 1, 2, ..., n, and T_m is the maximum desired span length. The upper value of i (namely n) is restricted by the minimum number of phase values required by the fitting procedure.

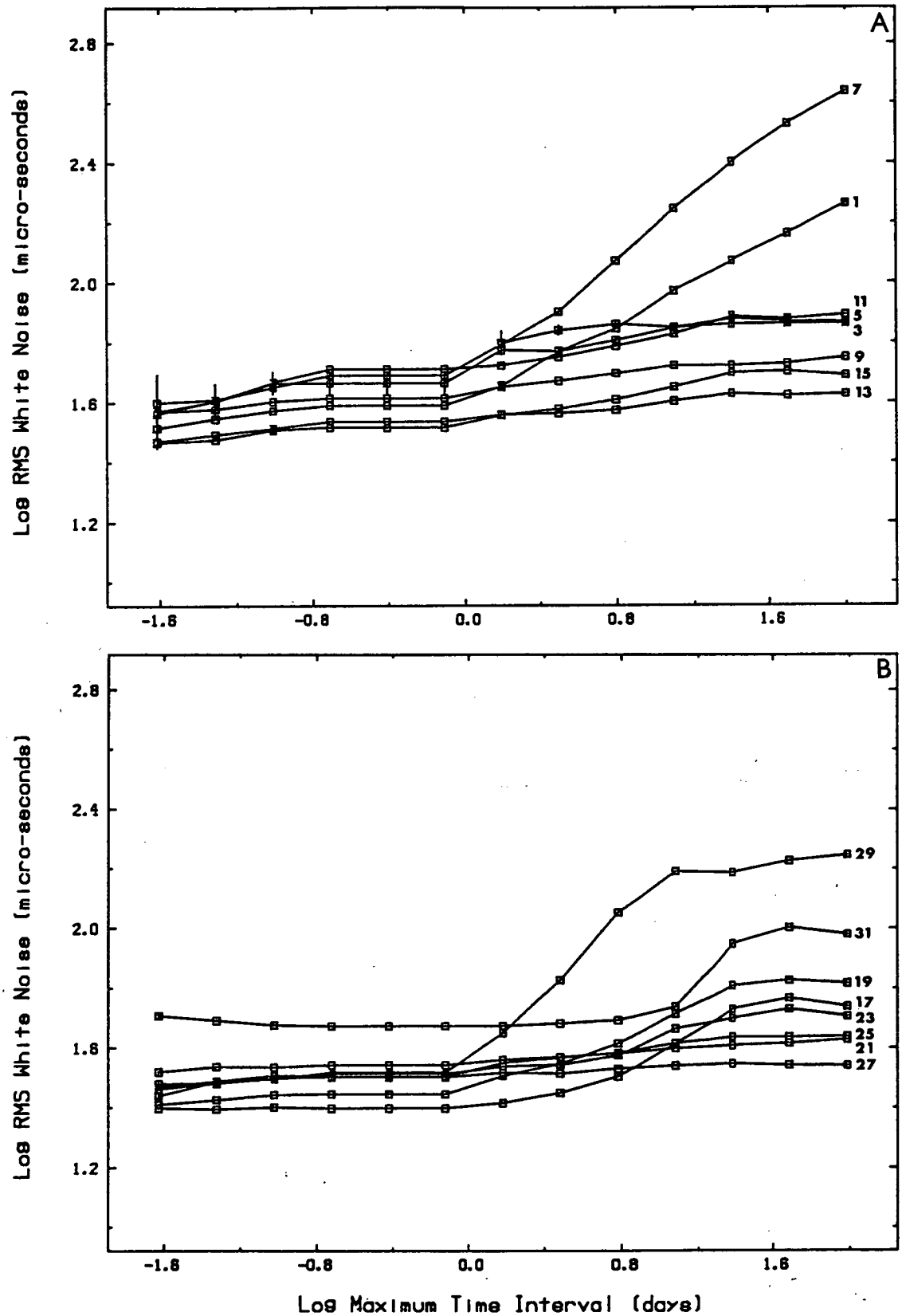

Fig. 5.2. Structure function analysis of residuals from cubic fits to compressed data. Plotted is the base-10 logarithm of the rms white noise strength σ_W as a function of Δt_{max}. For each plot, the model number (table I.1) of the spindown equation used to obtain the associated residual set is provided. Note the apparent stationarity of σ_W for $\Delta t_{max} < 2$ days, with an approximate rms magnitude of ~ 30 μs. Vertical error bars, (where apparent) were calculated using equation A.18.

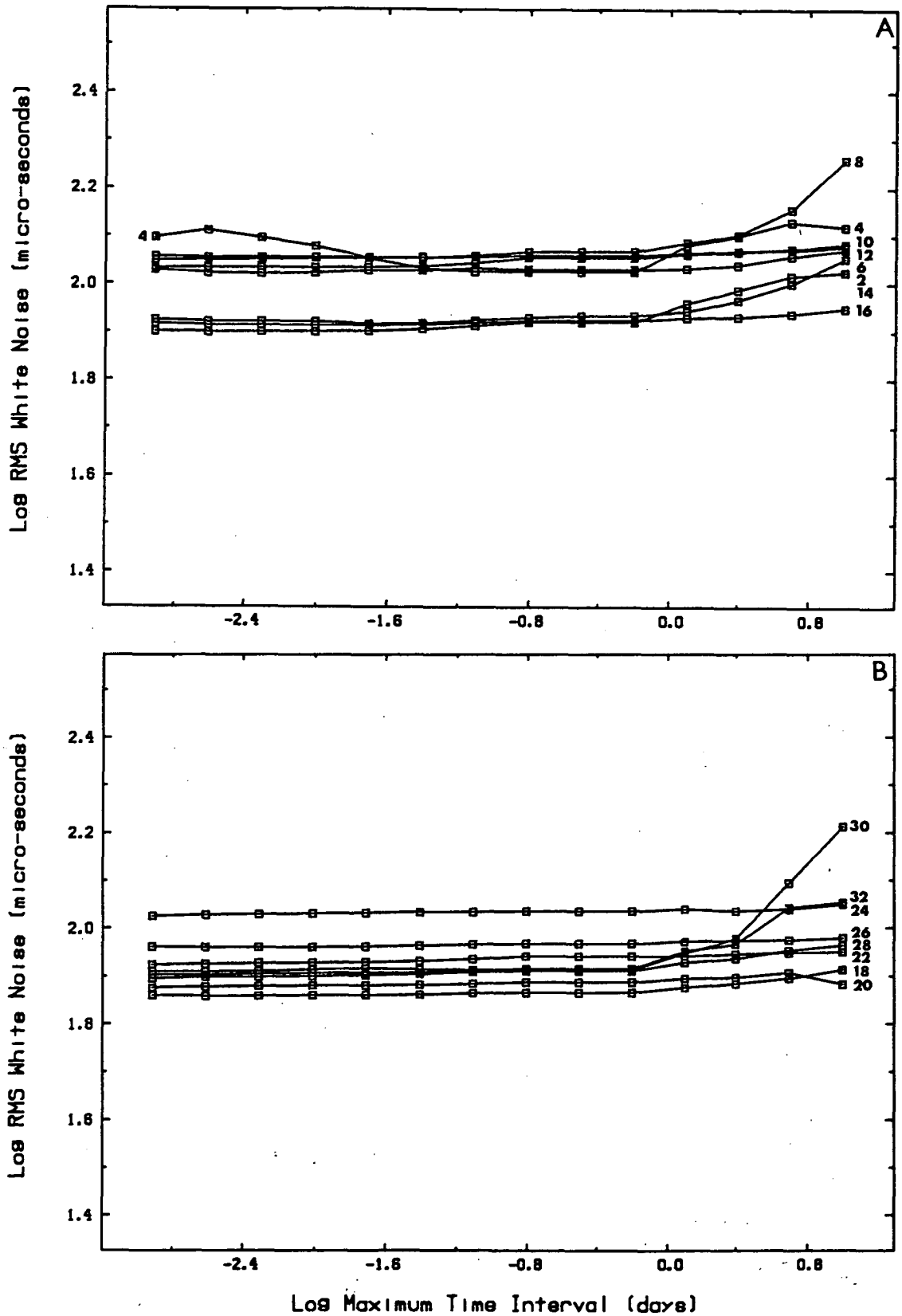

Fig. 5.3. Structure function analysis of residuals from cubic fits to high resolution data. For each plot, the model number (table I.1) of the spindown equation used to obtain the associated residual set is provided. No distinctive trends are apparent for maximum interval lengths less than 1 day. The approximate magnitude of σ_W on this timescale is 95 μs. Vertical error bars (where apparent) were calculated using equation A.18.

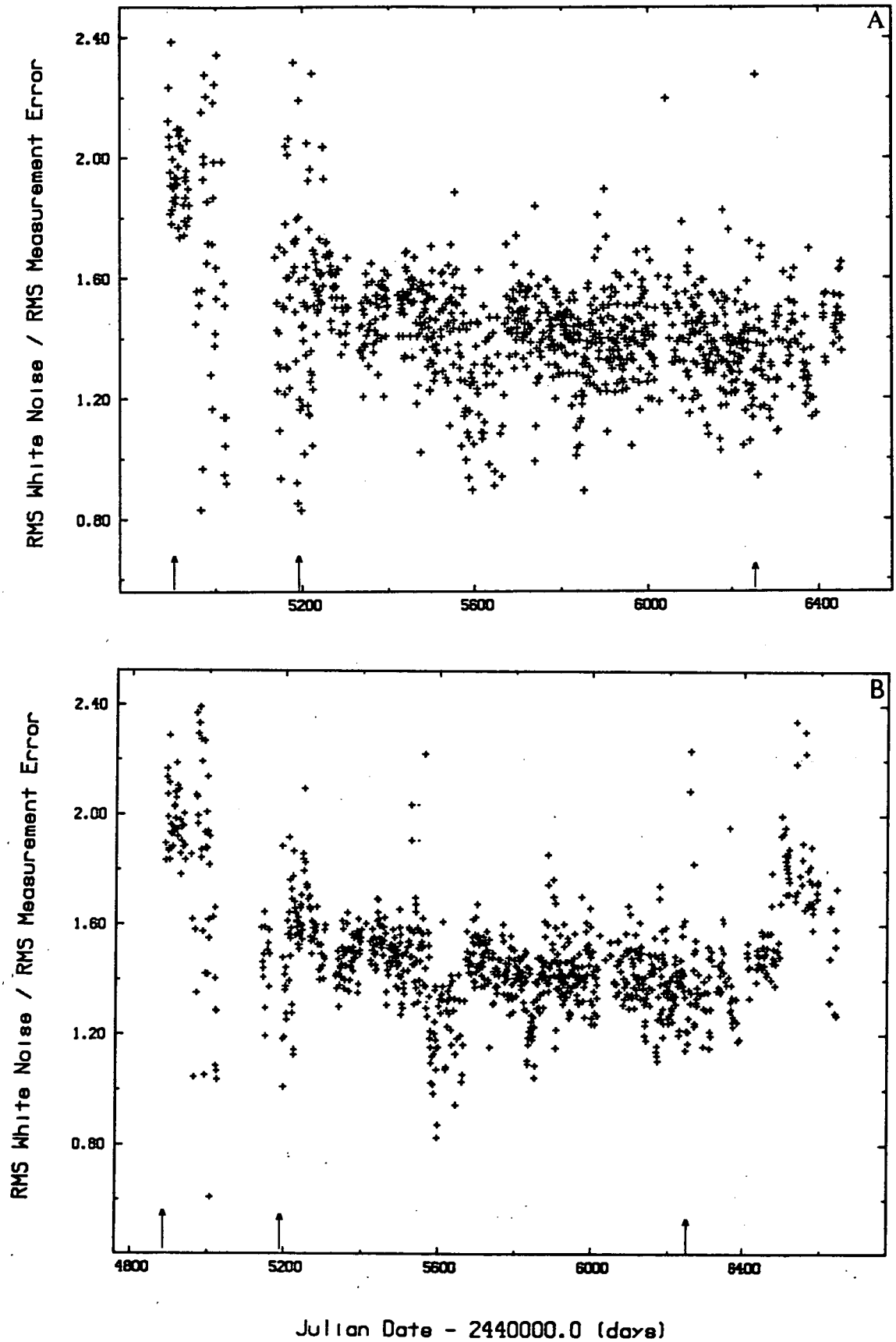

Fig. 5.4. Ratio of the rms white noise level to the rms measurement error as a function of epoch obtained (a) from the residuals of cubic models fitted over ~ 100 day spans to the high resolution timing data set, and (b) from linear spindown model fits to pairs of adjacent daily observations. The glitch epochs are indicated by arrows.

TABLE 5.1

PHASE NOISE PARAMETERS

Parameter	Value
Method 1	
rms r_σ	1.48
mean r_σ	1.45±0.29
mean r_σ (TJD > 5192)	1.44±0.19
mean σ_W (μs)	94±30
Method 2	
rms r_σ	1.51
mean r_σ	1.49±0.25
mean r_σ (TJD > 5192)	1.44±0.24
mean σ_W (μs)	94±27
Correlation of $r_{\sigma(1)}$ against $r_{\sigma(2)}$	
correlation coefficient r	0.5
number of observations	773
P(r)	~0
Measurement Uncertainty	
daily mean (μs)	64±15

Notes :

Methods 1 and 2 refer to estimates from cubic and linear model fits respectively. The error range quoted for mean values is the standard deviation of the pooled estimates. Unless indicated, the epoch range of the data used was TJD 4889.1-6490.0. P(r) is the probability of observing the correlation coefficient r between two samples drawn from a normally distributed population.

Figure 5.4 contains epoch ranges in which the scatter of r_σ appears enhanced. These are coincident with intervals during which the duration of the daily observations were restricted (January to August, 1982). Figure 5.4a has been replotted in figure 5.5 after arbitrarily confining the estimate of r_σ to only those sessions containing in excess of 50 integrations. In figure 5.6 the excess noise has been quantified as a function of epoch by the parameter

$$\sigma_E = \sqrt{\sigma_W^2 - \sigma_M^2} \qquad 5.2.$$

Systematic behaviour is apparent in this figure that does not appear related to the glitch events, particularly jump 7. Further discussion of this behaviour is presented in section 5.6.

5.4 PULSE SHAPE

The identification of the excess phase noise noted in the preceding section motivated DK-P to examine the influence of short timescale pulse shape fluctuations on the estimation of arrival times. DK-P quantified the shape of an integrated profile in terms of its moments about the axis of maximum correlation with the associated template. The j-th moment was defined as

$$\mu_{j_i} = \frac{\sum_k (\Phi_{k_i} - \phi_i)^j \, d_{k_i}}{\sum_k d_{k_i}} \qquad j = (1,3) \qquad 5.3$$

where Φ_{k_i} and d_{k_i} are the phase and data values of the k-th bin of the i-th profile respectively. In addition, the j-th difference moment was defined as

$$\mu_{d_{j_i}} = \frac{\sum_k (\Phi_{k_i} - \phi_i)^j \, (d_{k_i} - T_k)}{\sum_k d_{k_i}} \qquad j = (0,3) \qquad 5.4$$

where T_k is the value of the template scaled to the amplitude of the profile at Φ_{k_i}.

A geometrical pulse shape factor was also defined ;

$$K_{G_i} = A_i / l_i^2 \qquad 5.5$$

where A_i is the area under the i-th integration, and l_i is the length of the corresponding pulse perimeter.

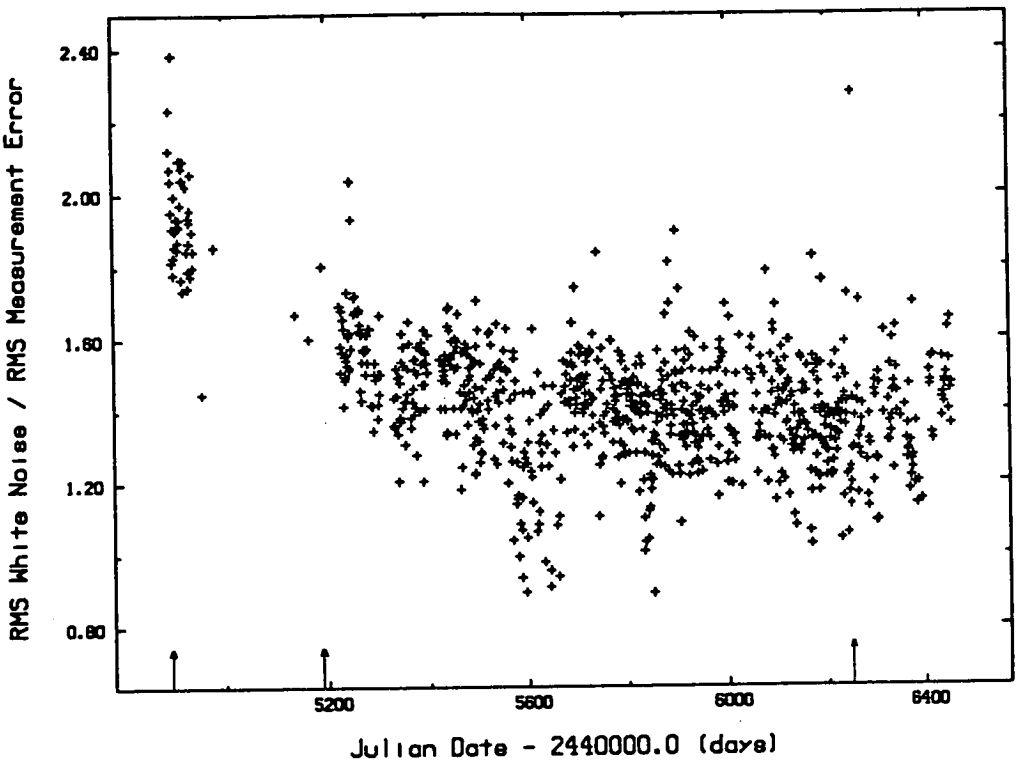

Fig. 5.5. Ratio of the rms white noise level to the rms measurement error as a function of epoch from figure 5.3a plotted for sessions containing more than 50 integrations. The glitch epochs are indicated by arrows.

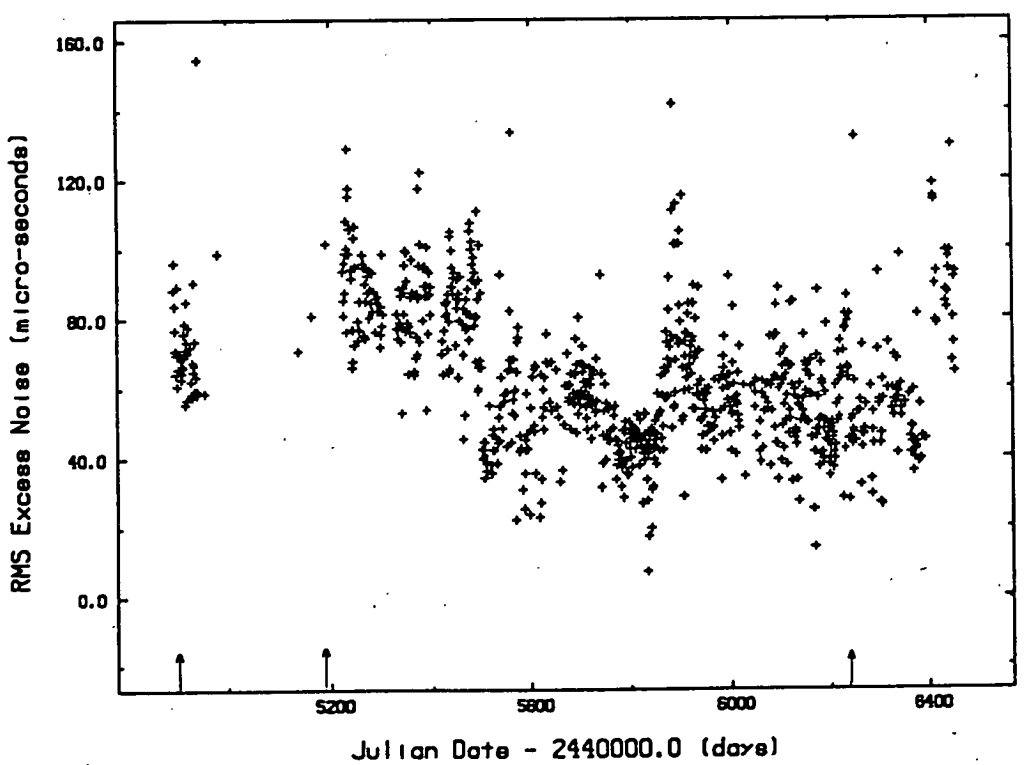

Fig. 5.6. Excess phase noise as function of epoch for sessions containing more than 50 integrations. The glitch epochs are indicated by arrows.

To examine the influence of noise on the above pulse shape parameters, a series of simulations were conducted. Gaussian noise of predetermined standard deviation was added to a template profile to create a simulated pulse and the shape parameters were then evaluated. The noise level was selected as a fraction of the template height from 0% to 50% in 5% increments. A total of 50 realizations were computed for each noise level. For each set of realizations, the mean and standard error of the mean for each shape parameter was evaluated.

From the simulations, it was apparent that noise has the effect of broadening the distribution of moments while not contributing a significant systematic trend. On the other hand, as shown in figure 5.7, K_G was underestimated in the presence of noise, demonstrating its general unsuitability as a measure of profile shape.

The shape parameters were paired with their corresponding residual using only those data sets of section 5.2 that did not exhibit any significant systematic trend. Cross-correlations were then performed. The results are summarized in table 5.3. The lack of any significant correlation indicates that pulse shape fluctuations over the integration timescale do not bias the pulse phase estimates. This conclusion was also reached by DK-P. Scatter diagrams are presented in figure 5.8 for those parameters exhibiting the largest correlation coefficient values.

5.5 RESIDUAL AUTOCORRELATIONS

In this section, the apparent partial correlation of timing residuals on the timescale of hours claimed by Downs and Krause-Polstorff (1986) is studied.

Sets of residuals obtained from cubic fits to 100 day data spans of section 5.2 formed the basis of the investigation. The data of each observing were firstly binned. A variety of bin widths were chosen and a standard value of 5 minutes was settled upon as this gave good protection against discontiguous sampling while at the same time providing good lag resolution. The values of the residuals lying within each bin were averaged. The autocorrelation function $R(\tau)$ (where τ is the lag) was then calculated for the binned data of each session. The values of a common lag within each data span were then pooled, and the population mean and standard deviation, and the standard error of the mean were calculated. A gaussian random number from a population with the same standard deviation as the residuals of each data span was paired with each residual value, and the binning and autocorrelation processes were repeated. The autocorrelation functions are displayed in figures I.1d-I.16d.

TABLE 5.2

CROSS-CORRELATIONS FOR PSR0833-45[a]

	Timing Model Number				
	10	12	14	16	18
μ_1	3.1	3.5	2.4	3.7	2.0
μ_2	0.4	0.2	-0.3	0.2	0.0
μ_3	0.1	-0.2	-1.4	0.7	-0.9
μ_{d_0}	1.5	3.2	7.0	4.3	1.6
μ_{d_1}	3.2	3.8	3.4	4.2	2.3
μ_{d_2}	0.5	0.4	0.2	0.4	0.2
μ_{d_3}	0.1	-0.1	-1.1	0.8	-0.8
K_G	-0.6	-0.8	6.6	0.5	1.9
SN ratio	-4.8	-22.7	-1.3	-18.8	2.8
σ_M	2.3	21.3	4.0	17.8	-1.9
–					
σ_C	2.2	2.0	2.0	2.1	1.8
N	8321	9924	9236	8485	12222

TABLE 5.2 (continued)

CROSS-CORRELATIONS FOR PSR0833-45[a]

	Timing Model Number				
	20	22	24	26	28
μ_1	0.4	2.0	5.4	-1.0	1.3
μ_2	0.2	-1.4	0.1	-4.9	1.4
μ_3	0.3	-1.8	0.7	-4.1	0.0
μ_{d_0}	0.6	2.5	6.9	-3.2	4.8
μ_{d_1}	0.4	2.4	6.3	-1.5	2.0
μ_{d_2}	0.3	-1.1	0.6	-4.9	1.7
μ_{d_3}	0.3	-1.8	0.9	-4.1	0.2
K_G	0.6	-0.3	2.5	-13.8	5.4
SN ratio	0.9	-0.7	-0.4	-13.5	-3.1
σ_M	2.1	8.6	-1.7	11.6	4.3
–					
σ_C	1.6	2.4	2.5	2.7	2.2
N	15126	6921	6364	5215	7968

Notes:

The tabulated values (except for those in the last row) are correlation coefficients (expressed in units of 10^{-2}). The first 7 parameters in the left hand column are the pulse shape parameters defined in section 5.4. The other parameters are; SN ratio = pulse signal-to-noise ratio, σ_M = theoretical measurement uncertainty, N = number of observations, and σ_C = 95% confidence limit.

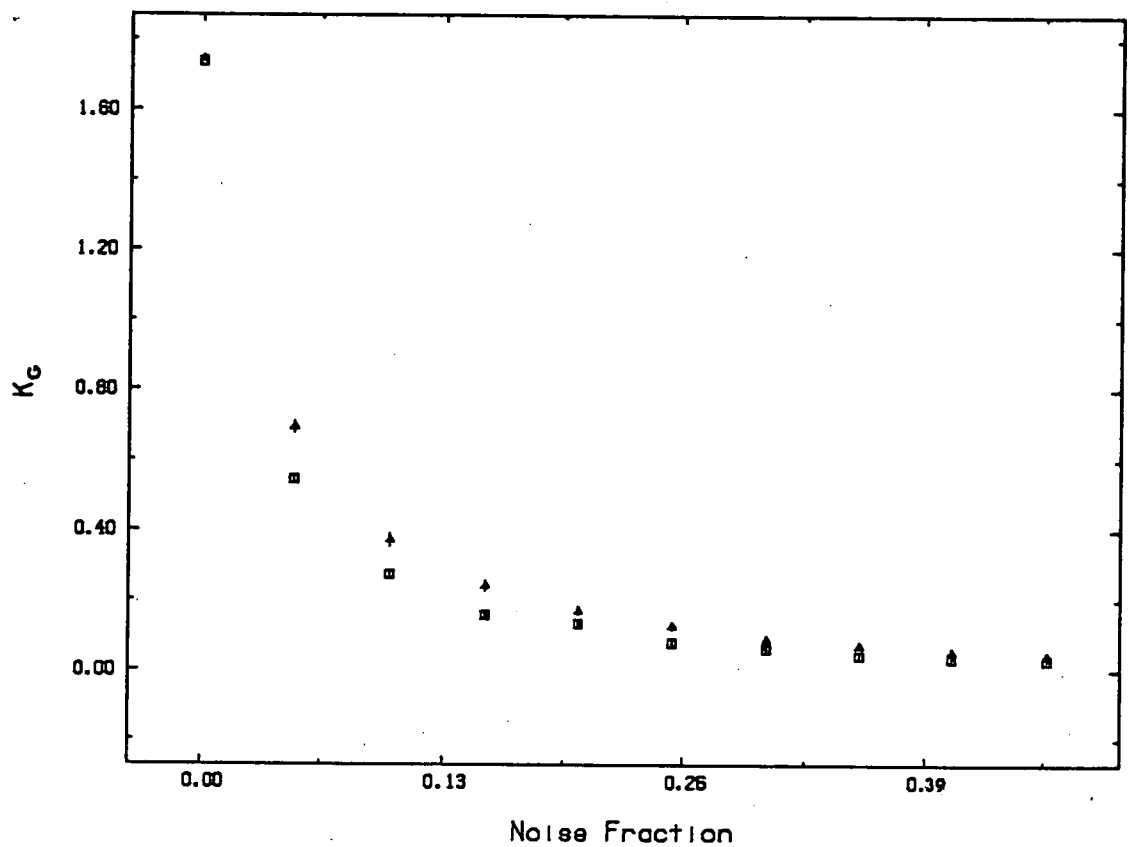

Fig. 5.7. Simulations of the influence of white noise on the determination of the pulse shape parameter K_G. Plotted are the results for simulations based on 635 MHz (*squares*) and 954 MHz (*triangles*) templates. For large noise levels (low SN ratios), the perimeter length tends towards being underestimated.

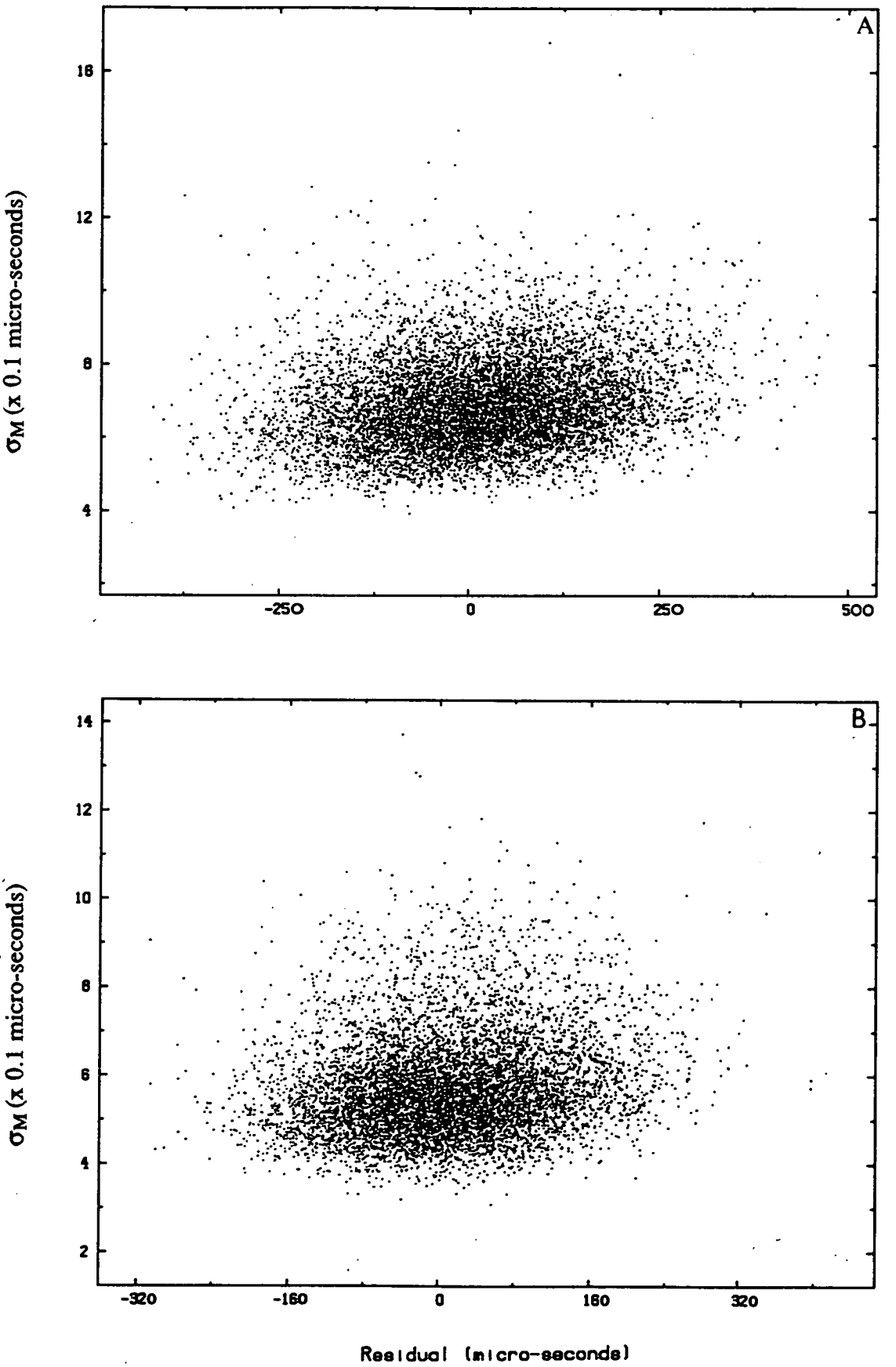

Fig. 5.8. Scatter diagrams from the cross-correlation analysis. (a) and (b) - measurement uncertainty σ_M against residual for spindown models 6 and 8 respectively.

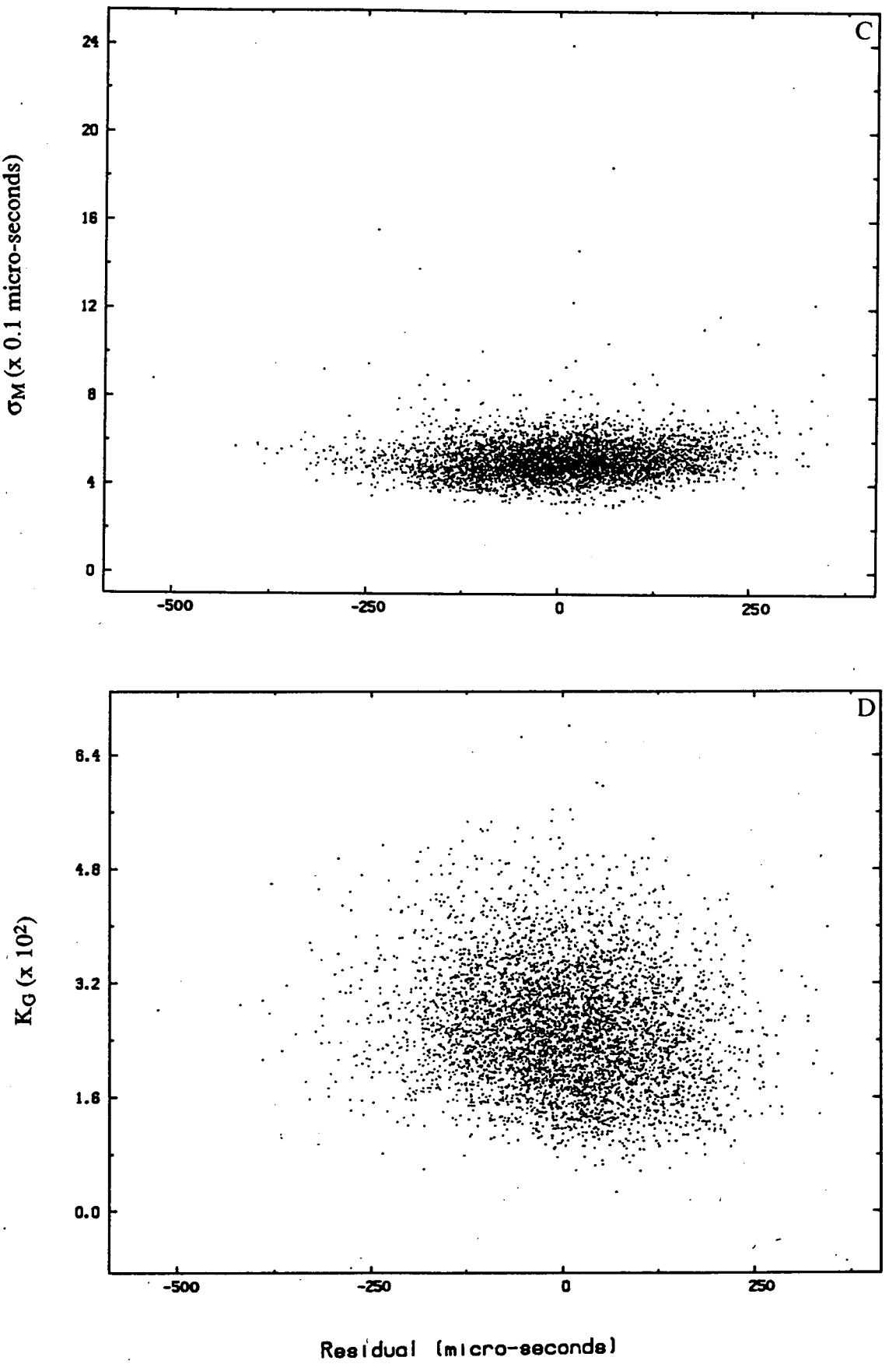

Fig. 5.8. (continued) Scatter diagrams from the cross-correlation analysis. (c) and (d) - measurement uncertainty and perimeter parameter K_g, respectively, against residual for model 13.

5.6 DISCUSSION

From section 4.11, pulse jitter was estimated as contributing rms fluctuations of order 20μs to each arrival time, while the dispersion fluctuation was estimated to be below 1 μs. From the simulation of section 4.6, the uncertainty of the correlation procedure was found to be less than 10μs over the range of typical SN values encountered[c]. The root-square sum of the three aforementioned white noise amplitudes is a factor of 2 to 3 less than the typical value of excess noise given by equation 5.2. DK-P found that the rms excess phase noise in the JPL timing data was 25 μs as compared with the 40-100 μs rms excess observed in the LRO data.

DK-P discussed possible origins for the excess phase noise in terms of fluctuations of the radiation beaming angle, the rotation frequency parameters, dispersive and geometrical scattering delays, and instrumental effects. The plausibility of an association of the observed excess with any of these processes was made difficult by their observation of an apparent positive autocorrelation of the phase residuals on short timescales. There is no convincing evidence for this behaviour in the LRO data, although where weak correlation is evident, it is of the positive sense. The measurement uncertainty of the LRO and JPL timing observations differ by a factor of approximately 8 owing to the higher sampling rate and (presumed) larger SN ratio achieved at the latter observatory. It is conceivable that the higher LRO measurement uncertainty overwhelms any underlying autocorrelation.

In order to account for the excess noise in terms of rotational variability, either of the fractional changes $|\Delta\nu/\nu| > 10^{-7}$ and $|\Delta\dot{\nu}/\dot{\nu}| > 10^{4}$ occurring on the timescale of an integration would be required. Both of these magnitudes significantly exceed the fractional jumps accompanying a typical glitch. The excess phase noise evidently scales with fluctuation frequency 1/T in a manner distinctly different to that of phase noise σ_{TN} on timescales exceeding one day. Cordes, Downs, and Krause-Polstorff (1988) have estimated $\sigma_{TN} \sim 320\ (T/300)^{1.5}$ μs for $T \leq 300$ days.

In terms of possible origins for the excess noise in Vela's magnetosphere, a spatial variation of ~ 20 km for the location of the emission site is suggested. This change is a factor of 5×10^{-3} less than the light-cylinder radius, and not unreasonable. Alternatively, the axis of the radiation beam would be required to vary in longitude by ~0.3°.

---

[c] This conclusion was reached by examination of the confidence limit of the difference between the observed and theoretical phase error between SN ~ 5 and SN ~ 20 for the simulation discussed in section 4.6.

Timing noise of rms amplitude 60μs would arise if the centre frequency of the receiver fluctuated about the nominal value of 635 MHz by ~ 30 kHz. The autocorrelation analysis suggested that the timescale of any such fluctuations would be on the order of minutes or less. The phase of the receiver's local oscillator was coherent with that of the Rubidium standard.. The stability of the standard on the timescale of minutes was examined with the aid of the phase-tracking VLF receiver. It was confidently predicted that fluctuations of the LO frequency would be less than 10 Hz due to 1/f noise on the 1 MHz reference output of the standard. An additional source of oscillator frequency changes would be the presence of noise on the oscillator control voltage. Through careful construction, considerable noise immunity was achieved. Based on measurements of the rms amplitude of control voltage fluctuations on the timescale of an integration, LO frequency changes of less than 1 kHz were expected.

Accurate knowledge of the commencement time of each integration at the microsecond level was assured by the construction of the timing hardware and its software interface.

At 635 MHz, a dispersion measure change of rms amplitude 6×10^{-3} pc cm^{-3} would give rise to the noted excess noise. Taking the transverse velocity of the pulsar relative to the scattering medium as ~ 50 km s^{-1} (table 1.1) and a fluctuation timescale of < 1 hour, then plasmoids of linear dimension ~ 10^{-3} pc, electron number density > 10^6 cm^{-3} and mean space density 2×10^{13} pc^{-3} throughout the line of sight would be required. The matter density value is far in excess of that expected for inertial turbulence at the proposed spatial scale, for which the fractional density fluctuation anticipated on the basis of measured scintillation parameters is $\delta n_e/n_e \sim 10^{-3}$ (Rickett, 1970). Given the separation of the observing frequencies used in the LRO and JPL timing programmes, any dispersion-related timing fluctuations in the LRO data would be expected to be a factor 14 larger than those in the JPL data. This scaling is a factor of ~ 4 greater than what was actually observed.

From results in table 7.3 which relate to LRO dual frequency observations, the magnitude of the excess noise σ_E at 635 MHz was 86±18 μs while at 954 MHz it was 50±12 μs. From DK-P, the excess noise at ~ 2.4 GHz was 24±4 μs. From the aforementioned results, the following power law dependence of σ_E (μs) on observing frequency f (GHz) was obtained :

$$\sigma_E = 54 \pm 7 \; f^{-0.9 \pm 0.2}$$

The magnitude of the correlation coefficient for the fit was 0.99. If the excess noise is due to changes of the longitude of the emission beam, then this scaling may in part be due to field line curvature and aberration.

The origin of the systematic behaviour apparent in figure 5.6 is unclear. One can only speculate that if this behaviour reflects a natural process, then the possibility of time-dependent spatial fluctuations of the emission source deserves consideration. A long series of precision measurements are required to test the stability or otherwise of the excess noise component.

5.7 CONCLUSIONS

The short timescale behaviour of the LRO data has been investigated and the following conclusions are drawn.

The phase noise on timescales less than one day is evidently white with a strength that is approximately a factor of ~1.5 greater than that expected simply through consideration of estimated uncertainty of each arrival time measurement. There is no strong evidence for short timescale correlated phase noise claimed by DK-P, although the level of the LRO measurement noise may preclude its clear identification.

None of the possible explanations for the excess noise proved to be convincing, although instability of the location and beaming angle of the radiation were favoured without a detailed investigation of the implications for the emission models. There was an indication that the level of phase noise has a power-law dependence on the observation frequency with a spectral index of -0.9±0.2. The possibility of a measurement-related origin was considered unlikely.

An aim of a future study would be to use high resolution single pulse observations to examine excess phase noise on a hierarchy of timescales, and its influence on pulse shape. Confirmatory observations of the frequency scaling of the excess noise suggested in the previous section are also required. In addition, the long-term behaviour of the excess noise should be examined.

CHAPTER 6 - THE ANALYSIS OF THREE GLITCHES

6.1 INTRODUCTION

In this chapter, analyses of Vela pulsar glitches 5, 6, and 7 which were observed in October, 1981, August, 1982, and July, 1985, respectively, are presented.

The work has addressed several aspects of the glitch phenomenon. Firstly, the adequacy of the existing models that have been employed to describe the post-jump relaxation have been examined. Significantly, because vital observations were secured within a day of each of the glitches, important new information was available on short-term effects. This has allowed the examination of the post-jump timing behaviour with unprecedented resolution. In addition, it has also been possible to examine the characteristics of the pulse radio emission at the time of the glitch with the aim of identifying any significant changes.

In order to fully exploit the LRO data set, additional information has been obtained from other observatories; attention is drawn to this fact as appropriate. An analysis of of glitch 5 has been published by McCulloch *et al.* (1983) while a preliminary comparison of parameters relating to the modified two-component model (described in section 6.5) for glitches 5, 6, and 7 has been provided by McCulloch *et al.* (1985). Cordes, Downs and Krause-Polstorff (1988) have presented an analysis of glitches 5 and 6 using JPL data.

This chapter opens with a description of the isolation of data pertaining to glitches (section 6.2) and moves to the presentation of data on precursor timing activity and pulse characteristics in sections 6.3 and 6.4 respectively. The glitch models that have evolved from the two-component and vortex-creep theories are then applied to the data in the remaining four sections.

6.2 IDENTIFICATION OF GLITCHES

As noted in section 4.9, each glitch was followed by an anomalous drift (of up to -33 milliperiods per hour) in the local pulse phases prior to the adjustment of the observing ephemeris. The time at which the effect of a glitch was first manifest in the data was readily identified by simply examining the behaviour of the local phase values. Unfortunately, none of the three glitches described herein occurred while

timing observations were being conducted. The epochs of the last preglitch and first postglitch barycentric arrival times are presented in table 6.1.

TABLE 6.1
EPOCHS OF PRE- AND POST-GLITCH ARRIVAL TIMES

Observatory	Glitch Number	Barycentric Arrival Times (TJD)	
		Last Pre-Glitch	First Post-Glitch
LRO	5	4888.4196	4889.3055
	6	5191.5897	5192.5568
	7	6257.7284	6260.5532
HRAO	7	6257.0046	6258.0175

Of initial importance for the fitting of glitch timing models to the data was the evaluation of a set of candidate jump epochs. A short span of compressed data (~8 points per day) prior to each glitch were fitted with a cubic phase model to obtain a preliminary secular trend. Glitch 5 occurred only 3 days after the commencement of the LRO timing programme. As a result, there were insufficient data for an adequate fit of a pre-glitch model. Fortunately, contemporary timing measurements were conducted at approximately weekly intervals using a 26m NASA dish at Tidbinbilla (Manchester *et al.*, 1983); Dr. R.N. Manchester kindly provided local arrival time data which were then used to evaluate the secular trend.

A preliminary set of phase residuals was obtained for each glitch by applying the appropriate pre-glitch secular model to the data spanning an interval of a few days either side of the jump. For each set, a candidate jump epoch was then evaluated by solving the extrapolations of linear equations fitted to the pre- and post-glitch residuals, as illustrated in figure 6.1. An estimate of the frequency jump $\Delta\nu$ associated with each glitch was provided by the gradient of the trend in the post-jump residuals.

In the case of glitch 7, the LRO post-glitch observations were sufficiently sparse to cause an ambiguity in pulse numbering. After appropriate adjustment for integral phase slippage, 5 possible candidate epochs were obtained (McCulloch *et al.*,

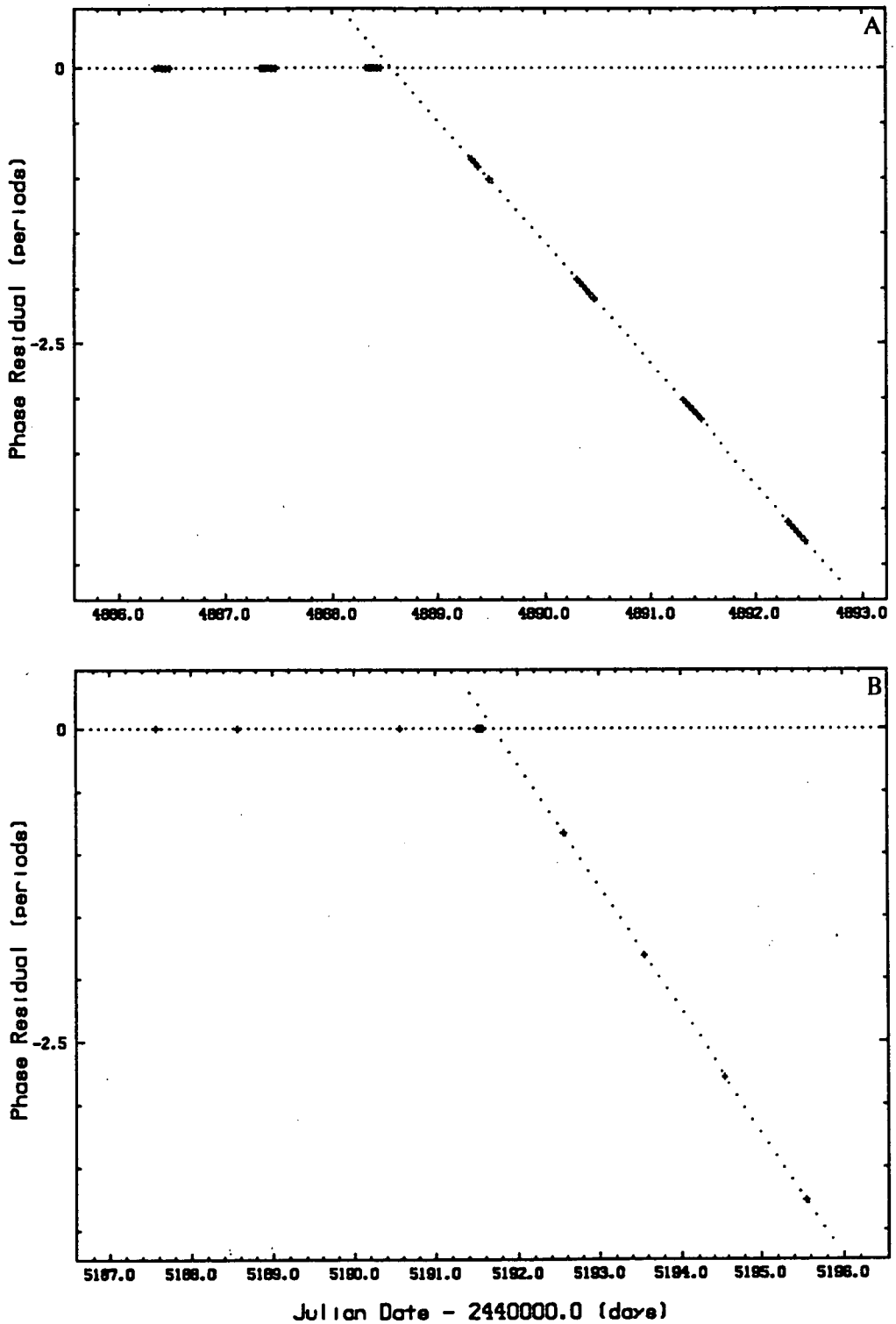

Fig. 6.1. The estimation of candidate glitch epochs for (a) glitch 5 (b) and glitch 6. Quadratic secular polynomial fits were made to the data prior to each jump. The linear trends in the pre- and post- jump residuals were then solved to yield an approximate jump epoch. Compressed data (~ 8 points per day) have been used in estimating the epochs. The extrapolations of formal linear fits are also shown.

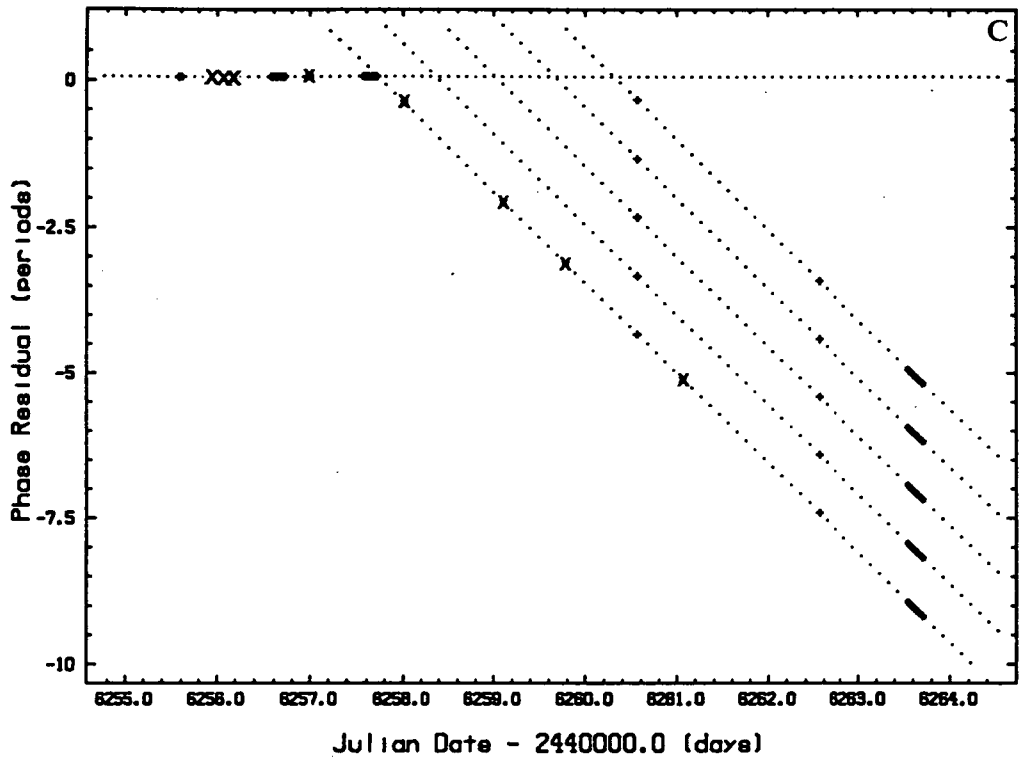

Fig. 6.1. (continued) The estimation of candidate glitch epochs for (c) glitch 7 based on LRO (*crosses*) and HRAO data (*diagonal crosses*). Note the close proximity of the unambiguous jump epoch to the last pre-glitch LRO observations.

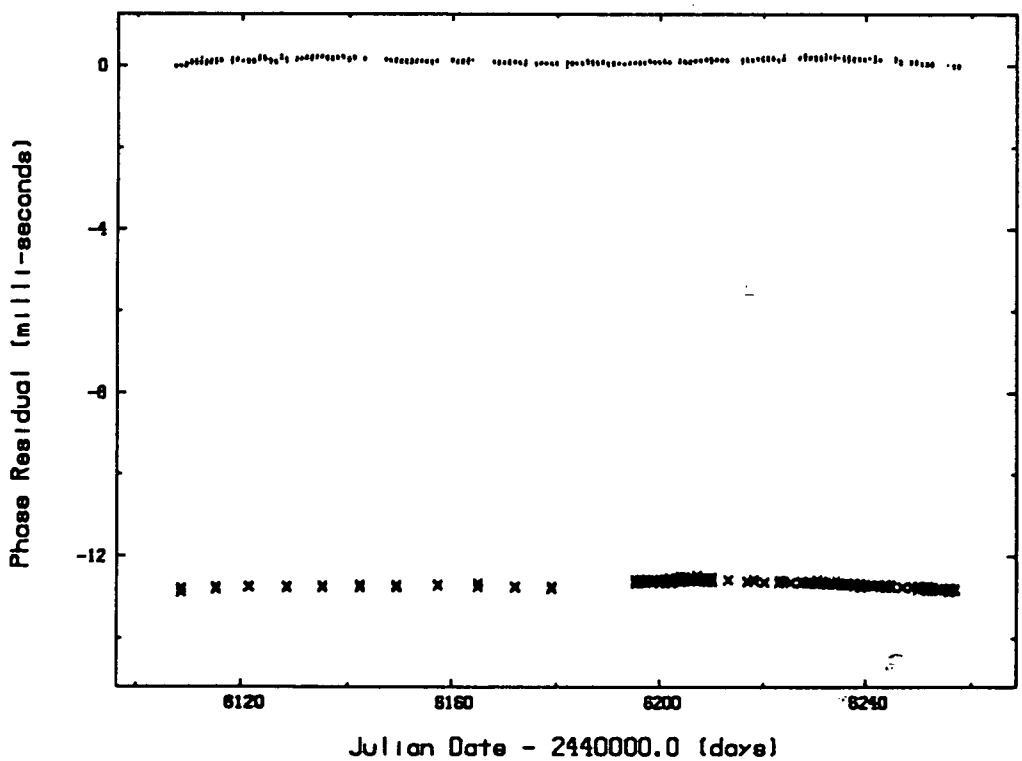

Fig. 6.2. LRO compressed data (*points*) for a 150 day span prior to glitch 7 have been fitted with a cubic polynomial. Residuals for HRAO data for the same span are also shown (*crosses*). They appear offset from the LRO data by ~ -0.0128 s.

1987). Fortunately, HRAO timing data were collected on the important post-jump days when LRO data was lacking which enabled the validity of the epochs to be assessed.

The use of this second data set was made with caution. The HRAO data were supplied as local arrival times corrected for clock offsets and drift. As for the LRO data, these were converted to barycentric times assuming DM = 69.08 pc cm^{-3}. Phase residuals were obtained from a set of pre-glitch HRAO data via the application of a cubic phase model fitted to an equivalent span of LRO times. This revealed the presence of a relative phase offset between two data sets (figure 6.2). After considering possible instrumental and ephemeris contributions to the discrepancy, it was concluded that a large portion of the offset was due to dispersion delay not accounted for in the conversion of arrival times to infinite frequency using the catalogued DM value. This aspect is further discussed in section 7.5.

Initially, the HRAO times were adjusted by -12.839 ms so that the residuals overlapped with those of LRO immediately prior to glitch 7. Significantly, the new data immediately suggested the viability of an epoch close to the time of the final LRO pre-glitch observation; this had initially been rejected because the extrapolations of residuals placed the epoch within the final LRO session.

The candidate epochs and jump magnitudes are presented in table 6.2. Notably, the candidate epoch for jump 5 was the first such unique parameter obtained for any pulsar glitch. Additionally, the epoch evaluated for jump 7 suggested that the glitch occurred tantalizingly close to the end of the LRO session of 11 July, 1985.

To illustrate the influence of glitches on the evolution of the pulse frequency, fits were made to ν over each pair of adjacent observing sessions; the results are presented in figure 6.3.

6.3 IMMEDIATE PRE-GLITCH BEHAVIOUR

Of particular interest is whether pre-glitch measurements contain any information as to the immanence of a glitch. This aspect was approached by examining the preglitch residuals for evidence of short-timescale deterministic behaviour. The cubic timing model obtained from the Tidbinbilla observations (model 33) was applied to the timing data for the three LRO sessions prior to glitch 5. For glitches 6 and 7, pre-jump fits were made to compressed data over spans of approximately 54 and 75

TABLE 6.2

CANDIDATE GLITCH EPOCHS AND MAGNITUDES

Number	Epoch		Magnitude	
	TJD	UT	$\Delta\nu$ ($\times 10^{-5}$ Hz)	$\Delta\nu/\nu$ ($\times 10^{-6}$)
5	4888.56	11 OCT 81	-1.3	1.1
6	5191.70	10 AUG 82	-1.1	1.0
7a[a]	6257.73	11 JUL 85	-1.8	1.6
7b	6258.36			
7c	6259.01			
7d	6259.66			
7e	6260.34			

[a]Obtained by incorporating HRAO data

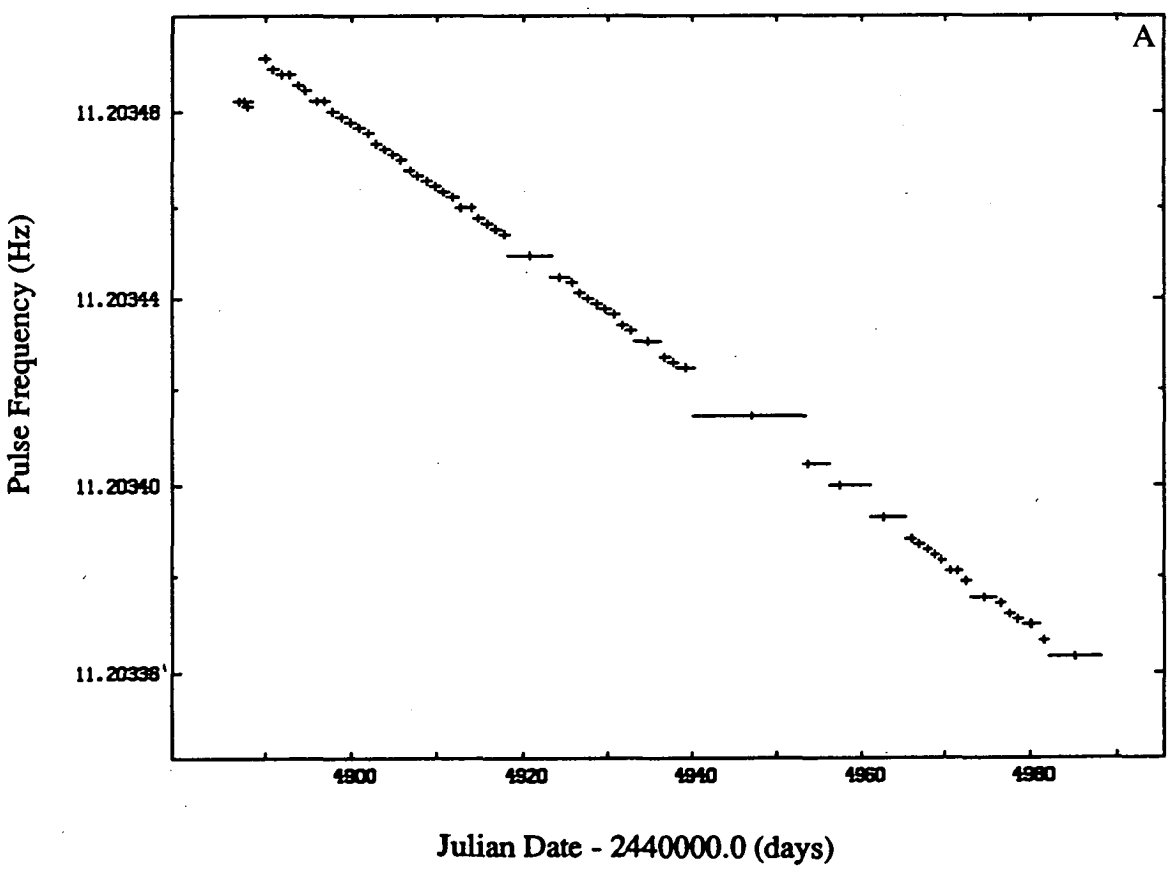

Fig. 6.3. Pulse frequency as a function of epoch obtained from linear spindown model fits to arrival times from pairs of adjacent sessions; (a) illustrating glitch 5. Each horizontal bar defines the fitting span. Each vertical bar is 2×10^{-6} Hz in length; the typical 95% confidence limit on each estimate is less than $\pm10^{-8}$ Hz.

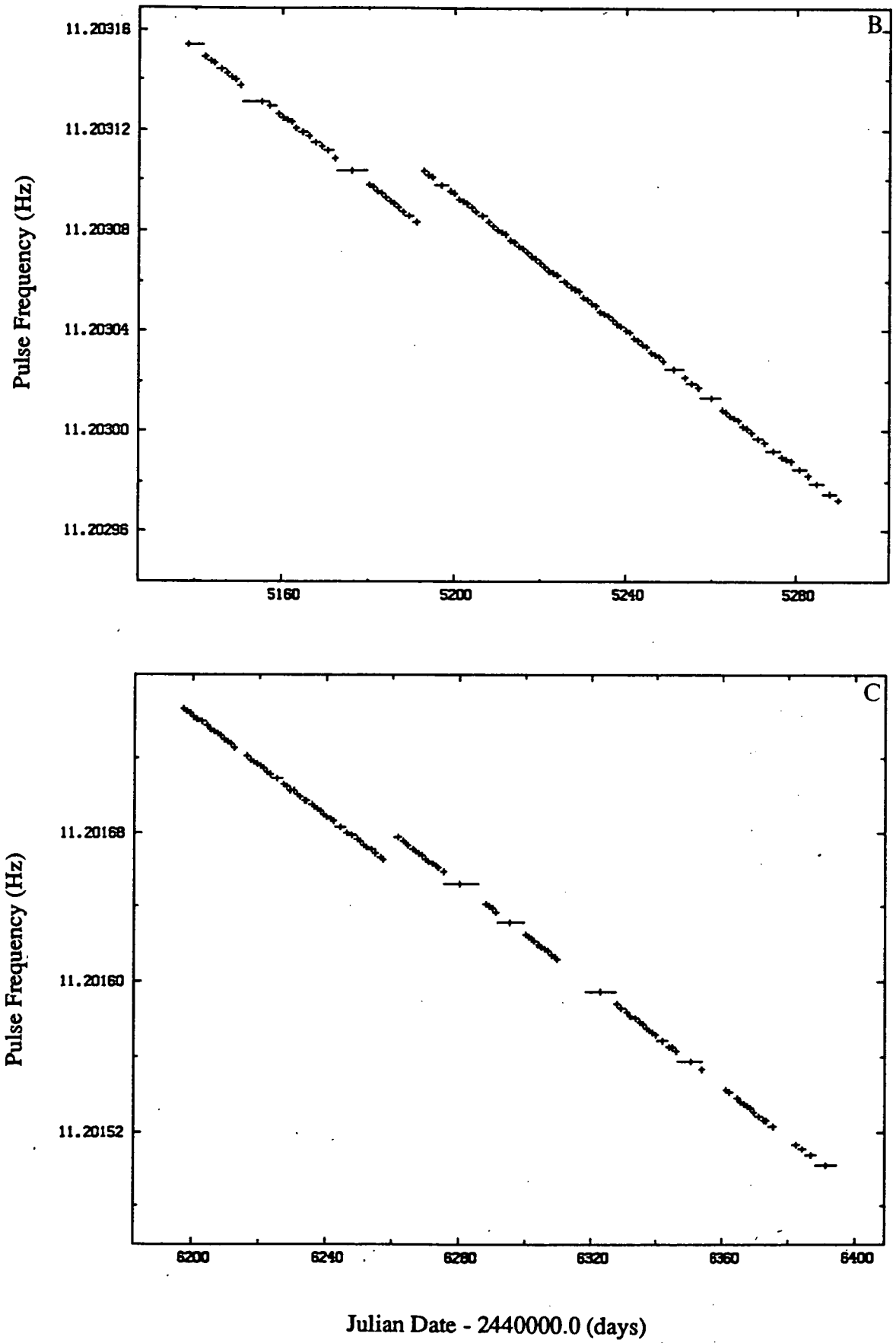

Fig. 6.3. (continued) Pulse frequency as a function of epoch obtained from linear spindown model fits to arrival times from pairs of adjacent sessions; (b) illustrating glitch 6, (c) illustrating glitch 7.

days respectively. Details of the fits are provided in table 6.3. The residuals for the immediate pre-glitch sessions are presented in figure 6.4.

The probability density function (PDF) was evaluated for the residuals of each immediate pre-glitch session using the method described in section 5.3. Each PDF was compared with a normal distribution having the same second moment and area through the calculation of a reduced χ^2 statistic. The results presented in table 6.4a and figure 6.5 indicate that each distribution is normal. The behaviour of the auto-correlation functions (section 5.5) shown in figure 6.6 provide further confirmation of the stochastic nature of the residuals.

The residuals were also subjected to three types of runs test. If n contiguous residuals $\{R_i\}$ satisfied a specific condition, they were regarded as forming a *run* of length n. The conditions used were ;

test A - relative runs :	$R_i > R_{i-1}$,	$R_i < R_{i-1}$	$(2 \le i \le n)$
test B - mean runs :	$R_i > \bar{R}$,	$R_i < \bar{R}$	$(1 \le i \le n)$
test C - median runs :	$R_i > R_{med}$,	$R_i < R_{med}$	$(1 \le i \le n)$

where $\bar{R}$ and R_{med} are the mean and median, respectively, of the residual set. Only the contiguous residuals of appropriate session were used. From each residual, the mean value over the session was subtracted. For glitches 5 and 7, three and five consecutive pre-glitch sessions, respectively, were pooled without regard for the influence of boundary values. Tallies were made of the number of occurrences of runs of length 1 to 9 for each of the conditions above using the residuals of pooled and individual sessions. Runs of length > 9 and < -9 were combined into single tallies. Runs tallies were also obtained for 5×10^4 and 160 gaussian random numbers. All of the distributions are compared with their theoretical expectations in the figures of Appendix K.

The theoretical and observed distributions were compared through the calculation of χ^2 and z statistics (as appropriate) as described in Appendix K. The results (table 6.4b) are somewhat inconclusive. In general, the residuals of the final pre-glitch sessions show more evidence of deterministic behaviour. However this observation can also be made for the simulations involving gaussian random numbers.

TABLE 6.3

PARAMETERS FOR PRE-GLITCH FITS[a]

Glitch (model)	Data Type[b]	ν (Hz)	$\dot{\nu}$ ($\times 10^{-12}$ Hz s^{-1})	$\ddot{\nu}$ ($\times 10^{-22}$ Hz s^{-2})	Fit Epochs (TJD) Mid	Range	Residual rms (μs)	n_B[c]
5 (33)	180T	11.2036049179±4	-15.5878±2	3.9±5	4795.8399000	4704.1-4887.5	7	18±2
6 (34)	54C	11.2031165806±2	-15.6305±1	19.8±3	5166.6505557	5137.8-5191.6	82	91±2
7 (35)	75C	11.20171872631±2	-15.60765±1	11.4±2	6217.8298453	6182.8-6257.7	34	52±1
7 (36)	75H	11.20171055088±2	-15.60713±1	6.5±2	6223.8931904	6179.1-6257.0	32	30±1
7 (37)	150C	11.20177117762±1	-15.610583±3	8.05±3	6178.9381016	6107.0-6257.7	128	37±0.2
7 (38)	150H	11.20171834188±1	-15.607592±8	8.57±3	6218.1154331	6108.3-6257.0	35	39±0.1
7 (39)	300C	11.20184805549±1	-15.613811±1	6.612±5	6121.9452433	5957.4-6257.7	107	30±0.02
7 (40)	300H	11.20177098818±2	-15.610372±5	6.87±1	6179.0790402	5961.8-6257.0	156	32±0.05
7 (41)	600C	11.20207664360±1	-15.623711±1	6.728±1	5952.5532653	5657.2-6257.7	1534	31±0.005
7 (42)	600H	11.20191604527±2	-15.616763±2	6.750±3	6071.5510247	5702.4-6257.0	254	31±0.01

[a] Errors are ± 1 σ in the last digit.

[b] Data types : C = compressed ~8 points per day, T = Tidbinbilla, H = HRAO. The number prefixing each data type indicator is the approximate length of the data span (in days) fitted.

[c] The theoretical braking index, n_B (equation 1.11), is provided using the model parameter values.

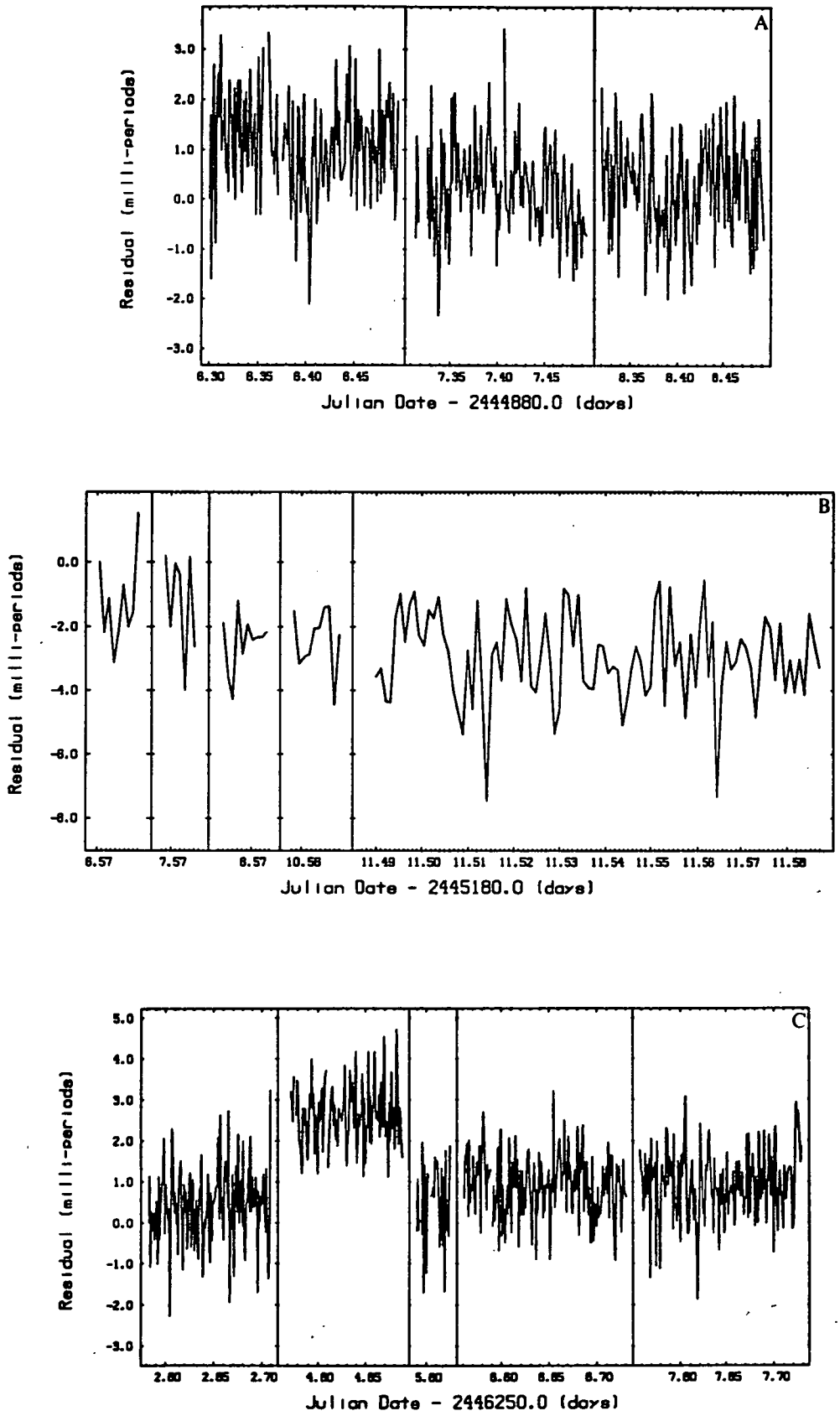

Fig. 6.4. Residuals from the application of cubic spindown models (table 6.3) to timing data prior to (a) glitch 5 (model 33), (b) glitch 6 (model 34), and (c) glitch 7 (model 38). Data for contiguous integrations are joined by line segments. Note the expanded time scale in (c) relative to (a) and (b).

TABLE 6.4

PRE-GLITCH RESIDUALS - TESTS OF NORMALITY AND RANDOMNESS

(A) RESIDUAL DISTRIBUTIONS

Glitch	Central Epoch of Data	Reduced χ^2	$\hat{\sigma}_W$	$\hat{\sigma}_M$
5	4888.4	0.47	89	46±8
6	5191.5	1.33	122	67±12
7	6257.6	0.62	77	55±6

Notes :
The effective degrees of freedom for each reduced χ^2 statistic is 48. The levels of white noise and mean measurement noise (in units of μs) are given under $\hat{\sigma}_W$ and $\hat{\sigma}_M$ respectively. The standard deviation of the pooled $\hat{\sigma}_M$ is also provided.

(B) RUNS TESTS

Glitch	Number of Sessions	Test	χ^2	z	probability
5	1 (3)	A	9.5 (7.4)		0.15(0.29)
		B		-1.5 (0.08)	0.13((0.93)
		C		-1.5 (-0.25)	0.13(0.80)
6	1	A	6.4		0.38
		B		-1.35	0.18
		C		-1.35	0.18
7	1 (5)	A	5.2 (1.7)		0.51(0.95)
		B		0.54 (0.15)	0.58(0.88)
		C		0.54 (0.56)	0.58(0.57)
$5x10^4$ gaussian numbers		A	6.5		0.37
		B		-1.7	0.09
		C		-1.8	0.07
160 gaussian numbers		A	6.3		0.39
		B		0.32	0.74
		C		0.0	1.0

Notes :
The number of consecutive pre-glitch sessions used in the tests are given in the second column. The effective number of degrees of freedom for the χ^2 statistic is 7. The z parameter is discussed in Appendix K. The final column gives the probability of observing the same distribution from a sample of gaussian random numbers.

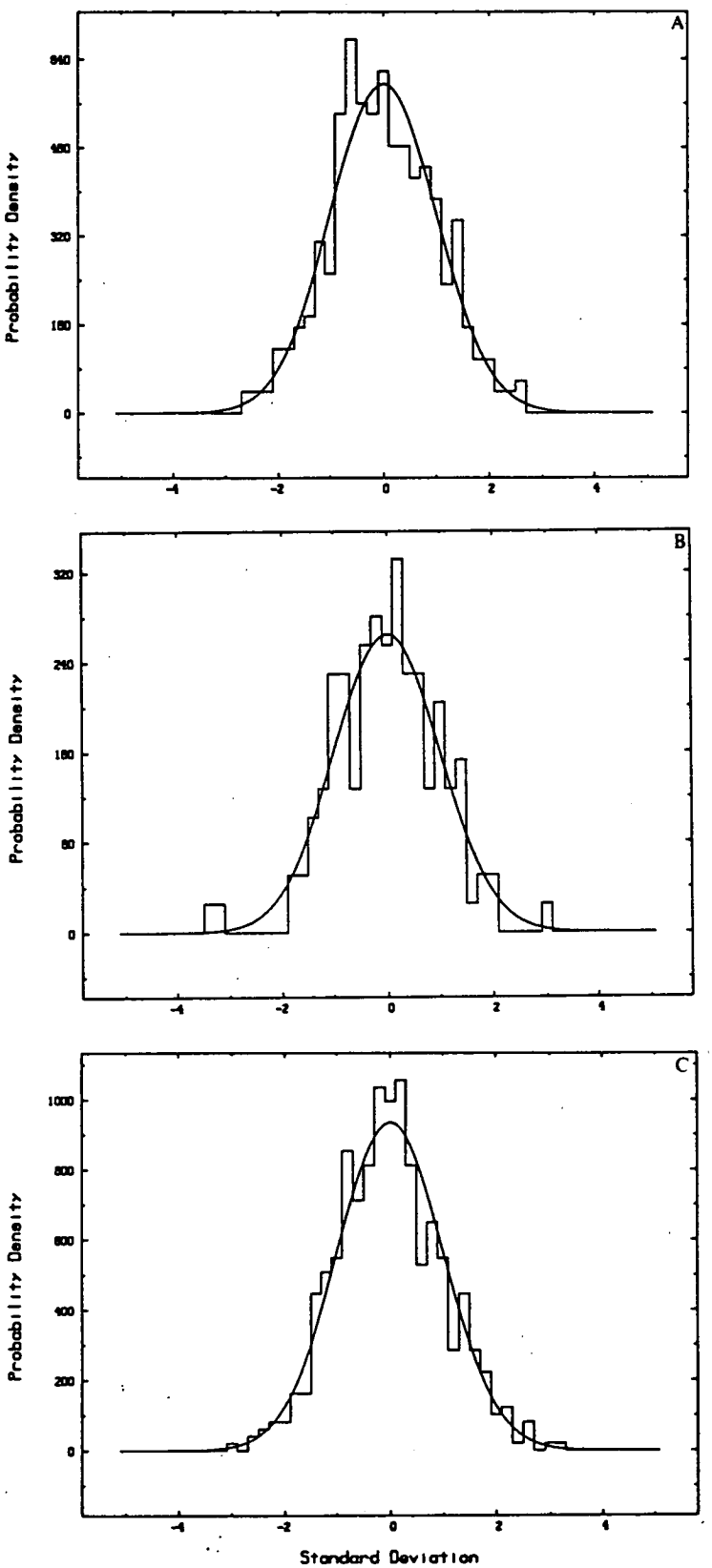

Fig. 6.5. Distribution of residuals for the final session prior to (a) glitch 5, (b) glitch 6, and (c) glitch 7. The probability density is numerically equal to $N\Delta x$, where N is the number of estimates which fall into a bin of width $\Delta r = 0.02\sigma$. Here σ is the standard deviation of the entire population. The values of σ for each plot are : (a) 97 μs, (b) 128 μs, and (c) 102 μs. Superimposed are gaussian functions with the same second moment and area as the corresponding observed distribution.

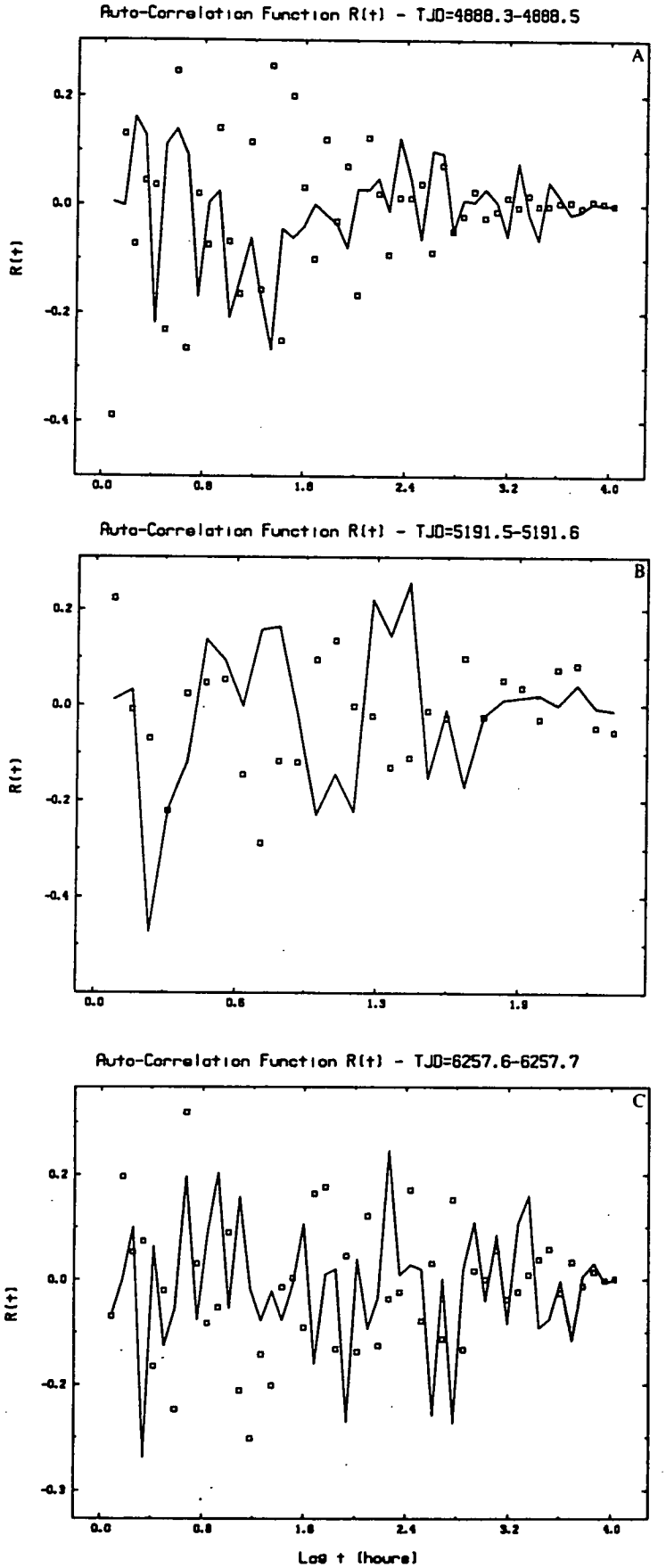

Fig. 6.6. Auto-correlation function (*line*) for the final session prior to (a) glitch 5, (b) glitch 6, and (c) glitch 7. The bin with used is 5 minutes. Gaussian random numbers with the same standard deviation as the pooled residuals have been subjected to the same analysis (*squares*).

6.4 PULSE CHARACTERISTICS

The stability Vela's pulse shape across the epochs of glitches 5 and 7 was also investigated[a]. Mean daily I_x, I_y, and I profiles were formed, and these are plotted in figures 6.7 and 6.8. From an examination of these figures, it is possible to qualitatively rule out gross changes in the pulse polarization characteristics following the glitches. However, a quantitative assessment cannot be made owing to the lack of full polarization information, namely the behaviour of the Stokes parameters as a function of pulse phase. The daily variability of the shapes of the I_x and I_y profiles before and after each glitch epoch is a likely result of temporal changes of the ionospheric rotation measure.

The last pre-glitch and the first post-glitch mean daily profiles are compared in figure 6.9. The I profiles show little difference across each glitch. The absence of significant change is also evident in the plots of the pulse shape parameters as a function of time in figure 6.10. The lack of a distinct glitch-related signature in figure 6.10 attests to the insignificance of the the increased pulse smearing following each glitch due to the discrepancy of the observing ephemeris. This is not surprising given that the observed phase drift rate of -33 milliperiods per hour has an effect equivalent to the convolution of rectangular filter of temporal width 0.21 bins with an unsmeared profile.

6.5 THE TWO-COMPONENT MODEL

In the following four sections, attention turns to the modelling of the post-glitch timing behaviour.

For a glitching pulsar, the pulse phase as a function of time may conveniently be expressed (following the notation of Cordes, Downs, and Krause-Polstorff, 1988) as

$$\phi(t) = \phi_0 + \nu_0(t-t_0) + \frac{1}{2}\dot{\nu}_0(t-t_0)^2 + \frac{1}{6}\ddot{\nu}_0(t-t_0)^3 + \sum_j \{\phi_{n_j}(t)\, U(t-T_{g_j})\, U(T_{g_{j+1}}-t)\} \qquad 6.1$$

The secular parameters ϕ_0, ν_0, $\dot{\nu}_0$, and $\ddot{\nu}_0$ are referenced to the epoch $t = t_0$. Here the subscript j identifies parameters pertaining to the j-th glitch; $\phi_n(t)$ is the phase term which describes a particular n-th glitch model, and T_g is the glitch epoch. The unit step

---

[a] Raw profile data near glitch 6 was not available.

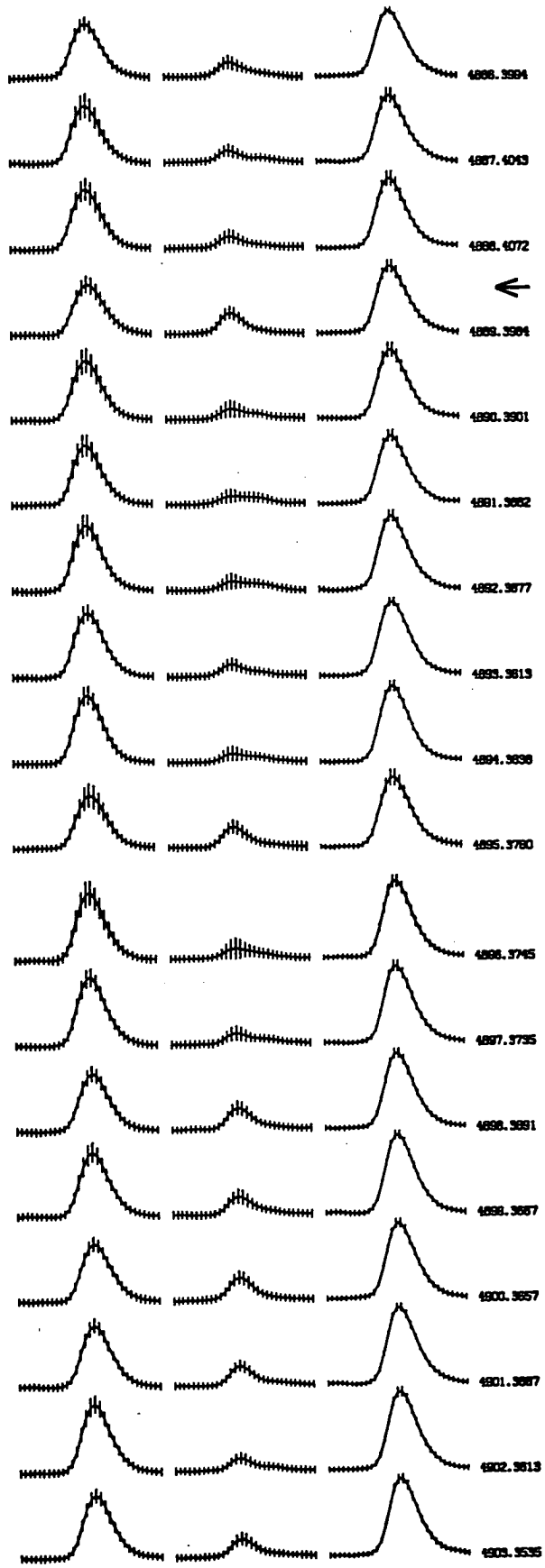

Fig. 6.7. Mean daily I_x, I_y, and I profiles for PSR0833-45 at 635 MHz about the time of glitch 5. Each vertical error bar represents the two standard deviation range of the pooled estimates at each phase bin. The vertical scale is arbitrary, but has been fixed so that the relative heights of the profiles may be compared. The central epoch of the associated observation session (expressed in TJD days) is also shown. The arrow separates pre- and post-glitch sessions.

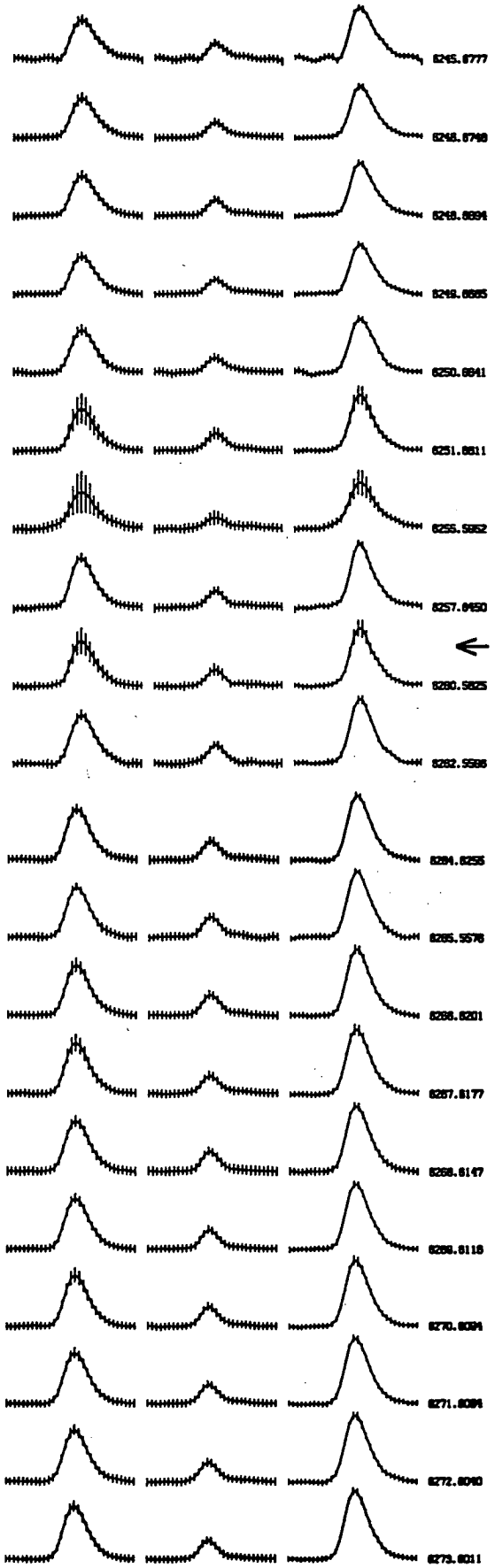

Fig. 6.8. As for figure 6.7, except showing the mean daily I_x, I_y, and I profiles for PSR0833-45 at 635 MHz about the time of glitch 7. It is unclear whether the larger on-pulse variability for the profiles of TJD 6251.6, 6255.6 and 6280.6 relative to other days is due to intrinsic pulse energy variations or significant dish tracking errors.

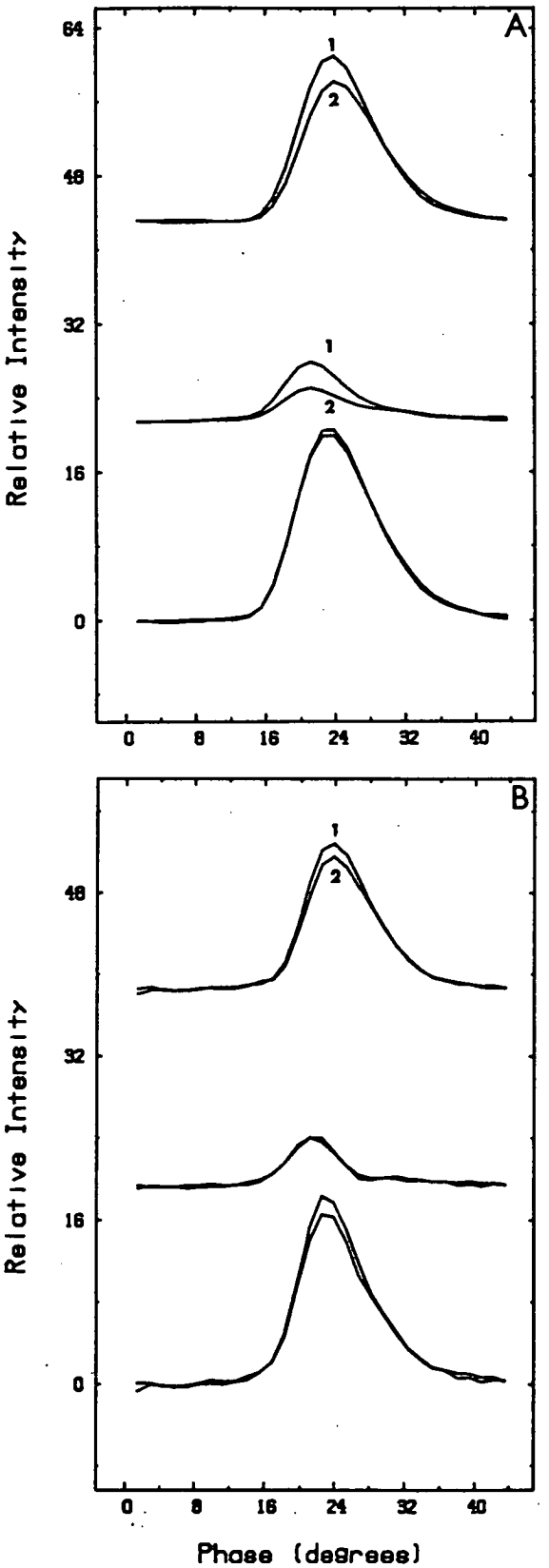

Fig. 6.9. Comparison of mean daily I_x, I_y, and I profiles for PSR0833-45 at 635 MHz for one observation session either side of (a) glitch 5, and (b) glitch 7. The vertical scale has been adjusted so that the off-pulse standard deviation for both I profiles is equal to one unit. The profiles labeled '1' and '2' correspond to observing sessions with central epoch TJD 4888.32 and TJD 4889.59 for (a), and TJD 6257.56 and TJD 6260.57 for (b), respectively.

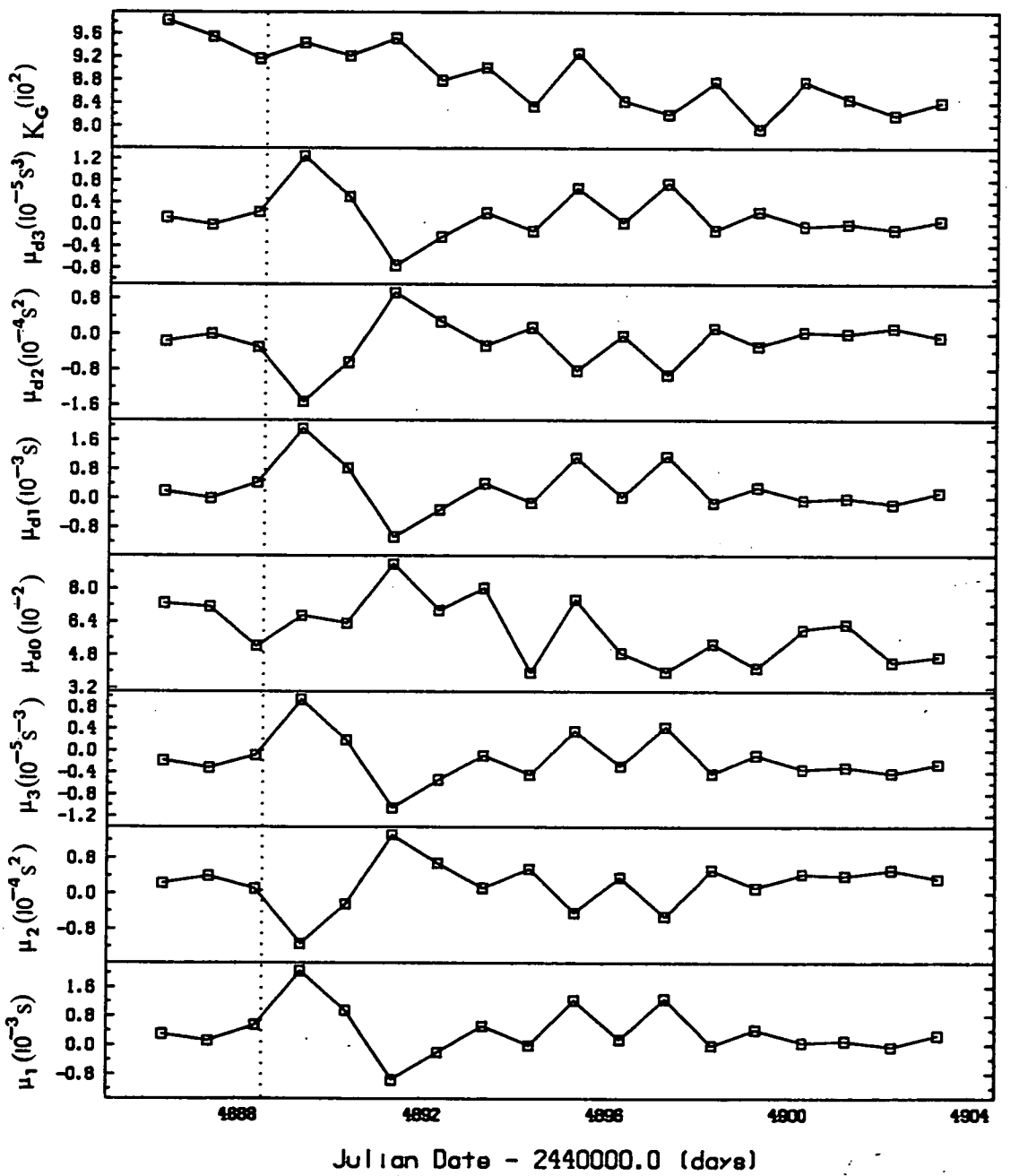

Fig. 6.10a. Pulse shape parameters obtained from mean daily I profiles as a function of time for observing sessions about the time of glitch 5. The dotted line marks the glitch epoch.

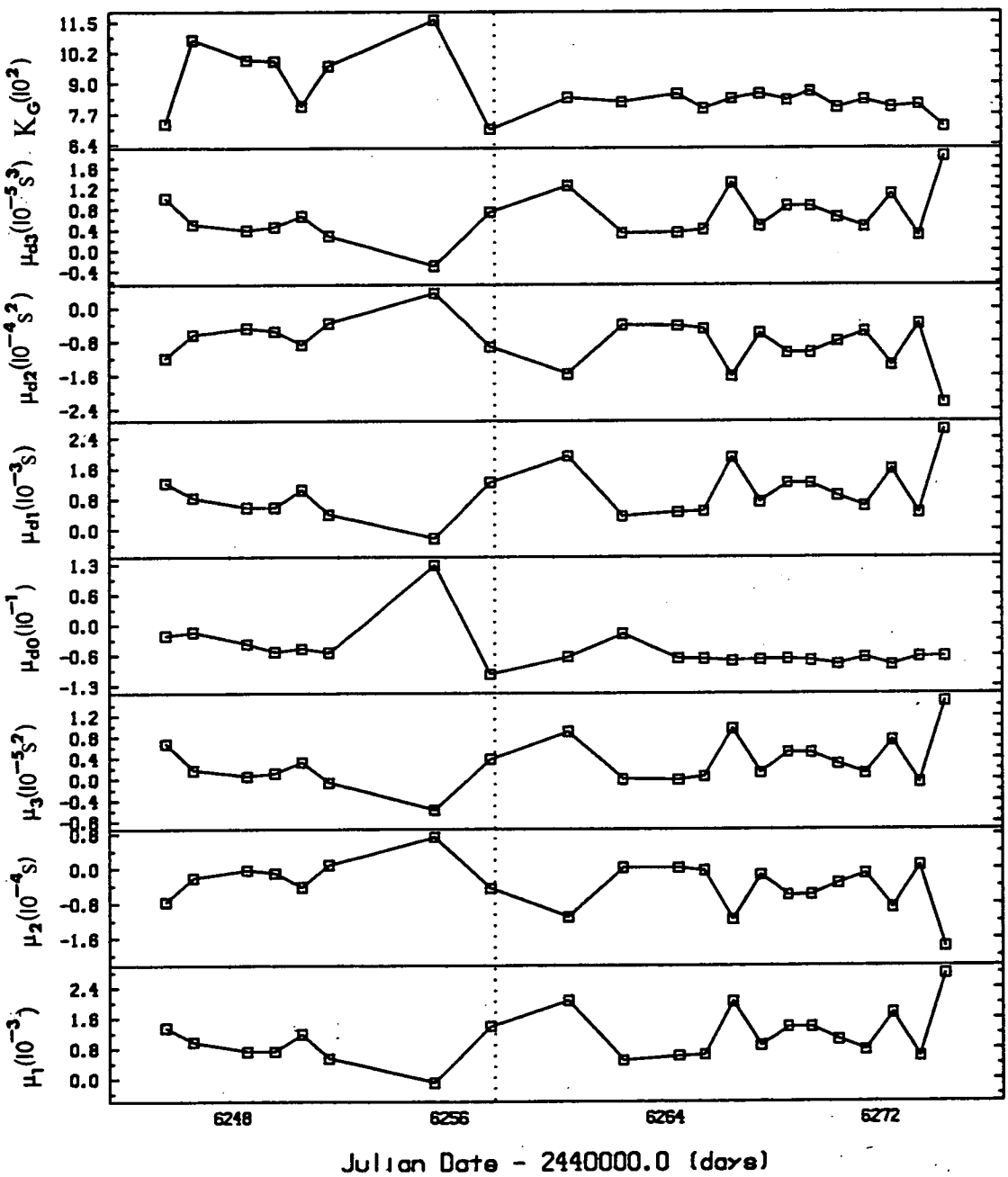

Fig. 6.10b. As for figure 6.10a, except showing the behaviour of the pulse parameters for the mean daily I profile about the time of glitch 7.

function $U(t-T_{g_j})$ restricts the glitch effect to $t \geq T_{g_j}$, while $U(T_{g_{j+1}}-t)$ terminates the relaxation at the time of the next jump, $T_{g_{j+1}}$.

From the two-component model (section 2.5), the glitch phase term ϕ_n may be expressed as

$$\phi_1(t) = \Delta\nu_c(t-T_g) - \Delta\nu_i \tau_i \exp[-(t-T_g)/\tau_i] \qquad t \geq T_g \qquad 6.2$$

where the subscript j has been dropped for clarity, and the subscript 1 denotes the model number. The parameter $\Delta\nu_c$ represents the constant component of the jump in pulse frequency that does not relax, while the second factor expresses the relaxation in terms of an initial amplitude $\Delta\nu_i$ and time-constant τ_i. In the analysis described below, each glitch was treated separately.

The spindown parameters required in equation 6.1 were obtained from the fit of equation 4.12 to an appropriate span of data immediately prior to each jump. The primary aim in choosing the span length was to avoid significant contamination from any non-cubic relaxation associated with the previous glitch, while at the same time ensuring that the accuracy of the parameter values was adequate. A feature of glitch 6 was that it followed glitch 5 by approximately 203 days. This interval was on the order of 1-2 times the typical long time-constant τ_i reported by Downs (1981) for fits of the two-component model to timing data following the first four Vela glitches. The likelihood that the secular behaviour prior to glitch 6 was contaminated by the relaxation from glitch 5 was kept in mind.

Cubic models were fitted to chosen pre-jump epoch spans, and the results are presented in table 6.3 and figure 6.11. Only a single fit was made to the Tidbinbilla data prior to glitch 5 owing to low number of observations available. A problem associated with obtaining secular fits prior to glitch 6 was the lack of LRO data from February through June, 1982, during which VLBI observations were made with the telescope (Preston *et al.*, 1984). The data coverage prior to glitch 7 was nearly complete, and four span lengths were chosen in order to test the influence of the presumed spindown behaviour on the subsequently fitted glitch relaxation models. In addition, fits were made to equivalent spans of HRAO data that were time-corrected as noted in section 6.2.

From table 6.3 it is obvious that the second frequency derivative assumed a significantly different value prior to each glitch. In addition, based on the values of the simple braking index inferred from the model parameters, it is evident that the underlying secular trend is dominated by a process other than simple electrodynamic braking. The value of $\ddot{\nu}$ prior to glitch 6 is a factor of at least ~2 greater than that

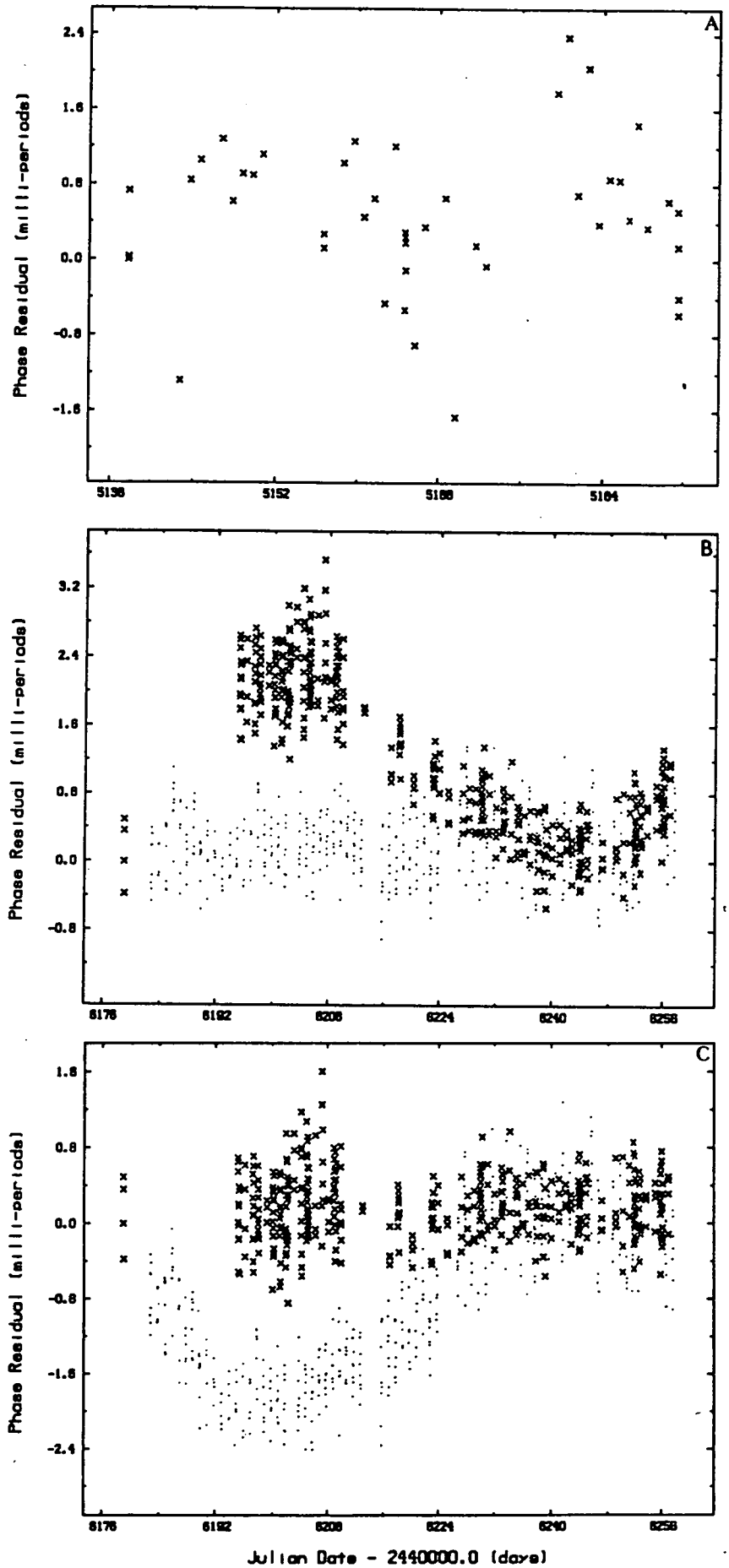

Fig. 6.11. Timing residuals from fits of cubic models to pre-glitch data. The residual values are relative to that of the first observation. (a) From model 34. (b) From model 35 applied to LRO data (*points*), and HRAO data (*crosses*). (c) As for (b) but using model 36.

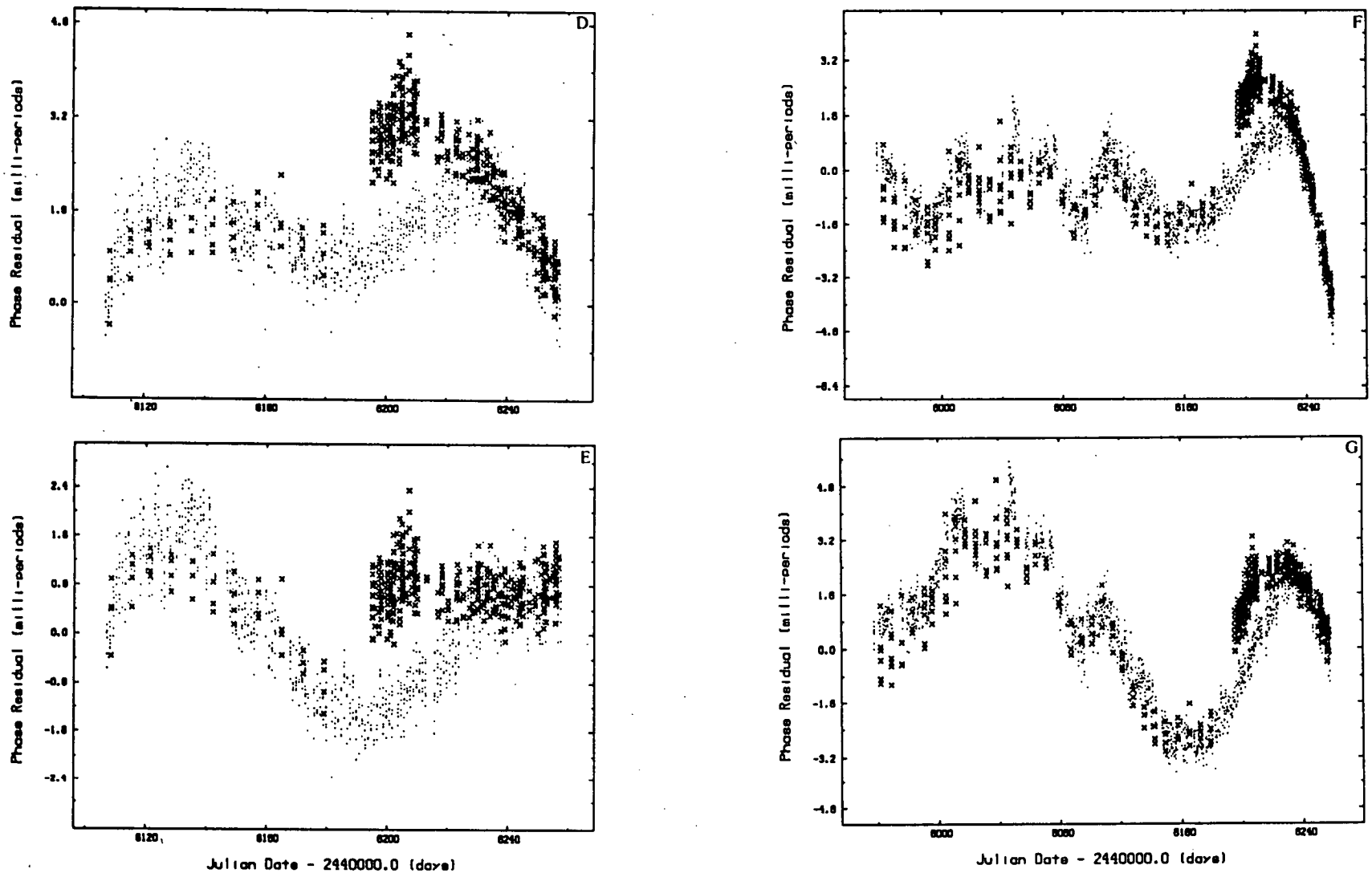

Fig. 6.11. (continued) (d) As for (b) but using model 37. (e) As for (b) but using model 38. (f) As for (b) but using model 39 (note the correlation of the two sets of residuals during the timing activity up until TJD ~ 6180). (g) As for (b) but using model 40.

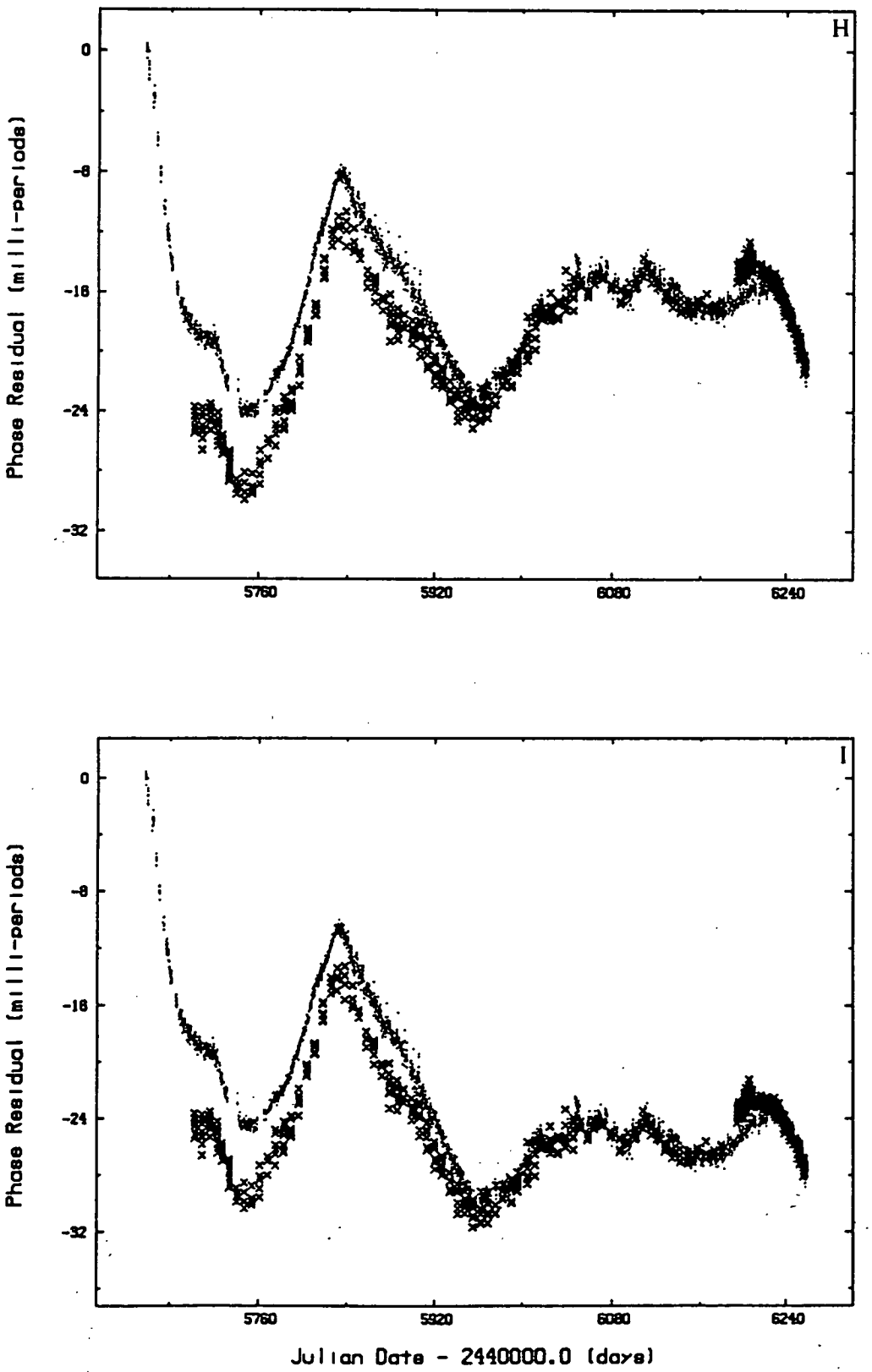

Fig. 6.11. (continued) (h) As for (b) but using model 41. (i) As for (b) but using model 42.

subsequent to glitches 5 and 7, and this was the likely result of the continued relaxation from glitch 5.

A requirement of the two-component model is that long term secular trend is well-behaved up until the glitch epoch. It is apparent from examining figures 6.11b-6.11i that non-stationary timing activity does occur prior to glitch 7. The residuals for both observatories exhibit good correlation over the majority of the fitted epoch ranges, although the difference between the residual sets just prior to glitch 7 slowly increased and then recovered. This behaviour is interpreted as the result of a dispersion measure fluctuation in section 7.6. The slow merging of the residual sets apparent over the initial 300 days of figures 6.11h and 6.11i is interpreted in a similar manner.

Fits were made to medium resolution compressed LRO data for a 50 day span following each glitch in order to obtain parameter values for the set $S_1 \equiv \{\Delta\nu_c, \Delta\nu_i, \tau_i, T_g\}$. The starting values for the fitted parameters were obtained from the combination of data presented in table 6.2 and the model fits made by Downs (1981) to the first four large jumps. The appropriate cubic model from table 6.3 was used as the spindown component of the glitch model. For glitches 5 and 6, the fits converged rapidly, resulting in the parameter values given in table 6.5 and the residuals plotted in figures 6.12a and 6.12b.

For glitch 7, spindown models 35 to 40 of table 6.3 were used, and fits were made to individual and *combined* LRO and HRAO data for the 50 day span following the glitch. However, convergence could not be achieved while at the same time satisfying $T_g > T_L$ (where T_L is the epoch of the last high resolution pre-glitch observation listed in table 6.1) unless the epoch parameter T_g was held constant. This situation was regarded as arising from the inability of the simple single exponential model to adequately describe the relaxation effect, the proximity of the glitch epoch to the last pre-jump observations and the apparent presence of post-jump timing activity. The value for T_g used in the fits was chosen as T_L. Data relating to the combined fits using HRAO pre-glitch secular models fits are presented in table 6.5 while an example of the residuals obtained is presented in figure 6.12c. The parameters obtained from the glitch model fits for various data sets and pre-glitch models of a fixed span length exhibited little variation. However, as can be seen in table 6.5, as the pre-glitch span length was increased, the parameter values systematically changed.

It is readily apparent that considerable short-term structure remains in the residuals of the above fits. In order to investigate the contamination of the process operating this timescale on the long-term relaxation, the data points within a fixed

TABLE 6.5

PARAMETERS FOR SINGLE EXPONENTIAL GLITCH FITS[a]

Glitch[b] (model)	Data Type[c]	$\Delta\nu_c$ (Hz)	$\Delta\nu_i$ ($\times 10^{-6}$ Hz)	τ_i (days)	T_g (TJD)	Post-Glitch Data Range (TJD)	Residual rms (μs)
5 (33)	50C	11.23±3	1.52±3	146±3	4888.5623±3	4889.3-4938.3	68
	50C[d]	10.94±4	1.79±4	179±5	4888.5599±4	4899.3-4938.3	74
	75C[d]	10.84±2	1.87±2	192±2	4888.5588±3	4899.3-4961.2	76
	100C[d]	10.11±3	2.62±3	282±4	4888.5520±5	4899.3-4988.1	109
6 (34)	50C	22.223±5	0.670±3	37.2±7	5192.1285±7	5192.6-5242.5	200
	50C[d]	22.04±1	0.79±1	61±2	5192.1082±9	5202.5-5242.5	62
	75C[d]	21.57±21	1.22±1	124±2	5192.0927±6	5202.5-5267.4	99
	100C[d]	21.05±2	1.71±2	199±3	5192.0819±7	5202.5-5290.4	153

TABLE 6.5 (continued)

PARAMETERS FOR SINGLE EXPONENTIAL GLITCH FITS[a]

Glitch[b] (model)	Data Type[c]	$\Delta\nu_c$ (Hz)	$\Delta\nu_i$ ($\times 10^{-6}$ Hz)	τ_i (days)	T_g (TJD)	Post-Glitch Data Range (TJD)	Residual rms (μs)
7 (35)	50CH	17.128±7	0.786±6	61.5±7	6257.7284[e]	6260.6-6307.9	113
7 (35)	50CH[d]	17.065±5	0.846±5	68.7±6	...	6270.7-6307.9	131
7 (35)	75CH[d]	16.625±1	1.273±8	119±1	...	6270.7-6332.8	247
7 (35)	100CH[d]	16.16±1	1.73±1	175±2	...	6270.7-6356.7	334
7 (37)	50CH	17.189±7	0.731±7	56.1±8	...	6260.6-6307.9	113
7 (37)	50CH[d]	17.123±6	0.793±6	63.9±7	...	6270.7-6307.9	151
7 (37)	75CH[d]	16.735±8	1.168±8	108±1	...	6270.7-6332.8	265
7 (37)	100CH[d]	16.34±1	1.55±1	157±1	...	6270.7-6356.7	351
7 (39)	50CH	17.281±2	0.651±7	46.4±8	...	6260.6-6305.5	178
7 (39)	50CH[d]	17.17±1	0.76±1	59.9±13	...	6270.7-6305.5	211
7 (39)	75CH[d]	16.80±1	1.10±1	102±1	...	6270.7-6332.8	308
7 (39)	100CH[d]	16.44±1	1.46±1	147±2	...	6270.7-6356.7	391

[a] Errors are ± 1 σ in the last digit(s).
[b] The bracketted model number refers to the secular trend used from table 6.3.
[c] Data type : C = compressed ~8 points per day. The number prefixing each data type indicator is the approximate length of the post-glitch span (in days) fitted.
[d] Data spanning ~10 days after each glitch have been excluded from the fits.
[e] Assumed value.

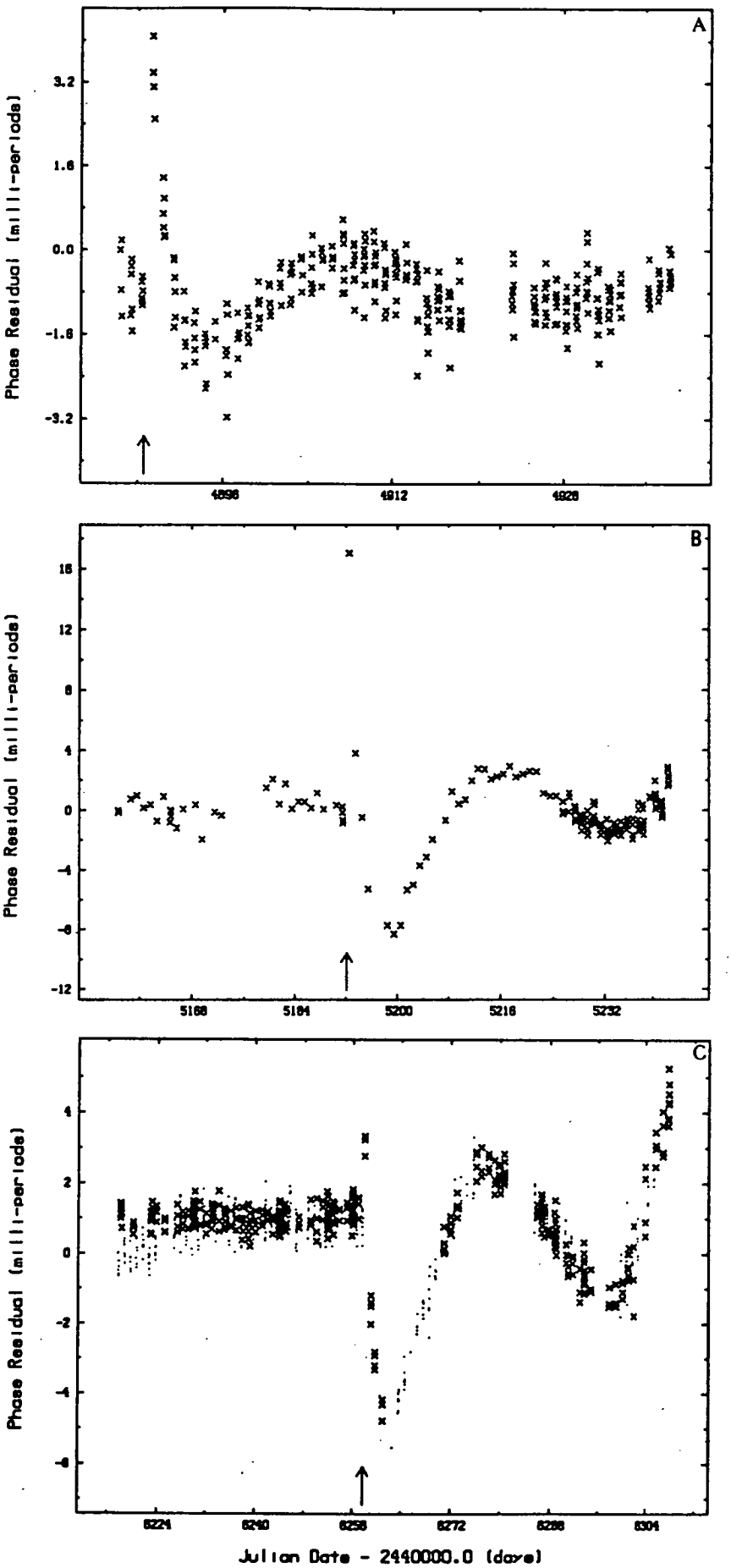

Fig. 6.12. Residuals from fits of single exponential glitch models to the data spanning an interval of 50 days following each jump. (a) for glitch 5, assuming spindown model 33, (b) for glitch 6 assuming spindown model 34, (c) for glitch 7 assuming fixed T_g and spindown model 38. In each case, the fitted or assumed glitch epoch is indicated by the arrow.

timespan $\Delta t_g \sim 10$ days following each glitch were zero-weighted. Fits were then made to the remaining observations within 50, 75, and 100 days following each glitch. In the case of glitch 7, spindown models 38, 40, and 42 were used to illustrate the dependence of parameters in the set S_1 on the assumed secular trend. The parameter values are summarized in table 6.5, and examples of residuals for the 100 day post-glitch span are plotted in figure 6.13. It is apparent from these results that the recovered relaxation timescale is dependent on the pre-glitch model assumed.

6.6 MODIFIED TWO-COMPONENT MODEL

The behaviour observed in figures 6.12 and 6.13 strongly implied a contribution from a short-timescale relaxation. This was first noted by McCulloch *et al.* (1983). In order to examine this behaviour, post-glitch span lengths of 6, 12, and 25 days were fitted with a single exponential relaxation model. As shown in table 6.6, the recovered time-constant was critically dependent on the length of the fitted span, while the parameter values in the case of glitch 7 were not significantly influenced by the choice of assumed underlying secular trend.

Following McCulloch *et al.* (1983), the glitch model of equation 6.1 was modified to incorporate an additional relaxation term with parameters subscripted by s;

$$\phi_2(t) = \phi_1(t) + \Delta\nu_s \tau_s \exp[-(t-T_g)/\tau_s] \qquad t \geq T_g \qquad 6.2$$

This equation was applied to various data spans to solve for the parameters in the set $S_2 \equiv \{\Delta\nu_c, \Delta\nu_s, \Delta\nu_i, \tau_s, \tau_i, T_g\}$ assuming particular underlying secular trends. The resulting parameter values and phase residuals are shown in table 6.7 and figure 6.14 respectively.

The modified two-component model provided an improved description of the post-glitch behaviour, particularly during the initial ~ 50 day span. However, as can be seen in table 6.7, the magnitude of the long time-constant τ_i was well correlated with the length of the fitted data span. A closer examination of the data was called for in order to resolve the origin of this behaviour.

Timing noise (including dispersion delay variations) would be expected to contribute to at least part of the discrepancy between model and data. For post-glitch spans exceeding ~ 150 days, it was not possible to obtain stable fits by giving all parameters simultaneous freedom. Again it must be recalled that the very nature of the model assumes that the underlying cubic trend is known with sufficient accuracy, and is invariant at the time of the glitch. The violation of either of these aspects will also contribute to the observed long-term discrepancy between model and data.

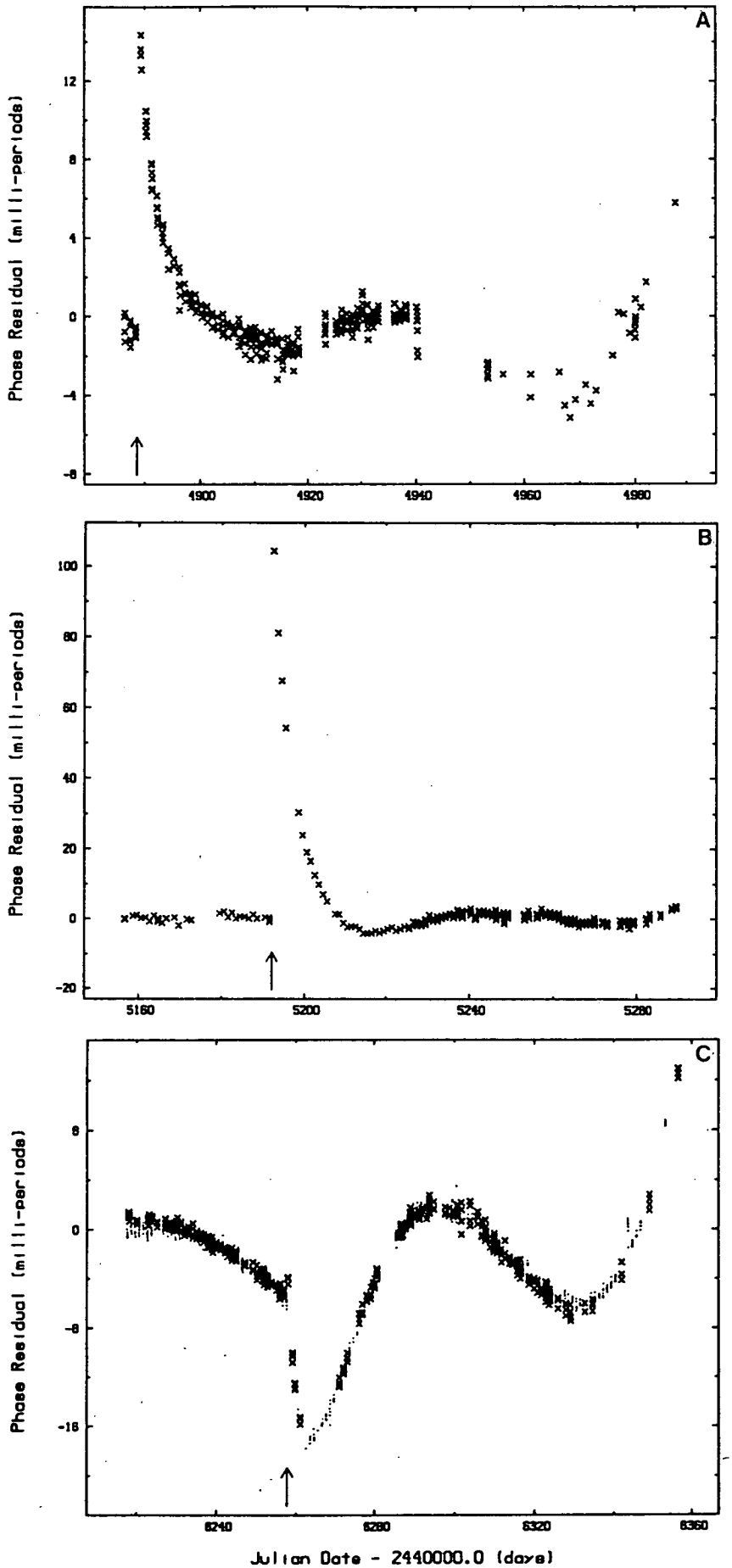

Fig. 6.13. Residuals from fits of single exponential glitch models to the data spanning an interval from between ~ 10 days to 50 days following each jump. (a) for glitch 5, assuming spindown model 33, (b) for glitch 6 assuming spindown model 34, (c) for glitch 7 assuming fixed T_g and spindown model 37. In each case, the fitted or assumed glitch epoch is indicated by the arrow.

TABLE 6.6

PARAMETERS FOR SINGLE EXPONENTIAL GLITCH FITS[a]

Glitch[b] (model)	Data Type[c]	$\Delta\nu_c$ (Hz)	$\Delta\nu_i$ ($\times 10^{-6}$ Hz)	τ_i (days)	T_g (TJD)	Post-Glitch Data Range (TJD)	Residual rms (μs)
5 (33)	6C	12.63±3	0.17±2	5.1±17	4888.5688±6	4889.3-4895.3	38
	12C	12.51±1	0.27±1	14.0±12	4888.5674±3	4899.3-4902.4	51
	25C	12.22±2	0.55±2	42±2	4888.5652±3	4899.3-4913.3	51
6 (34)	6C	22.77±3	0.367±2	2.3±7	5192.1409±8	5192.6-4895.3	71
	12C	22.65±1	0.403±7	5.7±5	5192.1395±5	5192.6-4902.4	74
	25C	22.498±8	0.479±5	13.5±6	5192.1365±6	5192.6-5219.5	121
7 (38)	6CH[d]	17.79±4	0.19±3	4.3±21	6257.7306±8	6258.0-6263.7	54
	12CH[d]	17.73±1	0.236±9	7.3±8	6257.7298±2	6258.0-6269.7	53
	25CH[d]	17.558±5	0.381±4	20.2±5	6257.7280±1	6258.0-6280.8	55

[a] Errors are ± 1 σ in the last digit(s).
[b] The bracketted model number refers to the secular trend used from table 6.3.
[c] Data type : C = compressed ~8 points per day, H = HRAO. The number prefixing each data type indicator is the approximate length of the post-glitch span (in days) fitted.
[d] The compressed data for the last LRO pre-glitch session were replaced by high-resolution data.

TABLE 6.7

PARAMETERS FOR DOUBLE EXPONENTIAL GLITCH FITS[a]

Glitch[b] (model)	Data Type[c]	$\Delta\nu_c$ (Hz)	$\Delta\nu_s$ ($\times 10^{-6}$ Hz)	τ_s (days)	$\Delta\nu_i$ (Hz)	τ_i (days)	T_g (TJD)	Post-Glitch Data Range (TJD)	Residual rms (μs)
5 (33)	25C	10.3±23	0.065±5	2.5±50	2.5±23	258±262	4888.56874±5	4889.3-4895.3	36
	50C	10.85±4	0.079±8	1.79±15	1.90±4	191±5	4888.5697±6	4889.3-4938.3	74
	75C	10.82±2	0.074±8	1.91±14	1.92±2	195±2	4888.5694±5	4889.3-4961.2	76
	100C	10.46±2	0.0744[d]	1.91[d]	2.28±2	238±2	4888.5682±3	4889.3-4982.1	103
6 (34)	25C	22.2±2	0.24±2	2.9±5	0.66±16	46±19	5192.1400±5	5192.6-5218.6	66
	50C	22.01±2	0.243±7	3.31±16	0.82±2	66±3	5192.1397±4	5192.6-5242.5	62
	75C	21.25±4	0.245±3	5.80±16	1.52±4	174±7	5192.1378±3	5192.6-5267.4	74
	100C	20.15±8	0.249±2	7.60±13	2.58±7	345±12	5192.1366±3	5192.6-5290.4	78
7 (38)	50CH[e]	16.17±9	0.095±2	4.24±17	1.70±9	188±12	6257.7300±2	6258.0-6307.9	51
	75CH[e]	15.43±4	0.097±1	5.18±12	2.43±4	288±6	6257.7290±1	6258.0-6332.8	51
	150CH[e]	13.13±4	0.0893±4	10.7±1	4.70±4	624±6	6257.72625±9	6258.0-6407.8	92
7 (38)	50H[e]	16.30±8	0.108±2	3.65±12	1.58±8	172±10	6257.7306±1	6258.0-6307.9	48
	75H[e]	15.60±3	0.112±1	4.32±7	2.26±3	264±5	6257.7304±1	6258.0-6332.8	46
	150H[e]	13.53±5	0.0972±8	8.8±2	4.31±5	345±7	6257.7281±1	6258.0-6407.8	69

[a] Errors are ± 1 σ in the last digit(s).

[b] The bracketted model number refers to the secular trend used from table 6.3.

[c] Data type : C = compressed ~8 points per day, H = HRAO. The number prefixing each data type indicator is the approximate length of the post-glitch span (in days) fitted.

[d] Fixed value.

[e] The compressed data for the last LRO pre-glitch session were replaced by high-resolution data.

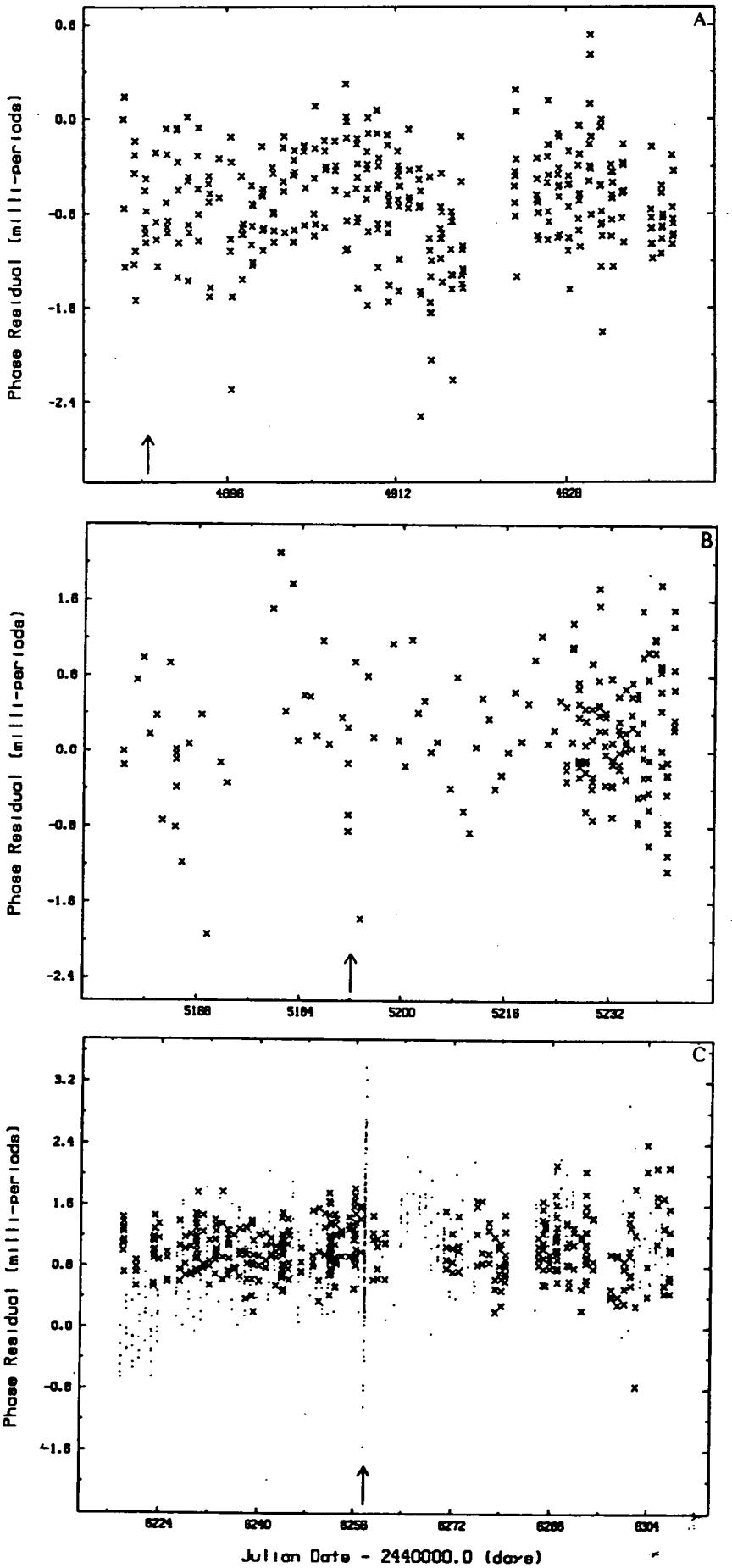

Fig. 6.14. Residuals from fits of double exponential glitch models to the data spanning an interval of 50 days following each jump. (a) for glitch 5, assuming spindown model 33, (b) for glitch 6 assuming spindown model 34, (c) for glitch 7 assuming spindown model 38. In (c) the fit was made to a combined set of LRO data (points) and HRAO data (crosses). In each case, the fitted glitch epoch is indicated by the arrow.

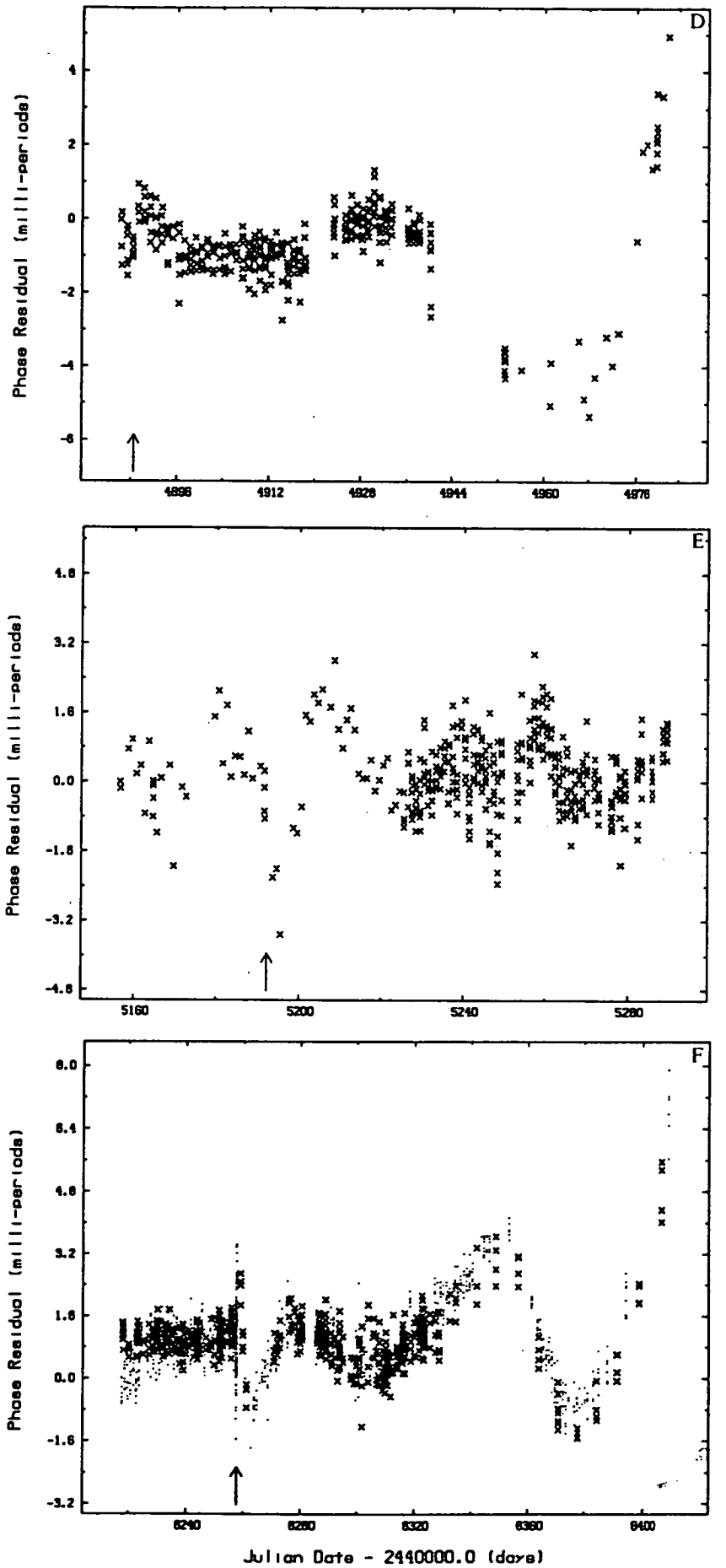

Fig. 6.14. (continued) Residuals from fits of double exponential glitch models to the data spanning an interval of 100 days following each jump. (c) as for (a). (d) as for (e). (f) as for (c). In each case, the fitted glitch epoch is indicated by the arrow.

TABLE 6.8

POST-GLITCH CUBIC FITS[a]

Glitch	Data Type[b]	ν (Hz)	$\dot{\nu}$ ($\times 10^{-12}$ Hz s^{-1})	$\ddot{\nu}$ ($\times 10^{-22}$ Hz s^{-2})	Fit Epochs (TJD) Mid	Range	Residual rms (μs)
5	50C	11.20345775120±8	-15.68409±6	83±2	4914.4110064	4889.3-4938.3	71
6	50C	11.2030543565±3	-15.6990±5	286±8	5229.3850627	5192.6-5242.5	193
7	50C	11.2016449399±1	-15.6953±1	154±3	6285.6339874	6258.0-6307.9	119

[a] Errors are ± 1 σ in the last digit(s).
[b] Data types : C = compressed ~8 points per day, H = HRAO.

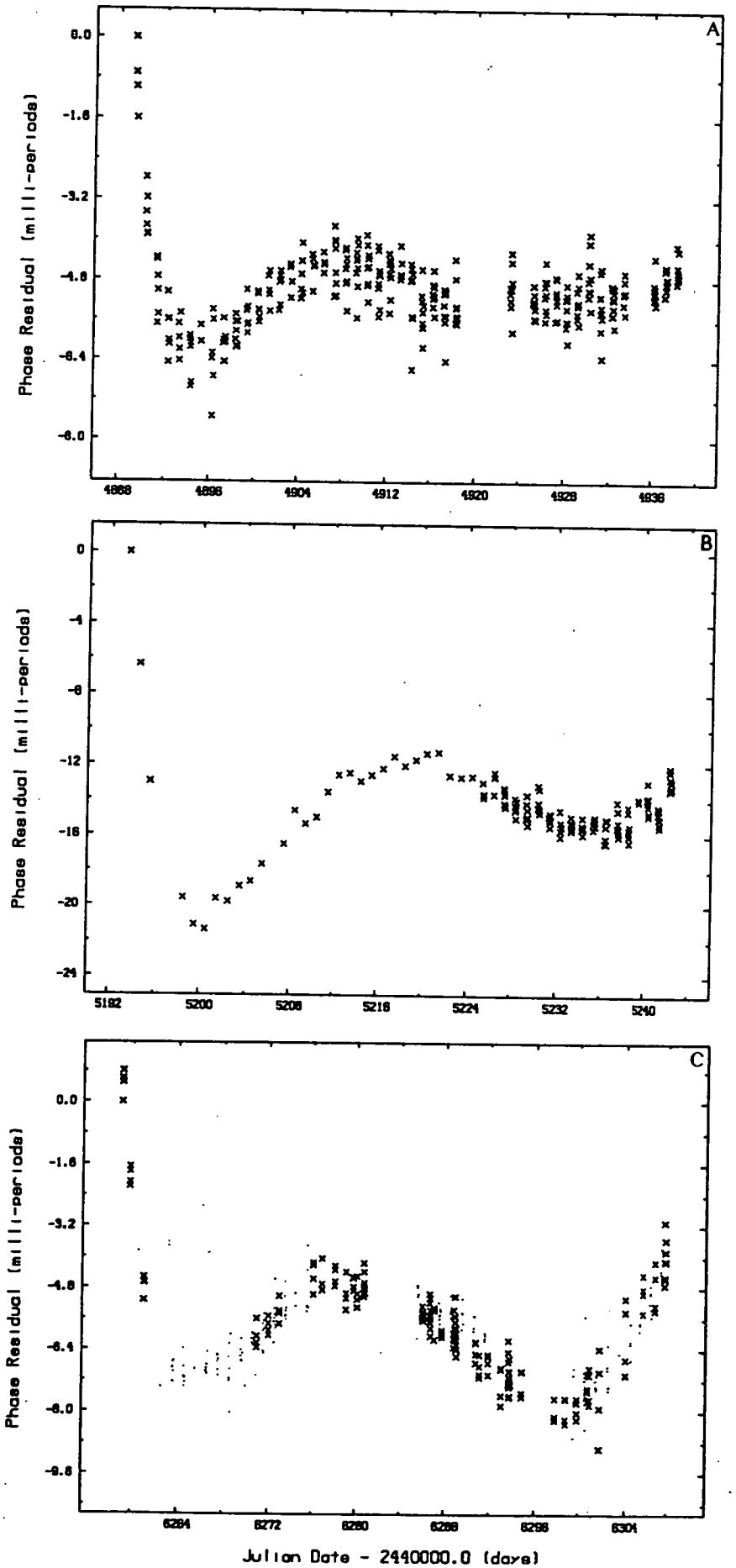

Fig. 6.15. Residuals from fits of cubic spindown models to the data the 50 days following (a) glitch 5, (b) glitch 6, and (c) glitch 7.

In table 6.8 and figure 6.15, the results of the application of a cubic spindown model to the 50 day span after each glitch are presented. The point illustrated here is that while the model does provide an adequate description in the short term, it does significantly account for the apparent long timescale relaxation.

The original two-component model was further modified, this time by allowing a jump in the first and second derivatives of the spindown at the time of the glitch;

$$\phi_3(t) = \phi_1(t) + \frac{1}{2}\Delta\dot{\nu}_0(t-T_g)^2 + \frac{1}{6}\Delta\ddot{\nu}_0(t-T_g)^3 \qquad t \geq T_g \qquad 6.3$$

As can be seen from table 6.9 and example plots in figure 6.16, this model is equally as successful as equation 6.2. Again the parameter values depend on the fit length. Clearly, additional guidance must be sought to uncover the relaxation behaviour.

6.7 EVOLUTION OF THE FREQUENCY DERIVATIVE

In order to examine the true nature of the relaxation process, quadratic fits were made over short spans to obtain $\dot{\nu}$. The minimum span length for which the fractional uncertainty was tolerable was 3 days. All of the (non-compressed) timing data were assembled into pre- and post-glitch sets of maximum length ~ 20 days and ~ 50 days respectively. For each set in turn, quadratic fits were made to data within windows of length 3 days and 6 days which were successively advanced to later times in 1 session increments. The epoch of each value of $\dot{\nu}$ so obtained was evaluated at the median barycentric arrival time of the window.

The results of this procedure are presented in figure 6.17. Immediately evident is the jump $\Delta\dot{\nu}/\dot{\nu} \sim 10^{-2}$ accompanying each glitch which subsequently recovered to a apparently linear trend. In general, fluctuations about the relaxation trend are not significant with respect to the measurement uncertainty. However, following glitch 5 there a small superimposed discontinuity of fractional magnitude $\Delta\dot{\nu}/\dot{\nu} \sim 10^{-3}$ with its own relaxation effect near TJD 4896 (arrowed) is apparent (figure 6.17a). This feature is also resolved using a window length of 4 days (figure 6.18).

In figure 6.19a, residuals from the fit of the double exponential model to all of the high resolution data during the initial 50 day span following glitch 5 are presented. Although there is the suggestion of a turning point in the general trend of the residuals at the inferred time of the feature in $\dot{\nu}$, this behaviour does not appear significant in the broader context of the remainder of the data set. The fractional upper limit for the discontinuity in rotation rate accompanying this event is $\Delta\nu/\nu \sim 2\times10^{-10}$. The inferred magnitudes for $\Delta\dot{\nu}/\dot{\nu}$ and $\Delta\nu/\nu$ are of similar order to the estimated timing noise fluctuations according to Cordes, Downs, and Krause-Polstorff (1988). The time

TABLE 6.9

PARAMETERS FOR SINGLE EXPONENTIAL + CUBIC GLITCH FITS[a]

Glitch[b] (model)	Data Type[c]	$\Delta\nu_c$ (Hz)	$\Delta\nu_s$ ($\times10^{-6}$ Hz)	τ_s (days)	$\Delta\dot{\nu}_0$ ($\times10^{-12}$ Hz s^{-1})	$\Delta\ddot{\nu}_0$ ($\times10^{-22}$ Hz s^{-2})	T_g (TJD)	Post-Glitch Data Range (TJD)	Residual rms (μs)
5 (33)	25C	12.735±6	0.066±5	2.5±5	-0.110±8	46±47	4888.56874±5	4889.3-4913.3	73
	50C	12.7390±5	0.078±8	1.8±1	-0.1133±4	59±2	4888.5696±5	4889.3-4938.3	74
	75C	12.7377±3	0.069±7	2.1±1	-0.1122±2	55.7±6	4888.5691±5	4889.3-4961.2	76
	100C	12.61±4	0.15±4	29±5	-0.073±8	-12±10	4888.5635±3	4889.3-4982.1	86
6 (34)	25C	22.84±2	0.24±2	2.8±4	-0.16±2	303±143	5192.1400±5	5192.6-5217.6	66
	50C	22.813±3	0.247±6	3.6±2	-0.131±2	152±7	5192.1397±4	5192.6-5242.5	62
	75C	22.759±2	0.245±3	6.1±2	-0.097±1	48±2	5192.1378±3	5192.6-5267.4	77
	100C	22.729±2	0.246±2	8.1±1	-0.0840±5	22.0±9	5192.1366±3	5192.6-5290.4	83
	200C	22.647±1	0.236±1	18.4±3	-0.0634±2	-3.8±2	5192.1258±6	5192.6-5393.1	189
	200C	22.721±1	0.247[e]	3.6[e]	-0.0774±3	8.6±3	5192.095±2	5192.6-5217.6	1000
7 (38)	50CH[e]	17.865±2	0.092±2	4.7±2	-0.102±1	50±4	6257.7291±2	6258.0-6307.9	96
	75CH[e]	17.865±2	0.092±2	4.7±2	-0.102±1	50±4	6257.7290±1	6258.0-6332.8	51
	150CH[e]	13.13±4	0.0893±4	10.7±1	4.70±4	624±6	6257.72625±9	6258.0-6407.8	92

[a] Errors are ± 1 σ in the last digit(s).
[b] The bracketted model number refers to the secular trend used from table 6.3.
[c] Data type : .C = compressed ~8 points per day, H = HRAO. The number prefixing each data type indicator is the approximate length of the post-glitch span (in days) fitted.
[d] Fixed value.
[e] The compressed data for the last LRO pre-glitch session were replaced by high-resolution data.

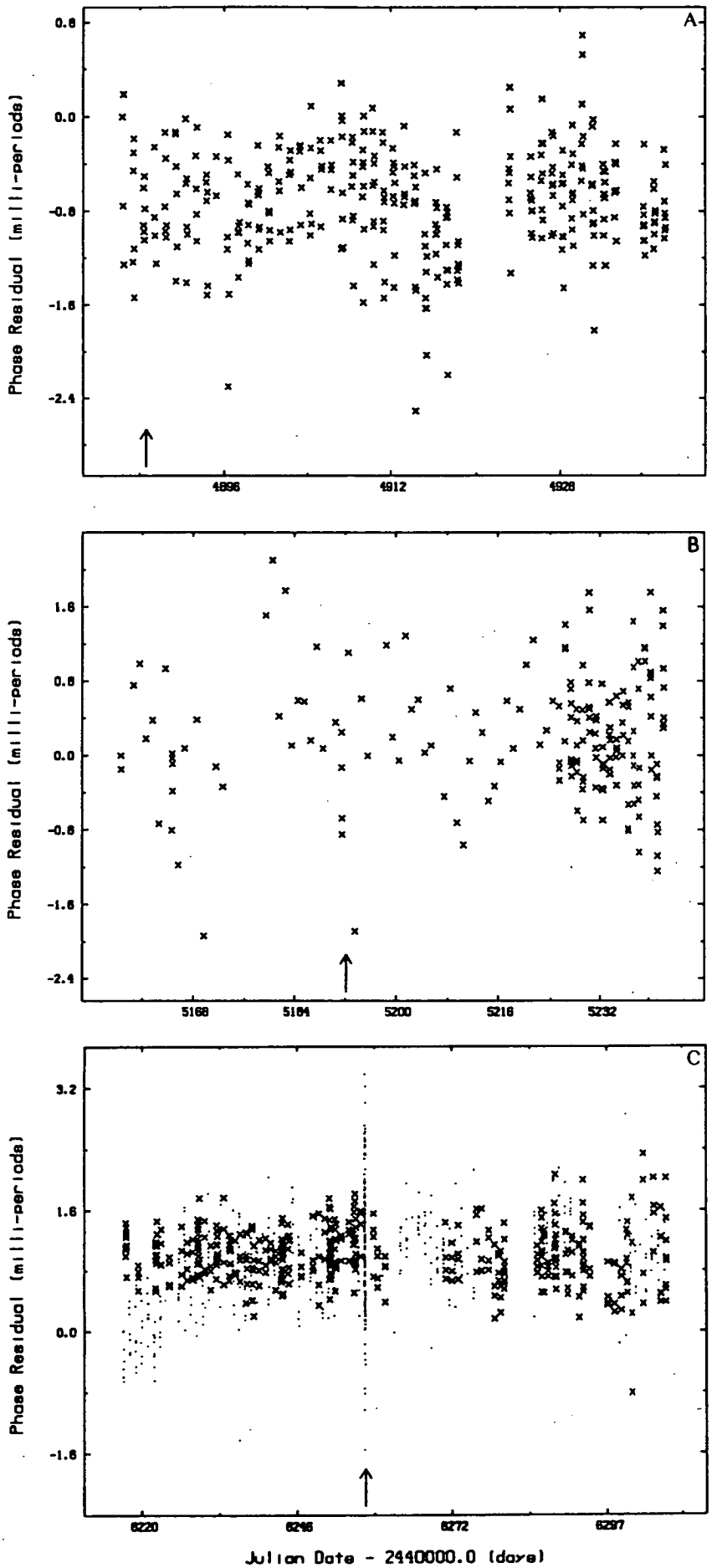

Fig. 6.16. As for figure 6.14, except showing residuals from single exponential plus perturbed cubic model to 50 day spans following each glitch. (a) for glitch 5. (b) for glitch (6). (c) for glitch 7.

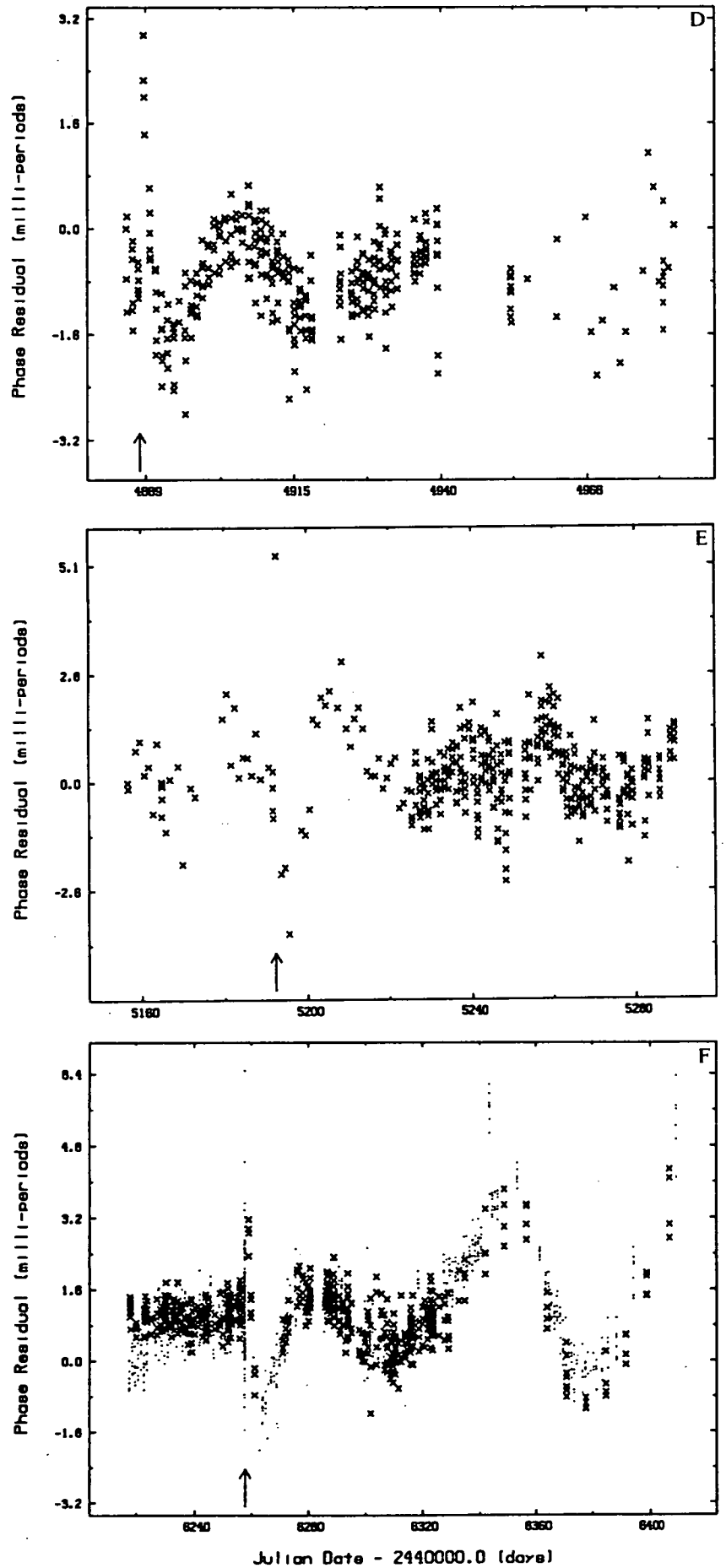

Fig. 6.16. (continued) As for figure 6.14, except showing residuals from single exponential plus perturbed cubic model to 100 day spans following each glitch. (d) for glitch 5. (e) for glitch (6). (f) for glitch 7.

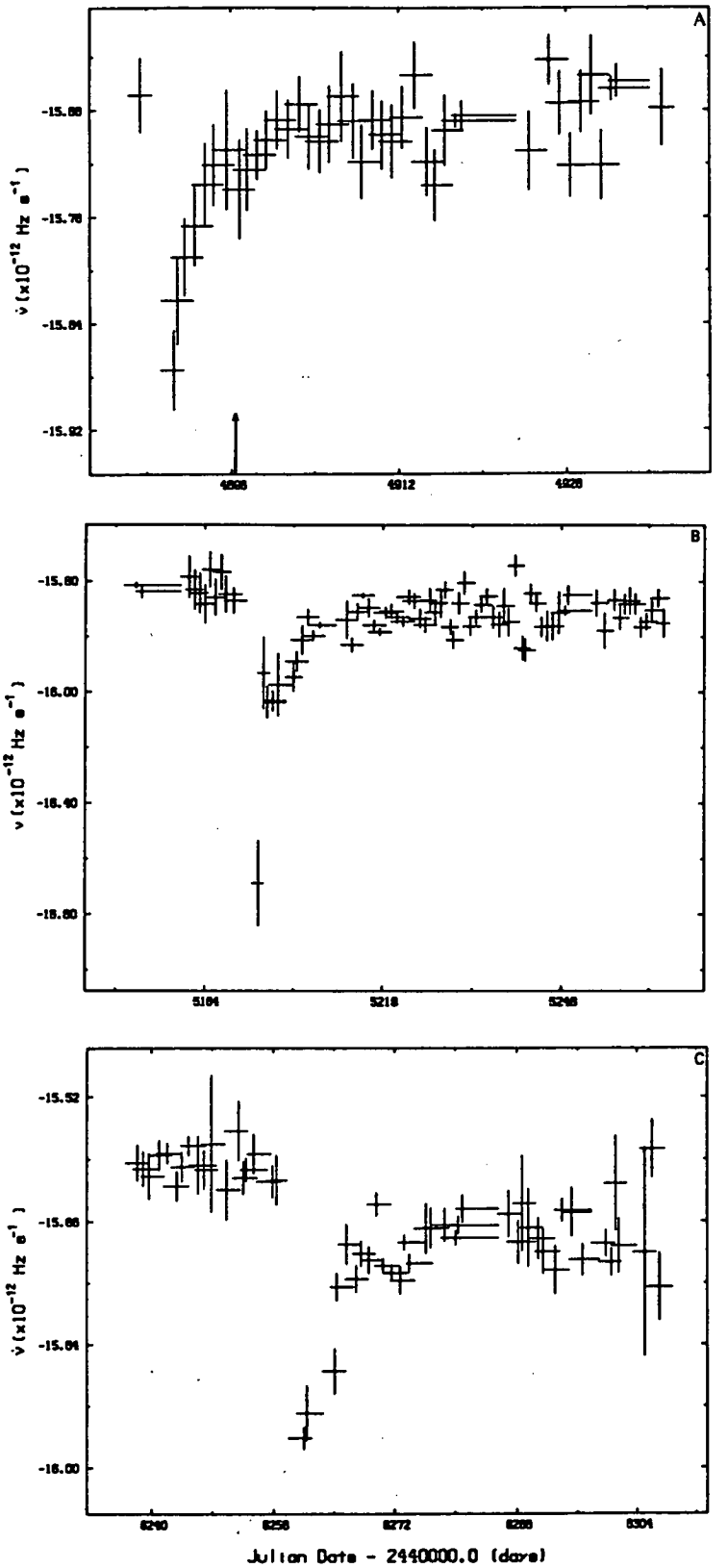

Fig. 6.17. Evolution of $\dot{\nu}$ following each glitch obtained using the method described in the text with a window length of three consecutive sessions. The vertical line at each point represents the $\pm 1\sigma$ error range. The horizonal line gives the epoch range over which the associated fit was made. (a) glitch 5, showing an apparent discontinuity (*arrow*) with a glitch-like signature. (b) glitch 6. (c) glitch 7.

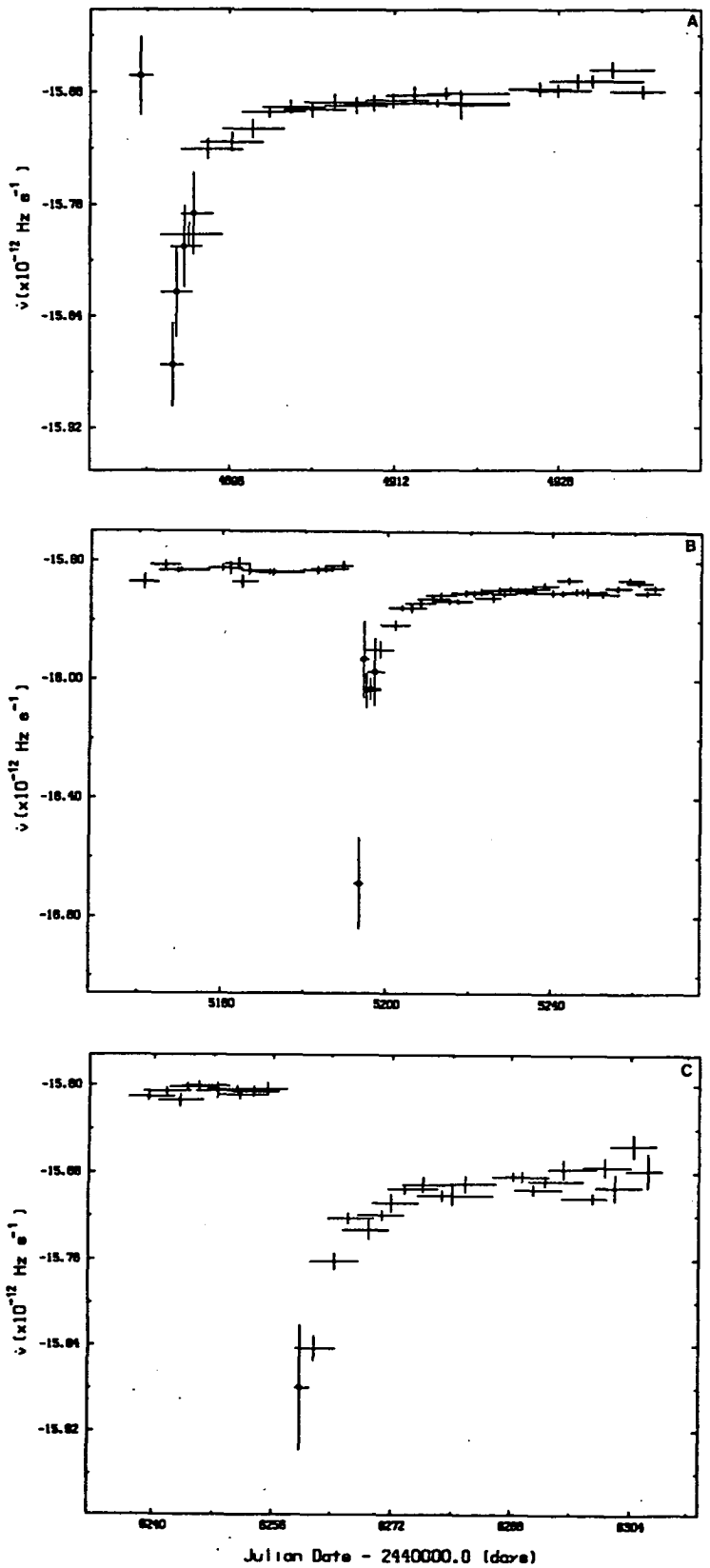

Fig. 6.17. (continued) Evolution of $\dot{\nu}$ following each glitch obtained using the method described in the text with a window length of six consecutive sessions. The vertical line at each point represents the $\pm 1\sigma$ error range. The horizonal line gives the epoch range over which the associated fit was made. Estimates marked with a filled circle were obtained using a window length of three consecutive sessions. (d) glitch 5. (e) glitch 6. (f) glitch 7.

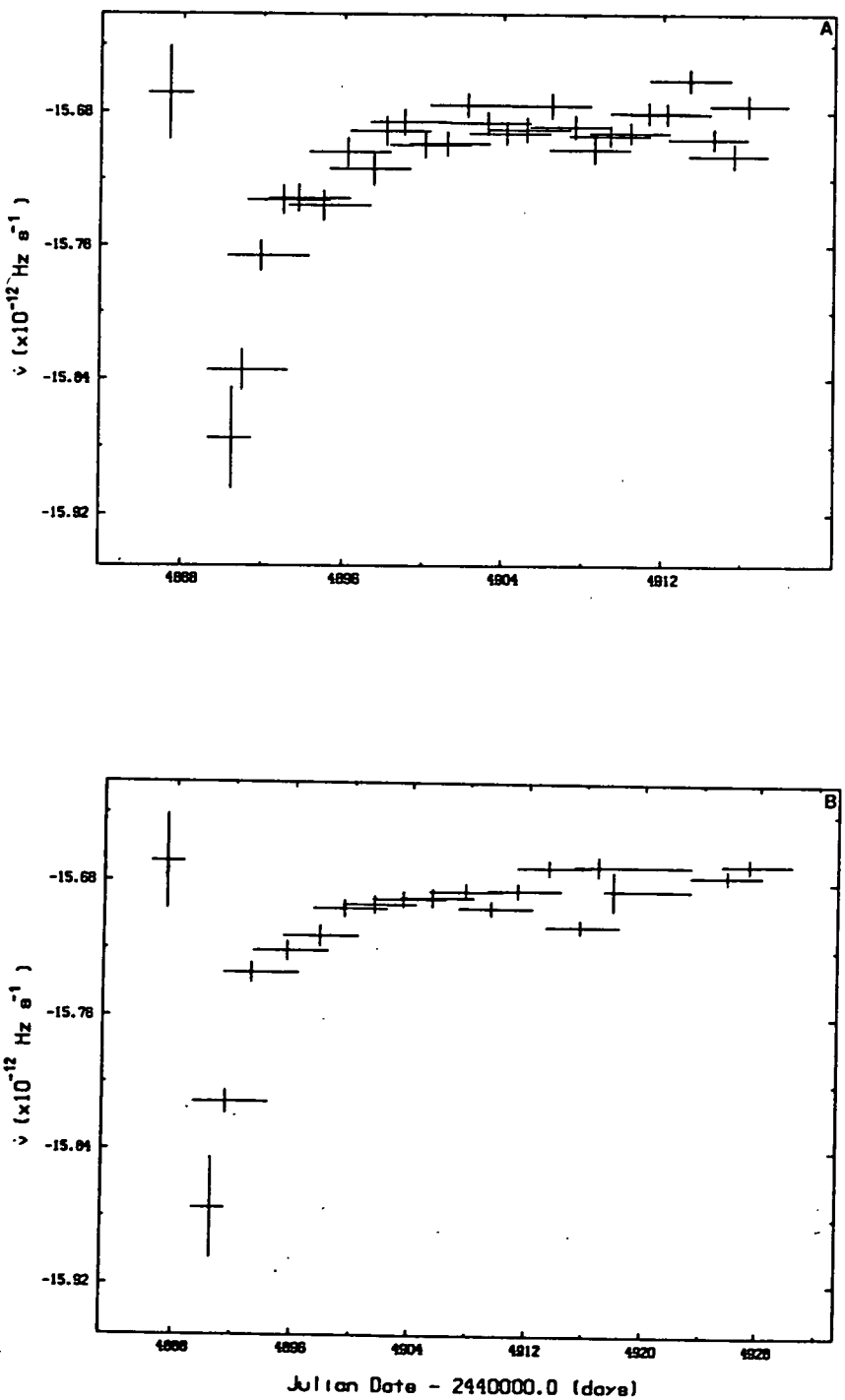

Fig. 6.18. As for figure 6.17a, except using window length of (a) 4 and (b) 5 consecutive sessions, respectively.

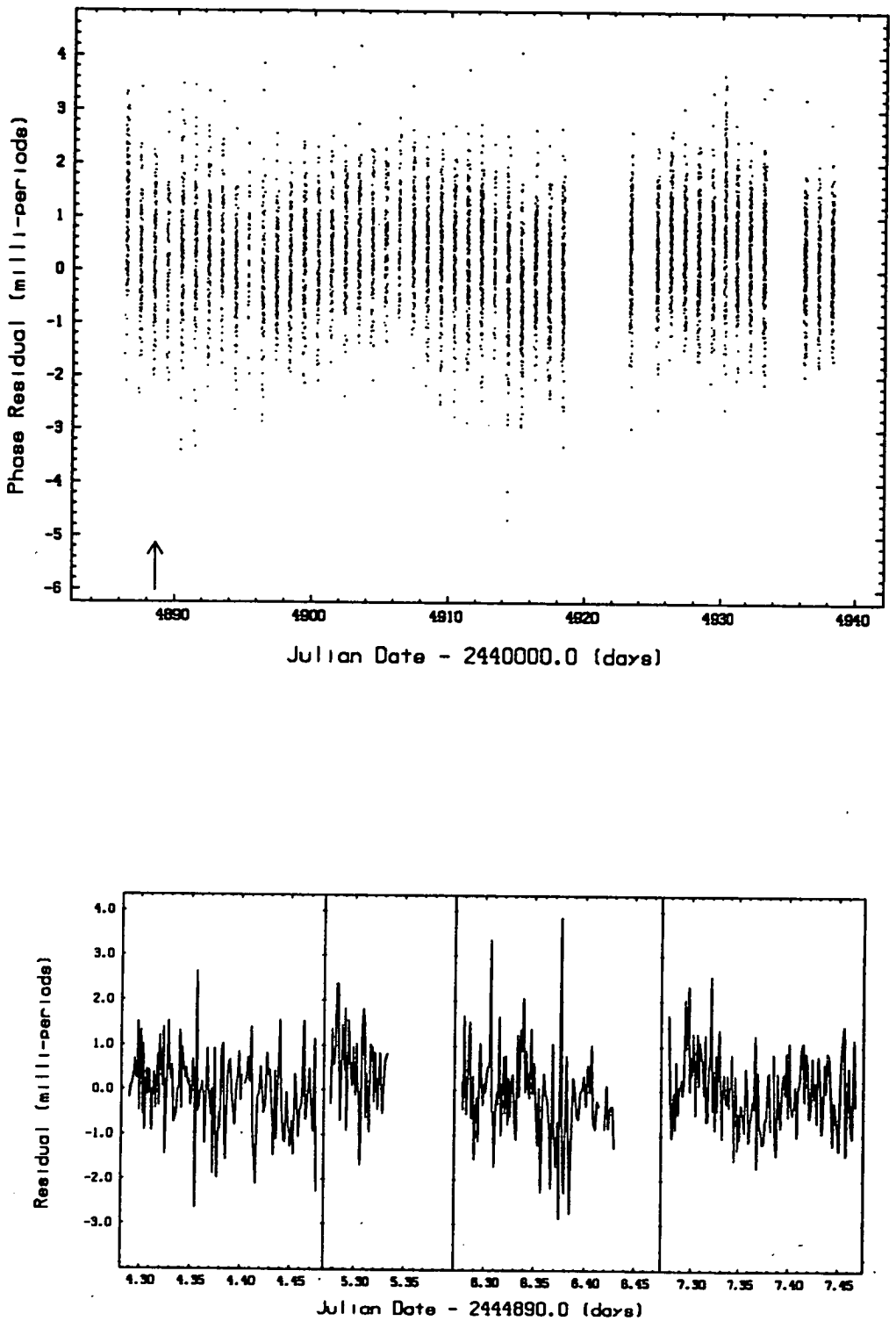

Fig. 6.19. (a) Residuals resulting from the application of the double exponential glitch model to high resolution data for the 50 day span following glitch 5. (b) Expanded time-sequence showing the residuals from (a) for two days either side of the jump in $\dot{\nu}$ apparent in figure 6.17a.

sequence of the residuals for the two days either side of the inferred epoch of the $\dot{\nu}$ feature are shown in greater detail in figure 6.19b.

As noted by Downs (1981a,b), in the long term $\dot{\nu}$ takes on a distinctly linear trend which has a gradient (the second frequency derivative) that depends on the magnitude of the preceding frequency jump. This phenomenon evidently causes the failure of models based on the simple two-component theory to adequately describe the long-term phase behaviour. This aspect was not addressed by McCulloch *et al.* (1983) who were primarily motivated to demonstrate the existence of the previously unseen rapid relaxation effect.

In figure 6.20, values of the first and second frequency derivatives are plotted as a function of epoch prior to glitch 7. These estimates were obtained via the application of quadratic and cubic spindown models to non-overlapping spans of LRO and HRAO data as appropriate. Of note are the apparently significant fluctuations of $\dot{\nu}$ that are visible in the plots for both observatories. The fluctuations near TJD 6080 coincide with the erratic behaviour of the residuals in figure 6.11f and figure 6.11g.

6.8 DISCUSSION

While it is apparent that the short term relaxation reported by McCulloch *et al.* (1983) to follow the 5th Vela glitch is manifest in the behaviour following the subsequent two glitches, the simple modification of adding a second relaxation term to the two-component model does not allow a suitable description of the timing behaviour in the long-term. In particular, long-term trend in the first-frequency derivative is seen to change at each glitch. This is not a specific prediction of the two-component theory, but has been incorporated in the vortex creep model as a manifestation of vortex pile-up in the boundary zone (figure 2.2).

The vortex creep theory of Alpar et al. (1984a,b) specifically predicts that the post-glitch evolution of $\dot{\nu}$ is controlled by three relaxation components which take effect after the passage of the decoupling time interval $t_0' = \Delta\nu/|\dot{\nu}_\infty|$ where $\dot{\nu}_\infty$ is the long-term value of $\dot{\nu}$, and $\Delta\nu$ is the jump of angular rotation frequency. Using reasonable parameter estimates, $t_0' \approx$ 15-20 days (table 2.1). This timescale is not supported by the rapid recovery of $\dot{\nu}$ apparent in figure 6.19.

In the framework of the vortex creep theory, this observation suggests that recoupling between the superfluid vortices and the boundary region (figure 2.2) through which the vortices move radially at the onset of a glitch has not taken place.

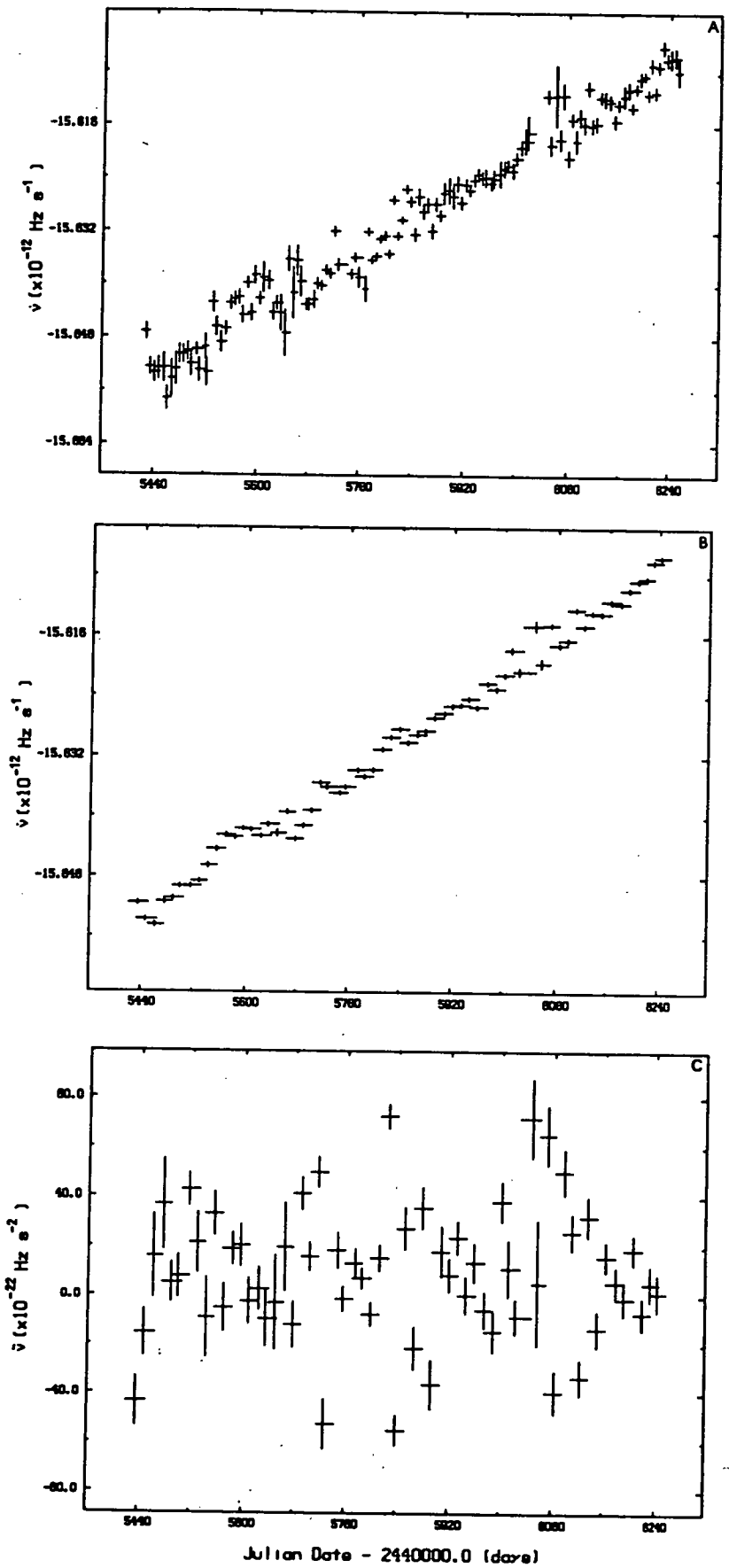

Fig. 6.20. Evolution of spindown parameters prior to glitch 7 obtained from LRO data. (a) $\dot{\nu}$ obtained from the fit of a quadratic model to data within non-overlapping spans of 13 day maximum duration. (b) as for (a) except for 27 day non-overlapping spans based on the fit of a cubic model. (c) $\ddot{\nu}$ obtained from a cubic model fit to 27 day non-overlapping spans.

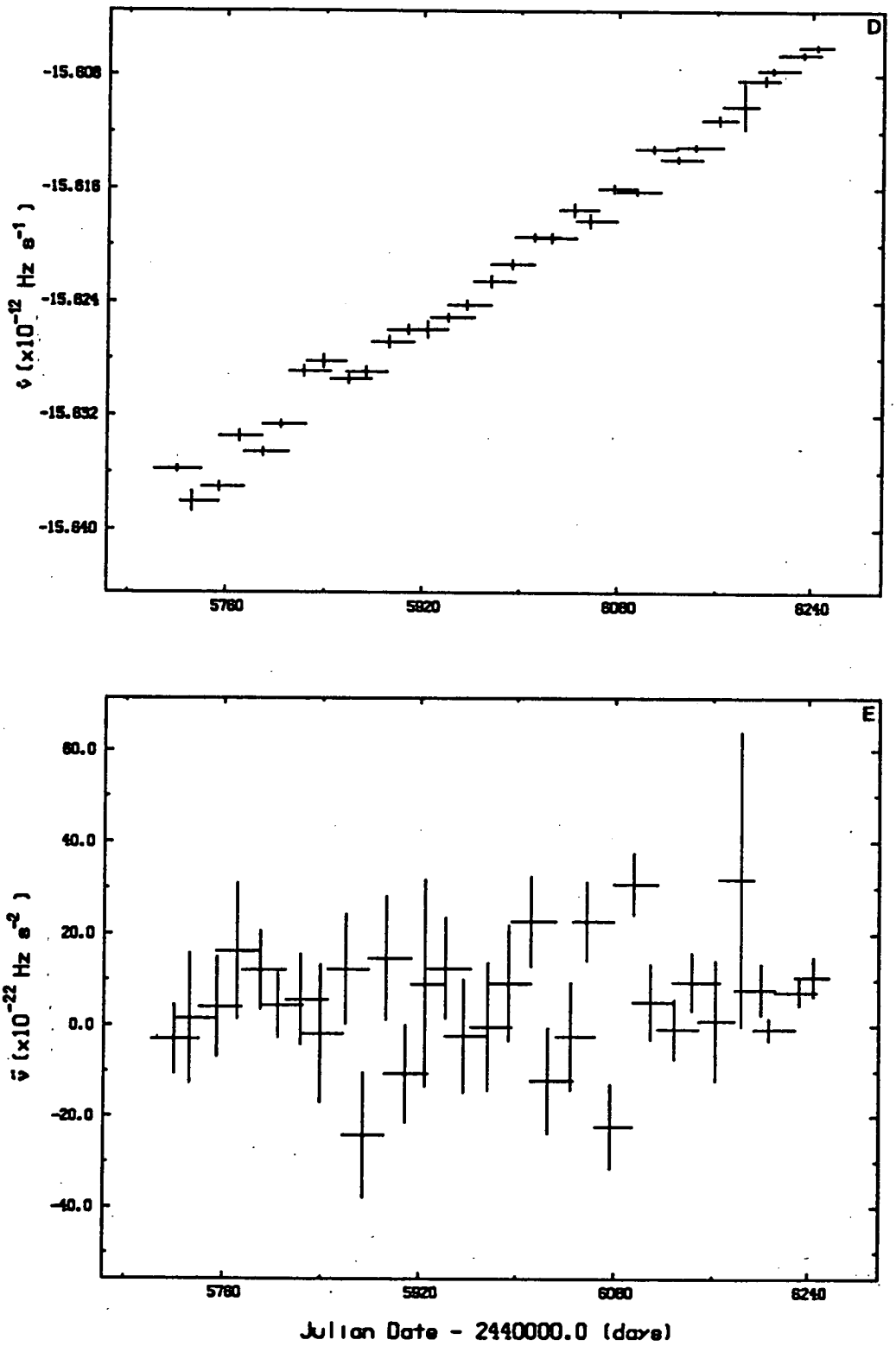

Fig. 6.20. (continued) Evolution of spindown parameters prior to glitch 7 obtained from HRAO data. (d) $\dot{\nu}$ obtained from the fit of a cubic model to data within non-overlapping spans of 34 day maximum duration. (e) as for (d) except showing the evolution of $\ddot{\nu}$.

Alpar et al. (1984b) have predicted that the timescale required for recoupling to take place is $t_0 = \Delta\nu_s/|\dot{\nu}_\infty|$ where $\Delta\nu_s$ is the change in the angular frequency of the pinned superfluid. Using reasonable parameter values they obtain $t_0 \sim 1500$ days, which is larger than, though of the same order as, the interval of 1065 days between the 6th and 7th glitches.

6.9 CONCLUSIONS

It is firmly established that the post-glitch behaviour for the Vela pulsar exhibits short (1-6 day) and intermediate (~ 20-100 day) relaxation timescales.

The modification of admitting a second exponential decay term to the phase model for the two-component theory of neutron star structure was found to be inadequate over timescales exceeding ~ 100 days.

CDK-P have modelled the glitch behaviour using

$$\phi_4(t) = \phi_0 + (\nu_0+U(t-T_0)\Delta\nu)(t-t_0) + \tfrac{1}{2}(\dot{\nu}_0+U(t-T_0)\Delta\dot{\nu})(t-t_0)^2 + \tfrac{1}{6}(\ddot{\nu}_0+U(t-T_0)\Delta\ddot{\nu})(t-t_0)^3 + U(t-T_0)[\dot{\nu}_s\tau_s\{t+\tau_s(e^{-t/\tau_s}-1)\} + [\dot{\nu}_i\tau_i\{t+\tau_i(e^{-t/\tau_i}-1)\}] \qquad 6.4$$

where $U(t-T_0)$ turns on the relaxation effect at $T_0 > T_g$. The form of this model was motivated by the post-glitch recovery of $\dot{\nu}$. They achieved some degree of success in obtaining stable parameter values, which support the view that the fast and intermediate relaxation timescales are ~ 5 days and ~ 50 days. This model requires future application to the LRO data, for which sufficient immediate post-glitch data is available to allow the estimation of model parameters with reduced uncertainty, particularly with respect to the rapid relaxation effect.

In addition, the recent work of Alpar *et al.* (1988) with regard to large glitch of PSR0355+54 reported by Lyne (1987) has suggested that linear (as distinct to non-linear) vortex creep within the neutron pinning zones may be responsible for the observed relaxation timescales and the absence of the delay time t_0 in the post-glitch data. This work requires application to the LRO glitch data.

The behaviour of the frequency derivative preceding the seventh glitch did not exhibit any significant fluctuations aside from those attributable to timing noise suggesting that the repinning of the superfluid vortices with the boundary region between the weak and superweak pinning zones in the vortex creep model of internal structure had not taken place.

The significance of changes to the mean pulse shape associated with the 5th and 7th Vela glitches has been examined, and no substantial modifications were apparent. Daily fluctuations of the shape of the I_x and I_y profiles were apparent about the time of each glitch, and this is interpreted as the result of variable ionospheric Faraday rotation. Future dual frequency polarimeter measurements are urged in conjunction with timing observations in order to examine the possibility of subtle magnetospheric changes which may accompany glitch events.

The phase residuals immediately prior to each of the large glitches studied did not exhibit any significant precursor activity. This conclusion was reached through an examination of the normality of each residual set by comparing the observed probability distribution function with that for a Gaussian population. In addition, the autocorrelation function and the outcome of runs tests for each set of residuals further confirmed their normality. In the case of the 1985 glitch, observations were secured to within perhaps 30 minutes of the jump, and yet no significant pre-jump activity was present.

An apparent timing discontinuity of low significance was found in the relaxation behaviour following the 1981 glitch. The fractional changes in the rotation parameters for this event were estimated as $\Delta\nu/\nu \sim 2\times10^{-10}$ and $\Delta\dot{\nu}/\dot{\nu} \sim 10^{-3}$. These values are consistent with those of discrete timing noise events observed by CDK-P. The jump appeared to be followed by a relaxation in $\dot{\nu}$ over an interval of 5-10 days which was qualitatively similar to that of a typical macro-glitch.

CHAPTER 7 - THE VARIABILITY OF DISPERSION MEASURE FOR PSR0833-45

7.1 INTRODUCTION

Significant changes have been observed in the dispersion measure (DM) for the Vela pulsar (Hamilton, 1977, Hamilton, Hall, and Costa, 1985; hereafter HHC), the Crab pulsar (Rankin and Roberts, 1971; Rankin *et al.*, 1988 and referenced therein), and the millisecond pulsar PSR1937+21 (Rawley, Taylor, and Davis, 1988). These changes are interpreted as due to the motion of large-scale electron density turbulence in the interstellar medium across the line-of-sight. For the Vela and Crab pulsars, it is plausible that the majority of the turbulence lies in the vicinity of their SNR shells.

Between March 1 and September 4, 1986, dual frequency timing observations of the Vela pulsar were obtained at Llanherne, with the aim of accurately measuring the dispersion delay between the pulse arrival times at the two frequencies in order to account for the influence of dispersion measure fluctuations on the barycentric times. Similar measurements were also made for PSR1749-28. In this chapter, the reduction and interpretation of these data are presented.

7.2 DISPERSION DELAY

Barycentric times T for which the dispersion correction was neglected were used in the determination of the dispersion delay $\Delta T = T_{954} - T_{635}$ (where the subscripts refer to the observation frequency). Because of the integration process, it was only possible to determine ΔT to within one pulse period. When the catalogue values of DM for each pulsar are considered, then

$$\Delta T_{0833\text{-}45} \approx 0.3955 \text{ s} \approx 4.4 / \nu_{0833\text{-}45}$$

$$\Delta T_{1749\text{-}28} \approx 0.2866 \text{ s} \approx 0.51 / \nu_{1749\text{-}28}$$

In order to obtain the true relative delay for PSR0833-45, the 635 MHz topocentric arrival times were incremented by $4P_a$ prior to the calculation of T_{635}.

7.3 DISPERSION PARAMETERS

7.3.1 Data Selection

The dispersion constant D associated with each pair of simultaneous dual frequency integrations was calculated using equation 1.2 irrespective of whether the arrival times passed the selection procedure described in section 4.10. Each value of D was then converted to an estimate of dispersion measure (DM) using equation 1.4. A standard measurement error $\hat{\sigma}_{DM}^2$ was assigned to each estimate using the values of the (assumed independent) arrival time uncertainties.

The failure of the arrival time estimation procedure in the presence of strong receiver noise lead to a small population of outlying DM estimates. The following procedure was used to reject these data with the aim of producing a representative sample. From the unweighted mean $\overline{DM}_u$ and standard deviation s_{DM} of the entire sample, the deviation parameter

$$d = \frac{\max(|DM_i - \overline{DM}_u|)}{s_{DM}}$$

was then obtained, together with the probability $P_p(d)$ of observing d in a normal population of the same size. The estimate responsible for the maximum deviation was removed from the population if $P_p(d) < 1 - \alpha$, where the significance level α was chosen as 0.9999, 0.999, and 0.99. Upon rejection of an estimate, the mean and standard deviation of the new population were recomputed, and the procedure was repeated until no further rejections occurred.

For PSR0833-45, use of the three significance levels resulted in the rejection of 3.8%, 2.1% and 1.8% of the observations respectively. The values of the reduced χ^2 statistic for the corresponding distributions were 3.6, 9.0, and 7.6 respectively for $\nu_{eff} = 98$ degrees of freedom. The 0.999 and 0.9999 significance levels offered sufficient protection against outlying estimates as indicated by the similarity of the resulting population sizes and the lack of truncation in the tails of their respective distributions (figure 7.1). The population of N = 17276 estimates obtained with α = 0.999 was arbitrarily chosen to form the representative sample.

A similar reduction procedure was adopted for the analysis of PSR1749-28 data. A value of $\alpha = 0.999$ was chosen which gave $\chi^2 = 1.47$ for $\nu_{eff} = 48$ (figure 7.2). This restriction removed 3.9% of the observations to yield a final population of N = 489 .

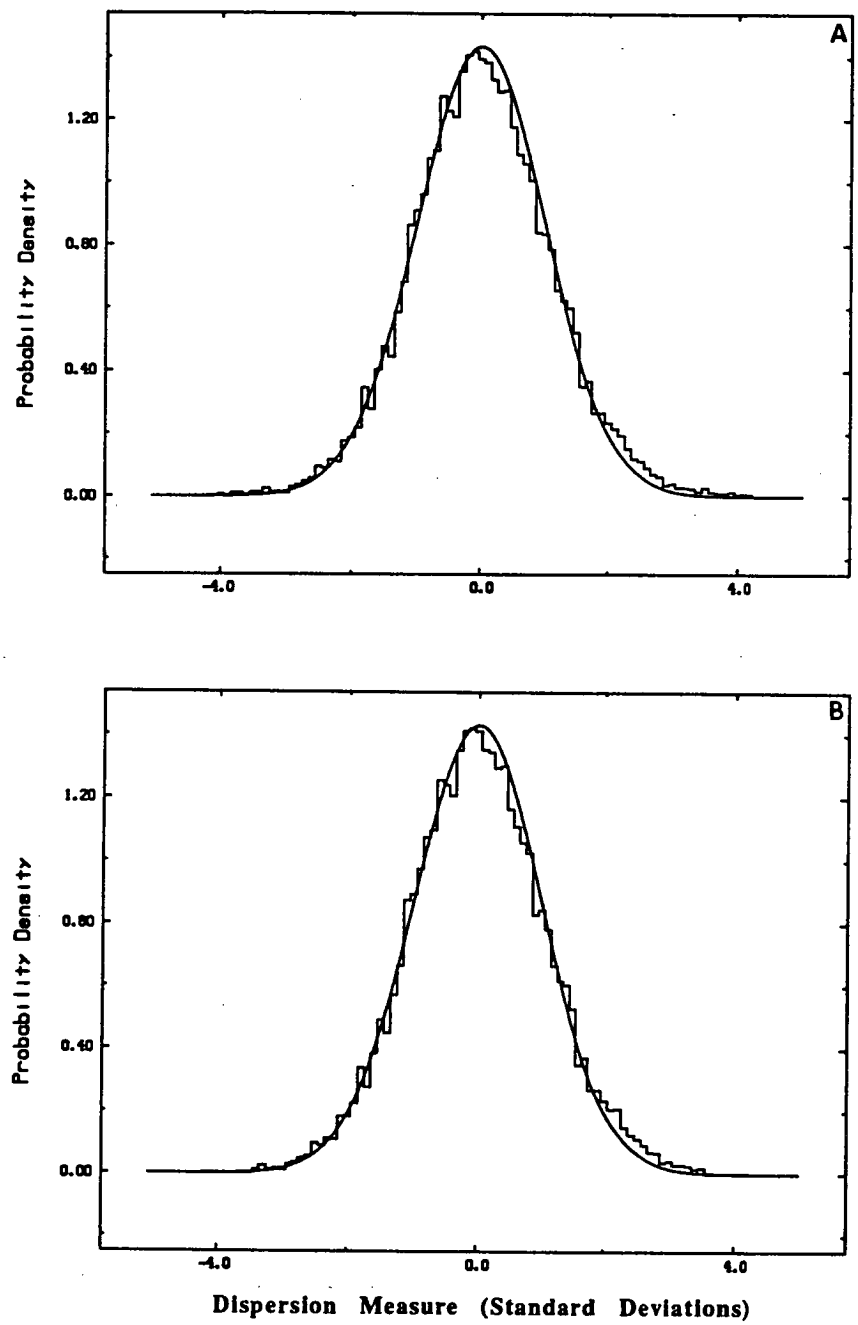

Fig. 7.1. Distribution of individual dispersion measure estimates for PSR0833-45 resulting from the rejection of outlying values using significance levels of (a) α = 0.9999 and (b) α = 0.999. The probability density is numerically equal to $N\Delta x$, where N is the number of estimates which fall into a bin of width $\Delta r = 0.02\sigma$. Here σ is the standard deviation of the entire population. Superimposed is a gaussian function with the same second moment and area as the corresponding observed distribution.

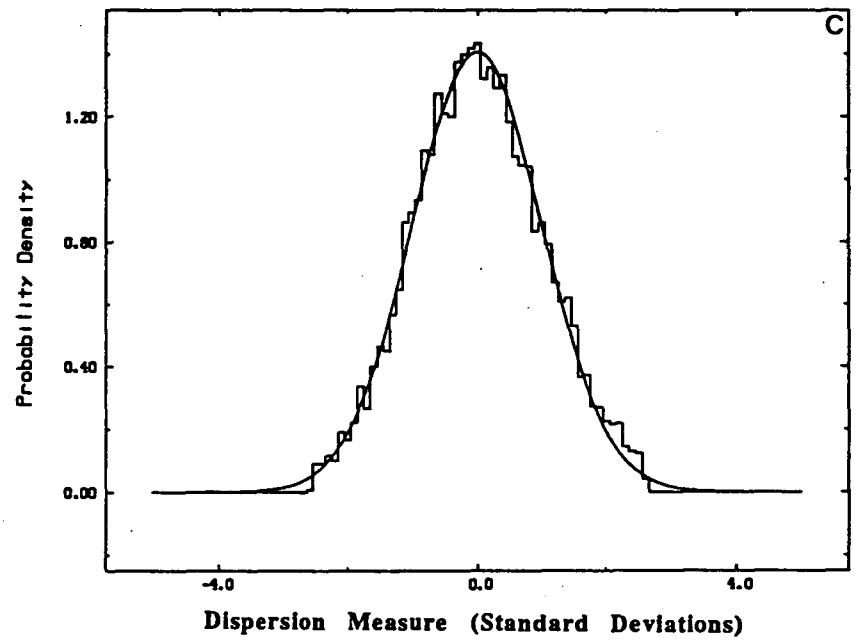

Fig. 7.1(c). As for figure 7.1 (a) and (b), except in this instance, $\alpha = 0.99$

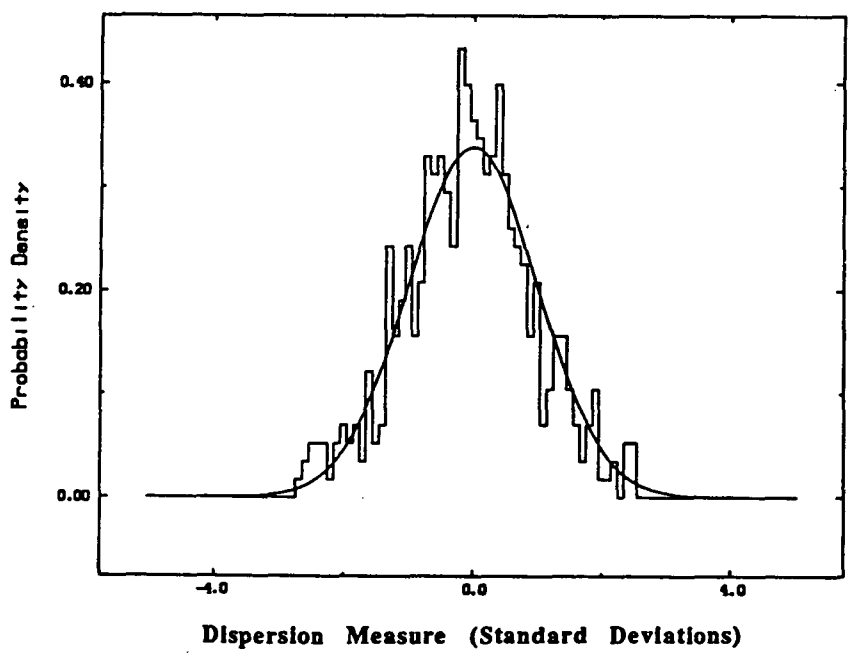

Fig. 7.2. As for figure 7.1 except in this instance $\alpha = 0.99$ for PSR1749-28.

7.3.2 Daily Samples

For both pulsars, the DM estimates within each session were expected to be normally distributed based on the similarity of the individual values of $\hat{\sigma}_{DM}$. The processes considered most likely to cause deviation from normality were pulse shape changes and short timescale dispersion variations. The significance of these effects was examined for PSR0833-45. Pulse shape parameters (section 5.4) and phase residuals from fits of cubic spindown models (figure H.1 and table H.1) were obtained at each frequency for the integrations that yielded a DM estimate. A series of cross-correlation analyses was performed between the shape parameters, the DM estimate, the arrival time uncertainties, and the residuals. The results are summarized in table 7.1, and scatter diagrams for the parameters exhibiting the largest correlations are shown in figure 7.3. The absence of any significant correlation between parameter pairs implies that the estimation of DM is not strongly influenced by fluctuations in pulse shape or signal-to-noise ratio at either frequency.

The influence of profile smearing due to the inexactness of the observing ephemeris is considered in section 7.3.

Shape parameters were also obtained for the mean I profile of each session in order to examine the stability of the pulse shape with time. These are plotted in figure 7.4.

The normality of each daily sample was examined by calculating the reduced χ^2 statistic from binned estimates. This parameter is plotted as a function of observation epoch in figure 7.5, demonstrating the consistent normality of the majority of samples.

A structure function based on equation 5.1 (replacing each residual with a DM estimate) was applied to all observations to yield daily strength values $\sigma_{DM(S)}(T)$ where T is the central epoch of the data span. In addition, the estimates $\hat{\sigma}_{DM}$ for each session were averaged to provide $\sigma_{DM(M)}(T)$. The noticeable offset between $\sigma_{DM(M)}$ and $\sigma_{DM(S)}$ in figure 7.6a is largely a consequence of the excess phase noise noted in Chapter 5. From the phase residuals for Vela at each frequency, the ratio σ_S/σ_M was obtained where the numerator and denominator represent the mean values of white noise and measurement uncertainty (both in units of time), respectively. The theoretical arrival time uncertainty of each integration was then scaled by the appropriate value of σ_S/σ_M, and the formal error for each DM estimate was recomputed. The effect of the rescaling on $\sigma_{DM(M)}$ is presented in figure 7.6b. As shown in figure 7.7, the distributions of $\sigma_{DM(M)}$ and $\sigma_{DM(S)}$, while having equivalent

TABLE 7.1

CROSS-CORRELATIONS FOR PSR0833-45[a]

	635 MHz			954 MHz		
	DM	σ_M	R	DM	σ_M	R
μ_1	4.3	2.4	2.9	-3.0	0.2	4.8
μ_2	0.0	-5.2	-2.0	0.2	-0.6	-0.3
μ_3	-0.3	-1.4	-1.7	0.2	-0.7	1.4
μ_{d_0}	6.2	-6.7	3.8	1.4	-7.8	-0.9
μ_{d_1}	5.0	1.3	3.3	-2.6	-1.4	4.5
μ_{d_2}	0.4	-5.4	-1.7	0.3	-1.4	-0.4
μ_{d_3}	-0.2	-1.6	-1.6	0.3	-0.1	1.3
K_G	4.5	-7.7	18.3	4.8	-10.5	14.3
SN ratio	-2.7	...	-28.1	-1.4	...	-28.5
σ_M	4.4	...	26.8	0.3	...	30.4
$\sigma_{M(954)}$	27.8	...	...	...	...	...
σ_{DM}	8.4	...	...	...	...	...
-						
σ_C	1.8	1.8	1.9	1.9	1.8	1.9
N	11220	11403	10527	11177	11408	10541

Notes:

The tabulated values (except for those in the last row) are correlation coefficients (expressed in units of 10^{-2}). The first 7 parameters in the left hand column are the pulse shape parameters defined in section 5.4. The other parameters are; SN ratio = pulse signal-to-noise ratio, σ_M = theoretical measurement uncertainty, σ_{DM} = uncertainty in DM estimate, σ_C = the 95% confidence limit for each correlation coefficient, N = number of observations, DM = dispersion measure, R = residual from the fit of a cubic spindown model. The epoch range of the data set was TDJ 6497.9 - 6648.5. Minor differences in the size of the data sets used are reflected in the values of N.

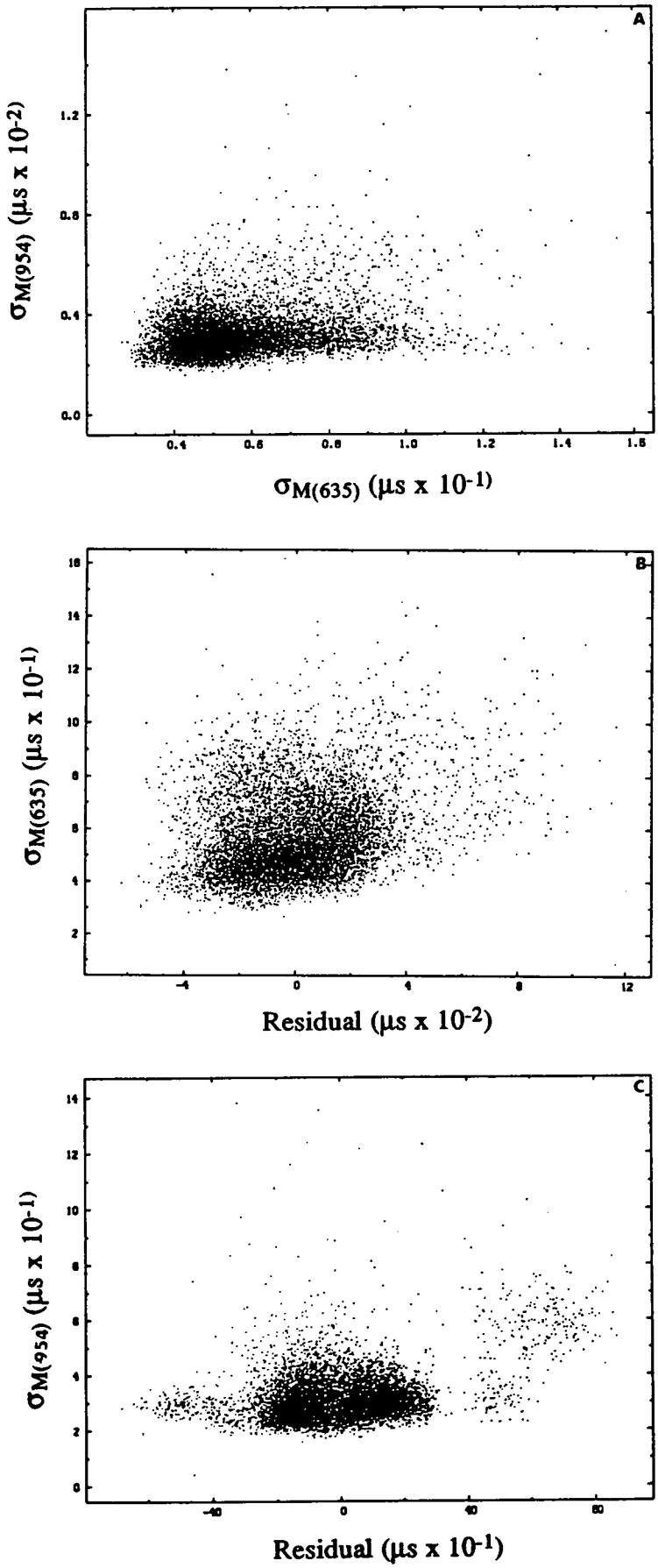

Fig. 7.3. Correlation diagrams : (a) σ_M at 635 MHz against σ_M at 954 MHz; (b) σ_M against residual from cubic spindown model at 635 MHz; (c) as for (b) except at 954 MHz. The epoch span of the data used in all figures is TJD 6497.9 - 6648.5.

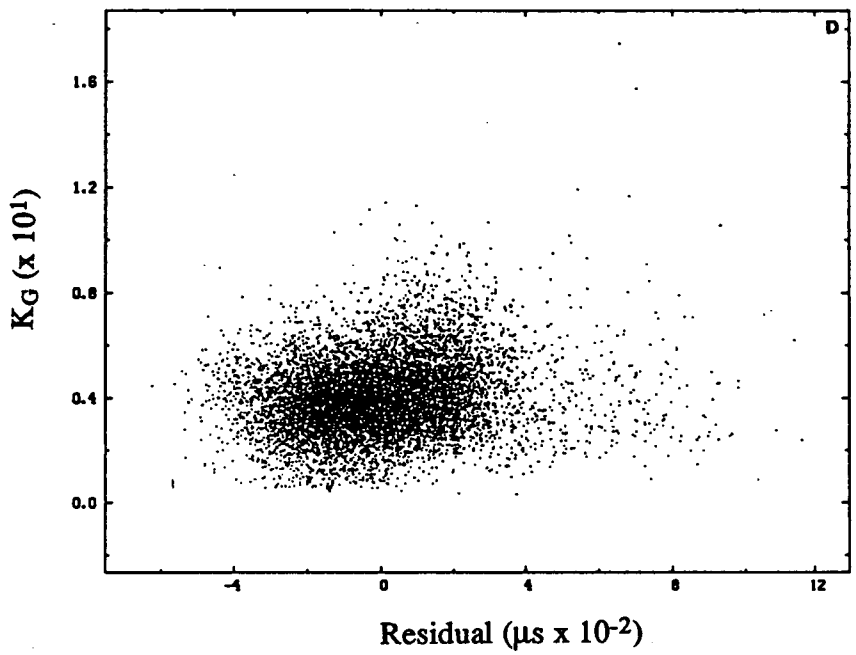

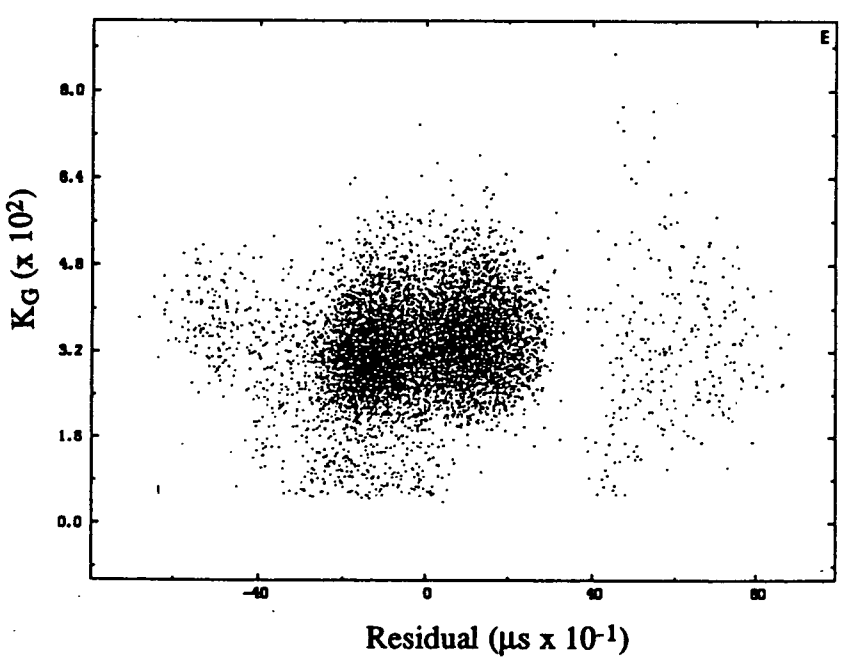

Fig. 7.3. (continued) Correlation diagrams : (d) pulse shape parameter K_G against residual from cubic spindown model at 635 MHz; (e) as for (d) except at 954 MHz.

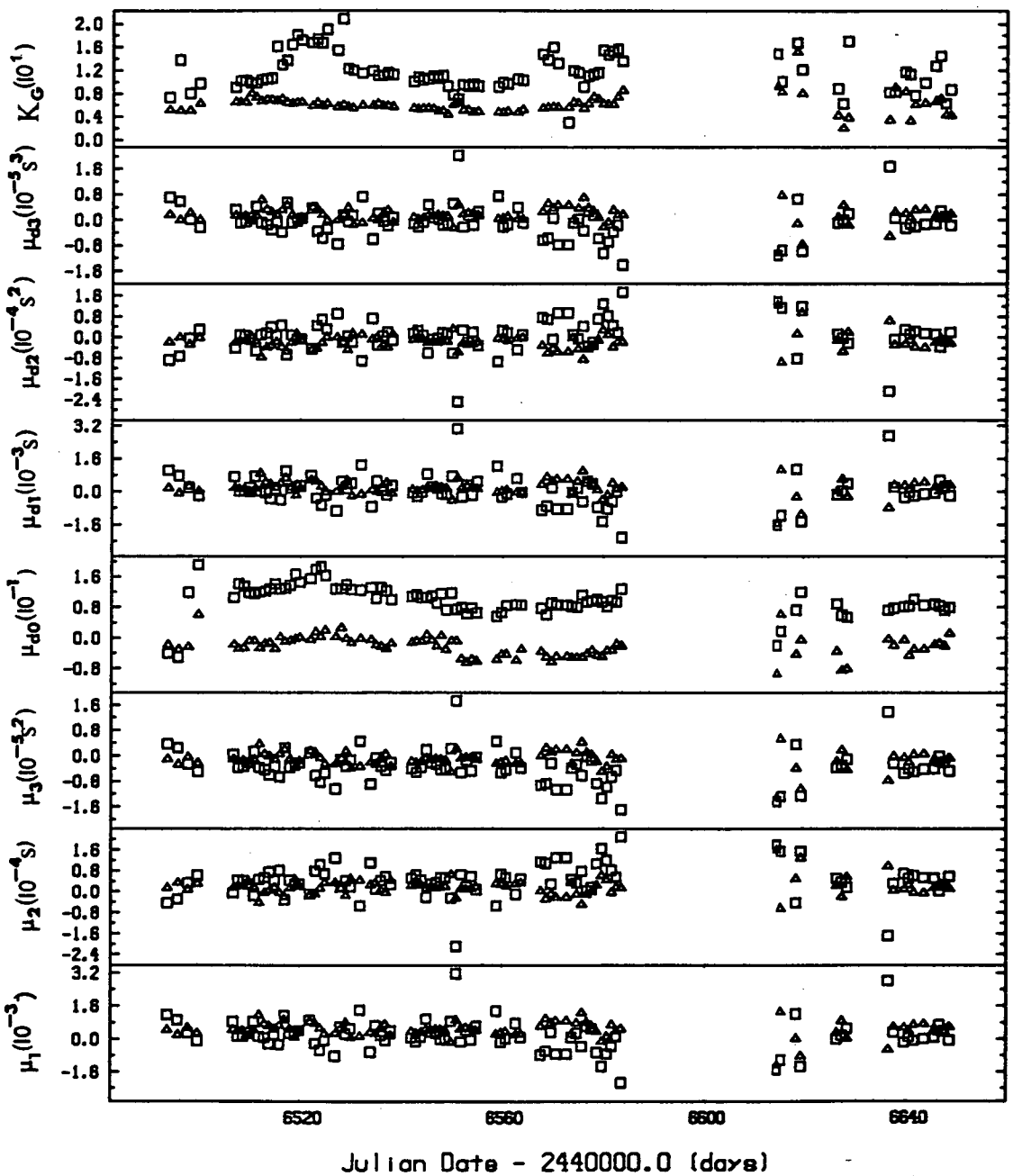

Fig. 7.4. Behaviour of the pulse shape parameters as a function of time as determined from daily mean profiles at 635 MHz (*squares*) and 954 MHz (*triangles*).

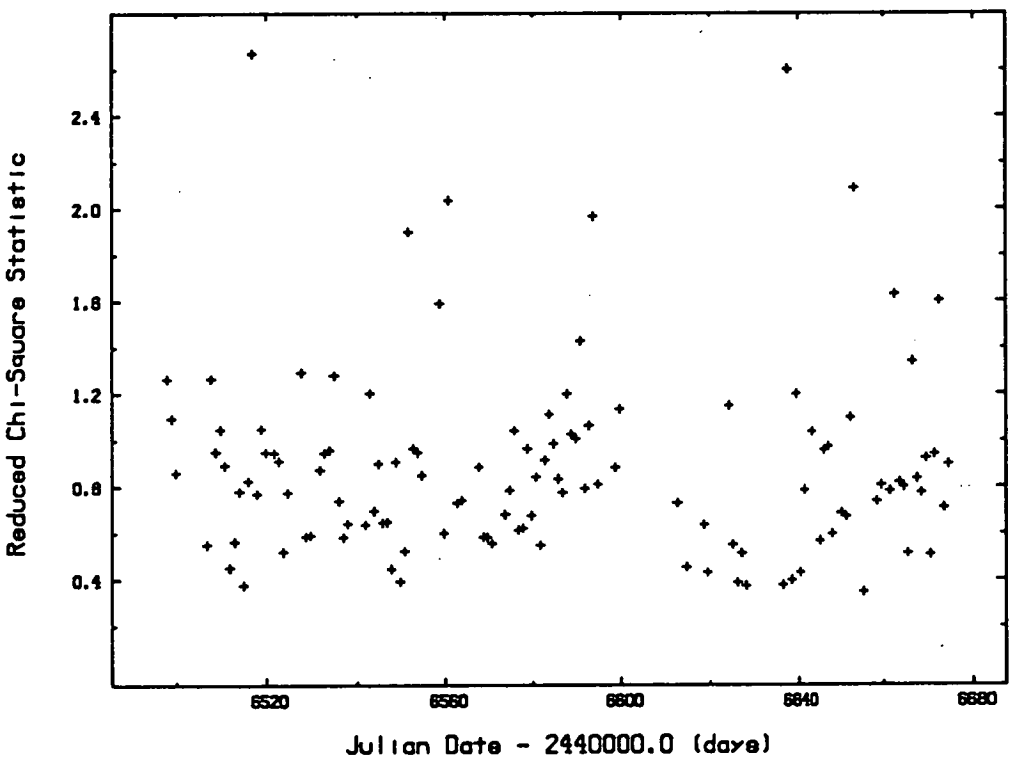

Fig. 7.5. Behaviour of the daily reduced χ^2 statistic as a function of epoch for the DM estimates of PSR0833-45.

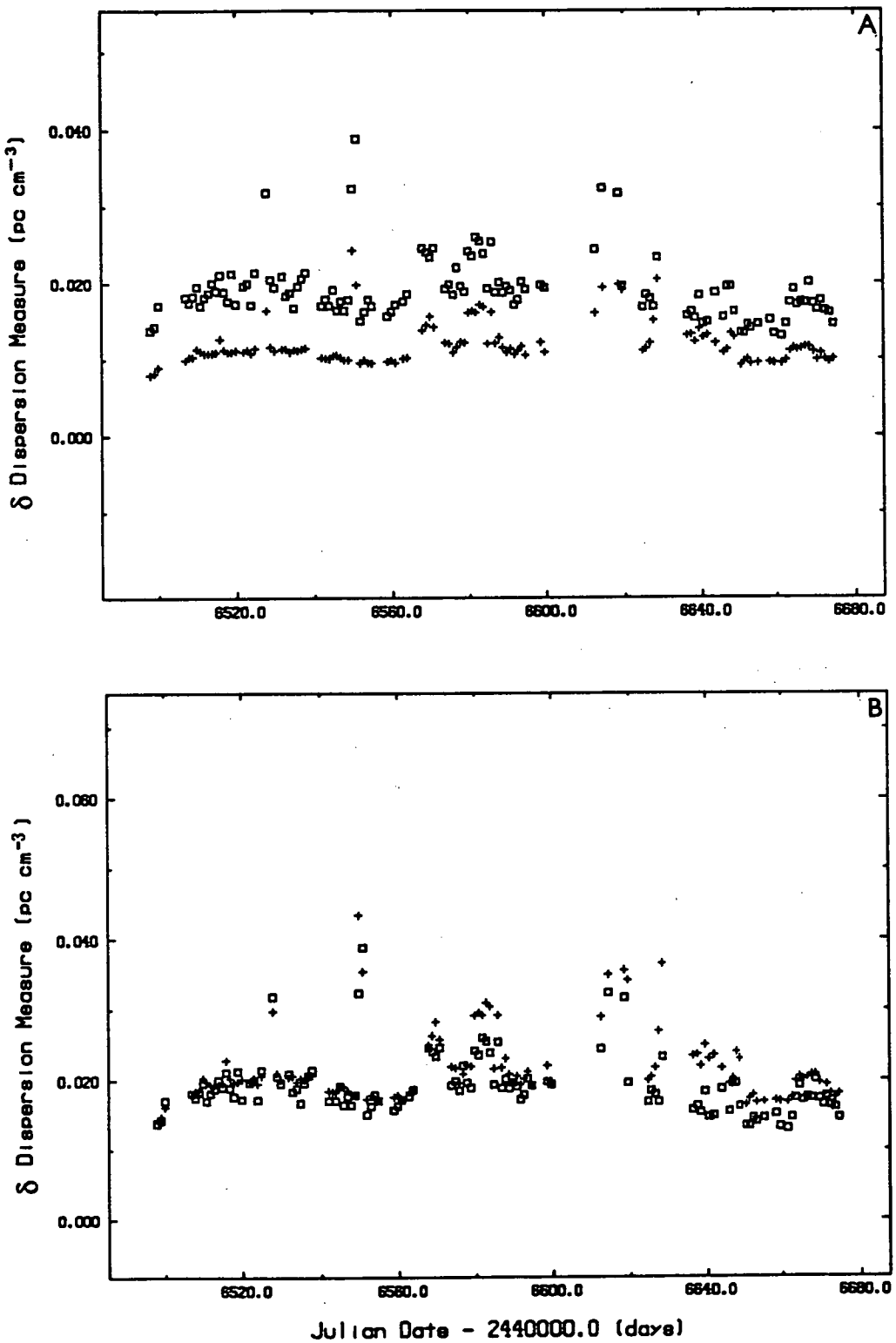

Fig. 7.6. Behaviour of the dispersion measure structure coefficient $\sigma_{DM(S)}$ (*squares*) and the formal dispersion measure uncertainty $\sigma_{DM(M)}$ (*crosses*) for PSR0833-45 as a function of epoch (a) from raw data; (b) after rescaling of the individual arrival time uncertainties to incorporate excess phase noise.

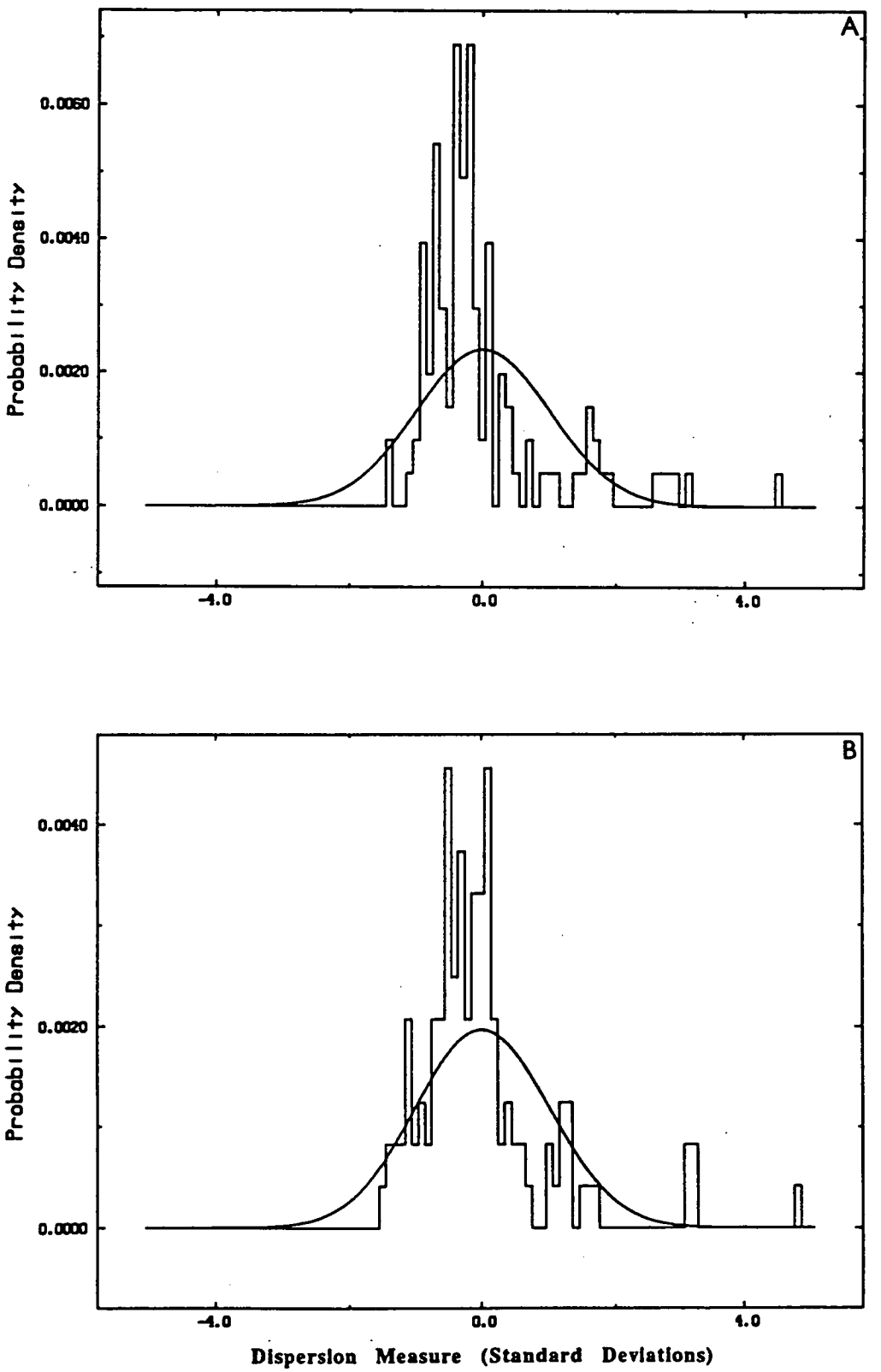

Fig. 7.7. Distribution of (a) dispersion measure structure coefficient $\sigma_{DM(S)}$ and (b) the rescaled formal dispersion measure uncertainty $\sigma_{DM(M)}$ for PSR0833-45.

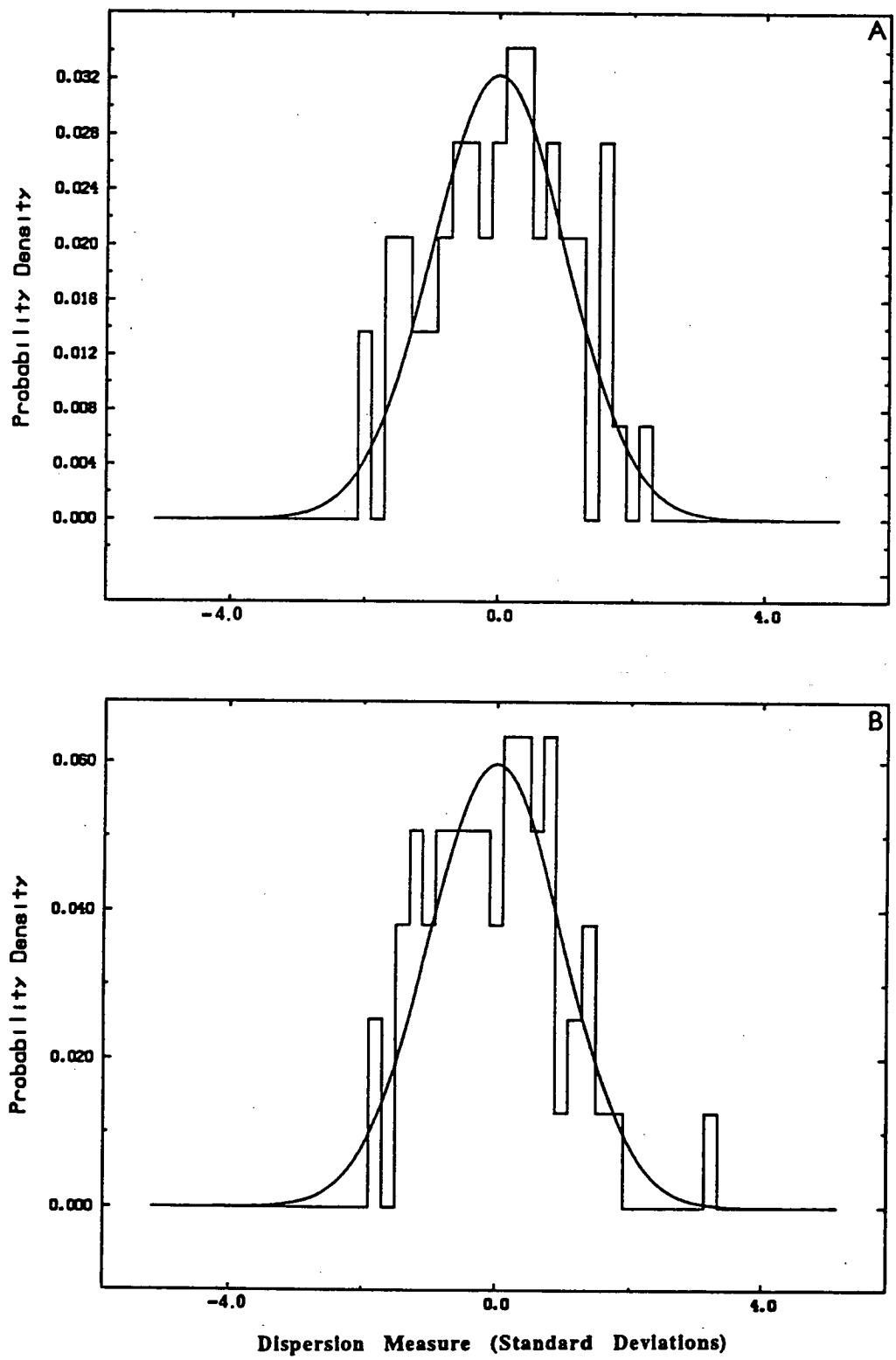

Fig. 7.8. Distribution of (a) dispersion measure structure coefficient $\sigma_{DM(S)}$ and (b) the formal dispersion measure uncertainty $\sigma_{DM(M)}$ for PSR1749-28.

means, are distinctly skewed. This is in contrast to the corresponding distributions for PSR1749-28 (figure 7.8), for which no evidence of excess phase noise is apparent (figure 7.9). Parameters for the distributions of $\sigma_{DM(M)}$ and $\sigma_{DM(S)}$ for both pulsars are summarized in tables 7.2 and 7.3.

An autocorrelation analysis, in a similar vein to that described in section 5.5, was applied to the DM estimates of each session to examine their independence. The results for 2, 5, 10, and 30 minute bin widths are shown in figure 7.10. There is no significant structure in comparison with the expectation for gaussian noise, although there appears to be a weak systematic trend.

7.3.3 Systematic Behaviour

Daily values were obtained of the weighted mean dispersion measure $\overline{DM}_d$ and its estimated 95% confidence interval

$$\sigma_{DM_d} = s_{DM_d}\left[1 + \frac{1}{4(N-1)}\right] \qquad N > 1$$

where s_{DM_d} is the sample standard deviation and N is the number of estimates. For Vela, these calculations were made for only those sessions containing 10 or more observations. The weighting parameter for each estimate was chosen as the inverse square of the formal error, which for PSR0833-45 was calculated from the rescaled measurement uncertainties at each frequency. The behaviour of $\overline{DM}_d$ as a function of epoch is presented for Vela and PSR1749-28 in figures 7.11 and 7.12 respectively.

The mean of the daily DM averages over the entire data set for PSR1749-28 was

$$\overline{DM}_{1749-28} = 50.323 \pm 0.024 \text{ pc cm}^{-3}$$

This is less than the catalogue value of 50.88 ± 0.14 pc cm^{-3}. The difference between the two values is equivalent to a phase offset of ~2 bins between the 635 MHz and 954 MHz pulses. A systematic error of this magnitude in the estimation of pulse phase values is considered highly unlikely.

For PSR0833-45,

$$\overline{DM}_{(0833-45)} = 68.4735 \pm 0.0017 \text{ pc cm}^{-3}.$$

This value is significantly different to other published measurements as summarized in figure 7.13. The error values quoted above are one standard deviation of the error in the mean.

The value of the fractional standard deviation s_f over the entire data set for each pulsar was

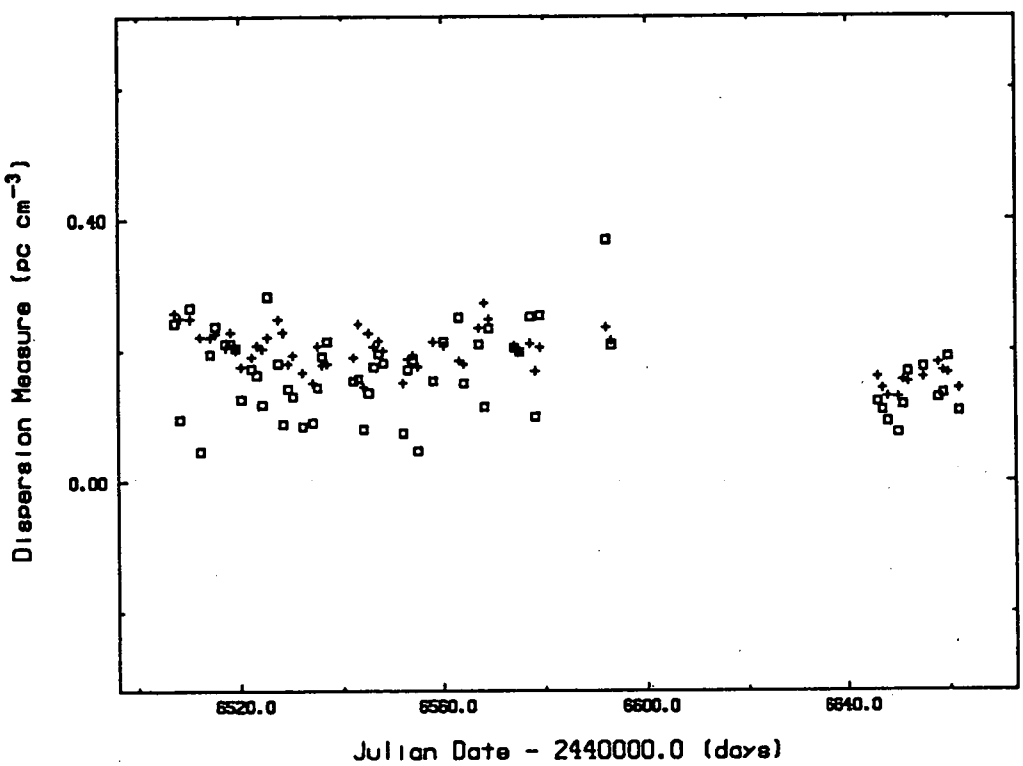

Fig. 7.9. Behaviour of the dispersion measure structure coefficient $\sigma_{DM(S)}$ (*squares*) and the formal dispersion measure uncertainty $\sigma_{DM(M)}$ (*crosses*) for PSR1749-28 as a function of epoch.

TABLE 7.2

DISTRIBUTION ANALYSIS

	PSR0833-45[a]	PSR1749-28
distribution of $\sigma_{DM(S)}$:		
reduced χ^2	55	0.72
mean (pc cm^{-3})	1.91×10^{-2}	0.18
standard deviation (pc cm^{-3})	0.27×10^{-2}	0.09
degrees of freedom	98	48
distribution of $\sigma_{DM(M)}$:		
reduced χ^2	137	0.45
mean (pc cm^{-3})	1.19×10^{-2}	0.19
standard deviation (pc cm^{-3})	0.42×10^{-2}	0.04
degrees of freedom	98	48

[a] The reported values were obtained prior to the rescaling of the measurement uncertainties at each frequency.

TABLE 7.3

DISTRIBUTION ANALYSIS FOR PSR0833-45 AFTER THE RESCALING OF THE MEASUREMENT UNCERTAINTY

scaling factors :	
σ_M at 635 MHz (μs)[a]	58±15
σ_M at 954 MHz (μs)[a]	34±10
σ_S at 635 MHz (μs)	104.5
σ_S at 954 MHz (μs)	60.0
σ_S/σ_M at 635 MHz	1.82
σ_S/σ_M at 954 MHz	1.75
distribution of $\sigma_{DM(M)}$:	
reduced χ^2	36
mean (pc cm^{-3})	2.15×10^{-2}
standard deviation (pc cm^{-3})	0.05×10^{-2}

[a] The error values quoted refer to one standard deviation of the pooled estimates.

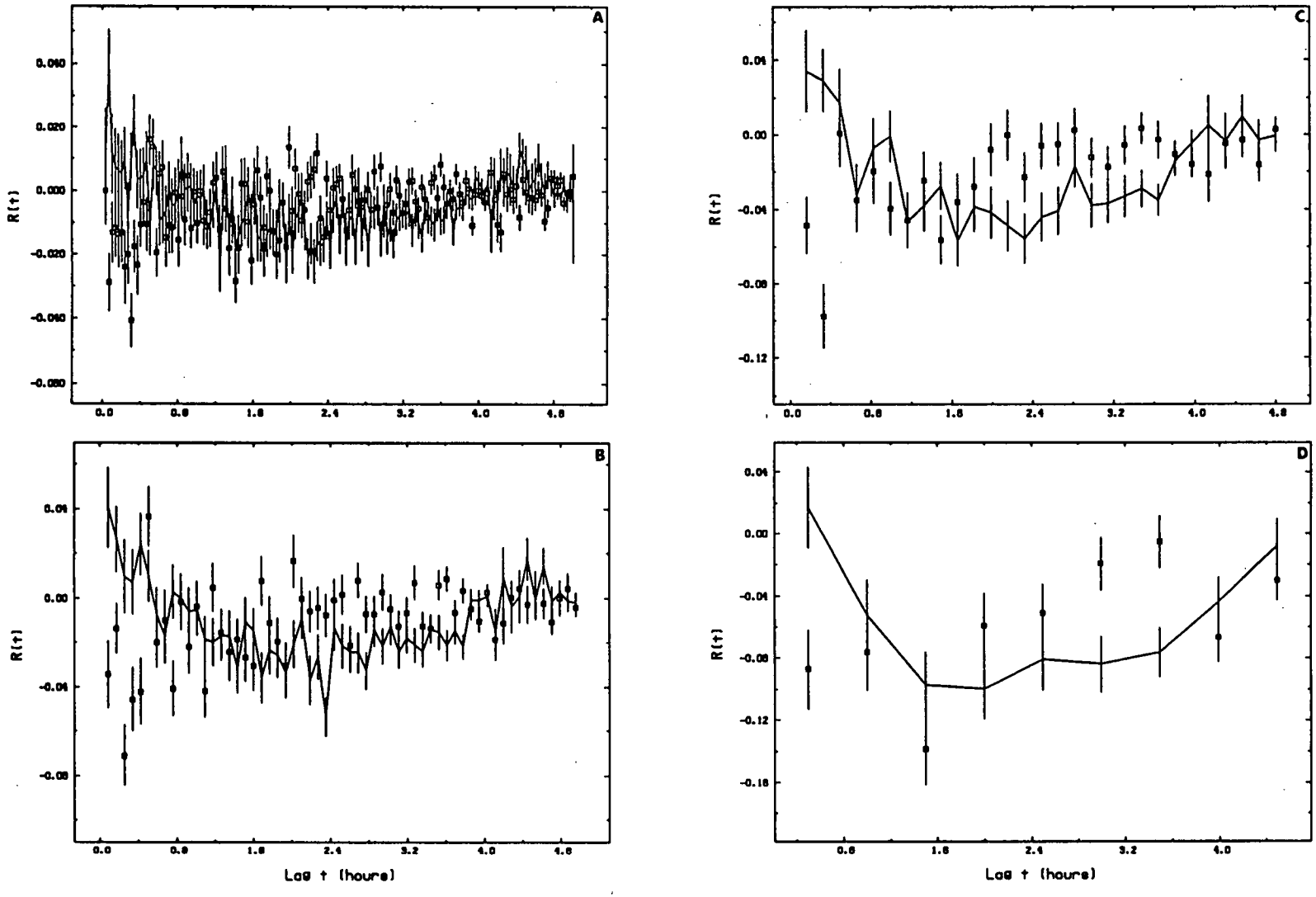

Fig. 7.10. Autocorrelation analysis applied to dispersion measure data. The autocorrelation function has been calculated for each session with bin widths of (a) 2 minutes, (b) 5 minutes, (c) 20 minutes, and (d) 30 minutes. DM estimates falling into each bin were averaged. The autocorrelation functions were stacked to obtain the mean (*connected points*) and an unbiased 95% confidence limit on the mean at each lag. For the estimates within each day, an equivalent number of gaussian samples with the same mean and variance of the observed population were generated. These random samples were subjected to the same analysis, providing means (*squares*) with associated confidence limits.

$$s_{f(0833-45)} = \frac{s_{DM}}{\overline{DM}} = 1.3\text{x}10^{-4}$$

$$s_{f(1749-28)} = 1.8\text{x}10^{-3}$$

The value of s_f for PSR1749-28 is larger than that for the Vela pulsar because of the comparatively longer sampling interval and the lower SN ratio of the integrated pulses.

As can be seen in figure 7.11, the dispersion measure of PSR0833-45 exhibits a quasi-linear trend. Similar behaviour for PSR1749-28 is far less obvious (figure 7.12) although the contiguity of the sampling is poor. A linear regression analysis was performed for both pulsars, and the results are presented in table 7.4.

A cross-correlation analysis was performed between the values of $\overline{DM}$ for each pulsar obtained on common days in order to examine the independence of the data sets. A correlation diagram is presented in figure 7.14. The results presented in table 7.4 indicate with high significance that the estimates are uncorrelated with and without trend removal from the Vela data.

In figure 7.15, the result of the application of a five day running binomial smoothing filter (with allowance for the regularity of the sampling) to the PSR0833-45 daily values is shown. While of little quantitative value, this plot highlights the possibility of systematic variations of the dispersion measure on short timescales. In order to test the significance of the variability, it was hypothesized that the estimates within each session were normally distributed and selected from a common normal population, and that the means of all sessions were identical. The following statistic was evaluated for sessions i and j;

$$z_{ij} = \frac{\overline{DM}_{d_i} - \overline{DM}_{d_j}}{\sqrt{\frac{\sigma_{DM_{d_i}}^2}{N_i} + \frac{\sigma_{DM_{d_j}}^2}{N_j}}}$$

where N is the number of estimates in each session. Under the above hypothesis, this parameter is normally distributed with zero mean and unit variance. A significance level of $\alpha = 0.01$ was decided upon, and the hypothesis was accepted if

$$z_{0.5\alpha} \leq z \leq z_{1-0.5\alpha}.$$

The confidence limit z_c is the abscissa of a normal distribution with zero mean below which the area is equal to c. For the chosen value of α, the confidence limit translates to $-2.58 \leq z \leq 2.58$. The value of z was calculated for the i-th and j-th sessions with $j \geq i$. From 7021 paired trials, the hypothesis was accepted on 3037 or 43% of occasions. The linear trend of equation 7.2 was subtracted, and the fraction of acceptances rose marginally to 55%. For $\alpha = 0.001$, the acceptance levels were 52% and 64% for the raw and detrended samples respectively.

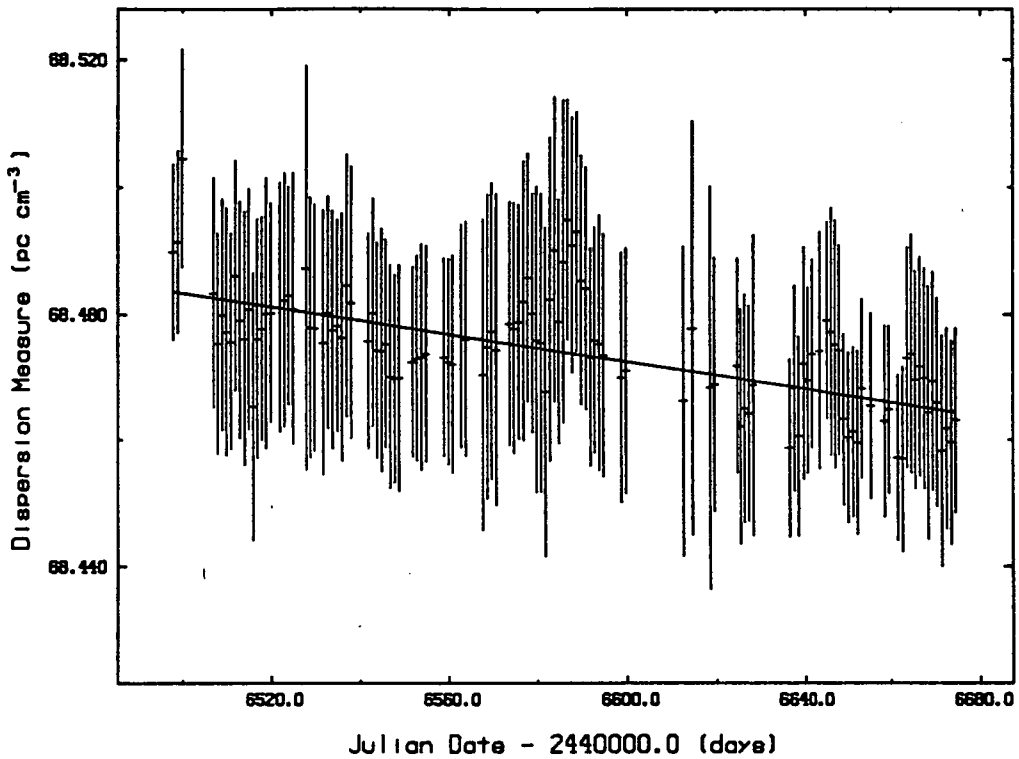

Fig. 7.11. Mean daily dispersion measure $\overline{DM_d}$ as a function of epoch for PSR0833-45. The linear trend obtained from the regression analysis summarized in table 7.4 is superimposed. The vertical error bars extend σ_{DM_d} either side of each mean.

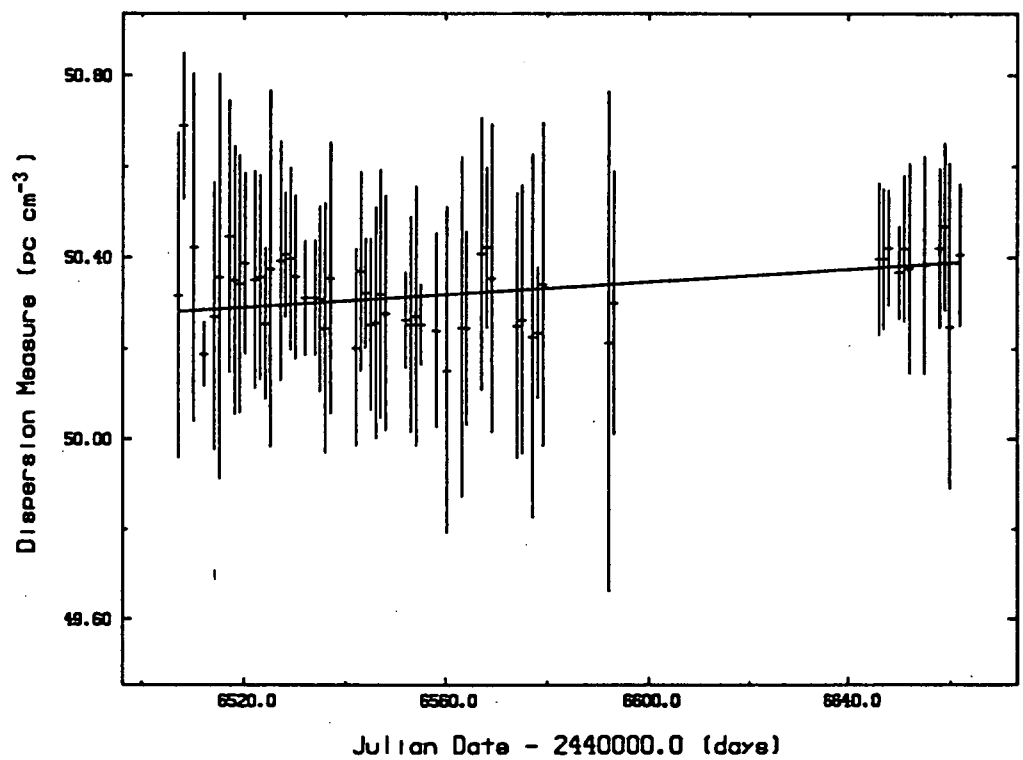

Fig. 7.12. Mean daily dispersion measure $\overline{DM_d}$ as a function of epoch for PSR1749-28. The linear trend obtained from the regression analysis summarized in table 7.4 is superimposed. The vertical error bars extend σ_{DM_d} either side of each mean. Note the difference in scales between this figure and figure 7.9.

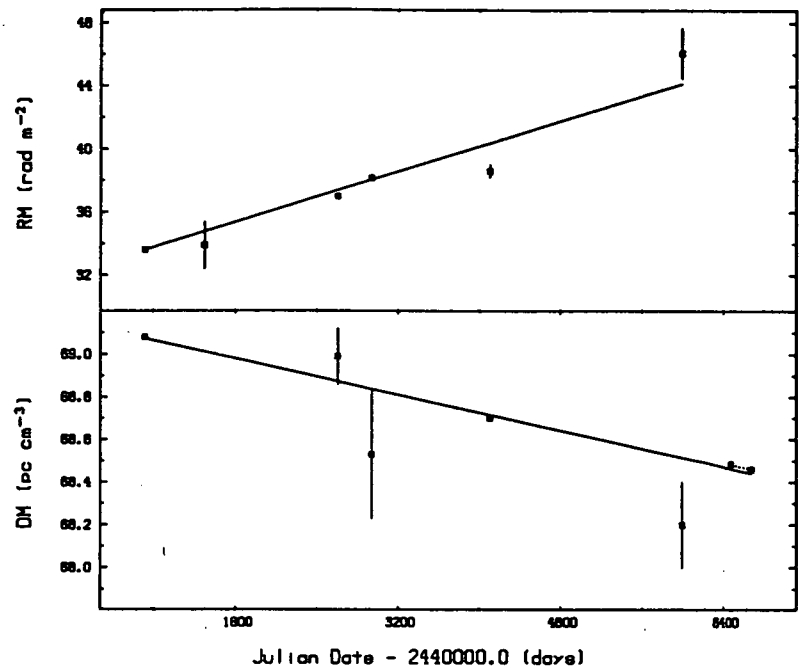

Fig. 7.13. Behaviour of (a) rotation measure (RM) and (b) dispersion measure (DM) for PSR0833-45. Weighted least-squares linear fits have been superimposed. The vertical error bars are represent the range of the 95% confidence limits. The trend obtained from the DM observations presented in this chapter is indicated by the dotted line connecting interpolated values at the limits of the observation timespan. All other data are from Hamilton, Hall, and Costa (1985).

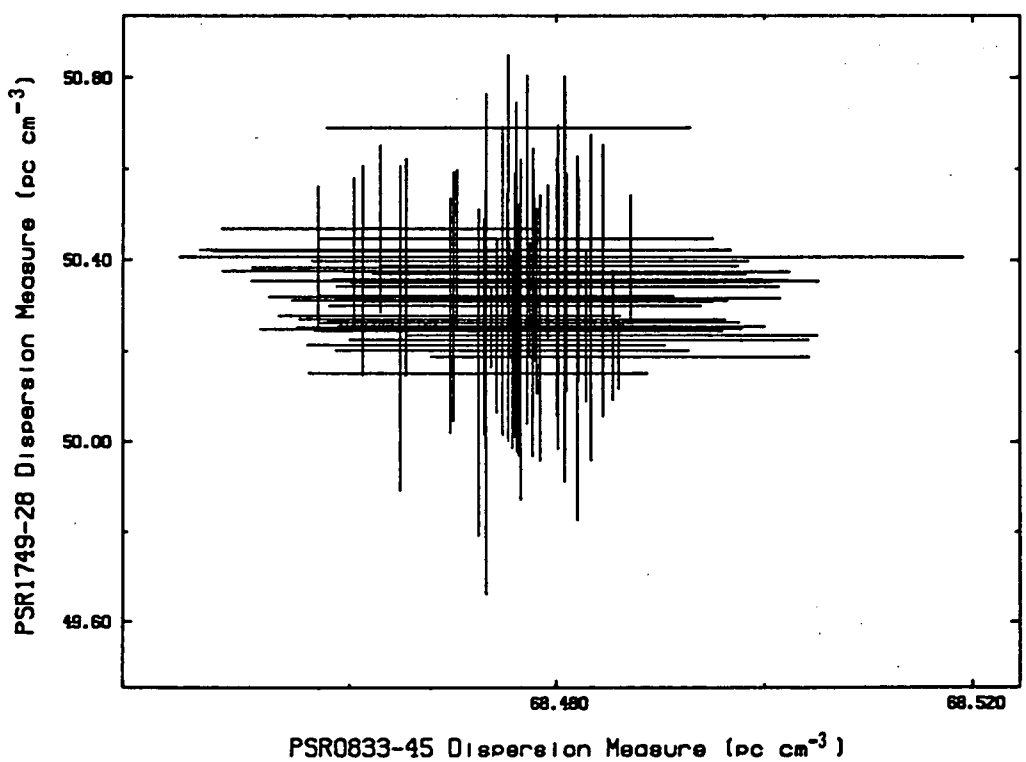

Fig. 7.14. Correlation diagram of mean daily dispersion measure $\overline{DM}_d$ for PSR1749-28 against that for PSR0833-45. The error bars extend σ_{DM_d} either side of each mean. The values of $\overline{DM}_d$ were paired providing that their epochs differed by 12 hours or less.

TABLE 7.4

LINEAR REGRESSION AND CROSS-CORRELATION ANALYSIS

	PSR0833-45	PSR1749-28
linear regression :		
gradient (pc cm^{-3} yr)	-0.040	0.26
error of gradient (pc cm^{-3} yr)	0.011	0.17
linear correlation coefficient r_l	0.69	0.38
lower 95% confidence limit on r_l	0.34	0.13
upper 95% confidence limit on r_l	1.03	0.66
$P(r_l)$	≈ 0	0.003
number of estimates	119	59
correlation of DM against $\sigma_{DM(S)}$:		
r_c	-0.02 (0.04)	0.04
lower 95% confidence limit on r_c	-0.20 (-0.15)	-0.22
upper 95% confidence limit on r_c	0.16 (0.22)	0.30
$P(r_c)$	0.83 (0.71)	0.75
correlation of DM against $\sigma_{DM(M)}$:		
r_c	0.18 (0.03)	-0.17
lower 95% confidence limit on r_c	0.00 (-0.15)	-0.44
upper 95% confidence limit on r_c	0.36 (0.22)	0.09
$P(r_c)$	0.06 (0.72)	0.19
correlation of $\sigma_{DM(M)}$ against $\sigma_{DM(S)}$:		
r_c	0.82	0.48
lower 95% confidence limit on r_c	0.96	0.27
upper 95% confidence limit on r_c	1.33	0.79
$P(r_c)$	≈ 0	≈ 0

Notes :

The 95% confidence error is quoted for the gradient of the linear fit. The observationally and uniformly weighted product-moment correlation coefficients are denoted by r_l and r_c respectively. The probability of exceeding $|r|$ for a random sample of uncorrelated variables is denoted by P(r). The bracketed values for PSR0833-45 were obtained after removal of the linear trend.

TABLE 7.5

CORRELATION OF $\overline{DM}_{0833-45}$ AGAINST $\overline{DM}_{1749-28}$

	raw	detrended
r_c	-0.02	-0.10
lower 95% confidence limit on r_c	-0.29	-0.36
upper 95% confidence limit on r_c	0.25	0.18
$P(r_c)$	0.88	0.50

Notes :

The *detrended* values have been obtained from paired observations for which a linear trend (table 7.4) has been removed from the estimates for PSR0833-45. The uniformly weighted product-moment correlation coefficient is denoted by r_c. The probability of exceeding |r| for a random sample of uncorrelated variables is denoted by $P(r_c)$. The number of paired observations used in the analysis was 55.

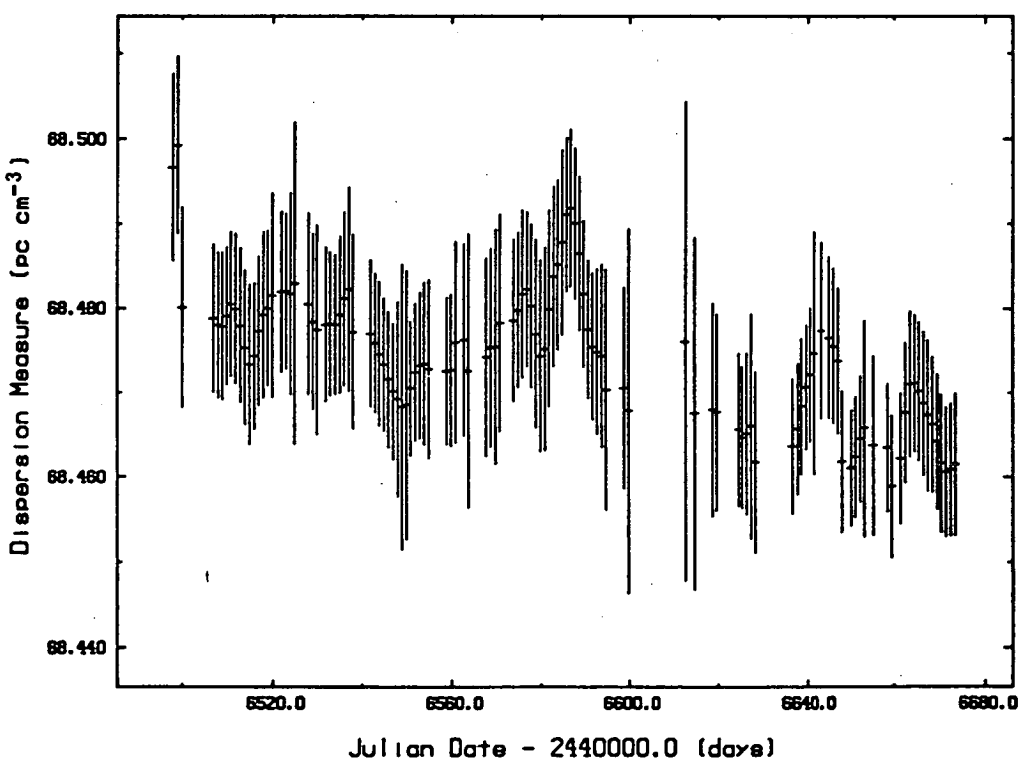

Fig. 7.15. Application of a 5 day running binomial smoothing filter (with adjustment for uneven sampling) to the dispersion measure data of PSR0833-45 in figure 7.11.

The data were partitioned into three sets. The overall linear trend was removed, and the hypothesis was tested with $\alpha = 0.001$ giving acceptance ratings of 72%, 7%, and 71% for the epoch ranges TJD < 6560, 6560 ≤ TJD ≤ 6600, and TJD > 6600, respectively.

For k trials, the probability of rejecting the hypothesis is $\alpha^k \approx 0$. Given the results above, the values of $\overline{DM}_d$ in the central epoch span show evidence of belonging to a distribution separate to that for the other epoch spans.

A comparison of figures 7.6b and 7.11 suggests the possibility of a weak correlation between $\overline{DM}_d$ and both $\sigma_{DM(M)}$ and $\sigma_{DM(M)}$, particularly within the central epoch span. As shown in table 7.5 and figure 7.16, the correlation of these parameters is of low significance, particularly when the linear trend is removed from $\overline{DM}_d$.

7.4 MEASUREMENT CONSIDERATIONS

It is of use to consider the significance of instrumental effects on the behaviour of the data presented in the previous section. By requiring the apparent systematic trend in DM for PSR0833-45 to be due to the frequency drift of one of the receiver centroids, then

$$f_1(t_i) - f_1(t_f) \approx 184 \text{ kHz} \quad \text{and} \quad f_2(t_i) - f_2(t_f) \approx -54 \text{ kHz}$$

where t_i and t_f are the initial and final epochs of the 200 day interval, respectively, and $f_1(t_i) = 635$ MHz, $f_2(t_i) = 954$ MHz are the nominal receiver centroids. Changes of either of these magnitudes would have been detected between the calibrations conducted at the start and end of the dual frequency timing programme. It is clear that the Rubidium standard would have contributed negligibly to any drift of the local oscillator and hence receiver centroids. In any case, such a drift would occur in the same direction for both receivers.

The discrepancy between the observed and catalogued value of DM for PSR1749-28 translates to an error of 2.0 MHz in $f_1(t_i)$ and -6.5 MHz in $f_2(t_i)$. Either of these errors would have been immediately obvious during the frequency calibration procedure.

If the frequency of each receiver centroid was a function of time, then based on the Vela observations

$$\frac{d\,DM}{dt} = k = \frac{-DM}{f_1^2 f_2^2 (f_2^2 - f_1^2)} \left\{ f_1^4 \frac{\partial[f_2^2]}{\partial t} - f_2^4 \frac{\partial[f_1^2]}{\partial t} \right\}$$

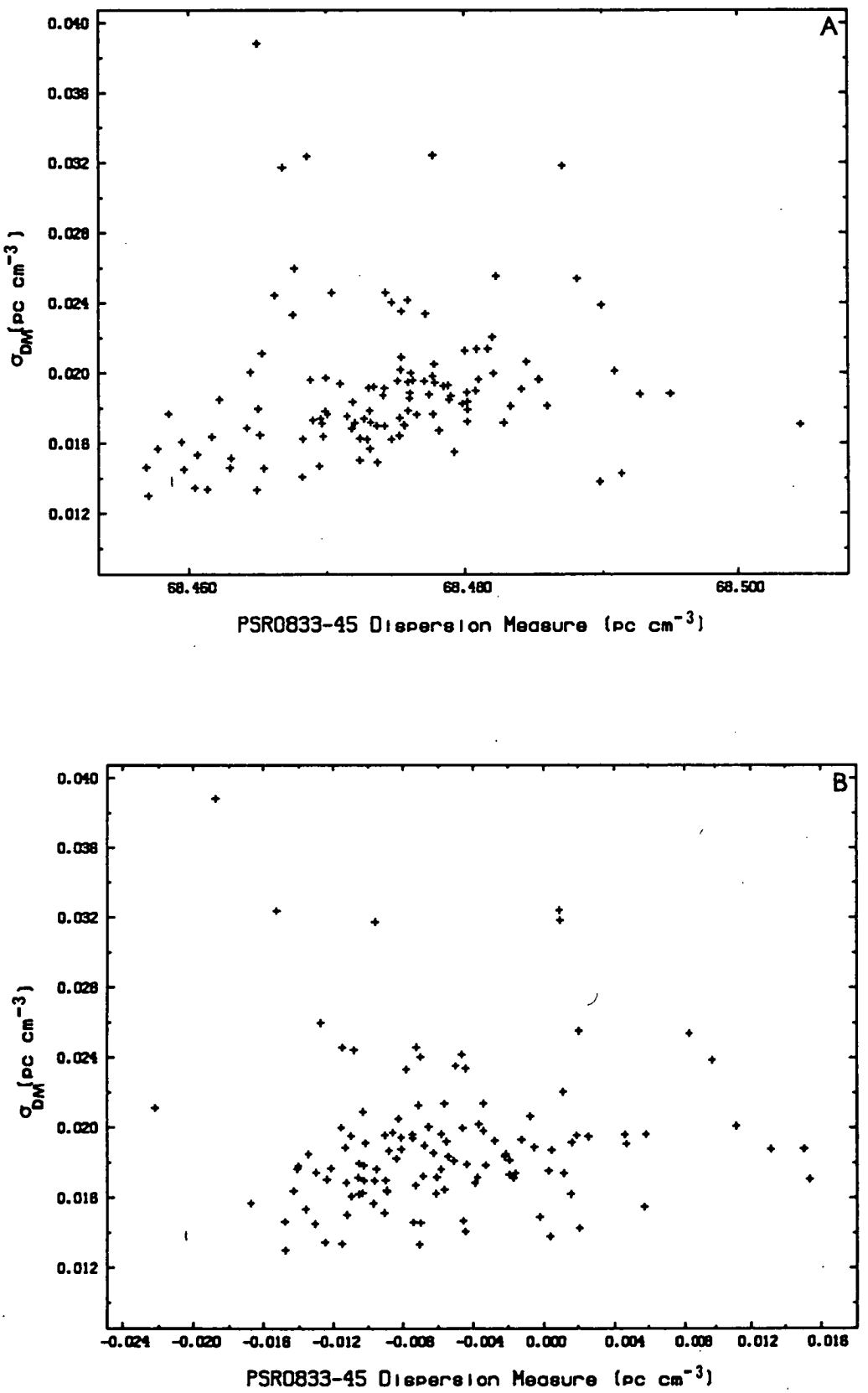

Fig. 7.16. Correlation diagram of $\sigma_{DM(M)}$ against $\overline{DM}$ for PSR0833-45 (a) prior to and (b) after the removal of the linear trend in DM.

where k is the observed slope of the linear trend. The form of the above expression suggests the non-linear variation of f_1 and/or f_2. These are difficult to conceive given their required consistency over the 200 day span.

The absence of any obvious time dependence of the moments of the mean daily profiles rules out significant variability of important instrumental parameters. In particular, a change in either or both of the receiver pre-detection bandpass shape and the post-detection time constant would be expected to influence pulse width and consequently the moment parameters. An additional source of pulse shape modification would have arisen from cross-coupling between the receiver channels in combination with the phase dependence of the pulse polarization vector and the time dependence of the amount of Faraday rotation. The latter effect was due to changes in the hour angle of the source and the variation of parameters within the ionosphere and ISM. Because the isolation between the receiver channels was better than -30 dB, the influence of variable Faraday rotation on the shape of the I profiles was considered inconsequential.

7.5 DISPERSION DELAY VARIATIONS DEDUCED USING HRAO DATA

As noted in section 6.6, the residuals obtained from the spindown equation applied to combined LRO and HRAO data sets suggested that dispersion delay variations were present.

The data studied consisted of the sets of residuals presented in figures 6.11b to 6.11i, inclusive, as well as the residual set obtained from the application of model 50 to combined pre- and post-glitch spans of length 600 and 400 days. All of the HRAO arrival times were delayed by 12.839 ms so that the last pre-glitch residuals for the two sites coincided.

Weighted averages of the residuals for each site and day were then evaluated. The temporal behaviour of each set of averages was approximated by a weighted cubic spline. The 'smoothness' of the spline function $S(t_i)$ was selected by requiring

$$A_S = \sum_{i=1}^{N} \left[\frac{S(t_i) - R(t_i)}{w(t_i)} \right]$$

to be less than an arbitrarily chosen value. Here $R(t_i)$ and $w(t_i)$ are the residual and weight associated with the i-th observation respectively. The difference

$$\Delta R = S(t_i)_{LRO} - S(t_i)_{HRAO}$$

was then obtained at regularly spaced epochs. As an example, the results of this procedure for residuals of figure 6.11i are presented in figure 7.17. In figure 7.18a, ΔR has been converted to a 'synthetic' dispersion measure ΔDM_S relative to the epoch of the last pre-glitch observations. In addition, the data from spline differences of other fitted models are overlaid to indicate the stability of the method. Data spanning the glitch are presented in figure 7.18b.

In the construction of the synthetic DM plots it was assumed that all of the variable differential timing behaviour between the sites was purely due to dispersive effects. The plots are only intended to provide general information on the history of dispersion measure changes. The variation prior to February, 1986 (~TJD 6458) is considered to be representative of the true DM variation given the accuracy of the absolute time maintained at each observatory. However, after this date the data trend may include the effects of LRO clock drift, as the uncertainty of absolute LRO barycentric arrival times was greater owing to a lack of time transference data needed for precise clock corrections.

Of note in figure 7.18b is the absence of any obvious glitch-related change. It is also useful to compare the DM value obtained by Hamilton, Hall, and Costa (1985) at TJD 5989 (figure 7.13) with that deduced using data from figures 7.11 and 7.18b. HHC obtained DM = 68.2±0.2 pc cm^{-3} (2σ error), while the timing data presented here suggested DM ~ 68.43±0.1 pc cm^{-3} (2σ error). The hypothesis that the two values differ because of sampling effects would be rejected with ~ 50% confidence. In any event, the suggestion that DM increased between the HHC observations and those made during 1986 at Llanherne are supported by the available data.

An additional remark concerns the time offset between the LRO and HRAO data of ~ 12.8 ms. If this was totally the result of an erroneously assumed DM when removing dispersion delay to obtain the barycentric times, then the suggested value is ~67.7 pc cm^{-3}, which is clearly inconsistent with the data in figure 7.11. The origin of the implied excess delay (which may be as large as 7 ms) is unknown.

7.6 DISCUSSION

7.6.1 The Vela Pulsar

The evidence for significant variability of Vela's dispersion measure is firm. The long-term change of ~ 0.04 pc cm^{-3} yr^{-1} observed during 1986 is consistent with previous measurements. Unfortunately, simultaneous rotation measure observations

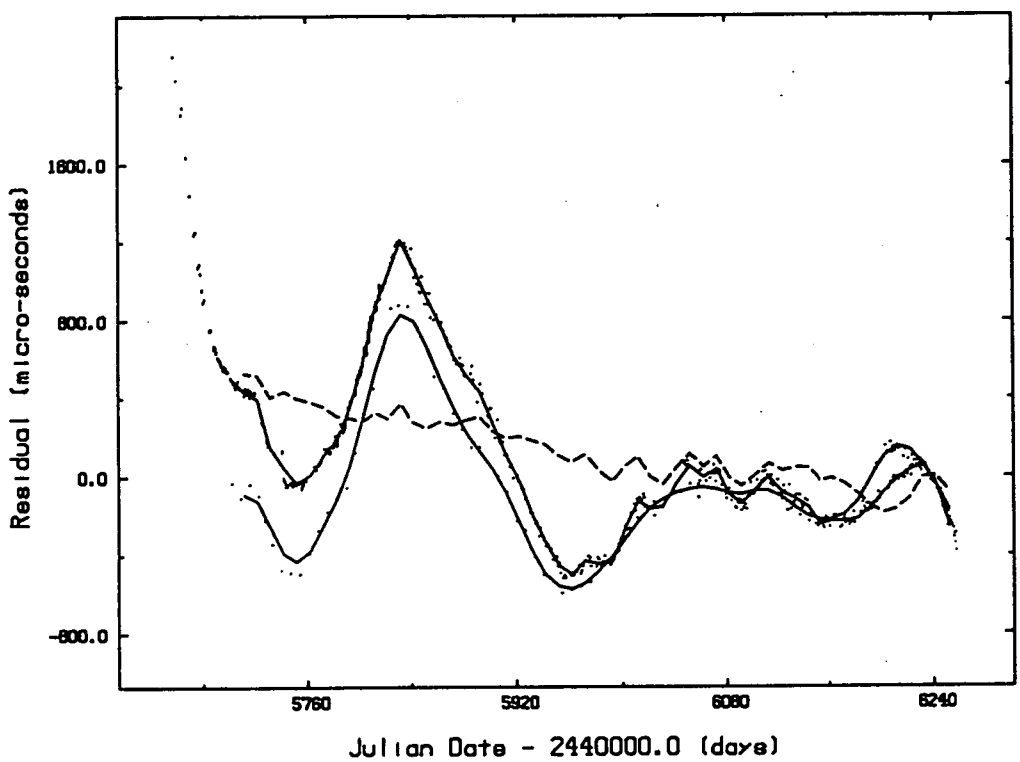

Fig. 7.17. Demonstration of the application of cubic spline approximations to the weighted mean daily residual for both sites from the data presented in figure 6.11i. The smoothness parameter A_S (equation 7.1) was arbitrarily set as 10^4 and 10^3 for the LRO and HRAO residuals, respectively. Values of the spline approximation at 10 day intervals for each data set are joined by solid line segments. For each curve, the associated mean residual values are plotted (*points*). The standard error of each mean is typically less than 10μs. The difference ΔR (equation 7.2) is plotted at 10 day intervals (*dashed curve*).

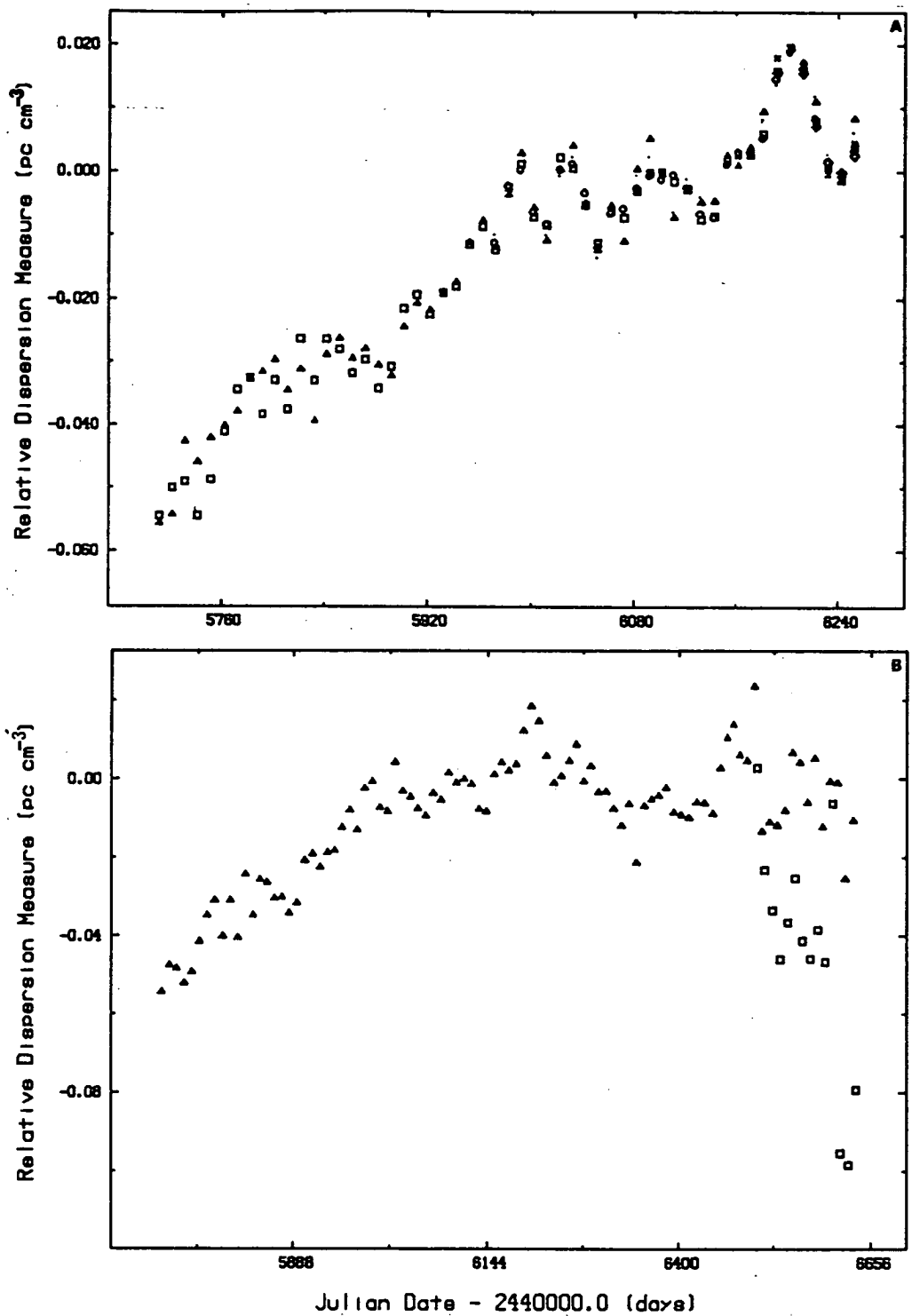

Fig. 7.18. (a) Synthetic dispersion measure ΔDM_S obtained from the conversion of spline differences presented in figure 7.17 (*squares*). Also shown are values of ΔDM_S obtained from splines constructed using residuals from models 41 (*triangles*), 39 (*circles*) and 40 (*points*). (b) Spline approximations have been constructed for residuals resulting from the application of the 13th model of table 6.7 to pre- and post-glitch data. The resulting ΔDM_S values have been plotted at 10 day intervals; *triangles* - from HRAO and LRO 635 MHz data, *squares* - from HRAO and LRO 954 MHz data. The 954 MHz residuals were offset by 3.44 ms. This delay represents the expected difference between the residuals of the two LRO frequencies given that the barycentric times were calculated assuming a dispersion measure of 69.08 pc cm^{-3} rather than 68.48 pc cm^{-3} which was evaluated at the start of the dual frequency observations from absolute dispersion delay measurements.

were not available, which would have proved useful in isolating the environment responsible for the observed changes in the light of the systematic RM and DM variability noted by HHC for Vela, and also by Rankin *et al.* (1988) for the Crab pulsar.

Here, the implications of the observed dispersion measure changes are discussed with reference to the sites which are likely to contain regions of turbulent enhanced plasma density.

The shock front of an expanding SNR is thought to be a natural site for the *diffusive* acceleration of interstellar cosmic rays (Blandford and Ostriker, 1978). Following Spangler *et al.* (1986), the extent of the acceleration layer where the plasma density is enhanced may be approximated as

$$l \approx \frac{v^2}{V} \frac{\gamma}{\Omega_c} \left(\frac{B_0}{b} \right)^2 \eta$$

where v and V are the speeds of the accelerated particles and the shock front, respectively, γ is the Lorentz factor of the particles that generate the wave layer, Ω_c is the non-relativistic cyclotron frequency, B_0 and b are the background and wave magnetic field strengths, respectively, and η is fractional bandwidth of the excited waves. As noted by Spangler *et al.* (1986) the estimation of l is subject to the uncertainty which accompanies each of the associated parameters. Using reasonable values for the above parameters, Spangler *et al.* (1986) find l to be on the order of a few parsecs.

If the region responsible for the changing plasma column density to the pulsar is associated with the diffractive scattering region, then a transverse speed of 50 km s^{-1} may be assumed (Cordes, 1986). If the excess plasma is confined to a slab of thickness Δz (pc) lying normal to the direction to the pulsar, then the density gradient across the slab scales as $\sim 3.8 \times 10^{-3} \Delta z^{-1}$ cm^{-3} AU^{-1}. By assuming that Δz is on the order of a few parsecs, then the inferred density gradient is not unreasonable given typical conditions for SNR interaction with the ISM (McKee and Ostriker, 1977).

The possibility of dispersion measure variations on the timescale of days was suggested by the LRO observations, although the significance of this activity in comparison with measurement uncertainties is low. Time-variable activity would be expected if filaments of enhanced plasma density transit the line of sight.

According to Kennel and Coroniti (1988), the Crab pulsar is immersed in a cavity of radius ~ 0.1 pc which is pervaded by the relativistically out-flowing pulsar wind. The majority of the rotational energy lost from the pulsar crosses this region in

the form of magnetohydrodynamic (MHD) waves which disipate their energy at a shock front located at a radial distance of ~2 pc where the supersonic flow is terminated. In the case of the Vela pulsar, it is evident that the wind zone may have a radial extent of ~ 25 pc (Seward, 1985).

Ögelman, Koch-Miramond, and Auriére (1989, *preprint*; hereafter ÖK-MA) have found evidence for a faint optical counterpart to the 2 arc-sec diameter X-ray nebula surrounding the Vela pulsar (Harnden *et al.*, 1985). If the optical nebulosity is not due to foreground emission from the surrounding SNR, then its energy content is four orders of magnitude less than the rotational kinetic energy loss of the pulsar. This would seem to imply that nebular region is wholly pervaded by the supersonic wind, and not subjected to significant energy input via shock disipation.

There is an indication that the optical emission from the wind zone possesses spatial structure (ÖK-MA). In the case of the Crab pulsar, filamentary nebulosity also exists in this region. Scargle (1969) found evidence that these features exhibit dynamic spatial and energetic activity, that may be associated with rotational fluctuations of the pulsar (in particular the September, 1969 glitch). Rees and Gunn (1974) tentatively associated the filaments with turbulence at the MHD shock front coinciding with the boundary of the wind zone. At this surface, the energy of the MHD waves accelerates electrons to relativistic energies, which then radiate via the synchrotron process in the toroidal field presumed to pervade the region. However, in the case of Vela, supersonic flow is regarded as extending beyond the field of view studied by ÖK-MA.

Dobrowolny and Ferrari (1976; hereafter DF) and Benford, Bodo, and Ferrari (1978; hereafter BBF) have sought an explanation for the origin of the Crab's wind-zone filaments in terms of plasma turbulence set up by parametric (electrostatic and electromagnetic) interactions between the energy transported by the wind and the magnetic dipole radiation generated at the rotational frequency of the pulsar. At a radial distance from the pulsar where the MHD wave and plasma frequencies are equal, standing waves of compressed plasma may be set up. ÖK-MA estimate that this situation arises for the Vela pulsar where the radial distance is a few multiples of $7 \times 10^{17} \sqrt{\gamma_6}$ cm where γ_6 is the Lorentz factor of the wind in units of 10^6. The motion of spatial structures this large could not account for short term fluctuations of DM but may be a plausible source of the slower variation. However, no information is available as to the expected velocity range of the wisps or even why such motion should occur. Scargle (1969) has suggested that the Crab wisps have velocities a substantial fraction of c. Taking 0.1 c as a velocity value for a moving wisp, then it will move its own width in approximately 6 years.

7.6.2 PSR1749-28

The mean plasma column density along the path to PSR1749-28 is ~ 0.03 cm^{-3} which is very close to the value of ~ 0.025 cm^{-3} held typical for the ISM (Ables and Manchester, 1974). Therefore even though the line of sight to this pulsar lies in the direction of the galactic centre, it evidently does not traverse regions of anomalous plasma density, in contrast to the situation for the Vela pulsar.

The observations of PSR1749-28 yielded a mean dispersion measure of 50.32±0.024 pc cm^{-3}. This value differed from that measured by Lyne and Rickett (1968) by $\delta DM \sim -0.56$ pc cm^{-3}. For the present observations, inaccurate knowledge of the receiver centre frequencies or a systematic error in the phase estimation procedure were unlikely to contribute to the majority of this discrepancy. It is possible that differential galactic rotation has resulted in the passage of a region of excess plasma density out of the line of sight. The excess density required to produce the suggested change of δDM over a timescale of 18 years is 0.56 Δz^{-1} cm^{-3} (where Δz is the thickness of region of excess plasma expressed in pc). By assuming a distance of 1 kpc, Cordes (1986) has estimated the relative transverse velocity between the pulsar and the scattering material along the line of sight as ~ 15 km s^{-1} using scintillation measurements. This value is similar to the expected maximum relative velocity between the Earth and the pulsar due to differential galactic rotation (Cordes, 1986). The density of a spherical plasma cloud of radius $r = 10^{-5} v_r$ pc moving out of the line of sight with relative velocity v_r (km s^{-1}) over an interval of 18 years would require a density of $\rho_e = 2.8 \times 10^4 v_r^{-1}$ cm^{-3} to produce the inferred DM change. For $v_r = 10$ km s^{-1}, $r \sim 10^{-4}$ pc, and $\rho_e \sim 3 \times 10^3$ cm^{-3}. The latter value would be anomalous given estimates of ρ_e thought typical of HI clouds and SNR shock fronts (McKee and Ostriker, 1977).

7.7 CONCLUSIONS

Observations have been presented which suggest that the dispersion measure for the line-of-sight to the Vela pulsar decreased at an average rate of 0.04 pc cm^{-3} yr^{-1} occurred during a 200 day span of 1986. This behaviour is consistent with the motion of an unresolved large-scale plasma structure, possibly associated with the foreground region of the SNR, across the sight-line.

The quality of the observations was tested in detail in order to ascertain at what level fluctuations of the deduced DM values were significant with respect to the

expectation of measurement effects. There was some evidence for fluctuations of DM on the timescale of a few days however independent confirmation is required.

It is clear that the pulsar's environment is particularly dynamic and there is much scope for further work. High time resolution DM and RM measurements should be an integral part of any timing programme. An immediate benefit for the timing data would be the ability to remove variable dispersive effects which act to contaminate the timing noise spectrum. Areas that demand additional effort are the characterization of the timescale of DM and RM variations, and their possible association with rotation fluctuations, and the accurate long-term monitoring of the pulse flux and scattering parameters. An additional use of polarization information would be in the investigation of the stability of the radiation mechanism.

The discrepancy between the value of DM deduced for PSR1749-28 from the LRO observations and that obtained by Lyne and Rickett (1968) suggested that the plasma density along the path to this pulsar may have decreased if either of the measurements are not subject to systematic errors. Further observations are required to verify the measurements of DM for this pulsar and to examine the possibility that this quantity is variable.

CHAPTER 8 - CONCLUSIONS

8.1 INTRODUCTION

Summarized in the following six sections are conclusions drawn from the pulse timing observations presented in this thesis. This work, together with the review of the current understanding of the nature of the Vela pulsar has suggested areas of future research that are discussed in the remaining two sections.

8.2 QUALITY OF THE LRO TIMING DATA

The LRO timing data represents the most contiguous high time resolution set available for glitches 5, 6, and 7 of the Vela pulsar.

The locally maintained version of UTC was known to an accuracy of better than 5 μs. The estimation of local pulse arrival times through the cross-correlation of integrated pulses and a standard template profile had a typical uncertainty of 40-60 μs. The method employed for this purpose was found to be robust for SN ratios in excess of 2.5. It was considered that PEP 311 solar system ephemeris that was used in the reduction of barycentric arrival times did not contribute significant periodic errors on timescales less than the epoch range of the LRO observations.

Little data was available to check the accuracy of the modelling of the clock drift during the last 7 months of observations during 1986. A discrepancy of no more than 150 μs was likely to have existed between the true and observed barycentric arrival times at the end of the observing programme.

8.3 THE GLITCH RELAXATION PROCESS

It is firmly established that the post-glitch behaviour for the Vela pulsar exhibits short (1-6 day) and intermediate (~ 20-100 day) relaxation timescales.

The modification of admitting a second exponential decay term to the phase model for the two-component theory of neutron star structure was found to be inadequate over timescales exceeding ~ 100 days. This was largely the result of the apparent change of the long-term trend in $\dot{\nu}$ which takes place at the time of each glitch.

The behaviour of the frequency derivative preceding the seventh glitch did not exhibit any significant fluctuations aside from those attributable to timing noise suggesting that the repinning of the superfluid vortices with the boundary region between the weak and superweak pinning zones in the vortex creep model of internal structure had not taken place.

There was no evidence of any significant change to the shape of the mean pulse profile as a result of the 1981 and 1985 glitches. In addition, the phase residuals for the observing session prior to each of these jumps, and the 1982 glitch were devoid of any significant timing activity. In the case of the 1985 glitch, the inferred epoch of the jump was within 30 minutes of the final pre-glitch observation. It is tantalizingly possible that the final few integrations obtained on TJD 6257 herald the onset of the glitch (figure 6.4c).

A timing discontinuity of low significance was found in the relaxation behaviour following the 1981 glitch. The magnitude of this event was estimated as $\Delta\nu/\nu \sim 2\times10^{-10}$ and $\Delta\dot{\nu}/\dot{\nu} \sim 10^{-3}$. These magnitudes are consistent with those of discrete timing noise events observed by CDK-P. The jump was followed by a relaxation in $\dot{\nu}$ that was qualitatively similar to the rapid recovery following a typical macro-glitch.

8.4 SHORT TIMESCALE PHASE NOISE

Phase noise in excess of that expected from measurement considerations was apparent in the LRO data on timescales less than the length of an observing session (5.4 hours). The influence of the observing equipment on this excess was not regarded as significant. The dual frequency data when combined with measurements by Downs and Krause-Polstorff (1986; hereafter DK-P) suggested that the excess noise has a power law dependence on observing frequency with a spectral index of -0.9±0.2.

The significant positive autocorrelation between phase residuals over timescales less than ~1 hour claimed by DK-P was not apparent in the LRO data. This may have been due to the fact that the ratio of the measurement noise to the excess noise was ~ 1.4 for the LRO data, whereas this ratio was ~ 4 for the JPL data. However, where the residual autocorrelation function $R(\tau)$ exceeded the expectation from purely white noise, it did so in the positive sense and for $\tau < 1.5$ hours (e.g.

figure I.6d). In addition, the excess level of $R(\tau)$ showed some evidence of epoch dependence.

Various origins for the excess noise were examined. Dispersion measure fluctuations were ruled out as the required excess electron density was several orders of magnitude greater than that considered reasonable for the ISM. In addition, the lack of significant autocorrelation between the dispersion measure estimates obtained from simultaneous dual frequency observations did not favour this hypothesis. It is also apparent that the excess noise is not a high frequency extension of the timing noise present over timescales in excess of one day, nor is it likely that fluctuations of either the rotation frequency or its first time derivative are responsible. A magnetospheric origin was considered possible given that small variations of the source position or the longitude of the radiation beaming angle are required. It is also apparent that the level of excess noise is epoch dependent, and is not influenced by the occurrence of glitches.

8.5 IMPLICATIONS OF DISPERSION MEASURE VARIATIONS

The variability of the dispersion measure for the Vela pulsar has been firmly established, and new data showing the behaviour on timescales less than 200 days has been presented.

During dual frequency observations made in 1986, the temporal variation of the dispersion measure was well approximated by a linear trend with gradient -0.04 pc cm^{-3} yr^{-1}. This behaviour was consistent with previous measurements, and has been interpreted as being the result of the motion of a plasma cloud situated within the advancing SNR shell out of the line of sight to the pulsar.

There was some additional evidence for short-timescale (10-20 day) fluctuations of DM. If this phenomenon is of a natural origin, then it may be the result of the motion of small plasma structures near the turbulent interface between the pulsar's wind zone and the ISM or within the large-scale plasma cloud responsible for the long term DM variations.

Combined LRO and HRAO timing data has suggested that slowly evolving though significant DM variations occurred prior to the 7th Vela glitch. A significant DM change at the time of this glitch was not evident, although a small and possibly coincident decrease in DM may have occurred in the 50 days prior to this event.

8.6 PSR1641-45 AND PSR1749-28

The LRO observations have shown that PSR1641-45 did not experience a significant jump in rotation frequency (i.e., of fractional magnitude in excess of $\sim 10^{-9}$) in the interval TJD 3452 (Manchester *et al.*, 1983) to TJD 6348. It is notable that a jump apparently occurred within the 80 days following the final 1985 LRO observation of this pulsar (Flanagan, 1986, *personal communication*, Manchester, 1986, *personal communication*). As shown in table H.1, the estimate of the second frequency derivative obtained from a quadratic fit to the 1983 data was significantly different to that obtained from a similar fit to the 1985 data. The latter value was in good agreement with that catalogued by Taylor and Manchester (1975). It is regarded that a systematic effect was present in the arrival times obtained during 1983 which arose from the phase estimation method. The effect of proper motion and positional uncertainties are not considered to be significant in this context.

A discrepancy was found between the DM measurement for PSR1749-28 reported by Lyne and Rickett (which is the only published source for this quantity that the author could locate) and that obtained from the LRO data. Further observations are required to provide an independent verification of both measurements, with a view to establishing if the dispersion measure for this pulsar is variable.

8.7 FUTURE WORK RELATING TO TIMING OBSERVATIONS

8.7.1 Glitches

Future observations should attempt to monitor known glitching pulsars as frequently as possible in the hope of observing a glitch in its entirety. This latter objective has recently been achieved by Hamilton *et al.* (1989) for the Vela pulsar.

In view of the availability of LRO timing observations immediately following glitches 5, 6, and 7, it is desirable to examine the applicability of equation 6.4 as a description of the short-term relaxation behaviour. This method has been used by CDK-P for glitches 5 and 6, and it would be of use to compare the parameter values obtained by these authors with those arising through the use of the LRO data. Preliminary work has suggested that reasonable agreement occurs, while the parameter values for the short term relaxation obtained from the LRO data are of significantly improved precision.

In addition, the recent work of Alpar *et al.* (1988) with regard to large glitch of PSR0355+54 reported by Lyne (1987) has suggested that linear (as distinct to non-linear) vortex creep within the neutron pinning zones may be responsible for the observed relaxation timescales and the absence of the delay time t_0 in the post-glitch data. This work requires application to the LRO glitch data.

It is probable that glitches, and indeed discontinuities in rotation frequency, are a feature of most pulsars. Efforts should be expanded to extend the number of pulsars, particularly those accessible from southern latitudes, for which long-term timing data is available. The aim of such work will be to extend the catalogue of glitching pulsars, and to gain a more representative picture of neutron star interiors through the interpretation of their timing data.

An area of further observational and theoretical development is with regard to possible MHD induced oscillations within a neutron star that are initiated by a glitch. Observationally, timing noise spectra would prove useful in establishing whether a dominant timescale exists for such oscillations.

Multi-wavelength monitoring of regularly glitching pulsars, most particularly Vela, is desirable in order to investigate the possibility that significant transient energy dissipation accompanies a glitch. Such occurrences are predicted on the basis of the corequake theory.

It is clear that further theoretical work is required in the area of coupling mechanisms between the plasma and superfluid components in order to account for the scatter of relaxation timescales exhibited by the Vela glitches. It is also important to account for the large difference between the magnitudes of the macro- and milli-glitches.

8.7.2 Timing Noise

There is considerable potential for the investigation of timing noise using the LRO data. Ultimately, dispersion measure fluctuations are likely to contaminate the timing noise spectrum particularly on long timescales. If a Kolmogorov ISM turbulence spectrum is assumed, then dispersion measure fluctuations will produce a timing noise spectrum of the form

$$S(f) \propto \lambda^4 f^{-2/3}$$

where f is the temporal frequency and λ is the observing wavelength (Armstrong, 1984). However, it is possible that short timescale DM fluctuations do occur, and these would provide an additional source of contamination.

In principle, the position and proper motion of the Vela pulsar are now known with sufficient precision so that barycentric arrival times should not contain significant diurnal or annual terms. In addition, the discovery of millisecond pulsars has provided a means of testing the accuracy of barycentric ephemerides, and eventually the influence of errors in the assumed planetary masses and positions on the inferred barycentric arrival times will be quantified to high precision.

The mathematical methods (Appendix A) are in place to provide a detailed description of the timing noise spectrum and the occurrence of discrete timing activity for the Vela pulsar. Aspects of such work have been published by various researchers, most notably Cordes and Helfand (1980), Alpar, Nandkumar, and Pines (1986), and CDK-P. An advantage associated with the LRO data is that there is adequate temporal resolution of the phase estimates to examine the seemingly abrupt timing jumps found by CDK-P in greater detail. Of interest is the occurrence rate of these discrete events, and their relationship with other observable parameters such as the characteristics of the radio emission.

Cheng (19887b) has proposed that micro-glitches initiated by an internal mechanism lead to fluctuations in the current braking torque. He has made specific predictions with regard to the form of the timing noise spectrum which require further observational testing.

It is clear that limits may be placed on the energy density of internal torque variations due to MHD oscillations through the use of timing spectra. A problem here is that theoretical development is required on the viability of such phenomenon given an understanding of the pinning and coupling processes within neutron stars.

8.7.2 Phase Noise

Simultaneous single pulse observations of high sensitivity should be conducted at two or more frequencies to further confirm the existence of the excess phase noise and investigate the radio-frequency scaling of its magnitude that has been suggested by the present work. These observations will also allow the noise contribution due to pulse width fluctuations to be distinguished from that due to variations of the longitude or radial position of the emission region. This work should be combined with the polarization study suggested in section 8.8.2 to ascertain whether the frequency scaling of the excess noise is related to the instability of the emission zone in combination with the topology of the magnetic field. In addition, the long-term stability of the level of excess noise should be examined.

8.7.3 Dispersion Measure

Further long-term monitoring of the dispersion measure is required to examine the variability of the plasma density within the line-of-sight ISM and the immediate pulsar environment. This is of particular importance if the intrinsic timing noise of the pulsar is to be investigated with high precision, particularly at observing frequencies below ~ 1 GHz.

In addition, the ability to simultaneously determine the rotation measure will prove useful in studying the magnetic field structure of the intervening plasma. This aspect is of interest with regard to glitches, as it is possible that magnetospheric disruption and the short term alteration of the emission geometry are initiated by these events.

The measurement of scattering parameters should be conducted in conjunction with DM observations in order to further knowledge of the plasma turbulence along the line of sight. Rankin and Counselman (1973) have shown that the level of scattering to the Crab pulsar shows evidence of time dependence. It would be of interest to ascertain is similar behaviour is exhibited by Vela's scattering media.

8.8 FUTURE STUDIES OF THE VELA PULSAR

It is now over two decades since the discovery of the Vela pulsar. During this interval, considerable insight as to the general nature of neutron stars as pulsars has been gained from the multi-wavelength study of this conspicuous object. However, it is clear that further knowledge is required in several key areas.

8.8.1 Distance

The distance of the pulsar is a fundamental parameter that was for many years accepted without serious reservation by most workers. The association of PSR0833-45 with the Vela SNR, first suggested in the discovery paper by Large, Vaughan, and Mills (1968) has been used as a key argument in support of 500 pc as a reasonable value. Recently Caraveo, Bignami, and Hermsen (1988) have questioned this association on the basis that the pulsar could not have travelled to its present position from the centre of the remnant during its presumed lifetime given the upper limit on its proper motion. The 4σ detection of proper motion by Ögelman, Koch-Miramond, and Auriére (1989, preprint) has suggested a space velocity (given the accepted distance) relative to the assumed fixed stars which is a factor of two greater than that derived

from scintillation measurements. Scintillation observations are used to obtain the transverse velocity of the line of sight *relative* to that of the scattering source. The influence of differential galactic rotation is dependent on the distance of the scattering region from the pulsar and the Earth. Optical and interferometric astrometry allow the measurement of the total transverse velocity of the pulsar relative to the Earth; this vector quantity has components due to differential galactic rotation (the magnitude of which is expected to be ~12 km s^{-1} for Vela according to Cordes, 1986) and peculiar motion. Astrometric VLBI observations are required for comparison with the optical measurements in order to confirm the space velocity of the pulsar and draw conclusions with regard to the accuracy of its currently inferred distance.

8.8.2 Radio Emission

The brightness of the Vela pulsar at radio wavelengths makes it a particularly easy object to detect. However, little has been published on the structure of the pulse profile at frequencies above ~ 1 GHz where it has been demonstrated by Manchester *et al.* (1980) and Krishnamohan and Downs (1983) that multiple components exist. Through high time resolution single pulse polarization measurements, the work of KD can be extended to gain further insight into the size and location of the emission regions, and the structure of the local magnetic field.

McAdam (1981) has suggested that the pulsar's radio flux is variable. It is unclear as to whether the origin of this behaviour is related to the emission mechanism or to refractive scattering within the ISM.

8.8.3 Studies at Other Wavelengths

Further optical measurements are required to confirm the existence of the variable unpulsed component detected by Manchester *et al.* (1980). In addition, it would be of use to ascertain the spectrum of the optical emission with greater precision. This project may be feasible using the next generation of large optical telescopes. Optical astrometry over several more years should result in refinement of the proper motion estimates, and examine the possible spatial variability of the faint structure that exists within the pulsar's wind zone.

Unlike the situation for the Crab pulsar, measurements have so far been unable to detect infra-red emission from Vela. Such observations are important in the context of the emission models based on outer magnetospheric gaps where a large flux of IR photons are thought to be generated as a result of the pair creation cascade (Cheng, Ho, and Ruderman, 1986a,b).

An important area of study which must await the launch into Earth orbit of instrumentation of increased sensitivity is the pursuit of the pulsed emission into the X-ray region of the spectrum. To date, only upper limits have been placed on the pulsed flux. In addition, measurements of improved sensitivity and spatial resolution should be able to better distinguish the blackbody spectrum of the surface of the neutron star from the synchrotron spectrum of the surrounding nebula, and thereby furnish a more accurate surface temperature estimate for comparison with the predictions of cooling models and internal energy dissipation mechanism such as vortex creep.

Measurements at gamma-ray energies are needed to confirm the evidence for linear polarization of the photons presented by Caraveo *et al.* (1988), and the variability of the flux and multiplicity of the source regions suggested by Greiner, Hermsen, and Clear (1988). Further observations are required to confidently extend knowledge of the spectrum above ~ 10 TeV.

8.9 GENERAL CONCLUSIONS

Sufficient data were available for two of the glitches studied to rule out significant changes to the shape of the mean pulse profile as a result of these events. In addition, it was found that the onset of a glitch is not obviously manifest in the immediate pre-jump LRO phase measurements. The inferred epoch of the 1985 glitch was tantalizingly close to the final pre-jump observations, and optimistic speculation would suggest that the signature of this event is present in the data.

A significant component of intrinsic pulse phase noise exists for the Vela pulsar on timescales of less than one day. The noise evidently does not conform to the frequency spectrum of long term timing noise. These is a suggestion that the level of noise has a power law dependence on observing frequency with a spectral index of -0.9 ± 0.2. The phase noise is tentatively regarded as originating within the magnetosphere of the pulsar due to instabilities within the emission zone. There is some evidence that the level of excess noise is time-dependent, and independent of the occurrence of glitches (figure 5.6).

The dispersion measure of the line of sight to the Vela pulsar is variable on timescales less than 200 days. A slow variation with a timescale of 1 - 10 years is suggested by this and previous work which is likely to be the result of the motion of plasma clouds in the ISM across the line of sight. Short-term variations occurring on the timescale of 10-30 days may be associated with fine structure turbulence within the

ISM or near the boundary between the pulsar's wind zone and its turbulent interface with the ISM.

If a significant systematic error is not present in the DM measurements for PSR1749-28 obtained by Lyne and Rickett (1968) or from the LRO observations, then the dispersion measure of this pulsar may also be variable.

PSR1641-45 did not undergo a glitch comparable in magnitude to that which occurred during 1977 (Manchester *et al.*, 1983) between TJD 3452 and TJD 6346.

APPENDIX A - TIMING NOISE ANALYSIS

A.1 INTRODUCTION

In the following sections, the three principle techniques that have found application for the assessment of timing noise are reviewed.

A.2 RANDOM WALK ANALYSIS

The methodology of random walk analysis has been detailed by Groth (1975b), Lamb, Pines, and Shaham (1978a), Cordes (1980), and Cordes and Downs (1985; hereafter CD).

A random walk in the k-th phase derivative $\phi^{(k)}$ is defined by

$$\phi^{(k)}(t) \equiv \frac{d^k\phi(t)}{dt^k} = \sum_i a_{i_k}\, u(t - t_i) \quad T_0 < t < T_1,\ k = 0,1,2,... \qquad A.1$$

where a_{i_k} is a random amplitude with zero mean, u is the unit step function (with zero rise-time), and steps occur at times t_i with an average rate R. The t_i are statistically distributed in the interval (T_0,T_1). By its definition, a random walk in $\phi^{(k)}$ requires the existence of stationary statistics in $\phi^{(k+1)}$; that is, the temporal fluctuations in $\phi^{(k+1)}$ have a white power spectrum (Groth, 1975b).

In equation A.1, it is assumed that $\phi^{(k)}(t) = 0$ for $t \le T_0$; that is, the random walk commences at some arbitrary time $t = T_0$. As discussed by Cordes and Greenstein (1981), the phase values $\phi_{R_k}(t)$ due to a k-th order random walk which is idealized as having commenced at $t = -\infty$ are related to the values $\phi_{R_k}(t - T_0)$ for a similar walk which commenced at $t = T_0$ by

$$\phi_{R_k}(t) = \phi_{R_k}(t - T_0) + \sum_{n=0}^{k} C_n \{t - T_0\}^n \qquad t > T_0 \qquad A.2$$

where the C_n are variables which depend only on the steps of the random walk prior to T_0. Fitting an n-th order polynomial to the phase data is equivalent to removing the terms involving $(t - T_0)^m$ for $m = [0,n]$ from equation A.2.

Is assumed that the phase values reflect only contributions from spindown (which is modeled by a low-degree polynomial), timing noise and measurement uncertainty. The observed phase values over the data span of length $T = T_1 - T_0$ are fitted with an m-th degree polynomial via a least-squares procedure to generate a final residual $R_i(m,T)$ for each t_i where $T_0 \le t_i \le T_1$.

The level of intrinsic timing noise is estimated by

$$\hat{\sigma}^2_{TN} = \sigma^2_R - \hat{\sigma}^2_W \qquad \text{A.3}$$

where $\sigma^2_R = \sigma^2_R(m,T)$ is the mean-square residual over the fitting span and $\hat{\sigma}_W = \hat{\sigma}_M + \hat{\sigma}_J$ is (from equations 4.1 and 4.6) the rms white noise contribution. CD have provided a suitable means of evaluating $\hat{\sigma}_W$ (section 5.2) and also an estimator for the error in $\hat{\sigma}_{TN}$ (section 9.2)

Cordes and Helfand (1980) have defined the *activity parameter* A to broadly quantify timing noise relative to that of the Crab pulsar ;

$$A = \log \left\{ \frac{\hat{\sigma}_{TN}(m,T)}{\hat{\sigma}_{TN}(m,T)_{CRAB}} \right\} \qquad \text{A.4}$$

From a study of 50 pulsars, A exhibited correlation of low significance with $\dot{\nu}$ (suggesting that timing noise is related to rotational energy loss), and weaker correlation with ν.

The moment of idealized random walks in the k-th phase derivative is characterized by the *strength parameter* S_k where

$$\begin{aligned} S_0 &= R \langle(\delta\phi)^2\rangle, \\ S_1 &= R \langle(\delta\nu)^2\rangle, \\ S_2 &= R \langle(\delta\dot{\nu})^2\rangle, \end{aligned} \qquad \text{A.5}$$

where $\langle\ \rangle$ denotes ensemble-average and

$$\begin{aligned} \delta\phi_i &= a_{i_0}, \\ \delta\nu_i &= a_{i_1} \{t - t_i\}^{-1}, \\ \delta\dot{\nu}_i &= a_{i_2} \{t - t_i\}^{-2} \end{aligned} \qquad \text{A.6}$$

CD have provided estimates for the strength parameters in terms of the mean-square timing noise level for the case of uniform sampling and RT >> 1;

$$\begin{aligned} \hat{S}_0 &= 2\, T^{-1}\, C^2_{0,m}\, \hat{\sigma}^2_{TN}(m,T), \\ \hat{S}_1 &= 12\, T^{-3}\, C^2_{1,m}\, \hat{\sigma}^2_{TN}(m,T), \\ \hat{S}_2 &= 120\, T^{-5}\, C^2_{2,m}\, \hat{\sigma}^2_{TN}(m,T), \end{aligned} \qquad \text{A.7}$$

where $C^2_{0,m}$, $C^2_{1,m}$, and $C^2_{2,m}$ are correction factors that compensate for the variance removed by the m-th order polynomial fit to the data; these latter quantities are given by Cordes (1980) and Deeter (1984). CD have discussed modifications to equations A.7 for the case of non-uniformly sampled data.

To test the applicability of a particular random walk model as a descriptor of timing noise, the associated strength parameter (for a particular m) is examined as a function of T. As pointed out by CD, for RT >> 1 and steps of uniformly distributed amplitude, then a random walk in the k-th phase derivative will exhibit $\hat{S}_k$ independent

of T. However, the behaviour of $\hat{S}_k(T)$ is modified if the steps are non-uniformly distributed.

A.3 STRUCTURE FUNCTIONS

Structure functions are useful for examining the range of time scales that contribute to fluctuations of a function of the form

$$\phi(t) = \sum_{k=0}^{N} \frac{A_k}{k!} t^k + x_s(t)$$

where A_k are random variables, and $x_s(t)$ is a stationary process (Rutman, 1978). The m-th order structure function of phase is defined as

$$D_\phi^{(m)}(t,\tau) \equiv \langle \{\Delta_\phi^{(m)}(t,\tau)\}^2 \rangle \qquad \text{A.8}$$

where

$$\Delta_\phi^{(m)}(t,\tau) \equiv \sum_{l=0}^{m} (-1)^l \, {}^mC_l \; \phi(t + \tau\{m - l\}) \qquad \text{A.9}$$

is termed the increment function. Here τ is the characteristic timescale probed by the differencing scheme, and t is the epoch of an individual measurement. The m-th order structure functions and increments may be defined for higher derivatives of ϕ. If ϕ is a polynomial of order $p < m$, then $\Delta_\phi^{(m)} = 0$, and $\Delta_\phi^{(m)}$ is independent of t for p=m. Additionally, step functions in the k-th derivative of ϕ have (k+1)-th increment functions that are pulses in time which are piecewise polynomials of order k with amplitude proportional to $A_k\tau^{k-1}$ (CD).

CD have provided a means of assessing the significance of apparent discontinuities in ϕ or its derivatives by comparing observed structure functions with those evaluated for idealized random walk processes. In the case of $R\tau >> 1$ (where R is the rate of discontinuities), $\Delta_\phi^{(k)}$ for a type k random walk process is a Gaussian random variable with variance given by $D_\phi^{(k)}(t,\tau)$. Structure functions find additional utility in assessing the order of a random walk process. For a random walk of order k, a structure function of order $\geq$ k+1 is time-independent, and has a power law relationship with τ with a spectral index of k (CD).

A.4 POWER SPECTRA

Spectral power density is usually estimated by squaring the linear form resulting from the application of a sampling function h(t) to the observed timeseries x(t) over an interval $a \leq t \leq b$,

$$P_x = \left\{ \int_a^b h(t)\, x(t)\, dt \right\}^2 \qquad \text{A.10}$$

Methodology for the recovery of power spectra characterised by an inverse integral spectral index, with particular application to pulsar timing data, has been developed by Deeter and Boynton (1982; hereafter DB) and Deeter (1984). These authors have built on the work of Groth (1975b,c) to overcome an inherent problem associated with conventional power spectrum analysis (based on sinusoidal sampling functions) that occurs whenever non-white noise is encountered, namely the under-estimation of power density due to leakage through the sidelobes of the frequency transfer function. The method summarized below aims to tailor the frequency response of the sampling function to faithfully recover the spectral density while sacrificing frequency resolution. Application of the technique to experimental data has been made by Boynton (1981), Boynton and Deeter (1986, *preprint*), and Deeter *et al.* (1989).

In order for P_x to be a valid estimate in the situation where S_x, the true power density at circular frequency f, obeys a power law with an even integral spectral index

$$S_x(f) = K_r\, (2\pi f)^{-2r} \qquad \text{A.11}$$

(that is, x(t) has an r-th order spectrum) then the sampling function must satisfy r *moment conditions*

$$\sum_{j=1}^{n} h_j\, t^i = 0 \qquad \text{for } 0 \leq i < r \qquad \text{A.12}$$

and the boundary condition

$$h^{(-i)}(a) = h^{(-i)}(b) = 0 \qquad \text{for } 0 < i \leq r \qquad \text{A.13}$$

where $h^{(-i)}(t)$ is the i-th integral of h(t). The factor K_r in equation A.11 is referred to as the noise *strength*.. Here, the application of the method to experimental data is anticipated by the use of discrete functions, which are related to their continuous analogues via

$$h(t) = \sum_{j=1}^{n} h_j\, \delta(t - t_j), \qquad x(t) = \sum_{j=1}^{n} x_j\, \delta(t - t_j) \qquad \text{A.14}$$

where $\delta(t - t_j) = 1$ for $t = t_j$ and zero otherwise. Here n is the number of individual observations. For each measured quantity x_j there is an associated weight w_j, which for the pulsar timing data is taken as $\hat{\sigma}_M^{-2}(t_j)$.

The expectation value of the power estimate is given by

$$\langle P_x \rangle = \int_{-\infty}^{\infty} |H(f)|^2 \, S_x(f) \, df \qquad \text{A.15}$$

where H(f) is the transfer function of h(t). Ideally, H(f) is unimodal and of narrow bandwidth. For r-th order noise, the expectation is given by

$$\langle P_x \rangle = K_r \frac{(-1)^r}{2(2r-1)!} \sum_{j=1}^{n} \sum_{k=1}^{n} h_j \, h_k \, |t_j - t_k|^{2r-1} \qquad \text{A.16}$$

If the expectation is evaluated for unit strength noise, then an estimate of the spectral density may be obtained from

$$\hat{S}_x(f_{med}) = \frac{P_x}{\langle P_x \rangle} \qquad \text{A.17}$$

where f_{med} is the frequency centroid of the bandpass of H(f).

The frequency response of a sampling function to white noise is given by

$$|H(f)|^2 = 2\left[\sum_{j=1}^{n} h_j \cos(2\pi f t_j)\right]^2 + \left[\sum_{j=1}^{n} h_j \sin(2\pi f t_j)\right]^2$$

The effective frequency response of h(t) for r-th order noise may be obtained from $H^{(-r)}(f)$, the transfer function of $h^{(-r)}(t)$, via

$$|H^{(-r)}(f)|^2 = (2\pi f)^{-2r} |H(f)|^2 \qquad \text{A.18}$$

DB have provided a convenient method to evaluate the median frequency associated with a sampling function satisfying m moment conditions in terms of the half-width $\Delta T(m)$ of $h^{(-r)}(t)$;

$$f_{med}(m,r) = \frac{\beta(m,r)}{\Delta T(m)} \qquad \text{A.19}$$

where β is a calibration factor tabulated by Deeter (1984). The half-width is evaluated from

$$\Delta T(m) = \left[\frac{M_2}{M_0} - \left\{\frac{M_1}{M_0}\right\}^2\right]^{1/2} \qquad \text{A.20}$$

where

$$M_k = (-1)^m \frac{k!}{(m+k)!} \sum_{j=1}^{n} h_j \, t_j^{m+k} \qquad k \geq 0 \qquad \text{A.21}$$

is the k-th moment of $h^{(-m)}(t)$.

The removal of a polynomial of degree m-1 from x(t) is related to imposing m moment conditions on h(t). Specifically,

$$\sum_{j=1}^{n} h_j \, [x_j - \bar{x}_j] = \sum_{j=1}^{n} [h_j - \bar{h}_j] \, x_j \qquad \text{A.22}$$

where the polynomial trend removed from the timeseries, $\bar{x}$, may be conveniently expressed as

$$\bar{x}_k = \sum_{i=0}^{m-1} p_i(t_k) \sum_{j=1}^{n} p_i(t_j)\, x(t_j) \qquad \text{A.23}$$

Here $p_i(t_j)$ is an orthonormal polynomial of i-th degree evaluated at time t_j. An equivalent expression exists for the sampling function :

$$\bar{h}_k = \sum_{i=0}^{m-1} p_i(t_k) \sum_{j=1}^{n} p_i(t_j)\, h(t_j) \qquad \text{A.24}$$

Each orthonormal polynomial is constructed from the following recurrence relation;

$$p_0(t_j) \equiv 1$$

$$p_i(t_j) = \left[t_j - \frac{\langle t_j\, p_{i-1} \mid p_{i-1} \rangle}{\langle p_{i-1} \mid p_{i-1} \rangle} \right] p_{i-1}(t)_j - \left[\frac{\langle p_{i-1} \mid p_{i-1} \rangle}{\langle p_{i-2} \mid p_{i-2} \rangle} \right] p_{i-2}(t_j) \qquad \text{A.25}$$

where

$$\langle f \mid g \rangle = \sum_{k=1}^{n} w_k\, f_k\, g_k$$

is the scalar product of functions f and g over the set of observational weights w. A condition on equation A.25 is that the second term is omitted in the case when i = 1.

Deeter (1984) has examined the bandpass characteristics of several types of sampling functions. He found a convenient sampling function for r-th order noise that satisfies the moment conditions to be an orthonormal polynomial of degree i > r. An advantage of this type of function is its ease of construction (via equation A.25), particularly if the sampling of the timeseries is irregular. In addition, the frequency response is largely unimodal, with a bandwidth that is approximately equivalent to the median frequency. In figure A.1, the frequency response of orthonormal polynomials satisfying m ≥ r moment conditions are shown for r=[1,3].

The individual power estimates P_i may be expressed as

$$P_i = P_{I_i} + P_{m_i}$$

where P_I and P_m are the contributions from the phenomenon under investigation, and the measurement procedure, respectively. An estimate of P_{m_i} may be evaluated. The aim is to obtain the maximum likelihood value of the intrinsic power, <P>. This is obtained through the weighted average of the pooled P_i

$$\langle P \rangle = \frac{\sum_i \frac{P_i}{(\sigma_i^2)^2}}{\sum_i \frac{1}{(\sigma_i^2)^2}}$$

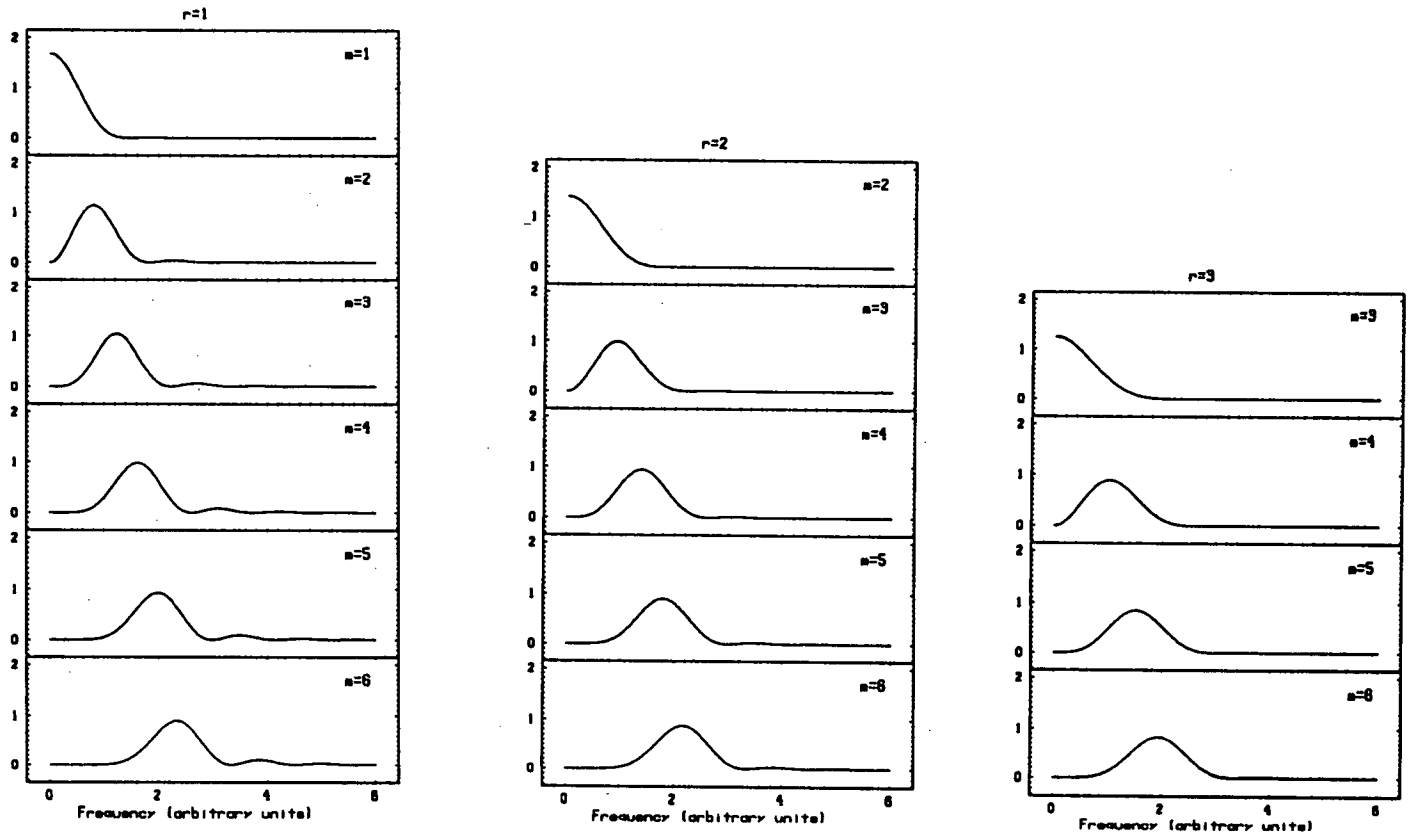

Fig. A.1. Frequency response of orthonormal polynomials satisfying m ≥ r moment conditions for r = [1,3].

where $\sigma_i^2 = P_i \approx \langle P \rangle + P_{m_i}$ (Boynton and Deeter, 1986; *preprint*). The median frequencies f_{med} for each power estimate are also pooled to produce a weighted average $\langle f \rangle$.

The effective number of degrees of freedom for each power estimate is given by

$$\nu_f = \frac{2\{\langle P \rangle\}^2}{\sigma_P^2} = \frac{\left[\sum_{j=1}^{n} \mathrm{var}(P_j)\right]^2}{\sum_{j,k=1}^{n} [\mathrm{cov}(P_j P_k)]^2} \qquad \text{A.26}$$

where n is the number of pooled estimates. Here account is made for correlations between power estimates of a common timescale when sub-intervals overlap due to uneven sampling. In the case of uniform sampling without overlapping, $\nu_f = n$ and $n = 2^h - 1$.

The utility of displaying power spectra in terms of $\langle \log P \rangle$ against $\langle \log f \rangle$ has been summarized by Deeter. The bias[a] introduced by the change of scale is given by

$$\langle \log P \rangle - \log \langle P \rangle \approx \left\{ \frac{1}{\nu_f} + \frac{1}{3\nu_f^2} \right\} \log e \qquad \text{A.27}$$

A model may then be fitted by minimizing S, the weighted sum of squares;

$$S = \sum_{j}^{g} \frac{\{\langle \log P_{obs} \rangle - \log P_{model}\}^2}{(\sigma_{\log P})^2} \qquad \text{A.28}$$

where the weighting term is the square of an approximation to the half-width of the distribution for $\log P_{obs}$;

$$(\sigma_{\log P})^2 \approx \left\{ \frac{2}{\nu_f} + \frac{2}{\nu_f^2} + \frac{4}{3\nu_f^3} \right\} (\log e)^2 \qquad \text{A.29}$$

---

[a] The factor of 3 in equation A.27 has been erroneously omitted by Deeter *et al.* (1989).

APPENDIX B - COORDINATE TRANSFORMATIONS

B.1 INTRODUCTION

In this section, the methods used to obtain the vectors **r** and **n** (which are directed from the observatory to the barycentre and from the barycentre to the pulsar, respectively) and the doppler correction to the observing frequency (which appear in equation 4.3) are presented.

B.2 OBSERVATORY COORDINATES

The motion of the Earth is modelled in gross characteristics as a diurnal rotation about a reference axis which moves with respect to the barycentric intertial frame in a manner described by the theories of precession and nutation (section B.5). The reference axis does not coincide with the axis of figure (maximum moment of inertia), but exhibits a quasi-circular motion about it. This so-called *polar-wandering* has an amplitude of ~ 0.3" (corresponding to a 9 m displacement on Earth's surface) with principal periods of 365 and 428 days reflecting geophysical influences. The departures $\Delta\lambda'$ and $\Delta\beta'$ from the mean longitude λ_m and latitude β_m, respectively, are given by

$$\Delta\lambda' = \{x'\sin(\lambda_m) - y'\cos(\lambda_m)\}\tan(\beta_m) \qquad \text{B.1}$$

$$\Delta\beta' = x'\cos(\lambda_m) - y'\sin(\lambda_m) \qquad \text{B.2}$$

The factors x' and y' are tabulated in The Astronomical Almanac (1987, Section K) and are usually expressed in arc-sec. The corrections are of importance for the precise determination of the local sidereal time and the zenith angle of a source. However, the light-travel delays introduced by equations B.1 and B.2 for pulsar timing studies are at the sub-microsecond level (table B.1).

The LRO geodetic coordinates are referenced to the 1965 Australian National reference spheroid. The offset of this reference frame from Earth's centre-of-mass is represented by the rectangular coordinates $(x_0, y_0, z_0) = (-122, -43, 138)$ metres.

The geocentric rectangular coordinates of the observatory are given by

$$x_G = x_0 + (aC + h)\cos(\beta')\cos(\lambda') \qquad \text{B.3}$$

$$y_G = y_0 + (aC + h)\cos(\beta')\sin(\lambda') \qquad \text{B.4}$$

$$z_G = z_0 + (aC + h)\sin(\beta') \qquad \text{B.5}$$

where $\beta' = \beta_m + \Delta\beta'$, $\lambda' = \lambda_m + \Delta\lambda'$, β_m and λ_m are measured in the 1965 reference frame, a = 6378160 m is the equatorial radius of the spheroid, h is the height above mean sea-level[a] (normally expressed in metres) and

$$C = \{(\cos^2(\beta') + (1 - f_f)^2) \sin^2(\beta')\}^{-1/2}.$$

In the above expression, f_f is the flattening factor with $1/f_f = 298.25$. The coordinates x_G, y_G, and z_G may be expressed in terms of the geocentric coordinates (λ,β) and radius R (metres);

$$x_G = R \cos(\beta) \cos(\lambda)$$
$$y_G = R \cos(\beta) \sin(\lambda)$$
$$z_G = R \sin(\beta)$$

Using equations B.3-5 with the above expressions, λ, β, and R may be solved for. Uncertainties in β and λ, and R, are estimated as < 0.5 arc-sec, and ~ 100 m, respectively, from the analysis of observations made during the SHEVE VLBI experiment (Preston *et al.*, 1984).

B.3 BARYCENTRIC VECTOR OF THE OBSERVATORY

The geocentric vector of the observatory (figure B.1) is

$$\xi = [R\cos(\lambda)\cos(\Gamma-\beta),\ R\cos(\lambda)\sin(\Gamma-\beta),\ R\sin(\lambda)]$$

The apparent *Greenwich sidereal time* (Γ) is given by

$$\Gamma = 2\pi \{(0.276919398 + 100.0021359\ T + 1.075\times10^{-6}T^2) \cdot (1 + 2.7853831\times10^{-3}S) + 7.716\times10^{-9}\ \Delta\Psi \cos(\varepsilon)\}$$

where T = (JD - 2415020.0)/36525, S is the number of seconds in the UT day, $\Delta\Psi$ is the nutation in longitude[b] obtained from the barycentric ephemeris, and ε is the obliquity of the ecliptic of date with respect to the mean equator of date;

$$\varepsilon = 0.40920620 - 2.27135\times10^{-3}\ T - 1.59\times10^{-9}\ T^2 + 8.83\times10^{-9}\ T^3$$

rad.

The barycentric vector of the observatory **r** is then calculated from

$$\mathbf{r} = \mathbf{PN}\xi \cdot \mathbf{q}$$

where **P** and **N** are rotation matrices describing precession and nutation (section B.4), respectively, and **q** is the barycentric vector of the geocentre (obtained from the ephemeris).

The observatory velocity vector in the frame of the barycentre is

$$\mathbf{V_B} = \mathbf{E_B} + \mathbf{V_G}$$

---

[a] Neglecting the variation in h due to gravitational tidal forces on Earth's elastic crust and the plate tectonic effects on β' and λ'.

[b] The nutations in longitude, $\Delta\Psi$, and latitude, $\Delta\varepsilon$, may vary by as much as 0.1 arc-sec d^{-1}. Formulae accurate to 0.01 arc-sec are given by Meeus (1979, p. 60).

where $\mathbf{E_B}$ is the barycentric velocity vector of the geocentre (obtained from the instantaneous derivatives of the components of $\mathbf{E_B}$), and

$$\mathbf{V_G} = [-\Omega_e R\cos(\lambda)\sin(\Gamma-\beta),\ \omega R\cos(\lambda)\cos(\lambda)\cos(\Gamma-\beta),\ 0]$$

where Ω_e is the angular rotational frequency of the Earth;

$$\Omega_e \approx 7.292115\times10^{-5} \text{ rad s}^{-1}.$$

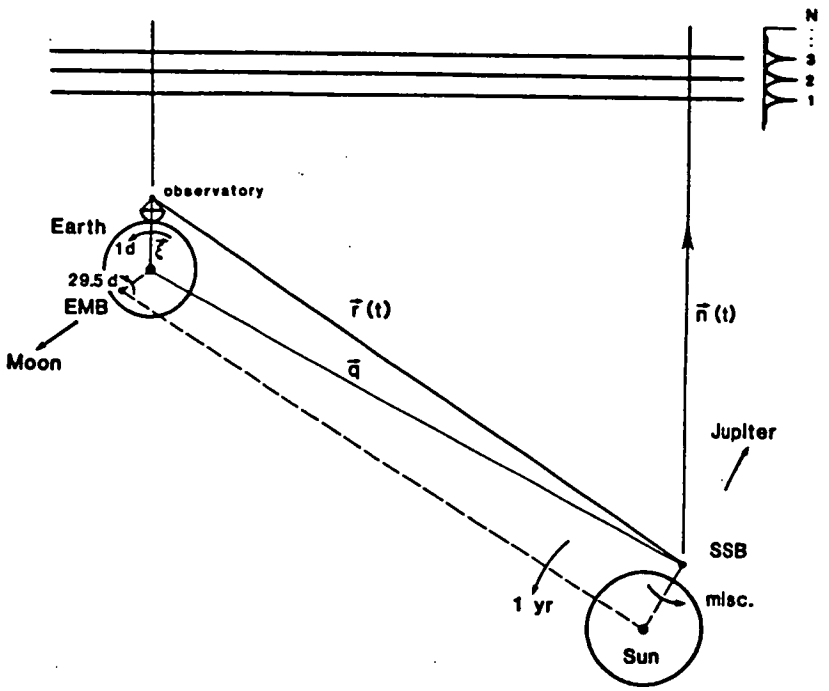

Fig. B.1. The calculation of the barycentric arrival time requires taking the dot product between the unit vector in the direction of source, **n**, and the vector between the barycentre and the observatory in light travel-time units **r**/c. (After Backer and Hellings, 1986).

B.4. PRECESSION AND NUTATION

The *precession* of Earth's rotation axis describes circular paths on the celestial sphere of radius ~ 23.5° centred on the ecliptic poles over a period of ~ 26,000 yr. This motion is the result of the influence of (principally) the lunar and solar gravitational fields on Earth's equatorial bulge.

Nutation is a superimposed oscillation of the polar motion with an 18.4 arc-sec amplitude and a period of 18.6 years which results from the precession of the nodes of the lunar orbit.

The *precession matrix* is given by

$$\mathbf{P} = \begin{bmatrix} \cos(\delta_A)\cos(z_A) & -\sin(\delta_A)\cos(\sigma_A)\cos(z_A) & -\sin(\sigma_A)\cos(z_A) \\ -\sin(\delta_A)\sin(\delta_A) & -\cos(\delta_A)\sin(z_A) & \\ \cos(\delta_A)\sin(z_A) & -\sin(\delta_A)\cos(\sigma_A)\sin(z_A) & -\sin(\sigma_A)\sin(z_A) \\ +\sin(\delta_A)\cos(z_A) & +\cos(\delta_A)\cos(z_A) & \\ \cos(\delta_A)\sin(\sigma_A) & -\sin(\delta_A)\sin(\sigma_A)\cos(\sigma_A) & \cos(\sigma_A) \end{bmatrix}$$

where δ_A, z_A and σ_A are the angles which specify the portion of the mean equinox and equator of date with respect to the mean equator of the standard epoch J1950.0.

$$\delta_A = 0.1117470\ T_E + 1.464\text{x}10^{-6}T_E^2 + 3.2\text{x}10^{-6}T_E^3$$

$$z_A = \delta_A + 3.835\text{x}10^{-6}\ T_E^2$$

$$\sigma_A = 9.716904\text{x}10^{-3}T_E - 2.065\text{x}10^{-6}T_E^2 - 2.04\text{x}10^{-9}T_E^3$$

Here

$$T_E = (JD - 243382.423)/36524.22$$

which is the number of tropical centuries elapsed since J1950.0.

The *nutation matrix* is given by

$$\mathbf{N} = \begin{bmatrix} 1 & \Delta\Psi\ \cos(\varepsilon) & -\Delta\Psi\ \sin(\varepsilon) \\ \Delta\Psi\ \sin(\varepsilon) & 1 & -\Delta\varepsilon \\ \Delta\Psi\ \sin(\varepsilon) & \Delta\varepsilon & 1 \end{bmatrix}$$

B.5 THE BARYCENTER-SOURCE VECTOR

The barycentric coordinates of the source are given by

$$\mathbf{n} = [\cos(\alpha_0)\cos(\delta_0),\ \sin(\alpha_0)\cos(\delta_0),\ \sin(\delta_0)]$$

where α_0 and δ_0 are the RA and the dec. of the source, respectively, for the standard epoch. These coordinates do not include the contribution from the slowly changing E-terms of annual aberration.

Thus if $\mathbf{r} = (X_B, Y_B, Z_B)$ are the barycentric coordinates of the observatory, then

$$\mathbf{r}\cdot\mathbf{n} = X_B\cos(\alpha_0)\cos(\delta_0) + Y_B\sin(\alpha_0)\cos(\delta_0) + Z_B\sin(\delta_0)$$

B.6 DOPPLER CORRECTION

The observing frequency in the inertial frame moving with the barycentre f is related to the apparent frequency f' at the observatory by

$$\frac{f'}{f} = \frac{(1 - v_r/c)}{\sqrt{1 - \beta_p^2}}$$

where $\beta_p = v_0/c$, and v_r is the true radial velocity with

$$v_0 = \sqrt{(v_x^2 + v_y^2 + v_z^2)}$$

$$V_r = - (x_B v_x, y_B v_y, z_B v_z)$$

Here x_B, y_B and z_B are the barycentric rectangular coordinates of the observatory, and v_x, v_y and v_z are their corresponding time derivatives (Stumpff, 1979).

B.7 MAGNITUDES OF POSITION CORRECTIONS

The magnitudes of the correction to the observatory and source coordinates relevant to the LRO observations are summarized in table B.1.

TABLE B.1

MAGNITUDES OF POSITION CORRECTIONS

TERM	MAGNITUDE (arc-sec)
Polar motion	
$(\Delta\lambda')_{max}$	0.4
$(\Delta\beta')_{max}$	0.4
Precession and Nutation	
$\alpha_{1950.0} - \alpha_{1987.0}$	66.2
$\delta_{1950.0} - \delta_{1987.0}$	-27.1

B.8 CONTRIBUTIONS TO ARRIVAL TIME UNCERTAINTIES

The effect of errors in pulsar and observatory coordinates, and the position of the barycentre on arrival times are summarised in table B.2.

TABLE B.2

ARRIVAL TIME UNCERTAINTIES

Source	Error	Timescale	Time Error
Geocentric Position	$\Delta\beta = 1"$	sidereal day	~ 100 ns
	$\Delta\lambda = 1"$	sidereal day	~ 100 ns
	$\Delta R = 100$ m	sidereal day	~ 350 ns
Pulsar Coordinates	$\Delta\alpha = 0.1"$	annual	~ 340 μs
	$\Delta\delta = 0.1"$	annual	~ 400 μs
Barycentric Position	planetary masses	$\leq$ 300 yr	~ 4 ms
		$\leq$ 10 yr	~ 0.1 μs

APPENDIX C - PLANETARY MASS UNCERTAINTIES

Consider the situation in figure C.1 where a planet is orbiting the true barycentre (TB) of the solar system. The aim is to determine the errors introduced in pulsar timing parameters when a barycentric ephemeris constructed using inaccurate planetary masses is used; a similar analysis has been performed by Mulholland (1971). Assume that points H, B, B', O and P (figure C.1) lie in the plane of the ecliptic, and define λ to be the longitude of the planet relative to the azimuthal direction of the pulsar as seen from B. We may put $\theta = \theta'$ as the parallax of the pulsar will be insignificant. The vectors **BS** and **B'B** are given by

$$\mathbf{BS} = [\cos(\theta), 0, \sin(\theta)]$$

$$\mathbf{B'B} = [\Delta r R\cos(\lambda), \Delta R \sin(\lambda), 0]$$

where $\Delta R = |R - R'|$ (here the Δ signifies a small perturbation). Thus the projection of **B'S** on **BS** is given by

$$|cT - cT'| = \Delta R \cos(\theta) \cos(\lambda).$$

From centre-of-mass considerations,

$$M/m = r/R \qquad \text{and} \qquad M/m' = r'/R'.$$

Because $r, r' >> R, R'$, then $r \sim r'$ and thus

$$\Delta R = R\, \Delta m/M$$

where $\Delta m = |m - m'|$. Thus,

$$|T - T'| = \frac{P\, \Delta m \cos(\theta) \cos(\lambda)}{cM} \qquad \text{C.1.}$$

Now if the planet moves with (constant) angular velocity v_λ (expressed in radians per unit time), then

$$\cos(\lambda) = \cos(v_\lambda t)$$

where t is measured from the epoch at which **BP** and **BO** were identically directed.

Equation B.1 may be re-expressed in terms of the time derivative expressed over one pulse period as

$$|\Delta P/P| = \frac{MR}{c\Delta m} v_\lambda \sin(v_\lambda t) \cos(\theta)$$

$$= A \sin(v_\lambda t) \qquad \text{C.2}$$

where $A = \frac{MR}{c\Delta m} v_\lambda \cos(\theta)$.

Similarly

$$|\Delta \dot{P}/\dot{P}| = A v_\lambda \cos(v_\lambda t) \qquad \text{C.3}$$

$$|\Delta \ddot{P}/\ddot{P}| = A v_\lambda^2 \sin(v_\lambda t) \qquad \text{C.4.}$$

Estimates for the deviations given by equations C.2-4 are given in table 4.4. Note that in this table, $\Delta(M/m) = M|1/m - 1/m'|$.

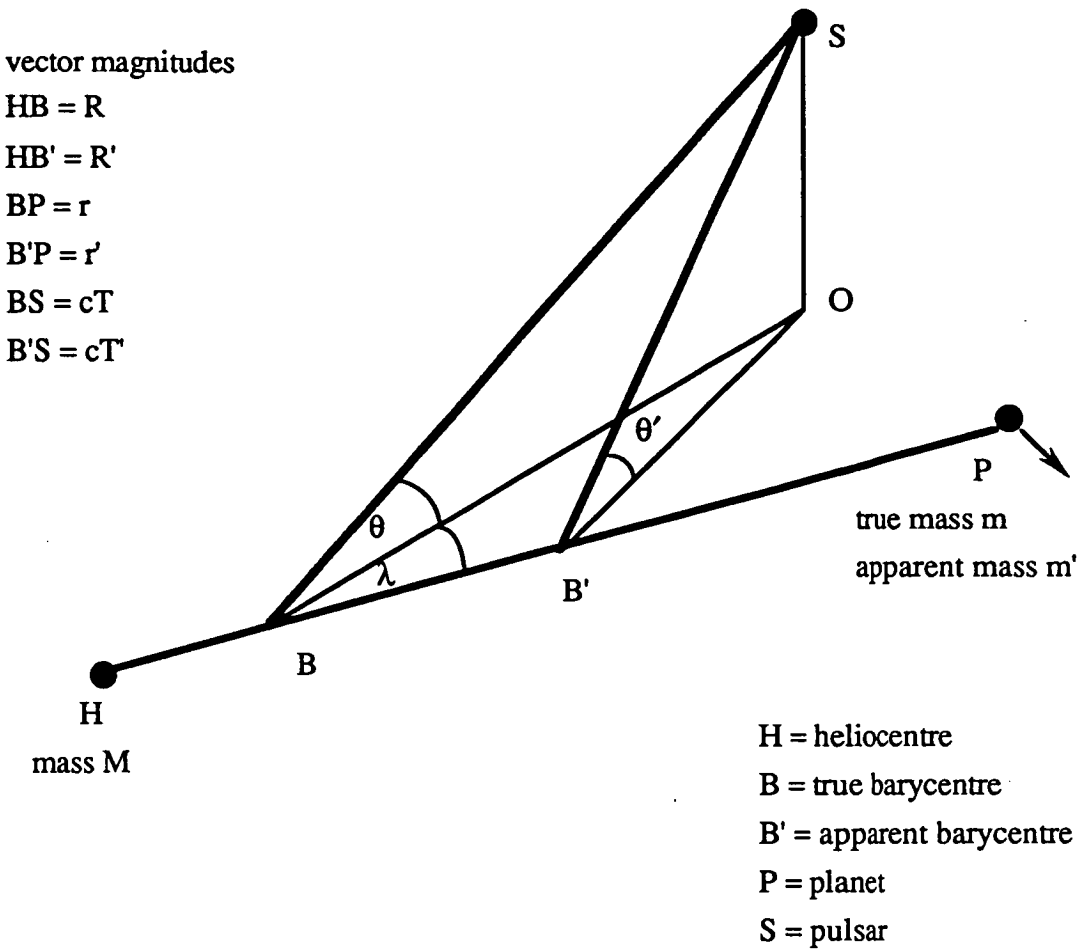

Fig. C.1 Geometry for determining the effect of planetary mass uncertainties on arrival times.

APPENDIX D - THE RELATIVISTIC CLOCK CORRECTION

The rate of a terrestrial clock as seen by an observer at an infinite distance in a frame inertial with respect to the barycentre varies with an annual cycle due to Earth's elliptical orbit within the gravitational potential of the solar system. Blandford and Teukolsky (1976) give an accurate approximation for the relativistic clock correction term in equation 4.3 ;

$$t_r = -1.66145\times10^{-3}\left\{\left(1 - \frac{e_e^2}{8}\right)\sin(M_e) + \frac{e_e\sin(2M_e)}{2} + \frac{3e_e^2\sin(3M_e)}{8}\right\} \qquad \text{D.1}$$

where $e_e = e_e(\tau)$ and $M_e = M_e(\tau)$ are the eccentricity and mean anomaly of Earth's orbit respectively, which are a function of the terrestrial time τ. Backer and Hellings (1986) consider that higher order terms neglected in equation D.1 contribute less than 100 ns to the correction term over a span of ~ 30 years.

APPENDIX E - RELATIONS FOR FREQUENCY AND PERIOD

The pulse *frequency* ν, and its derivatives $\dot{\nu}$ and $\ddot{\nu}$ are related to the pulse *period* P and its derivatives $\dot{P}$ and $\ddot{P}$ by the following transformations:

$$\nu = P^{-1} \tag{E.1}$$

$$\dot{\nu} = -P^{-2}\dot{P} \tag{E.2}$$

$$\ddot{\nu} = -P^{-2}\ddot{P} + 2P^{-3}\dot{P}^2 \tag{E.3}$$

These equations may be expressed in terms of perturbations, denoted Δ, as:

$$\Delta\nu = -P^{-2}\Delta P \tag{E.4}$$

$$\Delta\dot{\nu} = -P^{-2}\Delta\dot{P} + 2P^{-3}\dot{P}\Delta P \tag{E.5}$$

$$\Delta\ddot{\nu} = -P^{-2}\Delta\ddot{P} + 4P^{-3}\dot{P}\Delta\dot{P} + (2P^{-3}\ddot{P} - 6P^{-4}\dot{P}^2)\Delta P \tag{E.6}$$

The fractional changes in the frequency terms are obtained by dividing equations E.1-3 by the corresponding perturbations of equations E.4-6:

$$\Delta\nu/\nu = -\Delta P/P \tag{E.7}$$

$$\Delta\dot{\nu}/\dot{\nu} = \Delta\dot{P}/\dot{P} - 2\Delta P/P \tag{E.8}$$

$$\Delta\ddot{\nu}/\ddot{\nu} = [\Delta\ddot{P}/\ddot{P} - 2\varepsilon_P\Delta\dot{P}/\dot{P} - 2(1 - 3\varepsilon_P/2)\Delta P/P] \cdot (1 - \varepsilon_P)^{-1} \tag{E.9}$$

where

$$\varepsilon_P = 2P^2/P\ddot{P} \tag{E.10}$$

Similar expressions to the above have been provided by Cordes, Downs, and Krause-Polstorff (1988). The expressions of equations E.1-10 may be recast in terms of the pulsation period by simply exchanging the family of parameters based on ν with that based on P and vice-versa.

APPENDIX F - POSITION ERRORS AND PROPER MOTION

Manchester and Taylor (1977, pp. 105-106) give an expression for R_p in equation 4.8 in terms of position corrections in RA and dec., $\Delta\alpha$ and $\Delta\delta$, respectively, and the RA and dec. proper motion terms μ_α and μ_δ, respectively;

$$R_p = A\,[\Delta\alpha + \mu_\alpha(t_i - t_0)] + B\,[\Delta\delta + \mu_\delta(t_i - t_0)]$$

where t_i and t_0 are two epochs. The coefficients A and B are given by

$$A = \frac{r}{c}\cos(\delta_e)\cos(\delta)\sin(\alpha - \alpha_e)$$

$$B = \frac{r}{c}\,[\cos(\delta_e)\sin(\delta)\cos(\alpha - \alpha_e) - \sin(\delta_e)\cos(\delta)]$$

where (α,δ) and (α_e,δ_e) are the coordinates (measured in the frame of a standard epoch, e.g. J1950.0), as seen from the barycentre, of the pulsar and the Earth, respectively, and r is the barycentre-observatory distance.

The residual R_p has an annual term due to $\Delta\alpha$ and $\Delta\delta$. In the case of PSR0833-45, if $\Delta\alpha$ = 0.7 arc-sec or $\Delta\delta$ = 0.6 arc-sec, then $R_p \approx 250$ μs. If proper motion exist, then the residuals calculated between two epochs using equation 4.8 will exhibit a sinusoidal behaviour with period one year and increasing amplitude.

APPENDIX G - THE KINEMATIC CONTRIBUTION TO PULSE FREQUENCY

G.1 EVALUATION

Following Gallino and Silvestro (1971), consider a pulsar with intrinsic rotation frequency ν_0 lying at a distance R. The pulsar is moving with a velocity v in a direction which makes an angle θ with respect a barycentric observer's line-of-sight (figure B.1). The rotation frequency deduced by the observer is

$$\nu_k = \nu_0(1 + \beta)^{-1} \qquad \text{G.1}$$

where $\beta = v_r/c = v\cos(\theta)/c$, v_r being the radial component of the velocity. The subscript k distinguishes kinematic parameters.

By differentiating with respect to time t

$$\dot{\nu}_k = -\nu_0(1 + \beta)^{-2} v^2\sin^2(\theta)/(cR)$$
$$= -\nu_0 v_t^2(1 + \beta)^{-2}/(cR) \qquad \text{G.2}$$

where $v_t = v\sin(\theta)$ is the transverse component of the velocity. In addition

$$\ddot{\nu}_k = v\dot{\nu}_k[3\cos(\theta) - 2(1 + \beta)^{-1}v\sin^2(\theta)/c^2]/R \qquad \text{G.3}$$

For all θ, $\dot{\nu}_k < 0$, while for $\theta >,=,< \pi/2$, $\ddot{\nu}_k <,=,> 0$.

The above expressions have used the relations $d\theta/dt \approx -v\sin(\theta)/R$ and $dR/dt = -v_r$ where v_r is positive if the relative pulsar motion is away from the observer.

For PSR 0833-45, $R \approx 500$ pc and $v_t \approx 50$ km s^{-1} (table 1.2). Assuming $v_r << c$ and thus ignoring β

$$|\dot{\nu}_k|_{max} \approx -6.1\text{x}10^{-18} \text{ Hz s}^{-1}.$$

Further by putting $\theta = \pi/4$ rad

$$|\ddot{\nu}_k|_{max} \approx 5.9\text{x}10^{-32} \text{ Hz s}^{-1}.$$

By comparing these values with $\dot{\nu}$ and $\ddot{\nu}$ in table 1.2, it is apparent that the kinematic contributions to the observed pulsar rotation parameters are completely negligible.

Equations G.1-3 may be recast in terms of the period parameters :

$$P = P_0(1 + \beta)$$
$$\dot{P}_k = P_0 v^2\sin^2(\theta)/(cR) = P_0 v_t^2/(cR)$$
$$\ddot{P}_k = -3P_0 v^3\cos(\theta)\sin^2(\theta)/(cR) = -3v\dot{P}_k\cos(\theta)/(cR).$$

G.2 EFFECT ON BRAKING INDEX

The error expected in the determination of the braking index n_B based on the kinematic contribution to the observed spindown is:

$$\Delta n_B \approx - (n_B - 1)\frac{\nu_k}{\nu_k}$$

Putting $n_B = 3$, then $\Delta n_B \approx 6 \times 10^{-9}$ which is totally negligible.

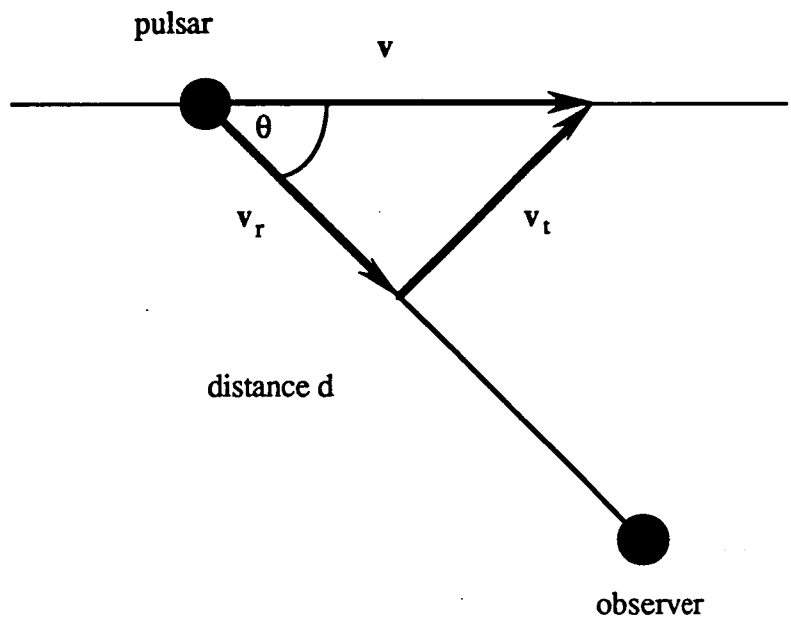

Fig. G.1 Geometry of doppler corrections.

APPENDIX H - TIMING MODEL FITS FOR PSR1749-28 AND PSR1641-45

H.1 PSR1748-28

Mean pulse profiles at 635 MHz and 954 MHz for a particular day are presented in figure H.1. In figure H.2, the mean I_x and I_y profiles for the same observing session are shown with the two standard deviation range at each phase bin superimposed. Note the large range of amplitude for the phase bins at the peak in comparison with the range for the off-peak bins. This is the result of intensity scintillations. In figure H.3, the I profiles spanning a 15 day range have been averaged at each frequency.

In figures H.4 and H.5, residuals from fits of quadratic and cubic spindown models are presented. The parameter values obtained are given in table 4.4 and table H.1 respectively. Arrival times producing obvious outlying residuals were removed prior to the final model fit. The typical arrival time uncertainty was 1 ms.

H.3 PSR1641-45

It was much more difficult to obtain accurate phase values for PSR1641-45 owing to the low signal-to-noise ratio of the pulses. Residuals from quadratic model fits to data obtained in 1983 and 1985 are presented in figures H.6a and H.6b respectively, while the model parameters are given in table H.1. Outlying observations were mechanically removed from separate fits to 1983 and 1985 data. It is evident that the value of $\dot{\nu}$ obtained from the 1985 data is in much better agreement with the catalogue value (section 4.13) than is the corresponding value obtained from the 1983 data. The latter discrepancy is related to the quality of the raw arrival time data. Residuals for a quadratic fit to the combined data set are shown in figure H.6c, highlighting the difference in the timing solutions for the two data sets. The typical arrival time uncertainty was 5-10 ms.

TABLE H.1

PARAMETERS FOR SECOND AND THIRD ORDER FITS[a]

Pulsar	Model	ν (Hz)	$\dot{\nu}$ ($\times 10^{-12}$ Hz s^{-1})	$\ddot{\nu}$ ($\times 10^{-22}$ Hz s^{-2})	Fit Epochs (TJD) Mid	Range	Residual rms (μs)
1741-28	1	1.777595488301±5	-0.02577±5	0.0	6552.1984179	6507.3-6593.1	530
	2	1.77759548785±8	-0.02566±4	-1115±175	6552.1984179	.....	423
1641-45	3	2.197521316±3	-0.088±7	0.0	5657.6371517	5639.7-5680.6	4544
	4	2.197516018±1	-0.09630±88	0.0	6289.9062455	6228.1-6343.7	8523
	5	2.197516533±1	-0.09635±5	0.0	6228.0577642	5639.7-6345.7	14372

[a] Errors are $\pm$ 1 σ in the last digit(s).

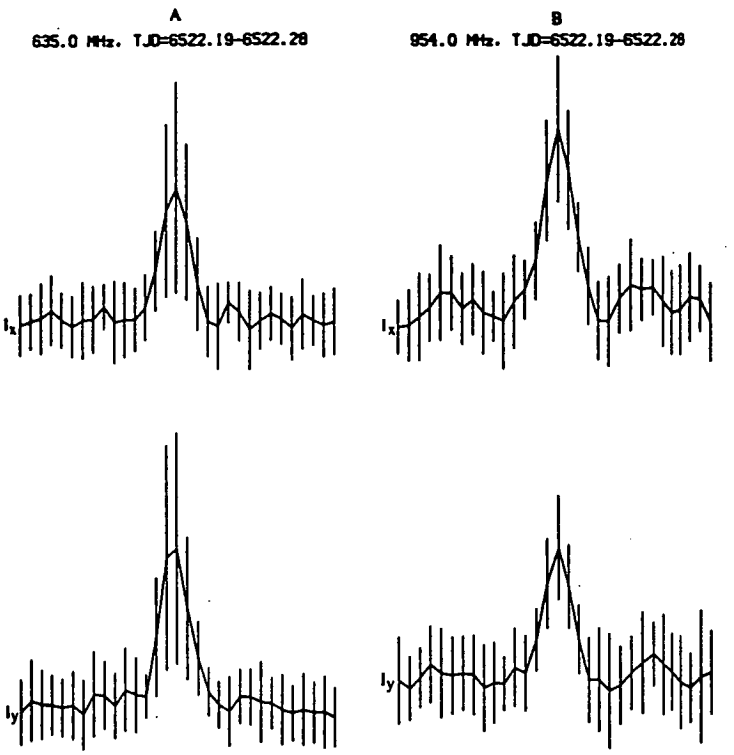

Fig. H.1. Mean I_x and I_y pulse profiles for PSR1749-28 at (a) 635 MHz, and (b) 954 MHz. The two standard deviation range of the pooled values at each phase bin is indicated.

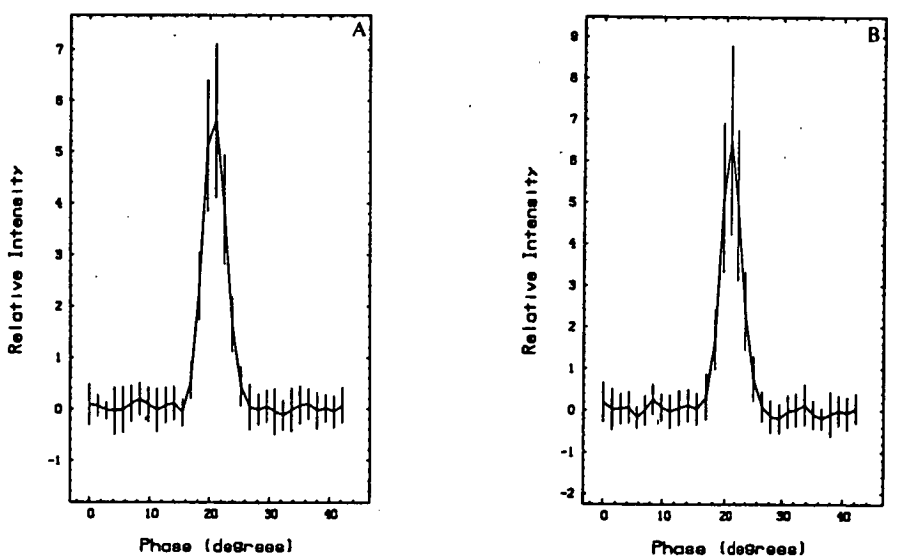

Fig. H.2. Total intensity profile for PSR1749-28 at (a) 635 MHz, and (b) 954 MHz. The epoch range of the summation was TJD 6507.23-6522.28. The two standard deviation range of the pooled estimates at each phase bin is also shown.

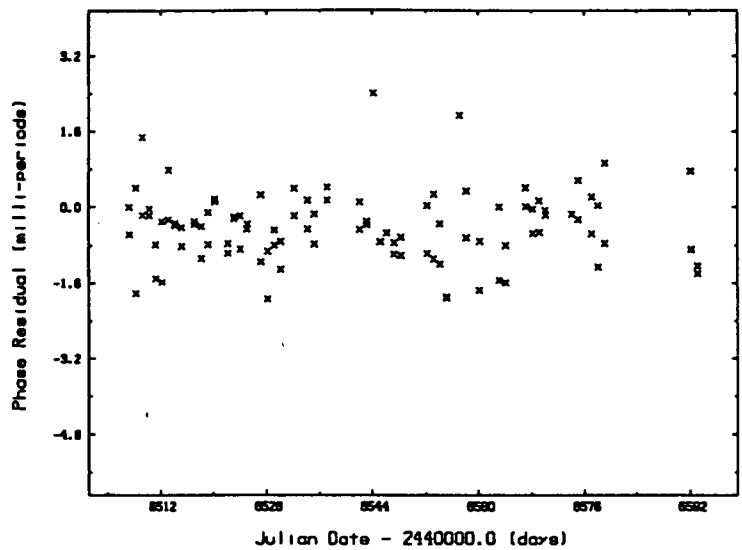

Fig. H.3. Phase residuals from the fit of a cubic spindown model to data for PSR1749-28.

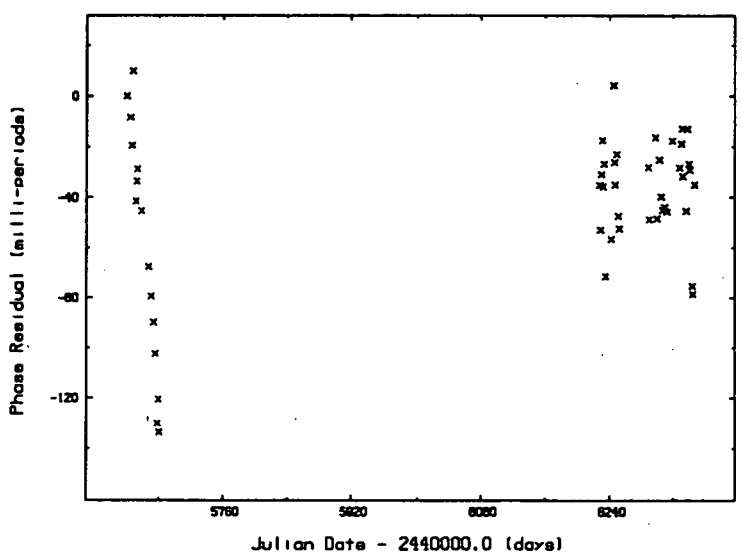

Fig. H.4. Residuals from the fit of a quadratic spindown model to data for PSR1641-45.

APPENDIX I - TIMING MODEL FITS

In this appendix, parameters and residuals for fits to Vela timing data are presented. Each model is identified by a sequence number. The residuals from the model fits, together with their probability distribution and autocorrelation function are provided. The model number used is indicated in the top left hand corner or each diagram.

TABLE I.1

PARAMETERS FOR SPINDOWN MODEL FITS[a]

Model	Data Type[b]	ν (Hz)	$\dot{\nu}$ ($\times 10^{-12}$ Hz s^{-1})	$\ddot{\nu}$ ($\times 10^{-22}$ Hz s^{-2})	Fit Epochs (TJD) Mid	Range	Residual rms (μs)
1	R	11.20345233231±2	-15.6817±2	52.1±2	4918.4114940	4889.3-4989.1	180
2	C	11.20345235267±8	-15.68172±8	52.1±6	4918.3964275	...	183
3	R	11.20323700101±7	-15.6485±2	23.0±1	5077.5324300	4990.1-5150.7	139
4	C	11.2033093637±1	-15.65907±7	22.9±2	5024.0290583	...	69
5	R	11.2031179218±1	-15.63067±5	20.0±14	5165.6575254	5137.7-5191.6	123
6	C	11.2031165809±2	-15.6306±1	17.5±28	5166.6505557	...	74
7	R	11.20302003146±5	-15.68929±3	77.6±3	5254.7016485	5192.6-5293.4	400
8	C	11.2030217046±2	-15.6900±1	73.3±11	5253.4677169	...	435
9	R	11.20288632209±2	-15.667934±7	13.20±8	5353.4310508	5294.2-5394.1	121
10	C	11.20288682452±4	-15.66795±1	13.3±2	5353.0598790	...	56
11	R	11.20275124209±1	-15.653633±7	5.42±7	5453.2674793	5394.9-5494.8	129
12	C	11.20275306546±4	-15.65370±2	5.4±2	5451.9193539	...	78
13	R	11.20262830583±1	-15.646044±4	13.15±5	5544.1843708	5494.7-5593.6	103
14	C	11.20262498575±2	-15.645834±8	13.4±1	5546.6404200	...	42
15	R	11.20249294981±1	-15.641584±4	1.23±5	5644.3354244	5594.4-5693.3	92
16	C	11.20249420849±3	-15.641591±9	1.2±1	5643.4040204	...	49

TABLE I.1(continued)

PARAMETERS FOR SPINDOWN MODEL FITS[a]

Model	Data Type[b]	ν (Hz)	$\dot{\nu}$ ($\times 10^{-12}$ Hz s^{-1})	$\ddot{\nu}$ ($\times 10^{-22}$ Hz s^{-2})	Fit Epochs (TJD) Mid	Range	Residual rms (μs)
17	R	11.202360353439±9	-15.636484±3	3.86±5	5742.4632733	5694.1-5791.0	95
18	C	11.20235964907±3	-15.636460±1	3.87±13	5742.9846672	...	55
19	R	11.202227549333±9	-15.629265±3	3.13±4	5840.7855541	5791.8-5891.7	96
20	C	11.20222764500±3	-15.62927±1	3.2±1	5840.7147472	...	66
21	R	11.20209558105±1	-15.624892±4	5.01±5	5938.5257003	5892.6-5991.5	96
22	C	11.20209435507±2	-15.624870±8	5.0±1	5939.4338208	...	43
23	R	11.20195614607±1	-15.618301±5	6.32±6	6041.8323810	5992.3-6093.1	125
24	C	11.20195819154±3	-15.61821±1	6.7±1	6040.3166493	...	51
25	R	11.201819646372±9	-15.612846±3	1.73±4	6143.0060403	6094.0-6192.9	94
26	C	11.20181980508±2	-15.612681±7	4.49±9	6142.8876785	...	44
27	R	11.20170957006±2	-15.607013±9	10.6±2	6224.6199296	6193.8-6257.7	90
28	C	11.20171065793±4	-15.60707±2	11.3±3	6223.8131823	...	35
29	R	11.20161418510±3	-15.68430±1	42.8±1	6308.3269009	6260.6-6361.4	189
30	C	11.2016152044±1	-15.68457±4	42.6±6	6307.5746981	...	177
31	R	11.20147632190±2	-15.663024±8	20.3±1	6410.1433847	6364.3-6454.2	135
32	C	11.20147631453±7	-15.66304±3	20.8±3	6410.1487277	...	95

[a] Errors are ± 1 σ in the last digit(s).

[b] Data types : R = raw (uncompressed), C = compressed ~8 points per day, S = compressed 1 point per day.

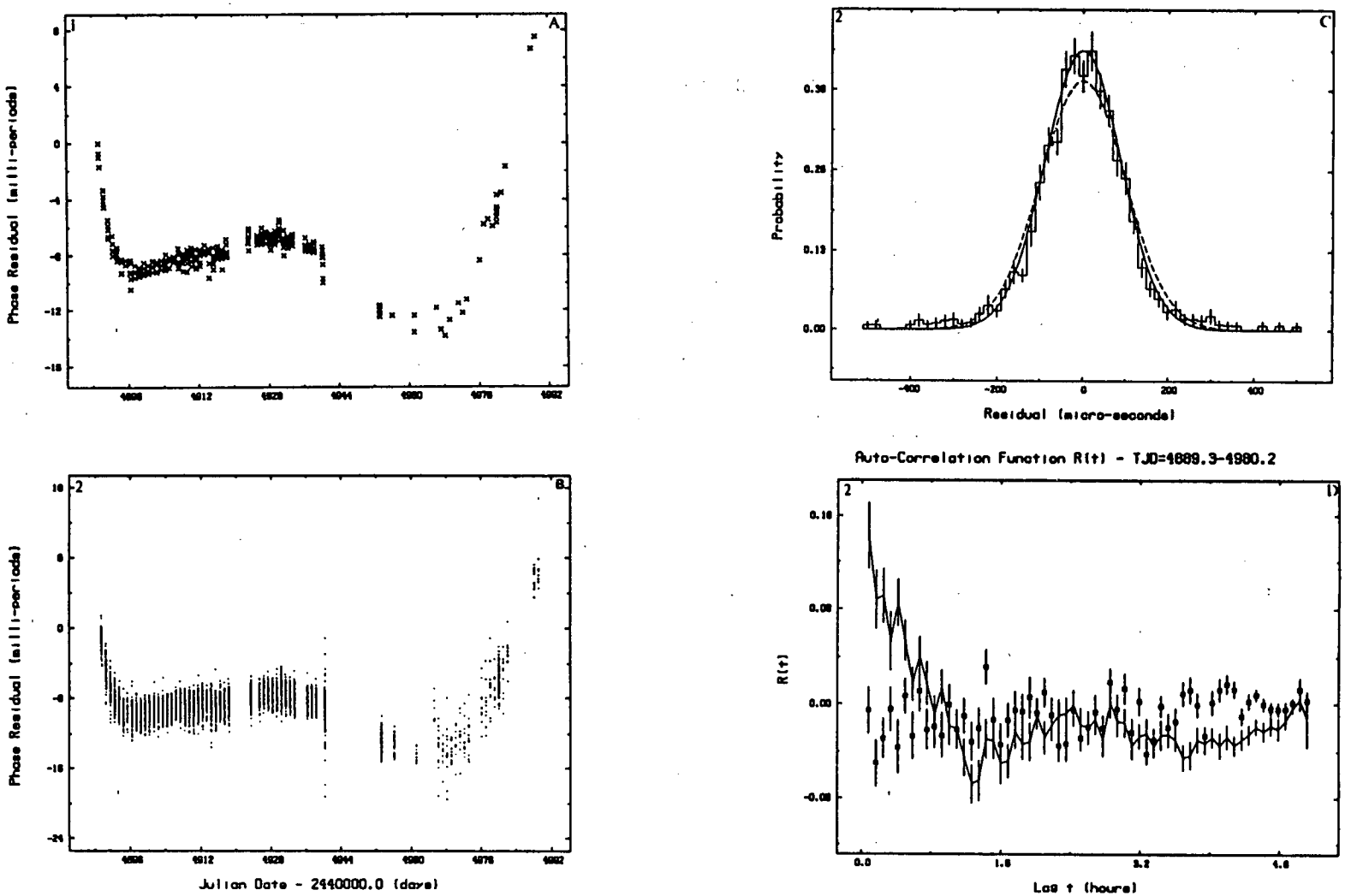

Fig. I.1. (a) Residuals from cubic model applied to medium resolution compressed data. (b) residuals from cubic model applied to high resolution data. (c) probability distribution of residuals from (b) superimposed with a best-fit gaussian with the same area and second moment as the observed distribution (*solid line*) and a gaussian with the same area as the observed distribution but with a half-width of 100 μs (*dashed line*). (d) averaged autocorrelation function of the daily residuals from (b) placed in 5 minute wide bins (*solid line*). The 1σ confidence limit for each mean is indicated by the extent of the associated vertical line. The averaged autocorrelation function for binned gaussian random numbers with the same variance as the each daily residual sample is also shown (*squares*).

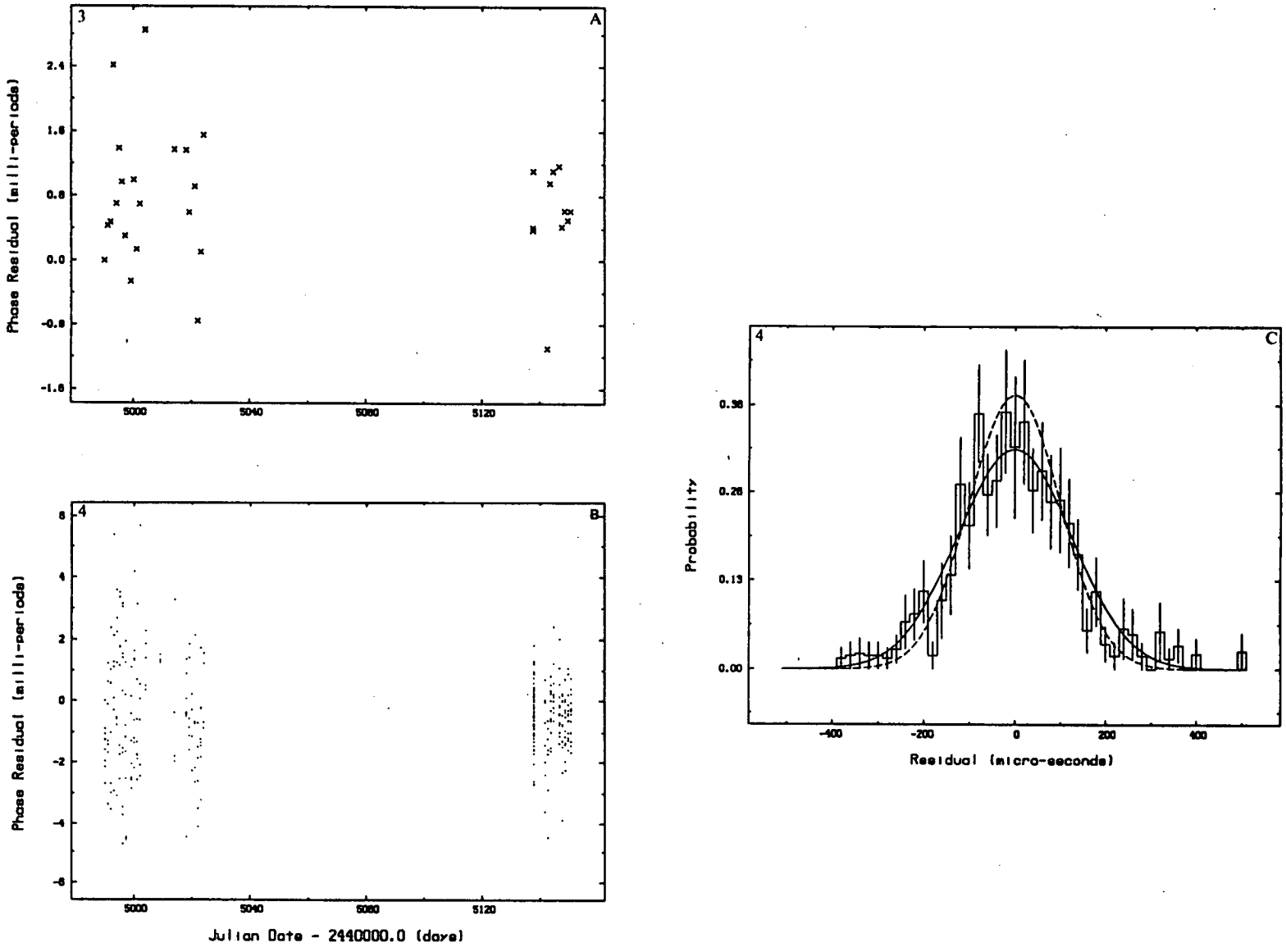

Fig. I.2. As for figure I.1.

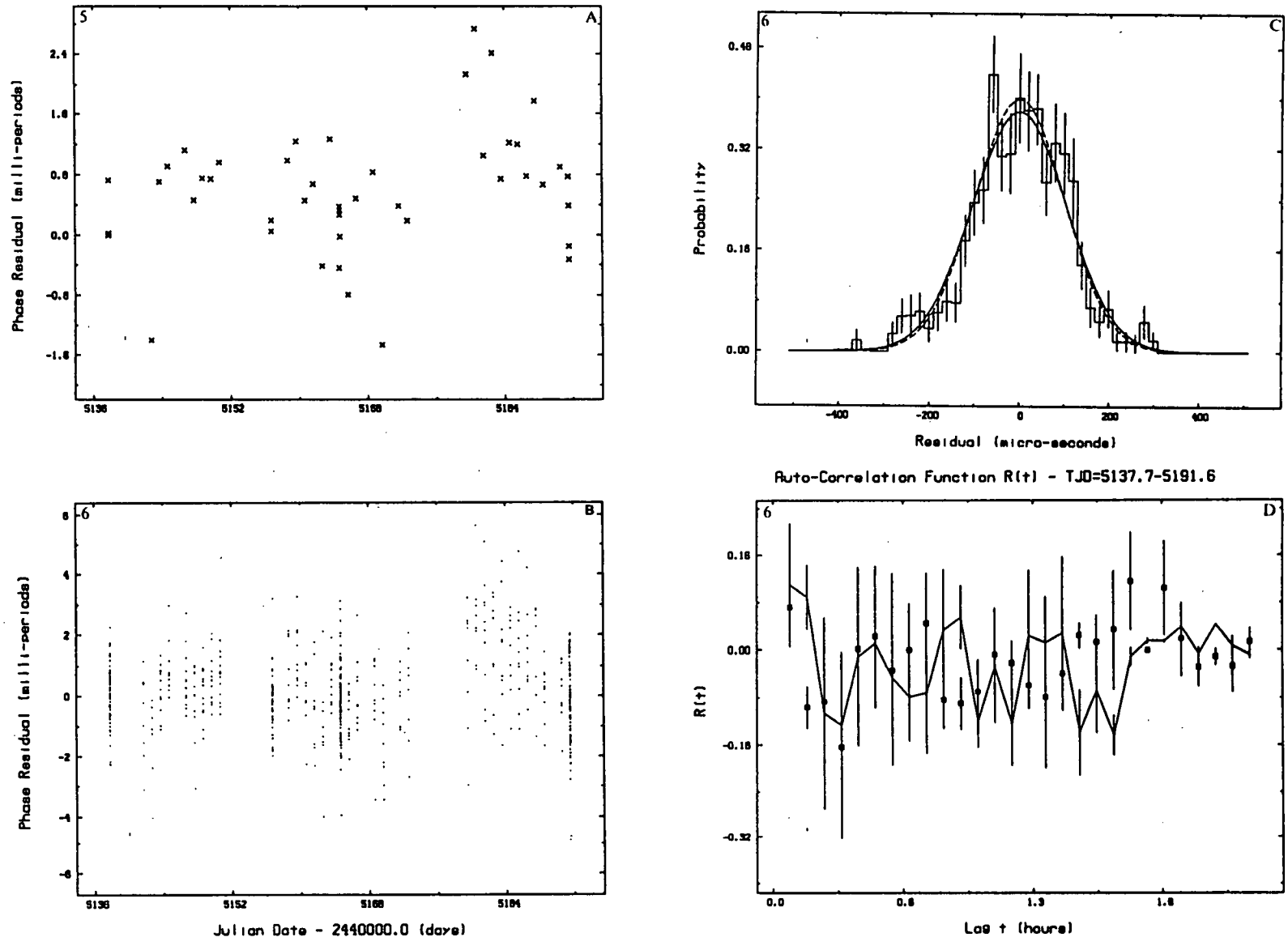

Fig. I.3. As for figure I.1.

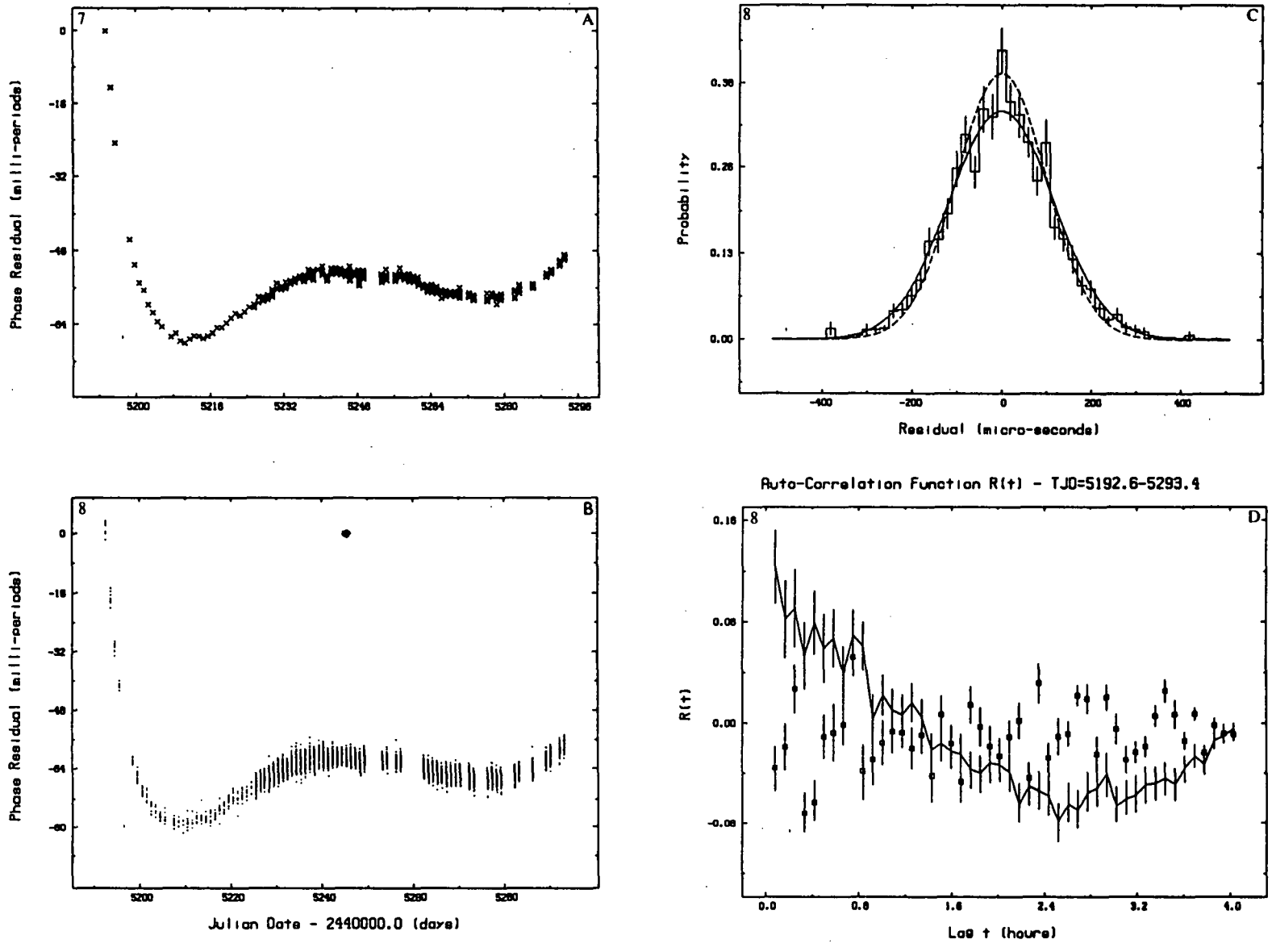

Fig. I.4. As for figure I.1.

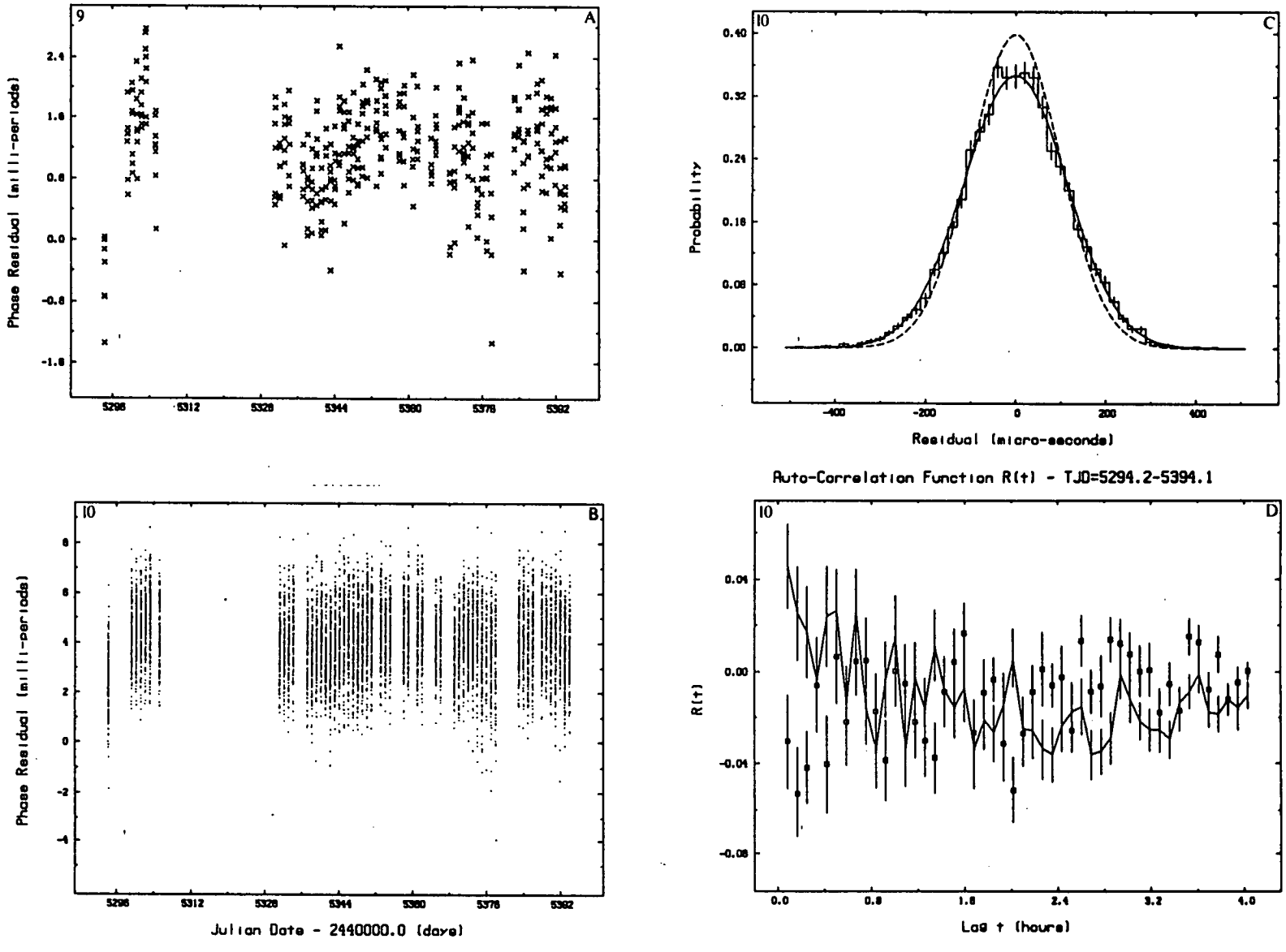

Fig. I.5. As for figure I.1.

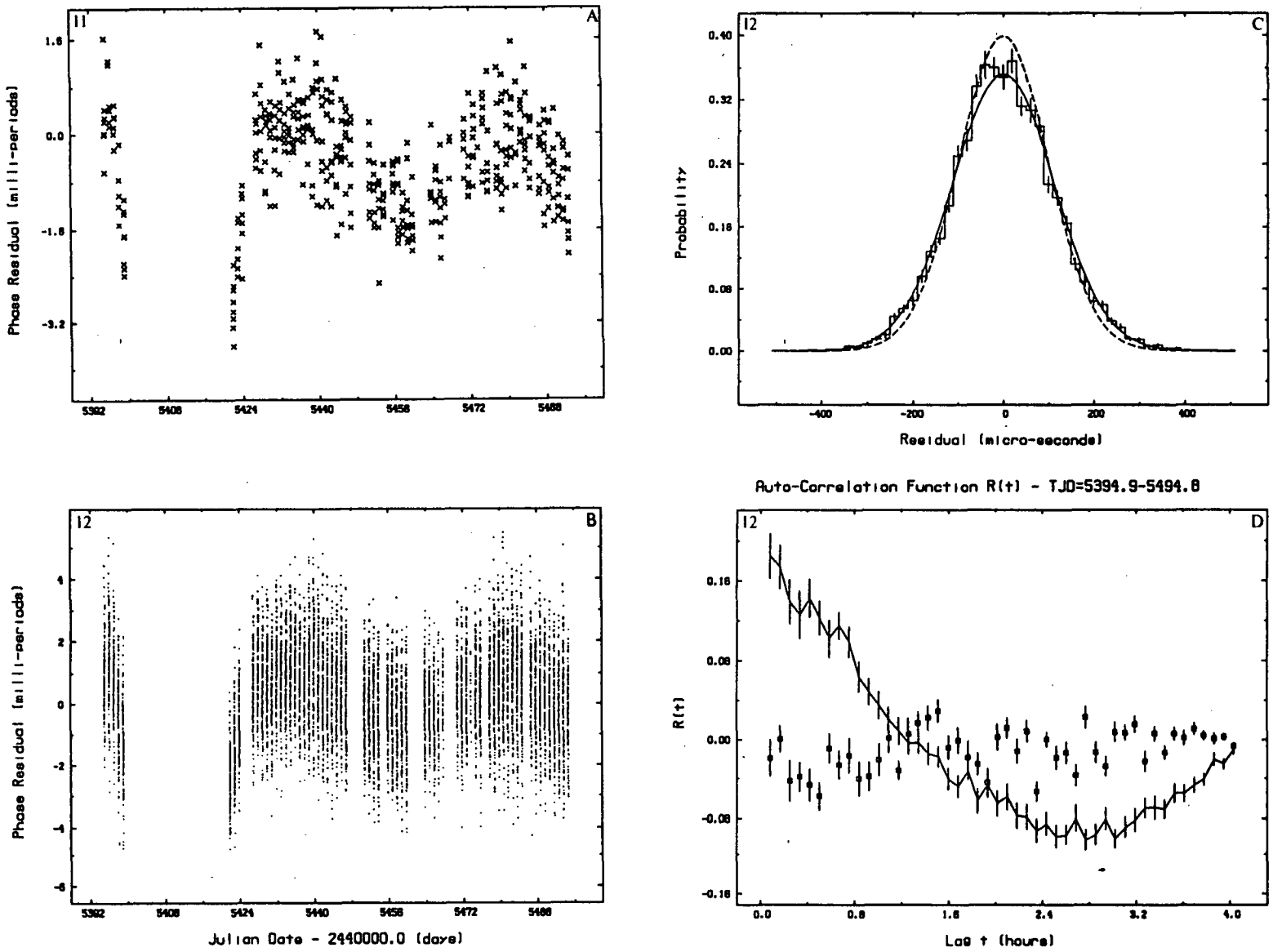

Fig. I.6. As for figure I.1.

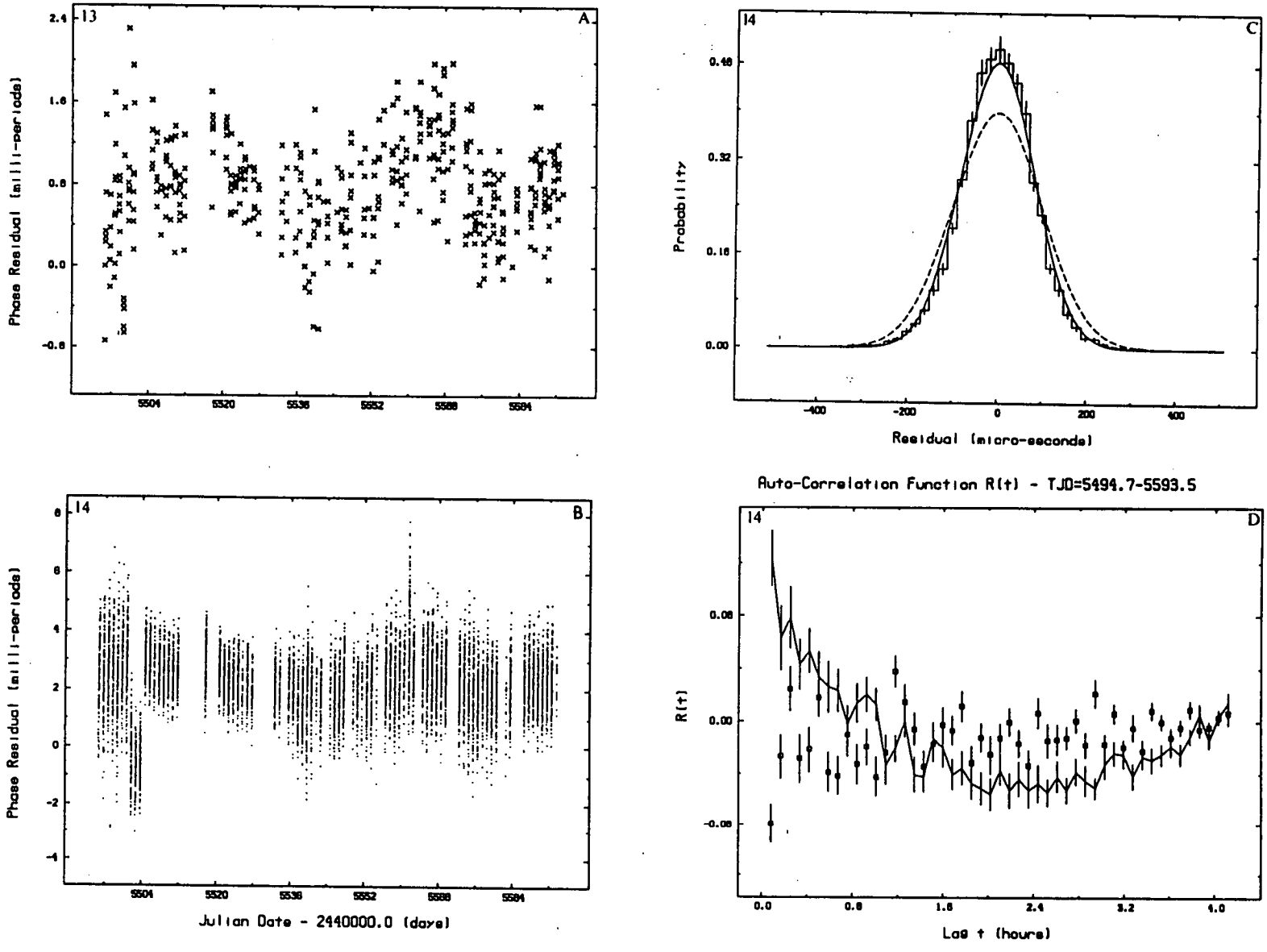

Fig. I.7. As for figure I.1.

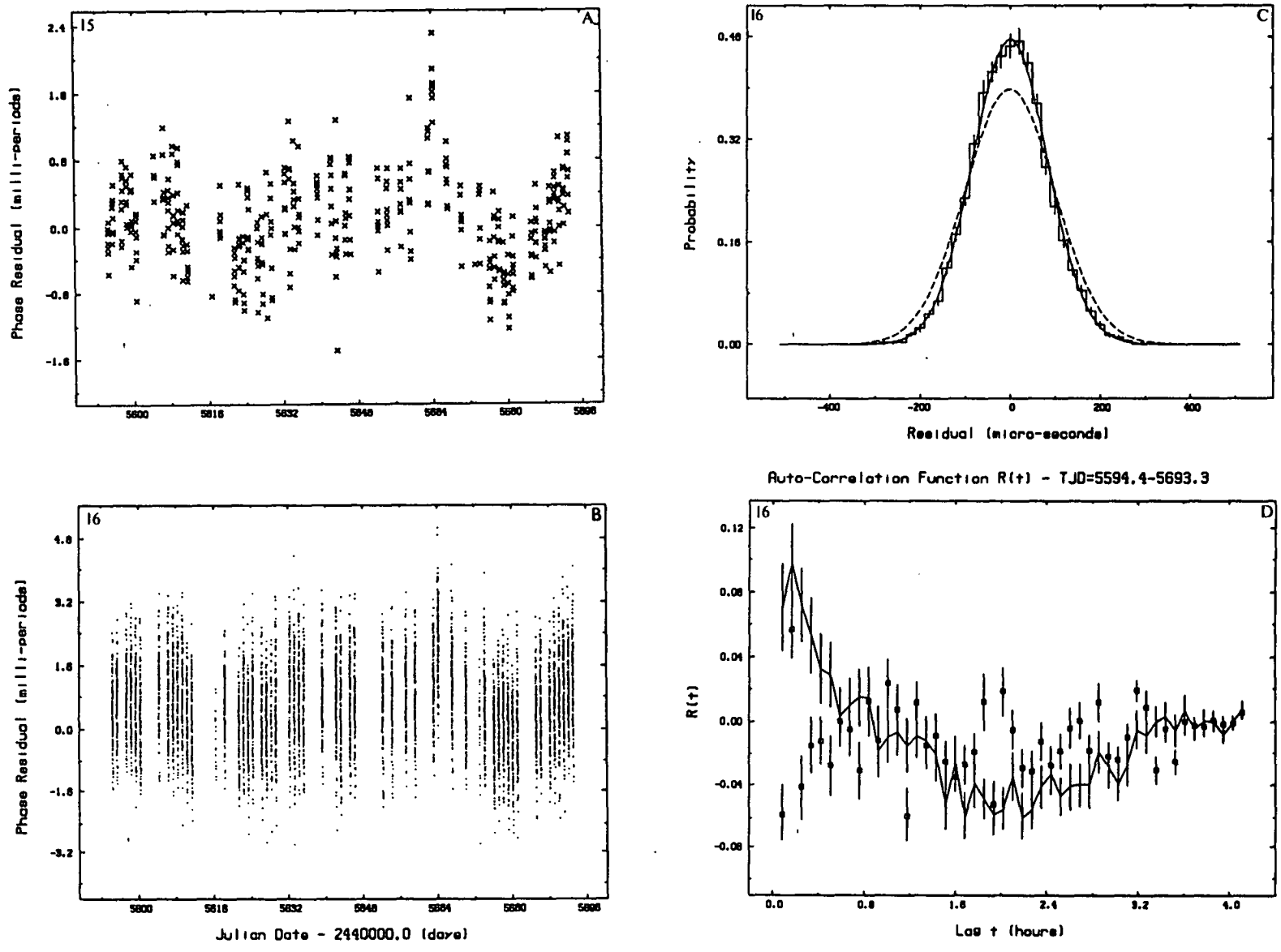

Fig. I.8. As for figure I.1.

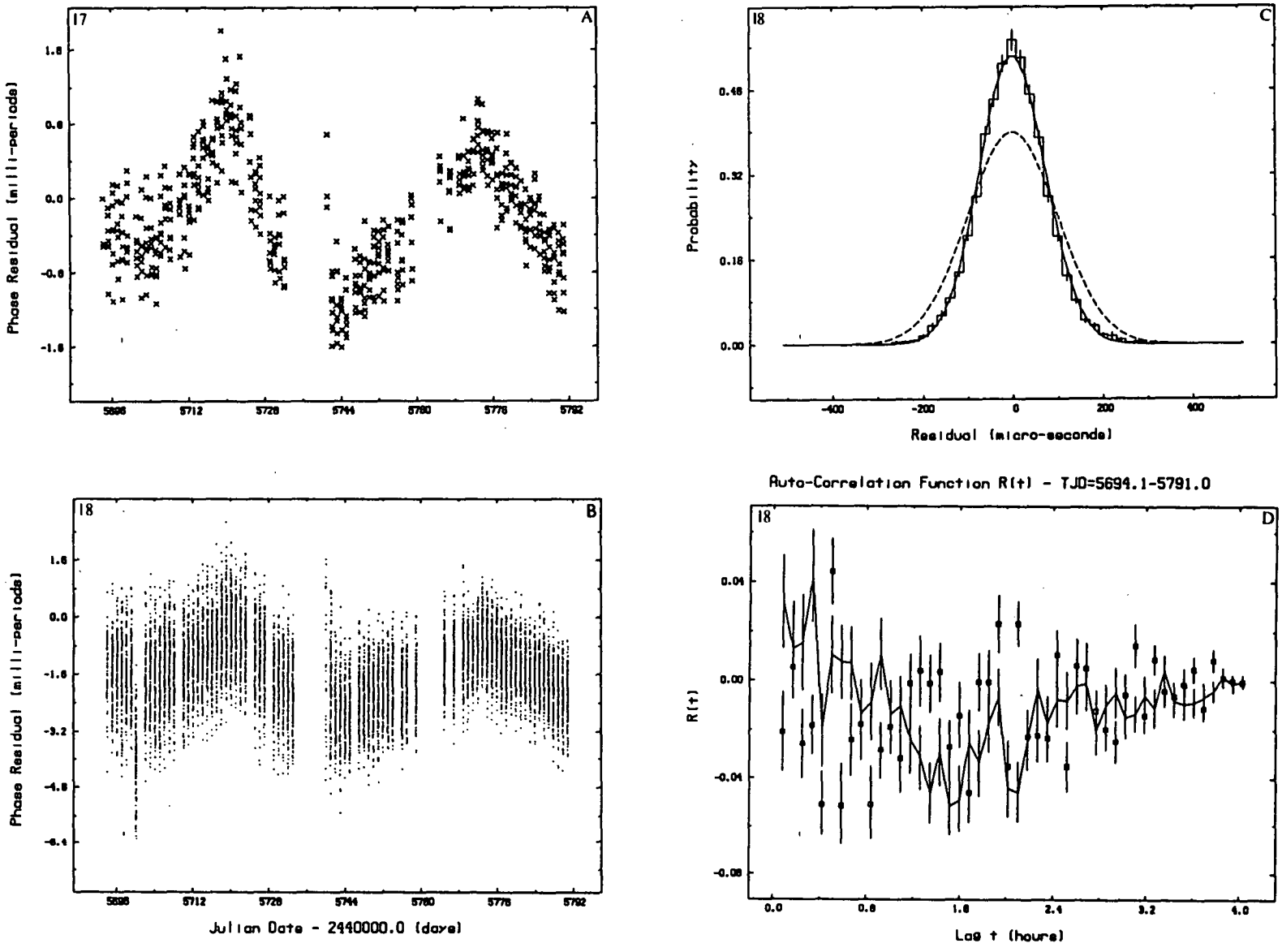

Fig. I.9. As for figure I.1.

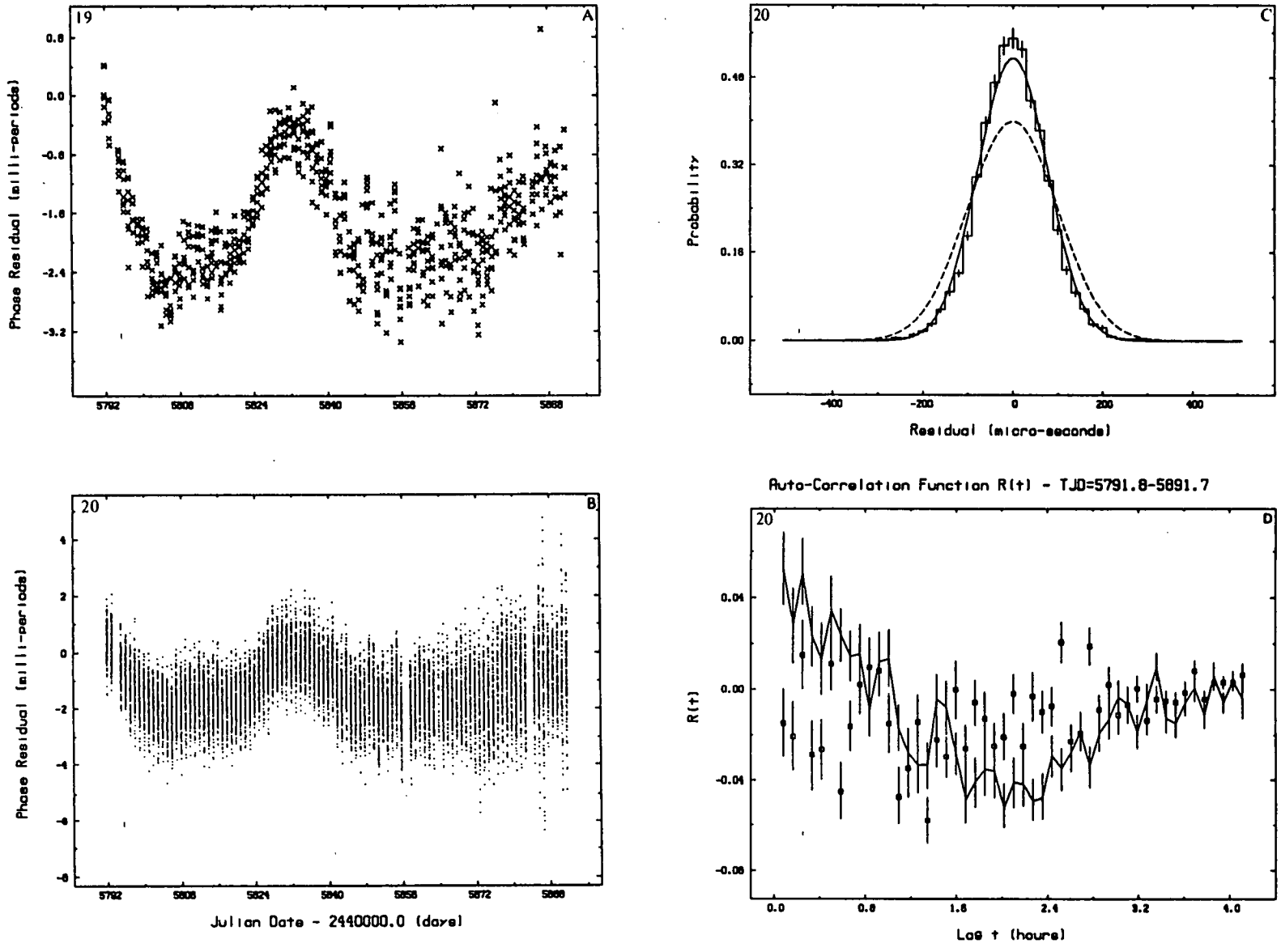

Fig. I.10. As for figure I.1.

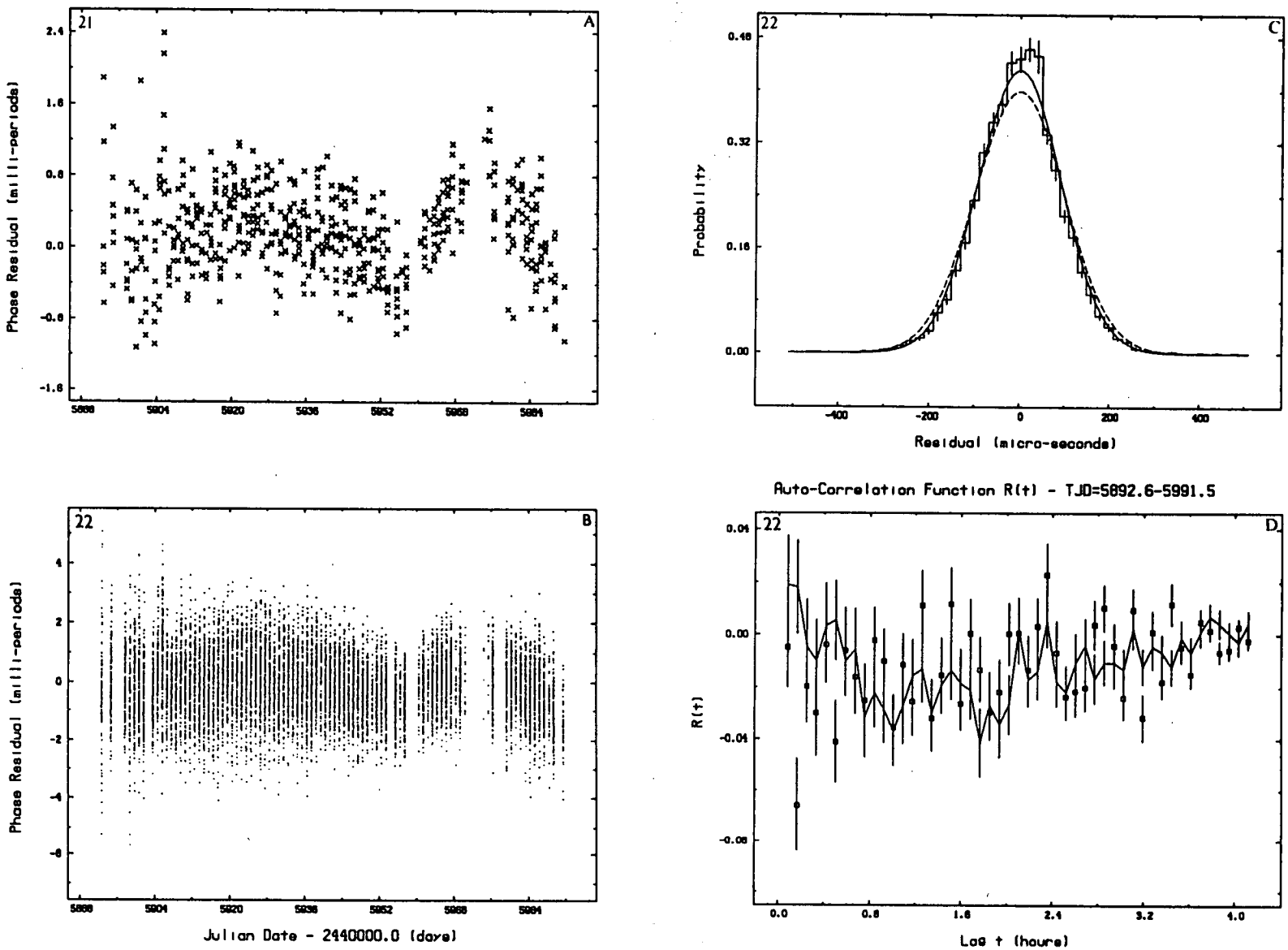

Fig. I.11. As for figure I.1.

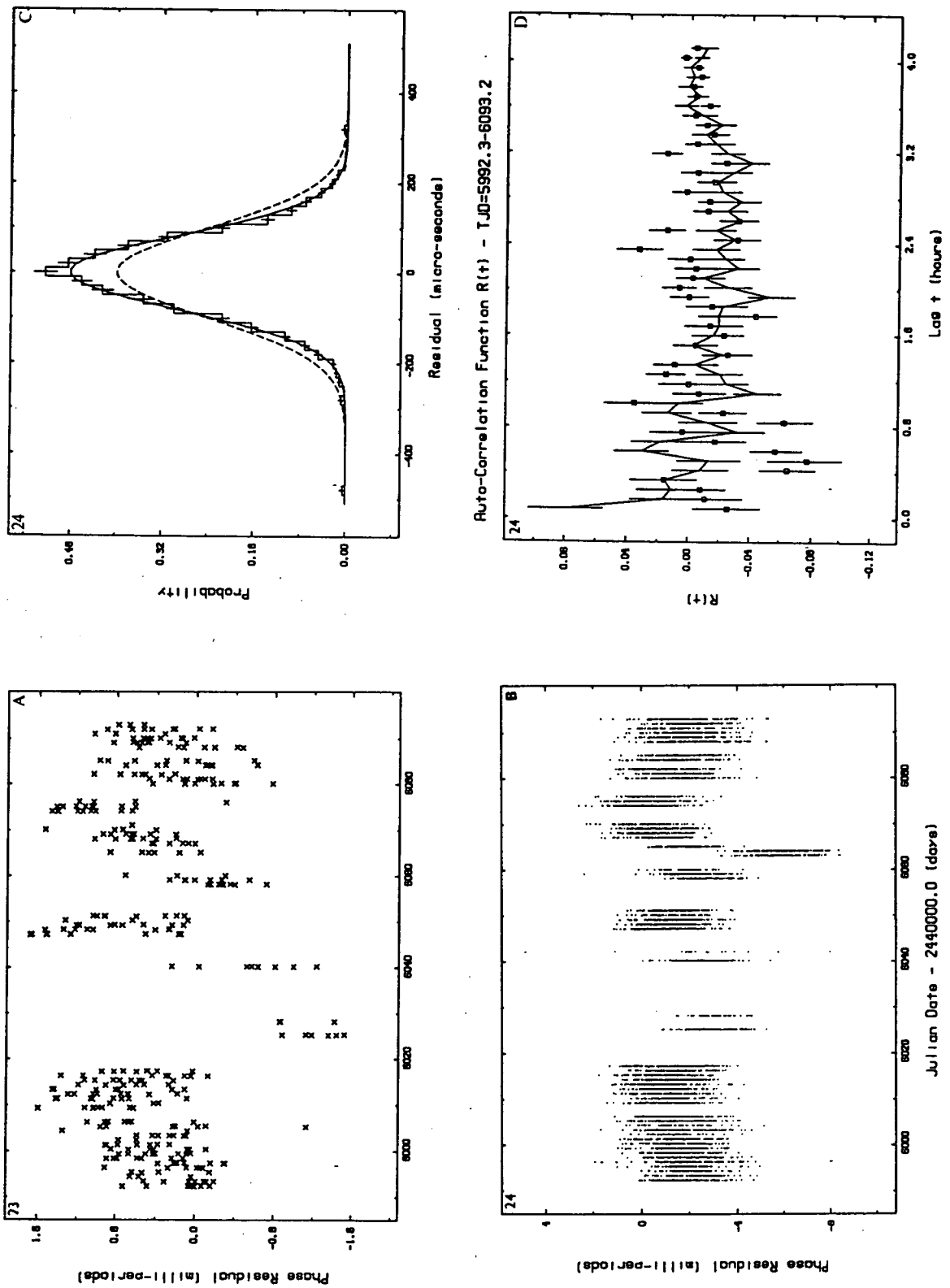

Fig. I.12. As for figure I.1.

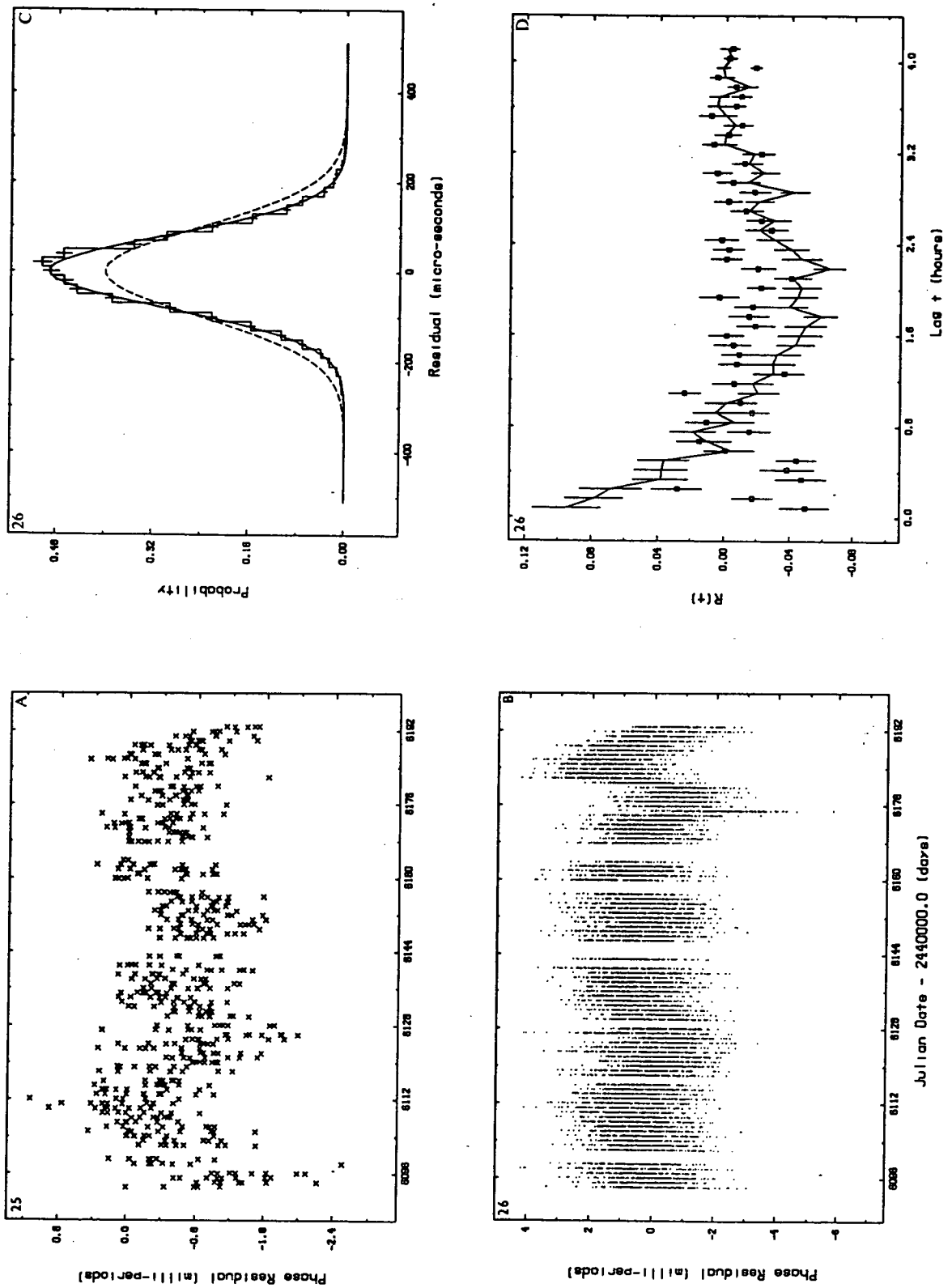

Fig. I.13. As for figure I.1.

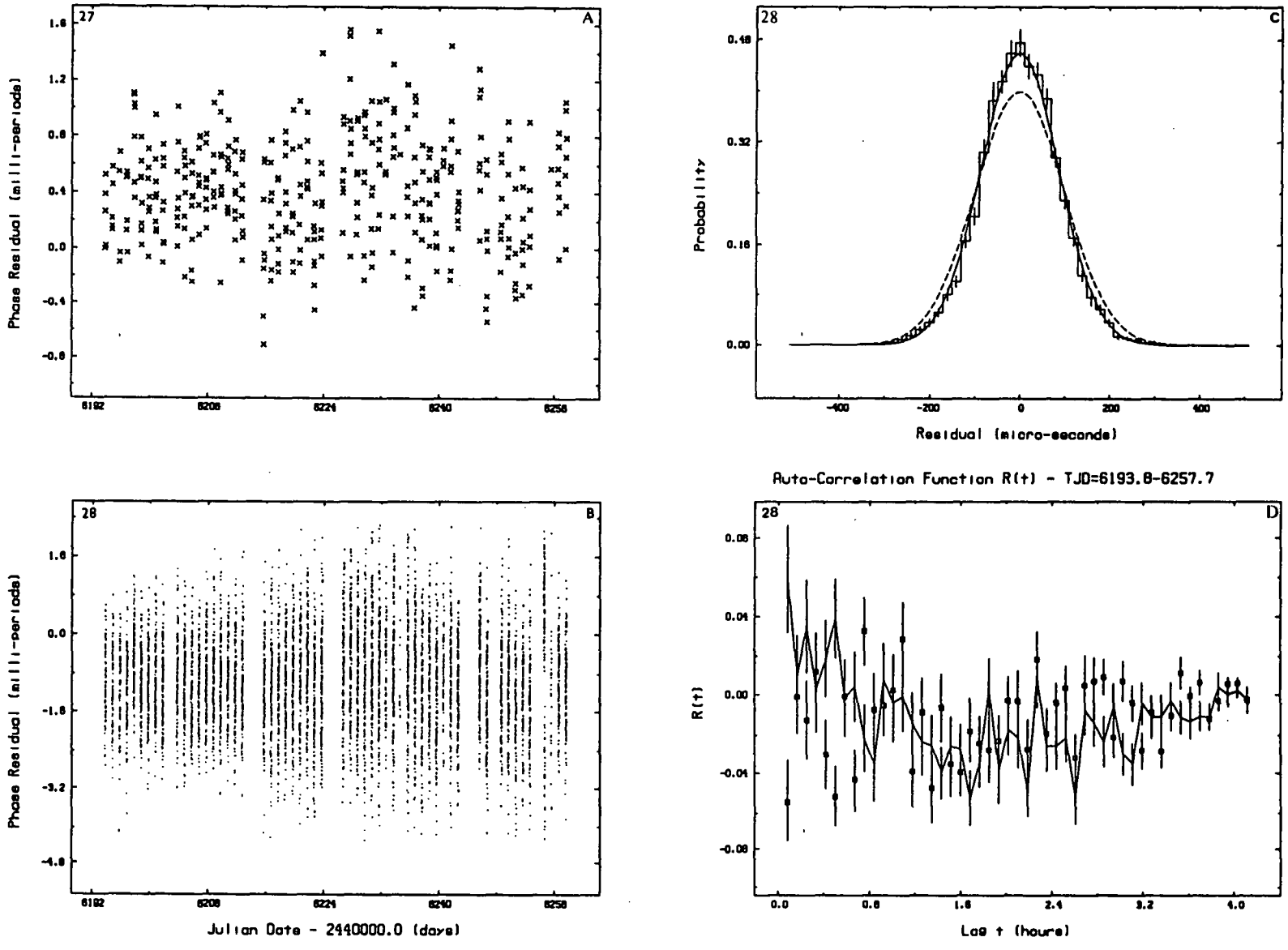

Fig. I.14. As for figure I.1.

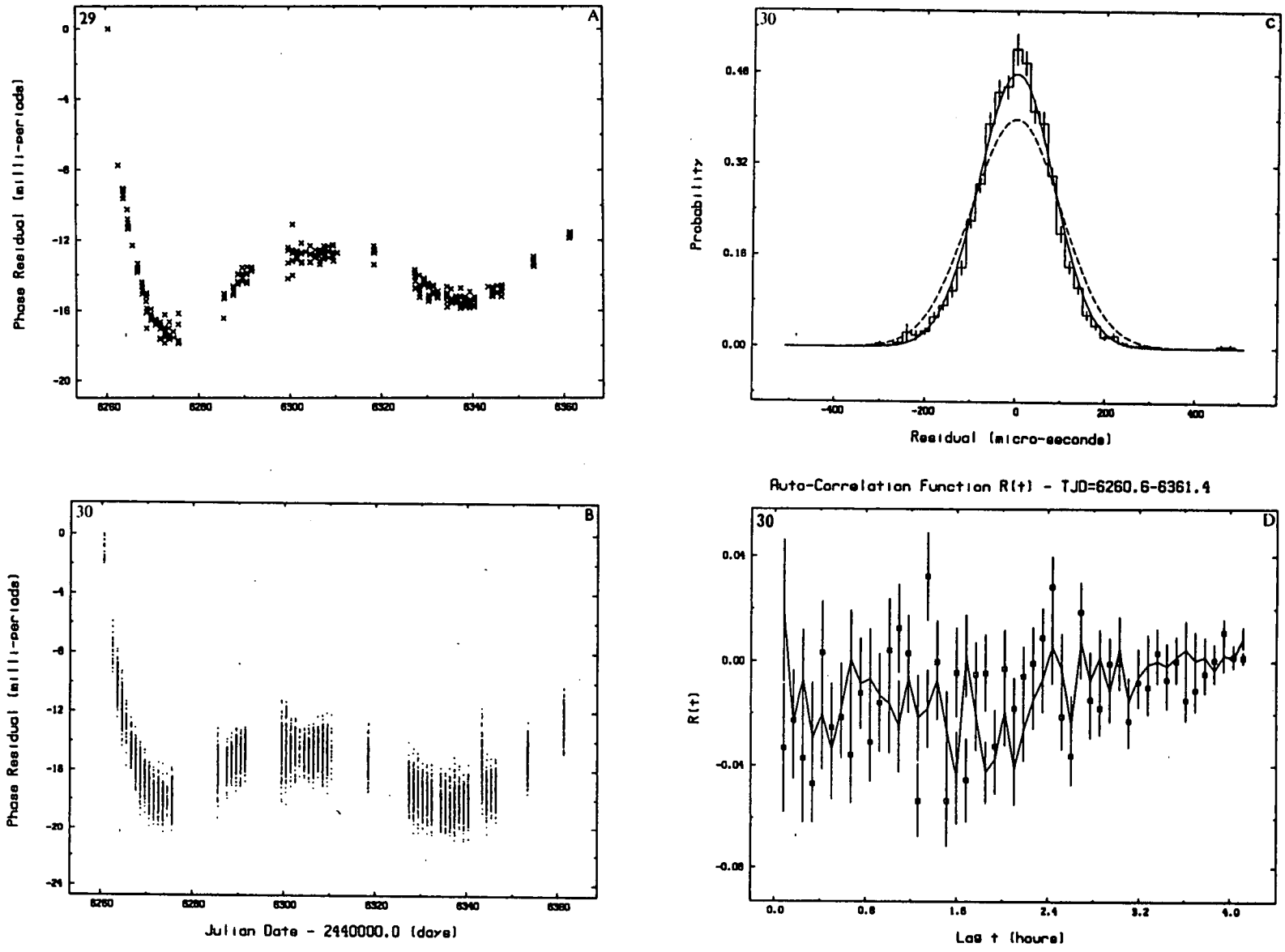

Fig. I.15. As for figure I.1.

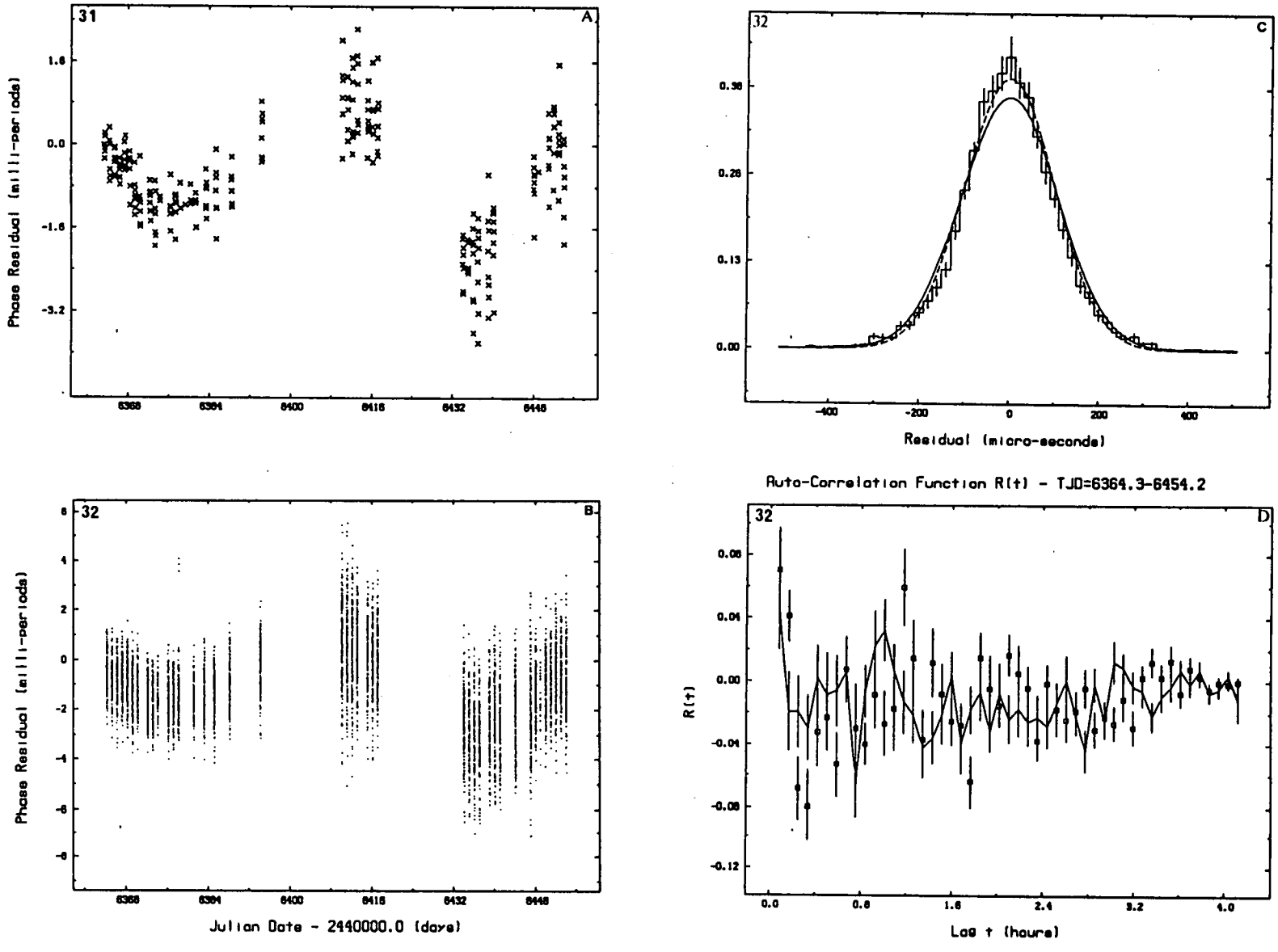

Fig. I.16. As for figure I.1.

APPENDIX J - RUNS TESTS FOR PRE-GLITCH RESIDUALS

In this appendix, the distributions for the runs test conducted on sets of pre-glitch residuals are presented. The distributions in figures J.1 to J.5 are compared with their theoretical expectations.

For relative runs, the sum of the expectations of positive and negative runs (i.e. $R_i > R_{i+1}$ and $R_i < R_{i+1}$ respectively) of length $j > 0$ is

$$E_j = \frac{2\,(N - 1 - 2)\,(j^2 + 3j + 1)}{(j + 3)!}$$

where N is the number of observations in the timeseries (Kendall, 1948, p. 125). For positive and negative runs (denoted by + and - respectively)

$$E_{j+} = E_{j-} = \frac{E_j}{2} \qquad \text{J.1}$$

The tallies for $j > 7$ have been pooled in the 8-th bin, for which

$$E_8 = \frac{2N - 7}{3} - \sum_{j=1}^{7} E_j.$$

The χ^2 statistic was calculated from

$$\chi^2 = \sum_{j=1}^{8} \frac{(O_j - X_j)^2}{X_j}$$

where O_j is the observed tally for the run of length j, and

$$X_j = E_j \sum_{k=1}^{8} \frac{O_j}{[(2N - 7)/3]}$$

as based on the discussion in Kendall (1948), page 126. The effective degrees of freedom is 7.

For mean and median runs, it can be shown that the total expectation is

$$E_j = \frac{N}{2^{j+1}}$$

The tallies for $j > 9$ were accumulated in the 10-th bin for which

$$E_{10} = \lim_{n \to \infty} \sum_{j=10}^{n} E_j = E_9.$$

Equation J.1 applies to the expectations of the positive and negative runs. The expected mean and variance of the total number of runs in a population of size N is

$$\mu_e = 0.5N + 1 \qquad \sigma_e = \frac{N\,(N - 2)}{4\,(N - 1)}$$

(Dixon and Massey, 1985, p. 394). The observed total number of runs u can be compared with the expectation value through use of the z statistic;

$$z = \frac{u - \mu_e + 0.5}{\sigma_e}$$

The probability of exceeding z by taking samples from a population of gaussian variable can be obtained from tables for the normal distribution.

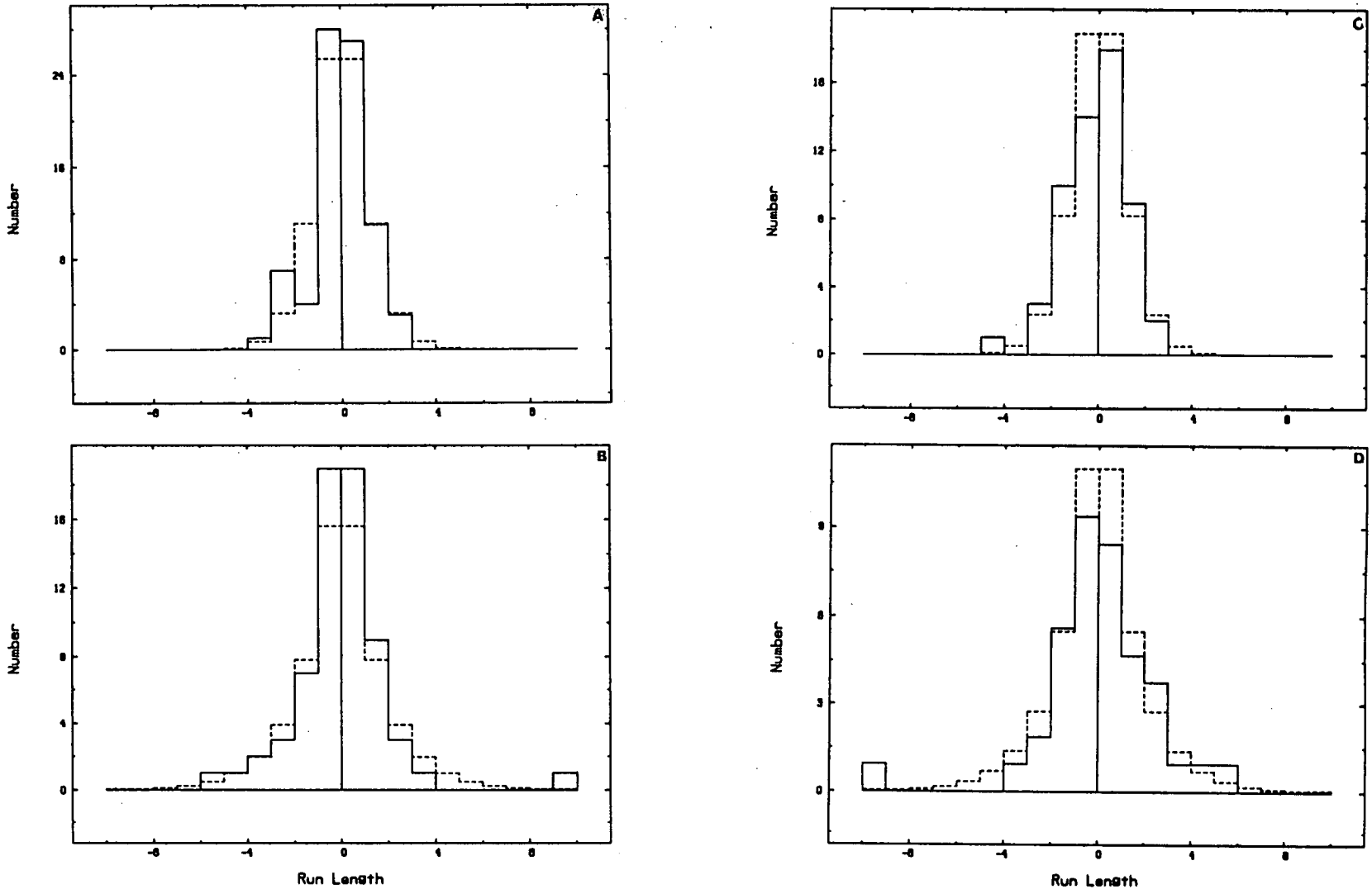

Fig. J.1. Distribution of residual runs prior to each glitch. *Solid line* - observed distribution, *dashed line* - expected distribution. The absissca represents the run length with negative and positive runs plotted left and right of the origin respectively. The ordinate represents the total number of runs for each run length. (a) and (b) relative and mean runs for the session prior to glitch 5. (c) and (d) relative and mean runs for the session prior to glitch 6.

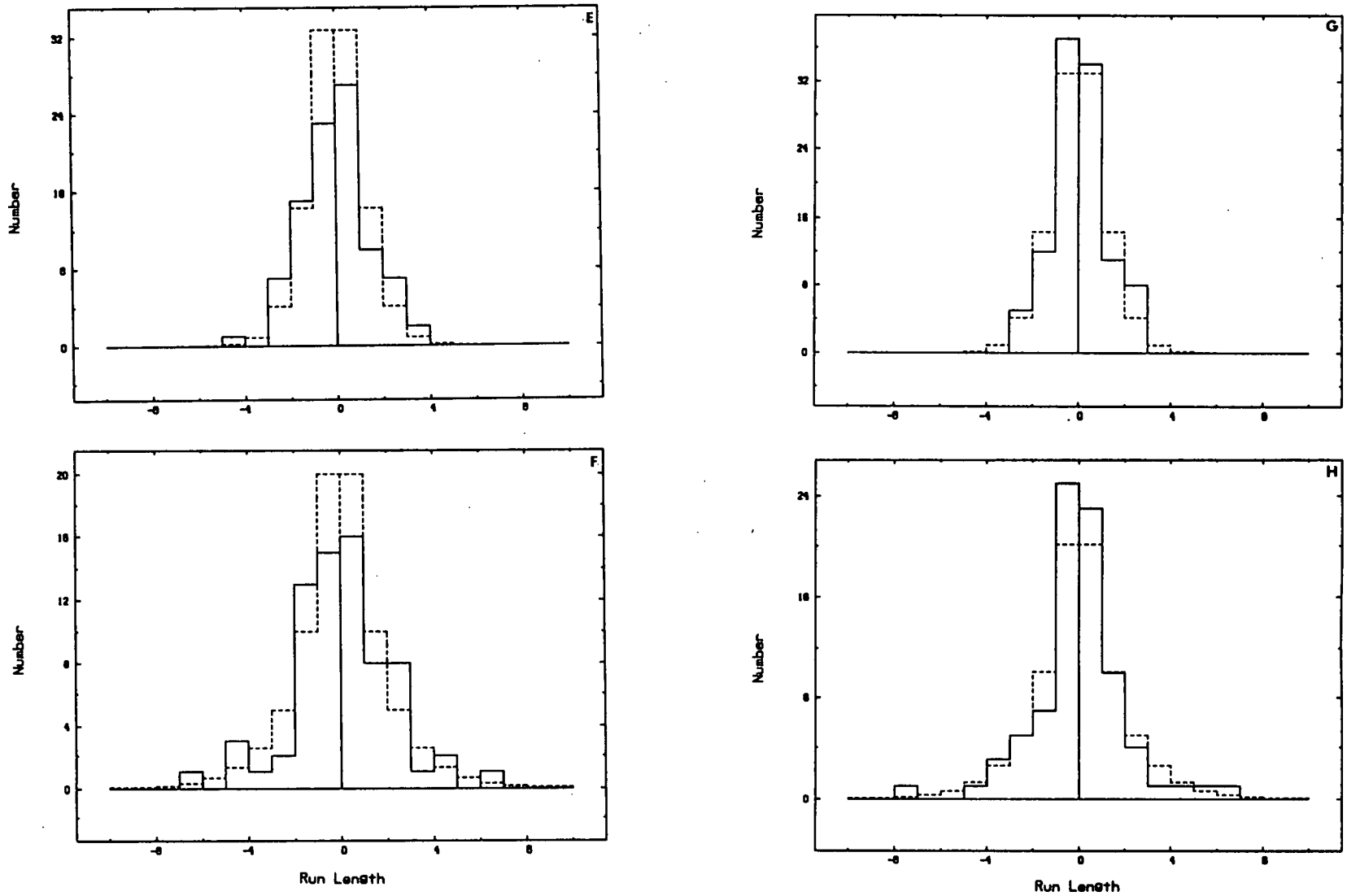

Fig. J.1. (continued) (e) and (f) relative and mean runs prior to glitch 7. (g) and (h) relative and mean runs for a simulation of 160 gaussian random numbers.

APPENDIX K - DUAL FREQUENCY ANALYSIS

In this appendix, the residuals from model fits (table K.1) to simultaneously obtained 635 MHz and 954 MHz, and selected mean autocorrelation functions are provided.

TABLE K.1

PARAMETERS FOR THIRD ORDER FITS TO HIGH RESOLUTION LRO DUAL FREQUENCY OBSERVATIONS[a]

Frequency (MHz)	Model	ν (Hz)	$\dot{\nu}$ ($\times 10^{-12}$ Hz s^{-1})	$\ddot{\nu}$ ($\times 10^{-22}$ Hz s^{-2})	Fit Epochs (TJD) Mid	Range	Residual rms (μs)
635	43	11.20127402485±1	-15.647174±4	12.70±3	6559.7095383	6497.9-6643.7	204.0
954	44	11.20127402479±5	-15.647178±4	12.65±3	6559.7095424	6497.9-6643.7	191.2

[a] Errors are ± 1 σ in the last digit(s).

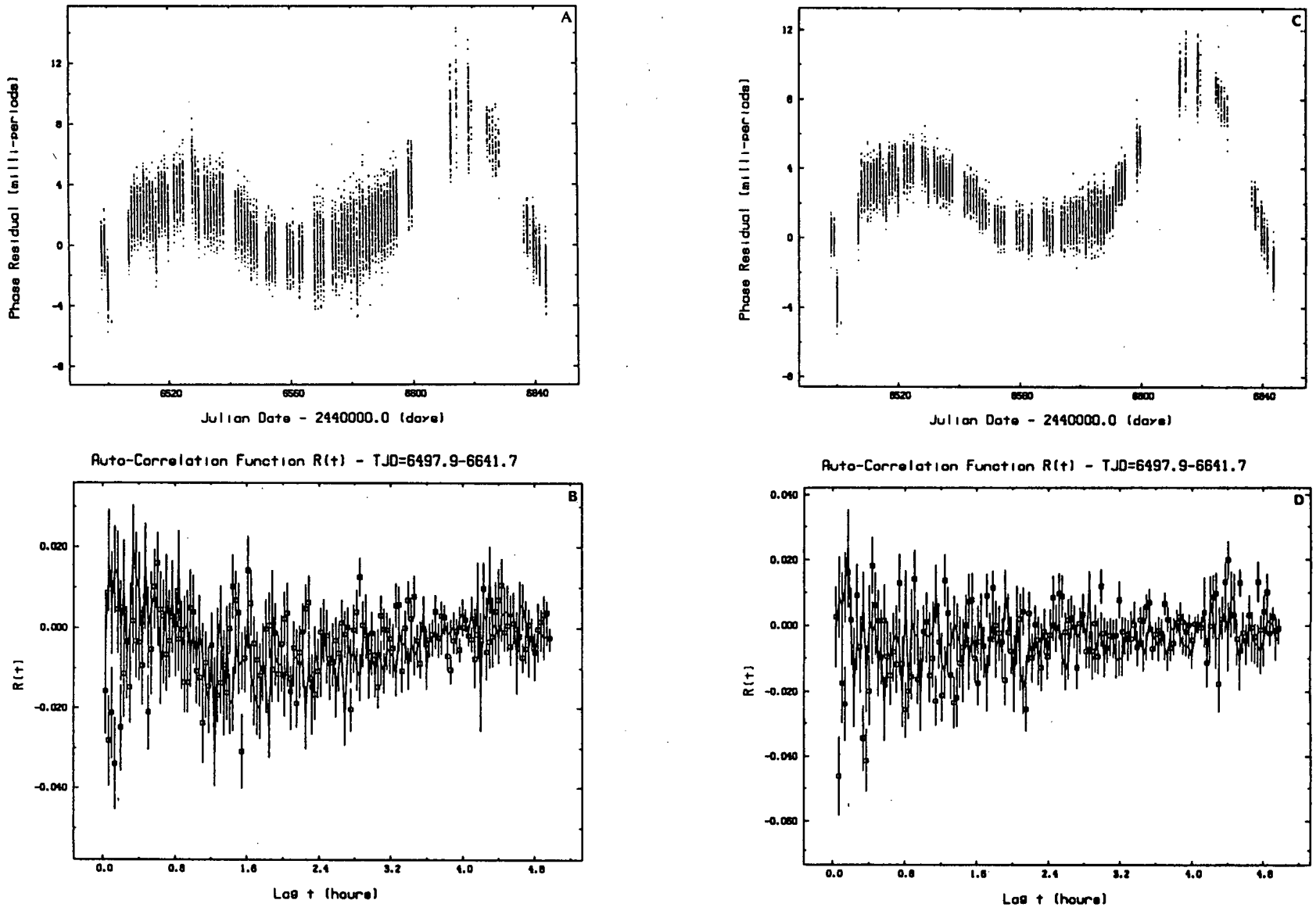

Fig. K.1. Residuals for (a) model 43 applied to 635 MHz data, and (c) model 44 applied to 954 MHz data. (b) and (d) corresponding mean autocorrelation functions obtained with a bin width of 2 minutes.

APPENDIX L - PUBLICATIONS

Klekociuk, A.R., McCulloch, P.M., and Hamilton, P.A., 1985. *I.A.U. Circ.* **4089**.

Ellis, G.R.A., Klekociuk, A.R., Woods, A.C., Reber, G., Goldstone, G.T., Burns, G., Dyson, P., Essex, E., and Mendillo, M., 1986. "Low-Frequency Radioastronomical Observations During the Spacelab 2 Plasma Depletion Experiment", *Aust. Physicist,* **24**, 56.

Ellis, G.R.A., Klekociuk, A.R., G., Goldstone, and Mendillo, M., 1986. "Radio Astronomy Through an Artificial Ionospheric Window - Spacelab 2 Observations", *Proc. Astron. Soc. Aust.,* **6**, 331.

Ellis, G.R.A., Klekociuk, A.R., Woods, A.C., Reber, G., Goldstone, G.T., Burns, G., Dyson, P., Essex, E., and Mendillo, M.,1988. "Low Frequency Radioastronomical Observations Associated with Ionospheric Plasma Depletion Experiments", *Advances in Space Research* , **8**, 63-66.

Klekociuk, A.R., 1987. "VLF Propagation Observations During the GLE of 1984 February 16", *Report UAG-96, WDC-A for Solar-Terrestrial Physics,* 265-268.

McCulloch, P.M., Klekociuk, A.R., Hamilton, P.A., and Royle, G.W.R., 1987. "Observations of Three Period Jumps of the Vela Pulsar", *Aust. J. Phys.*, **40**, 725.

Mendillo, M., Baumgardner, J., Allen, D., Foster, J., Holt, J., Ellis, G.R.A., Klekociuk, A.R., Reber, G., 1987. "Spacelab-2 Plasma Depletion Experiments for Ionospheric and Radiastronomical Studies", *Science,* **238**, 1260-1264.

Mendillo, M., Baumgardner, J., Ellis, G.R.A., Klekociuk, A.R., Reber, G., 1988. "Spacelab-2 Plasma Depletion Experiments and the Galactic Background Radiation", *Astrophys. Lett. Comm. (in press).*

Klekociuk, A.R., McCulloch, P.M., Hamilton, P.A., Flanagan, C., and Royle, G.W.R., 1989."Timing Measurements of the Vela Pulsar I : Glitches" *(In preparation).*

Klekociuk, A.R., McCulloch, P.M., Hamilton, P.A., Flanagan, C., and Royle, G.W.R., 1989. "Timing Measurements of the Vela Pulsar II : Timing Noise" *(In preparation)*.

REFERENCES

Arons, J., 1979. *Space Sci. Rev.*, **24**, 437.

Arons, J., 1981. *Astrophys. J.*, **248**, 1099.

Arons, J., 1983. *Astrophys. J.*, **266**, 215.

Arons, J., and Scharelemann, 1979. *Astrophys. J.*, **231**, 854.

Ables, J.G., Komesaroff, M.M., and Hamilton, P.A., 1970. *Astrophys. Letters*, **6**, 147.

Ables, J.G., and Manchester, R.N., 1974. *Astron. Astrophys.*, **50**, 177.

Alpar, M.A., 1977. *Astrophys. J.*, **213**, 527.

Alpar, M.A., and Ho, C., 1983. *Mon. Not. R. astr. Soc.*, **204**, 655.

Alpar, M.A., and Ögelman, H., 1987. *Astron. Astrophys.*, **185**, 196.

Alpar, M.A., and Sauls, J.A., 1988. *Astrophys. J.*, **327**, 723.

Alpar, M.A., Anderson, P.W., Pines, D., and Shaham, J., 1981. *Astrophys. J.*, **249**, L29.

Alpar, M.A., Anderson, P.W., Pines, D., and Shaham, J., 1984a. *Astrophys. J.*, **276**, 325.

Alpar, M.A., Anderson, P.W., Pines, D., and Shaham, J., 1984b. *Astrophys. J.*, **278**, 791.

Alpar, M.A., Cheng, K.S., Pines, D., and Shaham, J., 1988. *Mon. Not. R. astr. Soc.*, **233**, 25.

Alpar, M.A., Langer, S.A., and Sauls, J.A., 1984. *Astrophys. J.*, **282**, 533.

Alpar, M.A., Nandkumar, R., and Pines, D., 1985. *Astrophys. J.*, **288**, 191.

Alpar, M.A., Nandkumar, R., and Pines, D., 1986. *Astrophys. J.*, **311**, 197. (ANP)

Anderson, P.W., Alpar, M.A., Pines, D., and Shaham, J., 1981. in *IAU Symposium 95, Pulsars*, ed. R. Wielebinski and W. Sieber, Dordrecht, Reidel, p. 299.

Anderson, P.W., and Itoh, N., 1975. *Nature*, **256**, 25.

Armstrong, J.W., 1984. *Nature*, **307**, 527.

Armstrong, J.W., and Rickett, B.J., 1981. *Mon. Not. R. astr. Soc.*, **194**, 623.

Ash, M.E., Shapiro, I.I., and Smith, W.B., 1967, *Astron. J.*, **72**, 338.

Astronomical Almanac, The, 1987. U.S. Government Printing Office, Washington DC.

Baade, W., and Zwicky, F., 1934. *Phys. Rev.*, **45**, 138.

Backer, D.C., 1974. *Astrophys. J.*, **190**, 667.

Backer, D.C., and Hellings, R.W., 1986. *Ann. Rev. Astron. Astrophys.*, **24**, 537.

Backus, P.R., Taylor, J.H., and Damashek, M., 1982. *Astrophys. J.*, **255**, L63.

Barcons, X., Portilla, M., and Sanz, J.L., 1988, *Astrophys J.*, **331**, 397.

Barnard, J.J., and Arons, J., 1982. *Astrophys. J.*, **254**, 713.

Baym, G., and Pines, D., 1971. *Annals of Physics*, **66**, 816.

Baym, G., Lamb, D.Q., and Lamb, F.K., 1976. *Astrophys. J.*, **208**, 829.

Baym, G., Pethick, C., and Pines, D., 1969a. *Nature*, **224**, 673. (BPP)

Baym, G., Pethick, C., and Pines, D., 1969b. *Nature*, **224**, 674.

Baym, G., Pethick, C., Pines, D., and Ruderman, M., 1969. *Nature*, **224**, 872.

Baym., G., and Pethick, C., 1975. *Ann. Rev. Nucl. Sci.*, **25**, 27.

Baym., G., and Pethick, C., 1979. *Ann. Rev. Astron. Astrophys.*, **17**, 415.

Bedford, G., Bodo, G., and Ferrari., A., 1978. Astron. Astrophys., **70**, 815.

Bennett, K., Bignami, G.F., Boella, G., Buccheri, R., Hermsen, W., Kanbach, G., Lichti, G.G., Masnou, J.L., Mayer-Hasselwander, H.A., Paul, J.A., Scarsi, L., Swanenburg, B.H., Taylor, B.G., and Wills, R.D., 1977. *Astron. Astrophys.*, **61**, 279.

Bhat, P.N., Gupta, S.K., Ramana Murthy, P.V., Sreekantan, B.V., Tonwar, S.C., and Viswanath, P.R., 1987. *Astron. Astrophys.*, **178**, 242.

Biggs, J.D., Lyne, A.G., Hamilton, P.A., McCulloch, P.M., and Manchester, R.N., 1988. *Mon. Not. R. astr. Soc.*, **235**, 255.

Bignami, G.F., and Caraveo, P.A., 1988. *Astrophys. J. Letters*, **325**, L5.

Bignami, G.F., and Hermsen, W., 1983. *Ann. Rev. Astron. Astrophys.*, **21**, 67.

Blandford, R.D., and Ostriker, J.P., 1978. *Astrophys. J.*, **221**, L29.

Blandford, R.D., Appelgate, J.H., and Hernquist, L., 1983. *Mon. Not. R. astr. Soc.*, **204**, 1025.

Blandford, R., Narayan, R., and Romani, R.W., 1984. *J. Astrophys. Astr.*, **5**, 369. (BNR)

Blandford, R., and Narayan, R., 1985. *Mon. Not. R. astr. Soc.*, **213**, 591.

Blandford, R.D., and Romani, R.W., 1988. *Mon. Not. R. astr. Soc.*, **234**, 57p. (BR)

Boynton, P.E., 1981. in *IAU Symposium 95, Pulsars*, ed. R. Wielebinski and W. Sieber, Dordrecht, Reidel, p. 279.

Boynton, P.E., Deeter, J.E., Lamb, F.K., and Zylstra, G., 1986. *Astrophys. J.*, **307**, 545.

Boynton, P.E., Deeter, J.E., Lamb, F.K., and Zylstra, G., Pravdo, S.H., White, N.W., Wood, K.s., and Yentis, D.J., 1984. *Astrophys. J.*, **283**, L53.

Boynton, P.E., Groth, E.J., Hutchinson, D.P., Nanos, G.P.Jr., Partridge, R.B., and Wilkinson, D.T., 1972. *Astrophys. J.*, **175**, 217.

Brandt, J.C., Strecher, T.P., Crawford, D.L., and Maran, S.P., 1971. *Astrophys. J.*, **163**, L99.

Bruhweiler, F.C., Kafatos, M., and Brandt, J.C., 1983. *Comments Astrophys.*, **10**, 1. (BKB)

Canuto, V., and Chitre, S.M., 1973. *Phys. Rev. Lett.*, **30**, 999.

Caraveo, P.A., Bignami, G.F., Mitrofanov, I., and Vacanti., G., 1987. *Astrophys. J.*, **327**, 203.

Cesarsky, C.J., 1981. *Ann. Rev. Astron. Astrophys.*, **18**, 289.

Cheng, A.F., 1985. *Astrophys. J.*, **299**, 917.

Cheng, A.F., 1989. *Astrophys. J.*, **337**, 803.

Cheng, A.F., and Ruderman, M.A., 1977b. *Astrophys. J.*, **214**, 598.

Cheng, A.F., and Ruderman, M.A., 1980. *Astrophys. J.*, **235**, 576.

Cheng, A.F., Ruderman, M.A., and Sutherland, P., 1976. *Astrophys. J.*, **203**, 209.

Cheng, K.S., 1987a. *Astrophys. J.*, **321**, 799.

Cheng, K.S., 1987b. *Astrophys. J.*, **321**, 805.

Cheng, K.S., Alpar, M.A., Pines, D., and Shaham, J., 1988. *Astrophys. J.*, **330**, 835.

Cheng, K.S., Ho, C., and Ruderman, 1986a. *Astrophys. J.*, **300**, 500.

Cheng, K.S., Ho, C., and Ruderman, 1986b. *Astrophys. J.*, **300**, 522.

Coles, W.A., Frehlich, R.G., Rickett, B.J., and Codona, J.L., 1987. *Astrophys. J.*, **315**, 666.

Cordes, J.M., 1978. *Astrophys. J.*, **222**, 1006.

Cordes, J.M., 1980. *Astrophys. J.*, **237**, 216.

Cordes, J.M., 1986. *Astrophys. J.*, **311**, 183.

Cordes, J.M., and Downs, G.S., 1985. *Astrophys. J. Suppl.*, **59**, 343. (CD)

Cordes, J.M., and Greenstein, G., 1981. *Astrophys. J.*, **245**, 1060.

Cordes, J.M., and Helfand, D.J., 1980. *Astrophys. J.*, **239**, 640.

Cordes, J.M., Downs, G.S., and Krause-Polstorff, J., 1988. *Astrophys. J.*, **330**, 847. (CDK-P)

Cordes, J.M., Piderwebetsky, A., and Lovelace, R.V.E., 1986. *Astrophys. J.*, **310**, 737. (CPL)

Cordes, J.M., Weisberg, J.M., and Boriakoff, V., 1985. *Astrophys. J.*, **288**, 221. (CWB)

Davies, K., and Hartmann, G.K., 1976. *J. Geophys. Res.*, **81**, 3431.

Deeter, J.E., 1984. *Astrophys. J.*, **281**, 482.

Deeter, J.E., and Boynton, P.E., 1982. *Astrophys. J.*, **261**, 337. (DB)

Deeter, J.E., and Boyntron, P.E., 1986. in *Proc. of the Workshop on Timing Studies of X-Ray Sources*, ed. S. Hayakawa and F. Nagase, Nagoya, Nagoya University p. 29.

Deeter, J.E., Boynton, P.E., Lamb, F.K., and Zylstra, G., 1989. *Astrophys. J.*, **336**, 376.

Demiahski, M., and Prószyhski, M., 1983. *Mon. Not. R. astr. Soc.*, **202**, 437.

Dixon, W.J., and Massey, F.J., 1985. *Introduction to Statistical Analysis, 4th Edition*, McGraw-Hill, Singapore.

Dobrowolny, M., and Ferrari, A., 1976. *Astron. Astrophys.*, **47**, 97.

Downs, G.S., 1981a. in *IAU Symposium 95, Pulsars*, ed. R. Wielebinski and W. Sieber, Dordrecht, Reidel, p. 277.

Downs, G.S., 1981b. *Astrophys J.*, **249**, 687.

Downs, G.S., 1982. *Astrophys J.*, **257**, L67.

Downs, G.S., and Krause-Polstorff, J., 1986. *Astrophys J. Suppl.*, **62**, 81. (DK-P)

Downs, G.S., and Reichley, P.E., 1983. *Astrophys. J. Suppl.*, **53**, 169.

Easson, I., 1979a. *Astrophys. J.*, **228**, 257.

Easson, I., 1979b. *Astrophys. J.*, **233**, 711.

Ebel, A., Schmidt, G., and Taurianen, A., 1976. *J. atmos. terr. Phys.*, **38**, 207.

Ellison, D.C., and Kazanas, D., 1983. *Astron. Astrophys.*, **128**, 102.

Epstein, R.I., and Baym, G., 1988. *Astrophys. J.*, **328**, 680.

Feibelman, P.J., 1971. *Phys. Rev. D.*, **4**, 1589.

Ferguson, D.C., 1981. *Comments Astrophys.*, **9**, 127.

Flanagan, C., and Hamilton, P.A., 1988. *IAU Circ.*, **4695**.

Flowers, E.G., Lee, J-F., Ruderman, M.A., Sutherland, P.G., Hillebrant, W., and Müller, E., 1977. *Astrophys. J.*, **215**, 291.

Fomalont, E.B., Goss, W.M., Lyne, A.G., and Manchester, R.N., 1984. *Mon. Not. R. astr. Soc.*, **210**, 113.

Gallino, R., and Silvestro, G., 1971. *Geophys. and Space Sci.*, **12**, 415.

Goldstein, S.J., and James, J.T., 1969. *Astrophys. J.*, **158**, L179.

Green, D.A., 1984. *Mon. Not. R. astr. Soc.*, **209**, 449.

Greenstein, G., 1970. *Nature*, **227**, 791.

Greenstein, G., 1975. *Astrophys. J.*, **200**, 281.

Greenstein, G., 1976. *Astrophys. J.*, **208**, 836.

Greenstein, G., 1979. *Astrophys. J.*, **231**, 880.

Greenstein, G., 1981. in *IAU Symposium 95, Pulsars*, ed. R. Wielebinski and W. Sieber, Dordrecht, Reidel, p. 291.

Greenstein, G., and Cameron, A.G.W., 1969. *Nature*, **222**, 862.

Grenier, I.A., Hermsen, W., and Clear, J., 1988. *Astron. Astrophys.*, **204**, 117.

Groth, E.J., 1975a. *Astrophys. J. Suppl.*, **29**, 431.

Groth, E.J., 1975b. *Astrophys. J. Suppl.*, **29**, 443.

Groth, E.J., 1975c. *Astrophys. J. Suppl.*, **29**, 453.

Gullahorn, G.E., and Rankin, J.M., 1978. *Astrophys. J.*, **83**, 1219.

Gullahorn, G.E., and Rankin, J.M., 1982. *Astrophys. J.*, **260**, 520.

Gullahorn, G.E., Payne, R.R., Rankin, J.M., and Richards, D.W., 1976. *Astrophys. J.*, **205**, L151.

Hamilton, P.A., Hall, P.J., and Costa, M.E., 1985. *Mon. Not. R. astr. Soc.*, **214**, 5p.

Hamilton, P.A., King, E.A., McConnell, D., McCulloch, P.M., 1989. I.*A.U. Circ.*, **4708**.

Hamilton, P.A., McCulloch, P.M., Manchester, R.N., Ables, J.G., and Komesaroff, M.M., 1977. *Nature*, **265**, 224.

Harding, D., Guyer, R.A., and Greenstein, G., 1978. *Astrophys. J.*, **222**, 991.

Harnden, F.R.Jr., Grant, P.D., Seward, F.D., and Kahn, S.M., 1985. *Astrophys. J.*, **299**, 828.

Harvey, J.A., Ruderman, M.A., and Shaham, J., 1986. *Phys. Rev. D.*, **33**, 2084.

Hearn, D.R., Larsen, S.E., and Richardson, J.A., 1980. *Astrophys. J.*, **235**, L67.

Hellings, R.W., and Downs, G.S., 1983. *Astrophys. J.*, **265**, L39.

Hertz, D., and Azaria, M., 1985. *Signal Processing*, **8**, 235.

Higdon, J.C., 1984. *Astrophys. J.*, **285**, 109.

Higdon, J.C., 1986. *Astrophys. J.*, **309**, 342.

Howell, J.Q., 1975. *IEEE Trans. Antennas Propag.*, **23**, 90.

Irvine, J.M., 1978. *Neutron Stars*, Oxford University Press, Oxford.

Jenkins, E.B., Wallerstein, G., And Silk, J., 1984. *Astrophys. J.*, **278**, 649.

Jones, P.B., 1988. *Mon. Not. R. astr. Soc.*, **235**, 545.

Joss, P.C., and Rappaport, S.A., 1984. *Ann. Rev. Astron. Astrophys.*, **22**, 537.

Kendall, M.G., 1948. *The Advanced Theory of Statistics, Volume II*, Griffin, London.

Kennel, C.F., and Coroniti, F.V. 1984. *Astrophys. J.*, **90**, 163.

Klekociuk, A.R., McCulloch, P.M., and Hamilton, P.A., 1985. *IAU Circ.* **4089**.

Komesaroff, M.M., Ables, J.G., and Hamilton, P.A., 1971. *Astrophys. Letters*, **9**, 101.

Komesaroff, M.M., Hamilton, P.A., and Ables, J.G., 1972. *Aust. J. Phys.*, **25**, 759.

Krauss, J., 1986. *Radioastronomy, 2nd Edition*, Cygnus-Quasar Books, Ohio.

Krishnamohan, S., and Downs, G.S., 1983. *Astrophys. J.*, **265**, 372. (KD)

Lamb, F.K., Pines, D., and Shaham, J., 1978a. *Astrophys. J.*, **224**, 969.

Lamb, F.K., Pines, D., and Shaham, J., 1978b. *Astrophys. J.*, **225**, 582.

Large, M.I., Vaughan, A.E., and Mills, B.Y., 1968. *Nature*, **220**, 340.

Lee, L.C., and Jokipii, J.R., 1976. *Astrophys. J.*, **206**, 735.

Lewin, W.H.G., and Joss, P.C., 1981. *Space Sci. Rev.*, **28**, 3.

Lindsey, W.C., and Chie, C.M., 1976. *Proc. IEEE*, **64**, 1652.

Lodenquai, J., 1984. *Astrophys. Letters*, **24**, 91.

Loshen, E., 1972. *Nature Physical Science*, **236**, 70.

Loshen, E., 1975. *Nature*, **258**, 688.

Loshen, E., 1981. *Astron. Astrophys. Suppl.*, **44**, 1.

Lyne, A.G., 1987. *Nature*, **326**, 569.

Lyne, A.G., and Pritchard, R.S., 1987. *Mon. Not. R. astr. Soc.*, **229**, 223.

Lyne, A.G., and Rickett, B.J., 1968. *Nature*, **219**, 1139.

Lyne, A.G., Pritchard, R.S., and Smith, F.G., 1988. *Mon. Not. R. astr. Soc.*, **233**, 667.

Manchester, R.N., 1987. in *IAU Symposium 125, The Origin and Evolution of Neutron Stars*, ed. D.J.Helfand and J.-H. Huang, Dordrecht, Reidel, p. 3.

Manchester, R.N., and Taylor, J.H., 1974. *Astrophys. J.*, **191**, L63.

Manchester, R.N., and Taylor, J.H., 1977. *Pulsars*, Freeman, San Fransisco.

Manchester, R.N., Lyne, A.G., Goss, W.M., Smith, F.G., Disney, M.J., Hartley, K.F., Jones, D.H.P., Willgate, G.B., Danziger, I.T., Muriden, P.G., Peterson, B.A., and Wallace, P.T., 1978a. *Mon. Not. R. astr. Soc.*, **184**, 159.

Manchester, R.N., Murray, J.D., and Radhakrishnan, V., 1969. *Astrophys. Letters*, **4**, 229.

Manchester, R.N., Newton, L.M., Goss, W.M., and Hamilton, P.A., 1978b. *Mon. Not. R. astr. Soc.*, **184**, 35p.

Manchester, R.N., Hamilton, P.A., and McCulloch, P.M., 1980. *Mon. Not. R. astr. Soc.*, **192**, 153.

Manchester, R.N., Wallace, P.T., Peterson, B.A., and Elliot, K.H., 1980. *Mon. Not. R. astr. Soc.*, **190**, 9p.

Manchester, R.N., Newton, L.M., Hamilton, P.A., and Goss, W.M., 1983. *Mon. Not. R. astr. Soc.*, **202**, 269.

Mashhoon, B., 1982. *Mon. Not. R. astr. Soc.*, **199**, 659.

Matese, J.J., and Whitmire, D.P., 1980. *Astrophys. J.*, **235**, 587.

McAdam, W.B., 1981. *Proc. Astron. Soc. Australia*, **4**, 219.

McCulloch, P.M., Hamilton, P.A., Manchester, R.N., and Ables, J.G., 1978. *Mon. Not. R. astr. Soc.*, **183**, 645.

McCulloch, P.M., Hamilton, P.A., Royle, G.W.R., and Manchester, R.N., 1983. *Nature*, **302**, 319.

McCulloch, P.M., Klekociuk, A. R., Hamilton, P.A., and Royle, G.W.R., 1987. *Aust. J. Phys.*, **40**, 725.

McKee, C.F., and Ostriker, J.P., 1977. *Astrophys. J.*, **218**, 148.

Meeus, J., 1979. *Astronomical Formulae for Calculators,* Volkssternwacht Urania, Hove.

Metsel, L., 1971. *Nature Physical Science*, **233**, 149.

Michel, F.C., 1975. *Astrophys. J.*, **198**, 683.

Michel, F.C., 1982. *Rev. Mod. Phys.*, **54**, 1.

Michel, F.C., 1987. *Astrophys. J.*, **322**, 822.

Michel, F.C., and Dessler, A.J., 1981. *Astrophys. J.*, **251**, 654.

Migdal, A.B., 1959. *Zh. Eksp. Teor. Fiz.*, **37**, 243. [translation : 1960. *Soviet Physics J.E.T.P.*, **37**, 176.]

Migdal, A.B., Chernoustsan, A.I., and Mishustin, I.N., 1978. *Phys. Letters*, **83B**, 158.

Milne, D.K., *Aust. J. Phys.*, 1968. **21**, 201.

Muhleman, D.O., and Anderson, J.D., 1981. *Astrophys. J.*, **247**, 1093.

Mulholland, J.D., 1971. *Astrophys. J.*, **165**, 105.

Negele, J.W., and Vautherin, D., 1973. *Nucl. Phys. A*, **207**, 298.

Neuhauser, D., and Koomin, S.E., 1987. *Phys. Rev. A, Gen. Phys.*, **36**, 4163.

Newton, L.M., Manchester, R.N., and Cooke, D.J., 1981. *Mon. Not. R. astr. Soc.*, **194**, 841.

Nomoto, K., and Tsuruta, S., 1986. *Astrophys. J.*, **305**, 49.

Oppenheimer, J.R., and Volkoff, G.M., 1939. *Phys. Rev.*, **55**, 374.

Packard, R.E., 1972. *Phys. Rev. Letters*, **28**, 1080.

Padmaraj, M.C., and Nair, S.C.K., 1985. *J. Astron. Astrophys.*, **6**, 165.

Pandharipande, V.R., and Smith, R.A., 1975. *Nuclear Phys. A.*, **237**, 507.

Pandharipande, V.R., Pines, D., and Smith, R.A., 1976. *Astrophys. J.*, **208**, 550. (PPS)

Peng, Q-H., Huang, K-L., and Huang, J-H., 1982. *Astron. Astrophys.*, **107**, 258.

Perley, R.A., 1982. *Astron. J.*, **87**, 859.

Peterson, B.A., Murdin, P., Wallace, P., Manchester, R.N., Penney, A.J., Jorden, A., Hartley, K.F., and King, D., 1978. *Nature*, **276**, 475.

Pines, D., and Alpar, M.A., 1985. *Nature*, **316**, 27.

Pines, D., and Shaham, J., 1972. *Nature Physical Science*, **236**, 71.

Pines, D., Shaham, J., Alpar, M.A., and Anderson, P.W., 1980. *Progress Theoretical Phys. Suppl.*, **69**, 376.

Pines, D., Shaham, J., and Ruderman, M., 1972. *Nature*, **237**, 83. (PSR)

Preston, R.A., Jauncey, D.L., Tsiousmis, A., Meler, D.L., Skjerve, L.H., Ables, J., Batchelor, R., Faulkner, J., Hamilton, P.A., McCulloch, P., Hayes, R., Johnson, B., Louie, A., Niell, A.E., Robertson, J.G., Royle, G.W.R., Slade, M.A., Slee, O.B.,Watkinson, A.,Wehrle, A.E., Wright, A., 1984. in *IAU Symposium 110, VLBI and Compact Radio Sources,* ed. R. Fanti *et al.*, Reidel, Dordrecht, p. 67.

Radhakrishnan, V., and Cooke, D.J., 1969. *Astrophys. Letters*, **3**, 225.

Radhakrishnan, V., and Manchester, R.N., 1969. *Nature*, **222**, 228.

Radhakrishnan, V., Cooke, D.J., Komesaroff, M.M., and Morris, D., 1969. *Nature*, **221**, 443.

Rankin, J.M., 1983. *Astrophys. J.*, **274**, 333.

Rankin, J.M., and Counselman, C.C. III, 1973. *Astrophys. J.*, **181**, 875.

Rankin, J.M., Campbell, D.B., Isaacman, R.B., and Payne, R.R., 1988. *Astron. Astrophys.*, **202**, 166.

Rawley, L.A., Taylor, J.H., and Davis, M.M., 1988. *Astrophys. J.*, **326**, 947.

Rees, M.J., and Gunn, J.E., 1974. *Mon. Not. R. astr. Soc.*, **167**, 1.

Reichley, P.E., and Downs, G.S., 1969. *Nature*, **222**, 229.

Reynolds, R.J., 1976. *Astrophys. J.*, **206**, 679.

Richards, D.W., Pettengill, G.H., Counselman, C.C. III, and Rankin, J.M., 1970. *Astrophys. J.*, **160**, L1.

Rickett, B.J., 1970. *Mon. Not. R. astr. Soc.*, **150**, 67.

Rickett, B.J., 1977. *Ann. Rev. Astron. Astrophys.*, **15**, 479.

Rickett, B.J., Coles, W.A., and Bourgois, G., *Astron. Astrophys.*, **134**, 390.

Roberts, J.A., and Ables, J.G., 1982. *Mon. Not. R. astr. Soc.*, **201**, 1119.

Romani, R.W., and Taylor, J.H., 1983. *Astrophys. J.*, **265**, L35.

Romani, R.W., Narayan, R., and Blandford, R., 1986. *Mon. Not. R. astr. Soc.*, **220**, 19. (RNB)

Rosen, L.C, and Cameron, A.G.W., 1972. *Astrophys. and Space Sci.*, **15**, 137.

Ruderman, M., 1968. *Nature*, **218**, 1128.

Ruderman, M., 1969. *Nature*, **223**, 597.

Ruderman, M., 1970. *Nature*, **225**, 619.

Ruderman, M., 1974. in *IAU Symposium 53, Physics of Dense Matter*, ed. C.J.Hansen, Dordrecht, Reidel, p. 117.

Ruderman, M., 1976. *Astrophys. J.*, **203**, 213.

Ruderman, M., 1981. in *IAU Symposium 95, Pulsars*, ed. R. Wielebinski and W. Sieber, Dordrecht, Reidel, p. 87.

Ruderman, M., and Sutherland, P.G., 1974. *Astrophys. J.*, **190**, 137.

Ruderman, M.A., 1968. *Nature*, **218**, 1128.

Ruderman, M.A., and Sutherland, P.G., 1975. *Astrophys. J.*, **196**, 51.

Rutman, J., 1978. *Proc. IEEE*, **66** 1048.

Sauls, J.A., Stein, D.L., and Serene, J.W., 1982. *Phys. Rev. D.*, **25**, 967.

Scargle, J.D., 1969. Astrophys. J., **156**, 401.

Sedrakyan, D.M., 1986. *Astrofizika*, **25**, 323. [translation: 1987. *Soviet Astrophys.*, **26**, 539.]

Shaham, J., 1977. *Astrophys. J.*, **214**, 251.

Shaham, J., 1986. *Astrophys. J.*, **310**, 780.

Shakhabasyan, K.M., 1986. *Astrofizika*, **25**, 533. [translation : 1987. *Soviet Astrophys*, **25**, 665.]

Simonetti, J.H., Cordes, J.M., and Heeschen, D.S., 1985. *Astrophys. J.*, **296**, 46.

Smith, A., and Pounds, K.A., 1977. *Nature*, **265**, 121.

Sonin, E.B., 1987. *Rev. Modern Phys.*, **59**, 87.

Spangler, S.R., Mutel, R.L., Benson, J.M., and Cordes, J.M. 1986. *Astrophys. J.*, **301**, 312.

Stothers, R., 1980. *Publ. Astron. Soc. Pacific*, **22**, 145.

Sturrock, P.A., 1971. *Astrophys. J.*, **164**, 529.

Tanenbaum, B.S, Zeissig, G.A., and Drake, F.D., 1968. *Science*, **160**, 760.

Taylor, J.H, and Stinebring, D.R., 1986. *Ann. Rev. Astron. Astrophys.*, **24**, 285.

Taylor, J.H., and Manchester, R.N., 1975. *Astron. J.*, **80**, 794.

Tholen, D.J., 1985. *Astron. J.*, **90**, 2353.

Thompson, D.J., Fichtel, C.E., Kniffen, D.A., Ögelman, H.B., 1977. *Astrophys. J.*, **214**, L17.

Trümper, J., Kahabka, P., Ögelman, H., Pietsch, W., and Voges, W., 1986. *Astrophys. J.*, **300**, L63.

Tsuruta, S., 1986. *Comments Astrophys.*, **11**, 151.

Tsuruta, S., and Cameron, G.W., 1966. *Can. J. Phys.*, **44**, 1863.

Tümer, O.T., Dayton, B., Long, J., O'Neill, T., Zych, A., White, R.S., 1984. *Nature*, **310**, 214.

van den Heuvel, E.P.J., 1987. in *IAU Symposium 125, The Origin and Evolution of Neutron Stars*, ed. D.J.Helfand and J.-H. Huang, Dordrecht, Reidel, p. 393.

van der Klis, M., 1987. in *IAU Symposium 125, The Origin and Evolution of Neutron Stars*, ed. D.J.Helfand and J.-H. Huang, Dordrecht, Reidel, p. 321.

White, N.E., Swank, J.H., and Holt, S.S., 1983. *Astrophys. J.*, **270**, 711.

Woolsey, S.E., and Weaver, T.A., 1986. *Ann. Rev. Astron. Astrophys.*, **24**, 205.

Wolszczan, A., Kulkarni, S.R., Middleditch, J., Backer, D.C., Fruchter, A.S., and Dewey, R.J., 1989. *Nature*, **337**, 531.

Yang, D.H., and Clark, J.W., 1971. *Nucl. Phys. A.*, **174**, 49.